INVESTIGATION OF THE DILUTION EFFECT ON LAMINAR FLAME CHARACTERISTICS IN A CONSTANT VOLUME COMBUSTION CHAMBER

By

Berk Can Duva

A DISSERTATION

Submitted to
Michigan State University
in partial fulfillment of the requirements
for the degree of

Mechanical Engineering-Doctor of Philosophy

2021

ABSTRACT

INVESTIGATION OF THE DILUTION EFFECT ON LAMINAR FLAME CHARACTERISTICS IN A CONSTANT VOLUME COMBUSTION CHAMBER

By

Berk Can Duva

With increased interest in reducing emissions, the axial (sequential) stage combustion concept for gas turbine combustors and high exhaust gas recirculation rates for internal combustion engines are gaining in popularity. Despite the air-quality benefits of these technologies, introduction of inert combustion residuals into a combustion media affects the flame reactivity and stability. This dissertation examines the dilution effect on laminar flame characteristics of iso-octane/air, high/low research octane number gasoline/air, and methane/air mixtures through both experiments and numerical simulations.

Spherically expanding flames under constant pressure are employed in an optically accessible constant volume combustion chamber to measure fundamental characteristics of premixed flames. Spherically expanding flames are severely affected by flame stretch in the early stage of combustion and therefore stretch models are of great importance in determining the uncertainty of experimental laminar flame speeds and burned gas Markstein lengths. In order to prevent the existing large scatter in experimental data of these two fundamental flame parameters, the effect of the lower radius limit for the flame speed calculation on extrapolation results of the stretch models is investigated in Chapter 3. Results show that there is a critical lower radius limit, where all laminar flame speed and burned gas Markstein length values obtained by the extrapolation of the stretch models converge to the same laminar flame speed and burned gas Markstein length.

Chapter 4 presents the exhaust gas recirculation effect on CO₂-diluted iso-octane/air and high/low research octane number gasoline/air mixtures at 1 bar and 373-473 K. The results of the measurements reveal that flame speeds of commercial gasolines do not vary significantly with the research octane number whereas the iso-octane flame speeds are consistently slower than those of gasoline. Numerical analyses are used to determine the dilution, thermal-diffusion, and chemical effects of the CO₂ dilution on the flame speed, stretch, and stability.

Over the years, many studies have investigated diluted methane flame characteristics with one of the main exhaust gases or a mixture of two. Chapter 5 experimentally and computationally shows that real combustion residuals cannot be accurately represented with only one or two of the main exhaust gases, as the thermodynamic properties and chemical reactivities of the combustion residuals are very distinctive and vary with temperature, pressure, and equivalence and dilution ratios. In Chapter 5, laminar burning velocity and burned gas Markstein length correlations are developed from the methane/air flame measurements at 1-5 bar, 373-473 K, and with 0–15% dilution. The physical and chemical aspects of changes in the laminar burning velocity and flame front stability due to changes in temperature, pressure, and equivalence and dilution ratios are discussed in detail.

To my beloved family

ACKNOWLEDGEMENTS

This dissertation presents several series of experiments and numerical analyses on combustion characteristics of various fuel/oxidizer mixtures, some of which were financially supported by Fiat Chrysler Automobiles (FCA) US LCC. Therefore, I would like to thank FCA US LCC for their financial support and my colleagues from FCA US LLC, Amit Shrestha, Soumya Gudiyella, Fadi Estefanous, and Lurun Zhong, who provided insight and expertise that assisted this research.

My foremost appreciation goes to my supervisor, Dr. Elisa Toulson, for the endless support, experience, and guidance that she has provided me during my studies. She has valued my ideas and given chances to pursue them, for which I am very grateful. She has always created opportunities and encouraged me to improve my technical knowledge. She is a perfect problem solver even under pressure, which has relieved my burden. More importantly, she went out of her way to make me feel welcome not only in her research group but also in United States. Without her technical and mental support, I would have never been able to complete this dissertation.

I would like to express my appreciation to my PhD committee members, Prof. Indrek Wichman for many fruitful discussions on flames in general and on burning velocity and flame stretch in particular, Dr. Patton Manuel Allison for reviewing my research and providing insightful feedback, and Dr. Carl Lira for his evaluation and time.

I am deeply indebted to Tom Stuecken for his excellent technical assistance, without which I certainly never would have completed the experimental portion of this dissertation. I would like to acknowledge Jennifer Higel, Kevin Moran, Brian Rowley, Brian Deimling, and John Przybyl for their assistance in the design and construction of the constant volume combustion chamber. I also would like to thank Prof. Eric Petersen from Texas A&M University, Prof. Richard Stone

from University of Oxford, and Prof. Chung K. Law from Princeton University, who helped me to solve some design problems by sharing critical information about their combustion chamber designs.

I would like to acknowledge the contributions of my labmates for their support, advice, and most of all friendship during this time. They include Lauren Elizabeth Chance, Chaitanya Wadkar, Gerald Gentz, Masumeh Gholamisheeri, Prasanna Chinnathambi, and Grace Trombley. The undergraduate students who have worked in Dr. Elisa Toulson's research group also deserve recognition for their assistance with experiments, image processing, and numerical analysis. Many thanks to Yen-Cheng Wang, Nathan Engler, Sarah Plant, David Knapp, Andrew Dolenga, Zhan Liu, Claudia Chen, Jianyang Tang, and Jamal Nicholas Marquise Ardister. I also would like to thank Jaime Hainer for her help in processing the large number of schlieren images.

Very special thanks go to my parents who have always supported and encouraged me to further my education and have always been there for me throughout my entire life. Without their love, motivation, and endless sacrifice, I would not be able to come to this point. I owe my friends overseas a debt of gratitude for their moral support.

Finally, but most importantly, I am extremely grateful to my beautiful wife for her endless love, patience, friendship, support, and encouragement. She always believes in me and this made me keep going when the times got rough. Her "imaginative" songs have made even Michigan winters "warmer" and more enjoyable.

TABLE OF CONTENTS

LIST OF FIGURES	ix
LIST OF TABLES	xiv
KEY TO ABBREVIATIONS	xvi
1 INTRODUCTION	1 Turbine 5 9
2 BURNING VELOCITY OF LAMINAR PREMIXED FLAMES 2.1 Measurement Techniques for Laminar Burning Velocity. 2.2 Theory of Spherically Expanding Flames 2.2.1 Constant Volume Method. 2.2.1.1 Burned Mass Fraction Models. 2.2.2 Constant Pressure Method. 2.2.2.1 Stretch Correlations 2.2.3 PIV Method. 2.3 Flame Front Instabilities and Cellularity.	14 19 23 25 30 39
3 EXPERIMENTAL APPARATUS AND PROCEDURE AND COMBUMODELING. 3.1 Design and Hardware	5159698283848796
4 THE EXHAUST GAS RECIRCULATION EFFECT ON FUNDAM CHARACTERISTICS OF PREMIXED ISO-OCTANE/AIR AND GASOLI FLAMES. 4.1 Introduction and Literature Review	NE/AIR 115 115

	4.3	Numerical Results	122
	4.4	The CO ₂ Dilution Effect	124
4	4.5	Conclusions	128
_	T A	MINIAD EL AME CHADA CEEDICEICO DE DELMINED MEMIANE/AID I	
5 DI		MINAR FLAME CHARACTERISTICS OF PREMIXED METHANE/AIR F	
		ED WITH COMBUSTION RESIDUALS	
	5.1 5.2	Introduction and Literature Review The Equivalence Ratio Effect	
	5.2 5.3	The Unburned Gas Temperature Effect	
	5.3 5.4	The Initial Pressure Effect	
	5. 4 5.5	The Dilution Effect	
	5.6	Laminar Flame Speed Correlation	
	5.7	Burned Gas Markstein Length Correlation	
	5.8	Numerical Laminar Flame Speed Results	
	5.9	Conclusions	
6	SU	MMARY AND CONCLUDING REMARKS	174
۸ T	DENI	DICES	100
		ENDIX A: Technical Drawing of Main Cylindrical Body ENDIX B: Technical Drawing of Bolted End Cap	
		ENDIX C: Technical Drawing of Fused Quartz Window	
		ENDIX D: Technical Drawing of Window Cap	
		ENDIX E: Safety Factor Calculation for the Clamp between Bolted End Cap and	
	-	ENDIX F: Technical Drawing of Riser Support	
		ENDIX G: Technical Drawing of Gas Manifold	
		ENDIX H: Technical Drawings of Fuel Injector Assembly	
		ENDIX I: Laminar flame speeds, burned gas Markstein lengths, burned gas M	
		ers, and critical lower radius limits for the measurements with uncertainties	
		ENDIX J: Experimental and numerical laminar flame speeds and burned gas M	
		ns for methane/air, hydrogen/air, propane/air, and iso-octane/air mixtures for the v	
		perimental apparatus and procedure	
	APPE	ENDIX K: Numerical and experimental laminar burning velocity and burned gas N	Aarkstein
	lengtł	n results for iso-octane/air and high/low RON gasoline/air mixtures with and with	nout 15%
(CO_2 c	lilution at 1 bar and 373-473 K	196
		ENDIX L: Dilution effect of different combustion residuals on laminar burning v	
		urned gas Markstein lengths of premixed methane/air mixtures at 1 bar and 473	
		ENDIX M: Experimental and numerical laminar flame speed and burned gas N	
	length	n for diluted methane/air mixtures at 1-5 bar and 373-473 K.	200
RΙ	RI IO	GR A PHV	204

LIST OF FIGURES

Figure 1-1. Projected world energy consumption by energy source (left) and projected share of net electricity generation percent (right) by 2040, retrieved from [1]
Figure 1-2. Schematic of a typical gas turbine combustor, retrieved from [2]
Figure 1-3. Alstom GT24/GT26 sequential combustion system, retrieved from [31]
Figure 1-4. A schematic diagram of EGR system, retrieved from [43]
Figure 2-1. Schematic of the Bunsen burner (left [49]) and premixed biogas-hydrogen blending fuel Bunsen flames at different equivalence ratios (right [50])
Figure 2-2. Twin counter-flow/stagnation flames, retrieved from [13]
Figure 2-3. Schematic of the heat flux burner (left [55]) and premixed ethylene/air flat flames at different equivalence ratios (right [56])
Figure 2-4. Spherical flame propagation inside a constant volume combustion chamber (left) and cold flame front radius and pressure history for a methane/air mixture at 1 bar, 298 K and ϕ =1.0 after spark
Figure 2-5. Cold flame front radius growth and pressure history for a methane/air mixture at 1 bar, 298 K, and ϕ =1.0 showing the constant pressure region that is used for the laminar burning velocity measurements.
Figure 2-6. Schlieren images showing the cellular formation on the flame surface (left – stable flame, middle – thermal-diffusive cellularity, right – hydrodynamic cellularity)
Figure 3-1. Schematic of the optically accessible constant volume combustion chamber showing the schlieren imaging setup
Figure 3-2. Schematic of the screws between the main cylindrical body and the bolted end cap (left) and between the bolted end cap and the window cap (right)
Figure 3-3. Middle cross section of the constant volume combustion chamber
Figure 3-4. Schematic view of the experimental set-up used for the laminar burning velocity measurements
Figure 3-5. Modified spark plug geometry with tungsten electrode extension
Figure 3-6. Schematic of the inductive ignition system and the discharge energy measurement system
Figure 3-7. Burned gas flame speeds of propane/air mixtures at 1 bar, 298 K, and φ=1.5 ignited with different spark energies against the cold flame front radius

Figure 3-8. Measured oscilloscope data and calculated spark power for the ignition of propane/air mixture at 1 bar, 298 K, and ϕ =0.7 ignited with the discharge energy of 17.69 mJ (dwell time of 10 ms)
Figure 3-9. Coma and astigmatism, retrieved from [208]
Figure 3-10. Schlieren images showing the buoyancy effect on the flame front
Figure 3-11. Background subtraction/foreground extraction steps of image processing
Figure 3-12. Wrinkled flame with segmented pixel groups in flame boundary
Figure 3-13. Final stages of image processing
Figure 3-14. Variation in the S_L and L_b across the lower measurement limit on the R_f . (squares results obtained by the LS model [149], diamonds - results obtained by the NQ model [140], triangles - results obtained by the LC model [148], unfilled markers - S_L , and filled markers - L_b)
Figure 3-15. Polynomial fitting for S_L and L_b results of each stretch model and determination of the intersection points of S_L curves and L_b curves, i.e. the $R_{L,critical}$ (squares - results obtained by the LS model [149], diamonds - results obtained by the NQ model [140], triangles - results obtained by the LC model [148], unfilled markers - S_L , and filled markers - L_b)
Figure 3-16. Schlieren images of fuel/air mixtures with different L _b values
Figure 3-17. Polynomial fitting for S_L and L_b results of each stretch model and determination of the intersection points of S_L curves and L_b curves, i.e. the $R_{L,critical}$, with smaller upper measurement radius limits than 4.36 cm. (squares - results obtained by the LS model [149], diamonds - results obtained by the NQ model [140], triangles - results obtained by the LC model [148], unfilled markers - S_L , and filled markers - L_b)
Figure 3-18. Measured Markstein numbers over critical lower radius limit for methane, propane, iso-octane, and hydrogen flames (All S_L and L_b results with experimental uncertainties, $R_{L,critical}$ and Ma_b values are presented in Appendix I).
Figure 3-19. R _{L,critical} values of methane/air mixtures at high pressures and temperatures overlayed on the atmospheric pressure results in Figure 3-18
Figure 3-20. Mesh independency studies for the hydrogen/air mixture at 1 bar, 298 K and ϕ =1.0 (left) and the iso-octane/air mixture at 1 bar, 473 K and ϕ =1.0 (right)
Figure 3-21. Extrapolation of stretch models for different lower radius limits for laminar flame speed calculations of iso-octane/air mixture at 1 bar, 373 K, and φ=0.9 (black dots - experimental data, green line - the LS model [149], blue line - the NQ model [140], red line - the LC model [148])

Figure 3-22. Comparison of the experimental and numerical laminar flame speeds and experimental burned gas Markstein lengths of methane/air mixtures at 1 bar and 298 K from the current work with previously published experimental data. (black squares - present data, red diamonds - Bosschaart and de Goey [54], dark blue triangles - Liao et al. [88], light green triangles - Tahtouh et al. [90], light blue circles - Varea et al. [99], unfilled markers - S _L , and filled markers - L _b)
Figure 3-23. Comparison of the experimental and numerical laminar flame speeds and experimental burned gas Markstein lengths of hydrogen/air mixtures at 1 bar and 298 K from the current study with previously published experimental data. (black squares - present data, red diamonds - Dong et al. [264], dark blue triangles - Pareja et al. [265], light green triangles - Kuznetsov et al. [116], light blue circles - Krejci et al. [171], unfilled markers - S _L , and filled markers - L _b)
Figure 3-24. Comparison of the experimental and numerical laminar flame speeds and experimental burned gas Markstein lengths of propane/air mixtures at 1 bar and 298 K from the current study with previously published experimental data. (black squares - present data, red diamonds - Zhao et al. [266], dark blue triangles - Dirrenberger et al. [267], light green triangles - Lowry et al. [92], light blue circles - Miao et al. [268], unfilled markers - S _L , and filled markers - L _b)
Figure 3-25. Comparison of the experimental and numerical laminar flame speeds and experimental burned gas Markstein lengths of iso-octane/air mixtures at 1 bar and 373 K from the current work with previously published experimental data. (black squares - present data, red diamonds - Galmiche et al. [85], dark blue triangles - Varea et al. [99], light green triangles - Endouard et al. [269], light blue circles - Hu et al. [270], unfilled markers - S _L , and filled markers - L _b)
Figure 4-1. Laminar burning velocities of iso-octane/air and high/low RON gasoline/air mixtures at 1 bar and 373-473 K
Figure 4-2. Burned gas Markstein lengths for iso-octane/air and high/low RON gasoline/air mixtures at 1 bar and 373-473 K
Figure 4-3. Schlieren images of iso-octane/air flames at 1 bar and 373 K
Figure 4-4. Experimental (points) and numerical (lines) laminar flame speeds of iso-octane/ain mixtures at 1 bar and 373-473 K
Figure 4-5. Experimental (points) and numerical (lines - iso-octane/air only) laminar burning velocity (left) and burned gas Markstein length (right) results for iso-octane/air and high/low RON gasoline/air mixtures with 15% CO ₂ dilution by mass within the oxidizer at 1 bar and 473 K. 125
Figure 4-6. Contributions of the dilution and thermal-diffusion effects (yellow) and the chemical effect (red) on the decrease in the laminar burning velocities of iso-octane/air mixtures at 1 bar and 473 K due to the addition of 15% CO ₂ .
Figure 5-1 Schlieren images showing the flame front instabilities 138

Figure 5-2. Experimental S_L data for methane/air mixtures at 1, 3, and 5 bar
Figure 5-3. Experimental S_L data for methane/air mixtures at 373, 423, and 473 K
Figure 5-4. Experimental L _b data for methane/air mixtures at 1, 3, and 5 bar
Figure 5-5. Experimental L _b data for methane/air mixtures at 373, 423, and 473 K
Figure 5-6. Contour plots of the S_L (left) and L_b (right) of methane/air mixtures with respect to temperature and equivalence ratio at 1 bar
Figure 5-7. Contour plots of the S_L (left) and L_b (right) of methane/air mixtures with respect to pressure and equivalence ratio at 373 K
Figure 5-8. Laminar burning velocities of methane/air mixtures diluted with N_2 , H_2O , CO_2 , and a mixture of 71.49% N_2 + 19.01% H_2O + 9.50% CO_2 at 1 bar, 473 K, and ϕ =0.8, 1.0, and 1.2 146
Figure 5-9. Burned gas Markstein lengths of methane/air mixtures diluted with N_2 , H_2O , CO_2 , and a mixture of 71.49% N_2 + 19.01% H_2O + 9.50% CO_2 at 1 bar, 473 K, and ϕ =0.8, 1.0, and 1.2.
Figure 5-10. Contributions of the dilution, thermal-diffusion, and chemical effects of different combustion residuals to the decrease in the laminar burning velocity of methane/air/diluent mixtures at 1 bar and 473 K
Figure 5-11. Methane sensitivity factors at 1 bar, 473 K, and ϕ =1.0 for 5%, 10%, and 15% CO ₂ dilution.
Figure 5-12. Laminar flame speed comparison of stoichiometric methane/air mixtures diluted with different diluents at 1 bar and 473 K with a diluent level of 15%
Figure 5-13. Experimental S _L data for methane/air mixtures with 0%, 5%, 10%, and 15% diluent levels
Figure 5-14. Experimental L _b data for methane/air mixtures with 0%, 5%, 10%, and 15% diluent levels
Figure 5-15. Comparison of measured and predicted S_L data for methane/air mixtures
Figure 5-16. Comparison of measured and predicted L _b data for methane/air mixtures 164
Figure 5-17. Comparison of experimental, numerical, and predicted S_L data for methane/air mixtures at 3 bar and 423 K
Figure 5-18. Comparison of experimental, numerical, and predicted S_L data for methane/air mixtures at 1 bar and 423 K
Figure A-1. Technical drawing of main cylindrical body

Figure A-2. Technical drawing of bolted end cap.	182
Figure A-3. Technical drawing of fused quartz window.	183
Figure A-4. Technical drawing of window cap.	184
Figure A-5. Technical drawing of riser support	187
Figure A-6. Technical drawing of gas manifold.	188
Figure A-7. Technical drawing of fuel injector cartridge.	189
Figure A-8. Technical drawing of fuel injector hold down.	190
Figure A-9. Technical drawing of fuel injector hold down cap	191

LIST OF TABLES

Table 2-1. Comparison of laminar burning velocity measurement techniques
Table 2-2. Burned Mass Fraction Models
Table 2-3. Stretch models. 42
Table 2-4. Comparison of methods to measure the laminar burning velocity from spherically expanding flames
Table 3-1. Numerically calculated changes in the laminar flame speed and adiabatic flame temperature due to +/- 3.0 K fluctuation in the initial temperature
Table 3-2. Numerically calculated changes in the laminar flame speed and adiabatic flame temperature due to uncertainty in ϕ .
Table 3-3. Numerically calculated changes in the laminar flame speed and adiabatic flame temperature of methane/air mixtures due to uncertainty in dilution ratio
Table 3-4. Effect of upper radius limit on the R _{L,critical} , S _L , and L _b
Table 5-1. Past experiments on laminar flame speed of diluted methane/oxidizer mixtures 134
Table 5-2. Percentage reduction in laminar burning velocities of methane/air mixtures diluted with N_2 , H_2O , CO_2 , and a mixture of 71.49% N_2 + 19.01% H_2O + 9.50% CO_2 at 1 bar, 473 K, and ϕ =0.8, 1.0, and 1.2.
Table 5-3. Description of the diluent properties and effects for different computational models.
Table 5-4. Comparison of various S _L correlations against the current experimental results 161
Table 5-5. Comparison of various chemical mechanisms against current experimental results and S _L correlation
Table A-1. Experimental laminar flame speed, burned gas Markstein length, and burned gas Markstein number data at critical lower radius limit for methane, propane, iso-octane, and hydrogen
Table A-2. Experimental and numerical laminar flame speed and burned gas Markstein length data of methane/air mixture for the validation of experimental apparatus and procedure
Table A-3. Experimental and numerical laminar flame speed and burned gas Markstein length data of propane/air mixture for the validation of experimental apparatus and procedure

Table A-4. Experimental and numerical laminar flame speed and burned gas Markstein length date of iso-octane/air mixture for the validation of experimental apparatus and procedure
Table A-5. Experimental and numerical laminar flame speed and burned gas Markstein length date of hydrogen/air mixture for the validation of experimental apparatus and procedure
Cable A-6. Experimental and numerical laminar flame speed and burned gas Markstein length date of iso-octane/air mixture. 19
Cable A-7. Experimental laminar flame speed and burned gas Markstein length data of high RO casoline/air mixture. 19
Cable A-8. Experimental laminar flame speed and burned gas Markstein length data of low RO casoline/air mixture. 19
Cable A-9. Experimental laminar flame speed and burned gas Markstein length data of dilute nethane/air mixture. 19
Cable A-10. Experimental and numerical laminar flame speed and burned gas Markstein length Lata of methane/air mixture. 20

KEY TO ABBREVIATIONS

A Area

A_d Major-Diameter Area of Fastener

A_t Tensile-Stress Area of Fastener

ASME American Society of Mechanical Engineers

BPVC Boiler and Pressure Vessel Code

BTU British Thermal Unit

c_p Constant Pressure Specific Heat

CCS Carbon Capture and Storage

CH Chemical Effect

CH1 Chemical Effect due to the Active Participation of Combustion Residuals in the

Dissociation Reactions

CH2 Chemical Effect due to the Participation of Combustion Residuals in the Third Body

Reactions

CPM Constant Pressure Method

CVCC Constant Volume Combustion Chamber

CVM Constant Volume Method

d Diameter

d_{un} Unsupported Diameter of Window

D Mass Diffusivity

DAQ Data Acquisition

DI Dilution Effect

DLE Dry Low Emission

DNS Direct Numerical Simulation

E Joint Efficiency for, or Efficiency of, Appropriate Joint in Cylindrical or Spherical

Shells, or Efficiency of Ligaments between Openings, whichever is less

E_a Activation Energy

EGR Exhaust Gas Recirculation

EIA Energy Information Administration

EM Elastic Modulus

EPA Environmental Protection Agency

F_{ext} External Load

F_m Resultant Load on Connected Members

F_p Clamp Load/Preload

FCA Fiat Chrysler Automobiles

FGR Flue Gas Recirculation

fps Frames per Second

GC-MS Gas Chromatography–Mass Spectrometry

GRG Generalized Reduced Gradient

h Thickness of Washer and Clamped Material

HCCI Homogeneous Charge Compression Ignition

HP High Pressure

IC Internal Combustion

ID Inner Diameter

k_b Estimated Effective Stiffness of Bolt or Cap Screw in Clamped Zone

k_m Joint-Member Stiffness

Ka Karlovitz Number

1 Length

L Markstein Length

l_d Length of Useful Unthreaded Portion of a Screw

lt Length of Useful Threaded Portion of a Screw

L'_G Effective Grip of a Screw

L_T Threaded Length of a Screw

Le Lewis Number

LP Low Pressure

m Mass

Ma Markstein Number

MW Molecular Weight

n Number of Moles

NPT National Pipe Thread

NTP Normal Temperature and Pressure

OD Outer Diameter

P Pressure

PIV Particle Image Velocimetry

R² Coefficient of Determination

R_f Radius of the Cold Flame Front

R_L Lower Radius Limit for the Laminar Flame Speed Calculation

R_{L,critical} Critical Lower Radius Limit for the Laminar Flame Speed Calculation

Radius of the Spherical Flame detected by Schlieren Photography

R_u Ideal Gas Constant (8.314 J/mol·K)

R_{up} Upper Radius Limit for the Laminar Flame Speed Calculation

 $R_{\rm w}$ Radius of a Spherical Chamber (equivalent radius for cylindrical vessels = $(3v/4\pi)^{1/3}$)

Re Reynolds Number

RMSE Root Mean Square Error

RON Research Octane Number

S Flame Speed

So Unstretched Flame Speed

S_L=S_u^o Laminar Burning Velocity and Laminar Flame Speed

t Time

T Temperature

T Mass Average Temperature

TD Thermal-Diffusion Effect

thk Thickness

TJI Turbulent Jet Ignition

v Volume

V Gas/Flow Velocity

x Burned Mass Fraction

X Dilution Ratio

Ze Zeldovich Number

α Thermal Diffusivity

γ Heat Capacity Ratio

 δ_L Laminar Flame Thickness

κ Flame Stretch Rate

λ Thermal Conductivity

ρ Density

 $\overline{\rho_b}$ Mean Density of Burned Gases

 σ Stress

v Kinematic Viscosity

φ Equivalence Ratio

vppm Volumetric Parts per Million

Subscripts

adb,p Adiabatic Isobaric Flame

adb,v Adiabatic Isochoric Flame

b Burned Gases (products)

eff Effective

i Initial

m Maximum

o Reference Value

t Total

u Unburned Gases (reactants)

1 INTRODUCTION

1.1 Background and Motivation

The U.S. Energy Information Administration (EIA) has projected that fossil fuels will continue to supply the majority of world's energy demand through at least 2040 despite environmental concerns [1]. The U.S. EIA predicts a 28% increase (575 quadrillion BTU to 736 quadrillion BTU) in world energy consumption from 2015 to 2040 [1]. As seen in Figure 1-1 (left), renewable energy and natural gas are expected to cover most of this increase in demand, with natural gas anticipated to be the fastest growing fossil fuel with an increase in consumption by 43% expected from 2015 to 2040. The majority (75%) of the projected growth in total natural gas consumption is attributed to the power production and industrial sectors in many regions, particularly the Middle East, the United States, and China [1]. During this same time period, the share of petroleum and other liquids in the total world energy market is predicted to decrease from 33% in 2015 to 31% in 2040. However, petroleum and other liquid fuels are still expected to remain the largest source of energy through at least 2040 due to increased consumption in the industrial and transportation sectors [1].

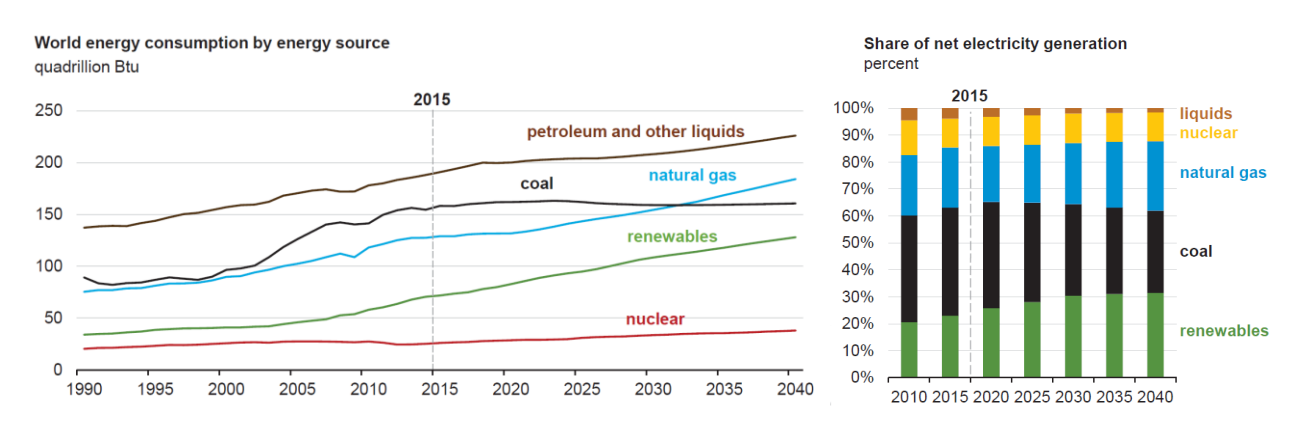


Figure 1-1. Projected world energy consumption by energy source (left) and projected share of net electricity generation percent (right) by 2040, retrieved from [1].

Although renewables are envisioned to be the fastest-growing sources of power production from 2015 to 2040 as can be seen in Figure 1-1 (right), the U.S. EIA [1] predicts that natural gas will still be attractive for electricity generation in 2040 due to its low capital costs, favorable heat rates, relatively low fuel cost, and high combined cycle efficiencies range between 60-65% [2]. Furthermore, natural gas-fired power plants are vital to overcome the stability problems that have emerged due to the intermittent nature of wind and solar power production [3]. On the other hand, natural gas combustion produces fewer greenhouse gas emissions relative to other fossil fuels, such as coal and petroleum, by releasing less CO₂ [4].

Despite the increasing electrification trend in the transportation sector, petroleum-derived liquid fuel consumption is projected to increase by 18% between 2015 and 2040 [1]. The transportation sector has the largest share in this growth and is projected to account for 55% of the total end-use of petroleum and other liquid fuels by 2040 [1]. This projection suggests that transportation sector will continue to be heavily dependent on internal combustion engines (IC engines) burning petroleum-derived liquid fuels for the coming decades since the greenhouse effect of battery electric vehicles would be worse if power production and the energy used for battery production are not sufficiently decarbonized [5]. Therefore, the electrification trend in transportation is expected to focus on hybrid systems in the near future [5]. Moreover, low-carbon and alternative fuels have entered the marketplace, but they are not envisioned to provide more than 10% of the total transport demand by 2040 [5]. In fact, gasoline including biofuel additives is expected to remain the primary fuel for transportation and is projected to account for 36% of the world's transportation-related energy use in 2040 [1].

One of the main concerns regarding the growth in projected total natural gas and petroleum consumptions is the pollution. Fossil fuel/oxidizer combustion can emit CO₂, CO, NO_x, SO_x,

smoke, and unburned hydrocarbons, depending on the composition of the fuel. With the lack of a carbon capture and storage (CCS) process, the carbon content of the fuel governs CO₂ emissions, which have a greenhouse effect and lead to global warming [6]. Therefore, the U.S. EIA [1] recommends decreasing energy-related CO₂ emissions by shifting from coal to natural gas and renewable energy sources for electricity generation. However, natural gas is predicted to exhibit the greatest CO₂ emission growth from 2015 to 2040 due to its increasing usage in power production [1].

Critical detrimental effects of other pollutants of natural gas-fired power plants, such as NO_x and SO_x, led the U.S. Environmental Protection Agency (EPA) to issue more stringent regulations to limit the emissions of gas turbines to 75 vppm NO_x and 150 vppm SO_x at 15% oxygen (dry basis) in 1977 [2]. Over the years, the emission limits for NO_x have been gradually decreased to 25 ppm with a new target set to 9 ppm, which has significantly changed the design of gas turbine combustors [2]. Similarly, stringent emission standards were introduced for the transportation sector [7-8] since petroleum and other liquids are projected to be responsible for the majority of the energy-related CO₂ emissions together with coal by 2040 [1].

Flue/exhaust gas recirculation (FGR/EGR) has been proposed as an effective way of reducing emissions by decreasing combustion temperatures in gas turbines operating both in premixed and non-premixed modes, e.g. axial (sequential) stage gas turbine combustors, and in internal combustion engines [9-10]. However, the dilution of a fuel/oxidizer mixture affects the flame reactivity and combustion stability [10].

Laminar burning velocity and burned gas Markstein length are essential universal parameters of a combustible mixture as they express the mixture reactivity and exothermicity [11], flame shape and stretch, and important flame-stability characteristics, such as blowoff, blowout,

flashback, and liftoff [12]. Therefore, experimentally obtained laminar burning velocity data is commonly used for the development, validation, and optimization of detailed chemical mechanisms [13]. Due to the complexity of many practical combustion phenomena, computer simulation models and turbulent flame theories are extensively used to simulate the combustion inside spark ignition engines and gas turbines. Many of these models and theories are based on the laminar burning velocity and turbulence intensity [12]. Thus, a thorough understanding of laminar premixed flames is essential for turbulent flame studies since many turbulent flame theories depend on an underlying laminar flame structure [12].

Laminar burning velocity also plays an essential role in many combustion applications, such as IC engines and gas turbines. For instance, laminar flame speeds are frequently used to predict the pressure rise inside a spark ignition engine [14]. Additionally, many combustion parameters are associated with flame propagation speed such as the ignition delay time; and therefore autoignition and engine knock [15], wall quench layer thickness [14], minimum ignition energy, heat release rate, flammability limits, emission characteristics [16], and burn duration, which has a direct influence on power output and efficiency of engines [17]. Therefore, it is essential to examine the effects of combustion residuals on the laminar burning velocity and burned gas Markstein length in order to advance our understanding about the effects of FGR/EGR. Nevertheless, studies focusing on the impacts of inert post combustion products on these two fundamental flame parameters at elevated pressures and temperatures are still rare. Hence, the present study aims to investigate the effects of flue gases on the laminar burning velocity and burned gas Markstein length of various fuel/oxidizer mixtures at elevated pressures and temperatures with and without different diluents at various dilution ratios.

1.2 Overview of Sequential Stage Combustion Concept in Stationary Gas Turbine Combustors

A stationary gas turbine converts the kinetic energy of the post combustion products flowing through the turbine blades to electrical power. In general, the overall efficiency of the gas turbine increases with higher component efficiencies, such as those of the compressor, combustor and turbine; with higher mass flow, and with higher turbine working temperatures, which is controlled by the steady flow combustion in which a hydrocarbon fuel is burned with a large amount of excess air [6]. In order to keep the temperature profile at the turbine inlet, i.e. the combustor exit, at an appropriate level, a modern combustor should be able to mix the fuel and air, ignite the mixture, and stabilize the flame in the primary zone as shown in Figure 1-2 [2]. This is followed by the oxidation of CO in the secondary zone and then with the lowering of the temperature of the post combustion products by excess air in the dilution zone [4].

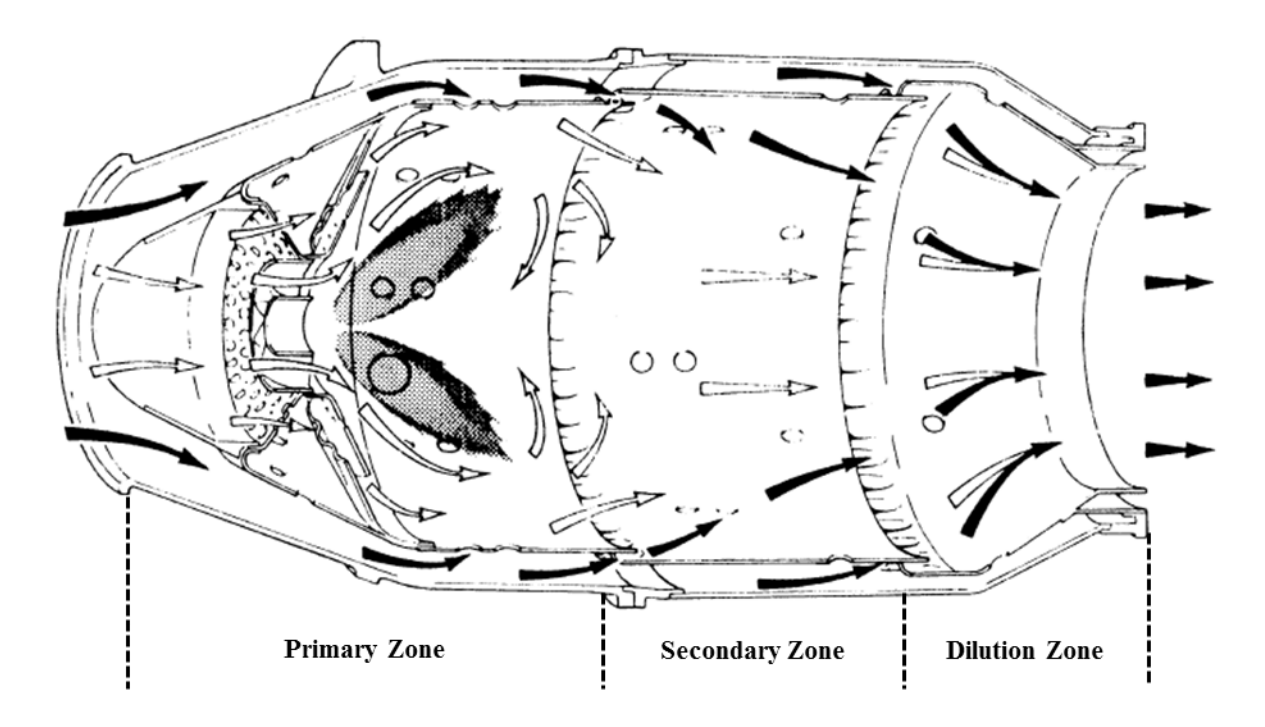


Figure 1-2. Schematic of a typical gas turbine combustor, retrieved from [2].

Since the first practical gas turbine was developed by Dr. Franz Stolze in 1872 [18], the main objectives for a stationary gas turbine combustor have been high combustion efficiency, reduction of visible smoke, minimum pressure loss in the combustor, self-sustaining flames, and stable combustion [2]. These goals were mostly achieved by the early 1970s. However, increasingly stringent emission regulations for CO₂, CO, NO_x, and unburned hydrocarbons still need to be met, while maintaining existing levels of reliability and affordable costs [6].

Although CO₂ emissions are inevitable when combusting fossil fuels, they can be captured with CCS technology, which allows the oxy-fuel combustion with a large amount of recycled flue gas to maintain optimum turbine inlet temperature for material safety [9, 19]. Unburned hydrocarbons and CO are more likely to be formed during incomplete combustion, such as near idle conditions, and these emissions can potentially be reduced with better atomization and higher local temperatures [2]. However, higher combustion temperatures increase NO_x formation, which is of great concern for photochemical smog, global warming, and the formation of acid rain precursors due to the poisonous character and abundance of NO_x [4].

In 1977, the U.S. EPA proposed a series of techniques for the reduction of NO_x emissions [2]. Initially, water/steam injection into the combustor became very popular in the 1980s and most of 1990s [2]. It was shown that an 85% decrease in NO_x emissions can be achieved with water/steam injection and optimized combustor aerodynamics by lowering the flame speed [2]. However, the amounts of demineralized water required to prevent corrosive deposits in the turbine are substantial and high water/steam injection caused a dramatic increase in emissions of unburned hydrocarbons and CO [6]. Consequently, dry control combustion technologies have become the preferred methods to prevent NO_x formation [2].

Since the 1980s, selective catalytic reduction systems for the conversion of NO_x to N₂ and H₂O with ammonia (NH₃) has been used to achieve very low NO_x emissions [6]. The catalytic reaction happens without a flame and only in a limited temperature range, typically 558-673 K [6]. Although there is a growing interest for catalytic converters in stationary gas turbine applications, they cause new problems, such as increased cost, issues with the handling and storage of ammonia, and flow control of NH₃ particularly in dealing with variable loads [6].

Since the 1990s, the favorable effect of premixed lean combustion on NO_x emissions has been well understood and Dry Low Emission (DLE) NO_x combustors were established [2]. The DLE approach proposes to mix the fuel and oxidizer prior to the mixture entering the combustor and to burn most of it at cool lean conditions to decrease the flame temperature and therefore the NO_x emissions [4]. Although most contemporary gas turbines use DLE NO_x combustors, this method can suffer from autoignition, flashback, blowoff, and combustion instabilities [20].

Auto-ignition can be avoided by adjusting the residence time of the fuel in the premixed region to less than the ignition delay time of the fuel, which may cause an incomplete mixing [2]. Flashback and blowout are related to the local flame speed and the velocity of the combustible mixture [12]; therefore, the prevention of these two phenomena needs accurate knowledge of laminar burning velocity information for the fuel/oxidizer flames at operating conditions. The lean combustion is also prone to combustion instabilities, defined as the pressure oscillations due to the fluctuations in the combustion heat release rate, i.e. oscillatory burning [2, 6, 20]. These oscillations cause wear, damage, and failure in extreme cases, of the combustor and downstream turbine [20].

In light of the studies showing combustion residuals suppresses flame instabilities [3, 19, 21], DLE NO_x combustors have started to take the form of the premixed sequentially staged

combustors (Figure 1-3). While the primary stage of this new concept provides stable combustion, the secondary stage, serial to the primary stage, uses hot post-combustion products of the previous stage, enabling the use of much leaner premixed air/fuel mixtures without stability issues or excessive CO emissions [22]. Inert post-combustion products have the ability to decrease combustion temperatures and therefore NO_x emissions, without changing the stoichiometry, which can be desirable at higher loads and enable the use of selective catalytic reduction systems [23-24].

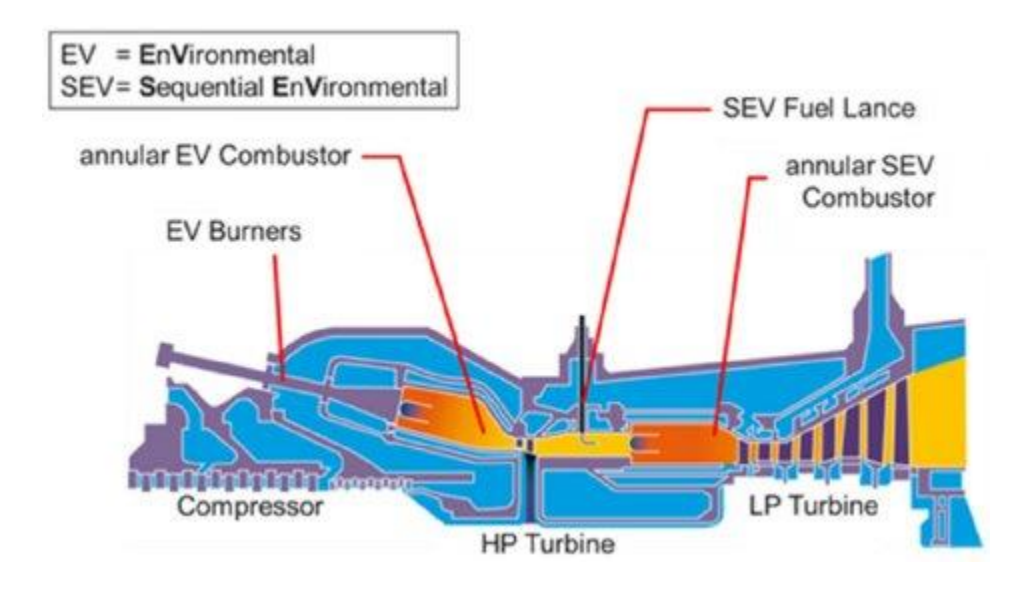


Figure 1-3. Alstom GT24/GT26 sequential combustion system, retrieved from [31].

Conventional stationary gas turbines are targeted to provide low emissions at high load operation and suffer from strongly increasing emissions with decreases in load [25]. High load flexibility has become increasingly important in order to compensate for power fluctuations that have emerged due to the intermittent nature of wind and solar power production [3]. Therefore, axial (sequential) stage combustion systems for stationary gas turbines have been gaining momentum since they provide enhanced operational flexibility [26], a wider range of stable performance modes [27], and lower emissions [25]. The axial staging concept also provides higher

fuel flexibility compared to conventional stationary gas turbines [26] and contributes to energy security, fuel diversity, and utilization of carbon-free fuels or synthetic fuels.

In sequential two-stage combustors, combustion in the second stage takes place at a lower oxygen concentration and higher temperature due to hot inert combustion residuals transferred from the initial stage onto the secondary stage. Higher firing temperatures within the latter stage enhances the combined cycle efficiency [28]. Recently, an axially staged lean-to-lean combustion concept was found to show promising results to reduce emissions with natural gas/air mixtures [25, 29-31].

1.3 Overview of Exhaust Gas Recirculation in Internal Combustion Engines

The first IC engines were produced due to the need for affordable and simple power generators, rather than expensive steam engines, as a result of the independent studies of Nikolaus August Otto in 1876, Karl Benz and Gottlieb Daimler in 1886, and Rudolf Diesel from 1893 to 1897 [32]. Therefore, the fundamental design of IC engines showed similarities to the steam engine [32]. The main problems of the early engines were ignition, mixture formation, and cooling, which were mostly solved through enhanced technology developments as the motor vehicle industry rapidly developed [32]. As the engine power and the speed and weight of vehicles increased, transportation emissions have been subjected to increasingly stringent regulations due to rising oil prices and the detrimental effects of exhaust gases on the environment and public health [33]. These emission gases, mainly CO₂, CO, NO_x, SO_x, and unburned hydrocarbons, can be reduced significantly by more efficient powertrains, exhaust gas after-treatment systems, and more stringent fuel requirements [34].

Enhanced efficiency and engine design improvements can decrease CO₂ emission, which are directly related to the amount of fuel burned and unburned hydrocarbon emissions from

incomplete combustion [33]. Another product of incomplete combustion is CO, whose emission can be lowered by using catalytic converters [34]. In addition to CO and hydrocarbon oxidation, 3-way catalytic converters reduce NO_x to N₂ [34]. However, they can only operate close to stoichiometric conditions and at 558-673 K [6]. Additionally, catalytic converters can cause resource depletion, waste generation, and N₂O emissions, which has a global warming potential 310 times than of CO₂ [35]. However, their ability to clean up the vast majority of CO, hydrocarbon, and NO_x emissions has led the U.S. government to require all spark ignition engine vehicles to have catalytic converters since 1975 [33].

Similar to lean stationary gas turbine combustors, lean burn technology in spark ignition IC engines is a promising way to reduce NO_x emissions due to lower combustion temperatures [4] while increasing engine thermal efficiency and reducing pumping losses [36]. Improved fuel efficiency also decreases CO₂ emissions and therefore greenhouse gas emissions [33]. However, lean burn is not compatible with three-way catalyst operation, which is one of the main methods to reduce CO, NO_x, and unburned hydrocarbons emissions in spark ignition engines [33]. Although this problem can be partially solved with selective catalytic reduction systems [6, 37-39], like in stationary gas turbine combustors, issues with the handling and storage of ammonia, higher N₂O emissions, and flow control problems of NH₃ still need to be overcome [6, 40]. Furthermore, lean combustion is prone to combustion instabilities due to the narrow flammability limits of most fuels, which causes an increase in unburned hydrocarbon emissions due to misfire and partial burning [2, 6, 33]. Slower local flame velocities of lean mixtures are the main reasons behind the partial burning [33]. Therefore, advanced combustion strategies, such as homogeneous charge compression ignition (HCCI) and turbulent jet ignition (TJI), are being developed to increase flame speed by raising the ignition energy and intensifying turbulence [33].

Exhaust gas recirculation (EGR) is a common method to reduce NO_x emissions in IC engines (Figure 1-4) since it decreases combustion temperatures without changing the stoichiometry, which enables the use of a three-way catalyst [41]. EGR also lowers the pumping losses, heat rejection, and chemical dissociation at partial load and improves the detonation/knock resistance at full load [23, 34]. Although higher EGR fractions promote brake thermal efficiency with more advanced spark timing [33], EGR affects the reactivity of the combustible mixture and thus combustion stability [10]. Furthermore, hot post combustion gases can increase deposit formation in port fuel injectors and intake valves during their circulation [42].

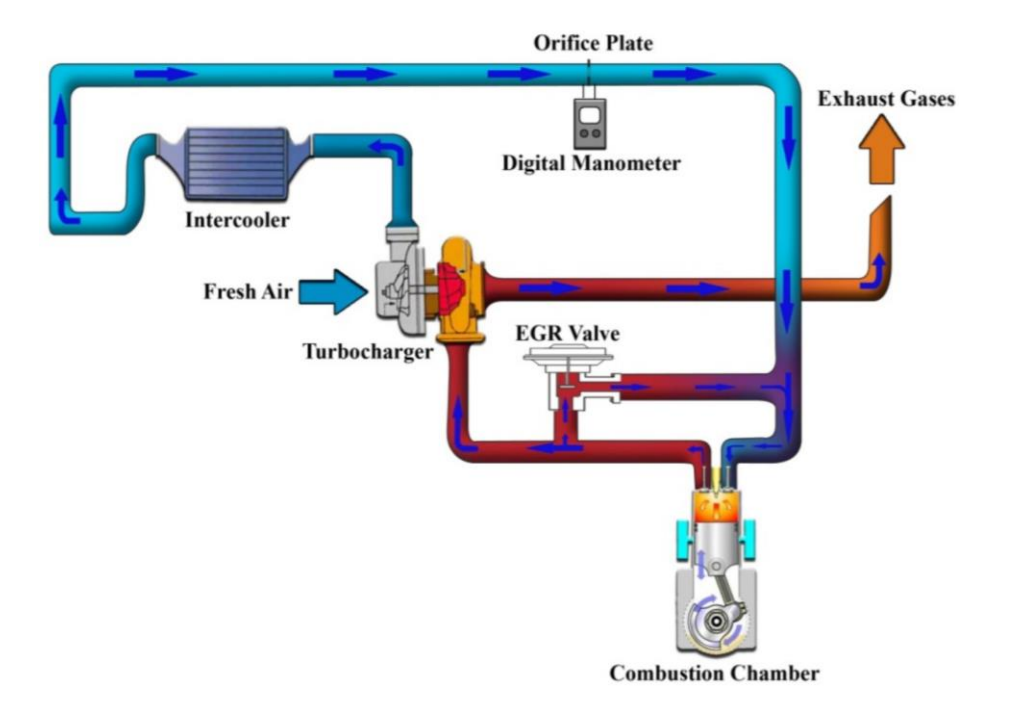


Figure 1-4. A schematic diagram of EGR system, retrieved from [43].

1.4 Research Questions and Objectives

In order to understand the underlying theory behind fuel/air/diluent flames that occur in modern stationary gas turbine combustors and internal combustion engines, the present study investigates the effect of dilution on the laminar burning velocities of fuel/air mixtures at high temperatures and pressures with various dilution gases and ratios. Initially, the fundamentals of

laminar premixed flames, laminar burning velocity measurement techniques, theory behind spherically expanding flames, and flame front instabilities are discussed in detail. Subsequently, a newly designed optically accessible constant volume combustion chamber is introduced together with the flame speed calculation methodology used in the present study. Accuracy assessment of stretch extrapolation models comes next. This study is followed by the explanation of the computational framework and the validation of the experimental apparatus. Finally, numerical and experimental results for the laminar burning velocities of fuel/air/diluent mixtures at elevated temperatures and pressures are presented. The aim of this research is to answer the following questions:

- 1. What is the effect of the measurement range on the stretch model accuracy?
- 2. How different are the effects of various diluents on the laminar burning velocity and flame stability of a combustible mixture?
- 3. How do combustion residuals affect the laminar burning velocity and the flame stability of various fuel/oxidizer mixtures at elevated pressures and temperatures?
- 4. What are the main causes for the change in the laminar burning velocity and burned gas Markstein length of a combustible mixture due to the diluent addition?
- 5. How accurately can currently available chemical mechanisms predict the effect of dilution on the laminar burning velocity at elevated pressures and temperatures?

In order to answer the above posed questions, the following objectives were carried out:

- Design and construction of an optically accessible high pressure and high temperature constant volume combustion chamber.
- Assessment of accuracies of stretch extrapolation methods from spherically expanding flames

- Investigation of the effects of different flue gases on laminar burning velocities and burned gas Markstein lengths of premixed methane/air mixtures
- Measurements of the laminar flame speed and burned gas Markstein length of isooctane/air, high/low research octane number (RON) gasoline/air, and methane/air mixtures diluted with combustion residuals at high pressures and temperatures
- Numerical quantification of the main causes of combustion residuals on the laminar burning velocity reduction
- Evaluation of various chemical mechanisms against experimental laminar flame speed data

2 BURNING VELOCITY OF LAMINAR PREMIXED FLAMES

2.1 Measurement Techniques for Laminar Burning Velocity

A self-sustaining, localized combustion zone/wave of a premixed fuel/oxidizer mixture propagating with subsonic velocities, i.e. deflagration, is defined as a premixed flame [12]. One of the most significant global parameters of a laminar premixed flame is the laminar burning velocity (S_L), which is the speed of a steady, one-dimensional, planar, and adiabatic laminar flame. There are various measurement techniques for the laminar burning velocity, which can be categorized as stationary flame methods and propagating flame methods [44]. Methods for stationary flames consist of Bunsen burner flames, stagnation flames (counter-flow method), and burner stabilized flat flames (heat flux method) [45].

In the Bunsen flame technique, the laminar flame speed is usually deduced from a conical Bunsen burner flame (Figure 2-1) with the cone angle method [46-47] or the flame surface area method [48]. In both methods, the flame is optically observed to determine the Bunsen cone angle or flame outer surface area. The volumetric flow rate at Bunsen tube exit should also be known to calculate the velocity of unburned mixture leaving the Bunsen burner. Then, the laminar burning velocity is calculated with the multiplication of the velocity of the unburned mixture at the Bunsen tube exit and the sine of the Bunsen cone angle in the cone angle method. In the flame surface area method, the laminar burning velocity is computed by diving the volumetric flow rate at the Bunsen tube exit by the flame area.

Until the complex physics behind the Bunsen flames were discovered in the last thirty years, e.g. negatively stretched main flame surface and strong curvature effect at the flame tip, the Bunsen burner method was commonly used for laminar flame speed measurements without any flame stretch treatment because the apparatus is inexpensive, versatile, and easy to use [13].

However, the Bunsen flames can exhibit severe instabilities at small and large Lewis numbers (Le) [13].

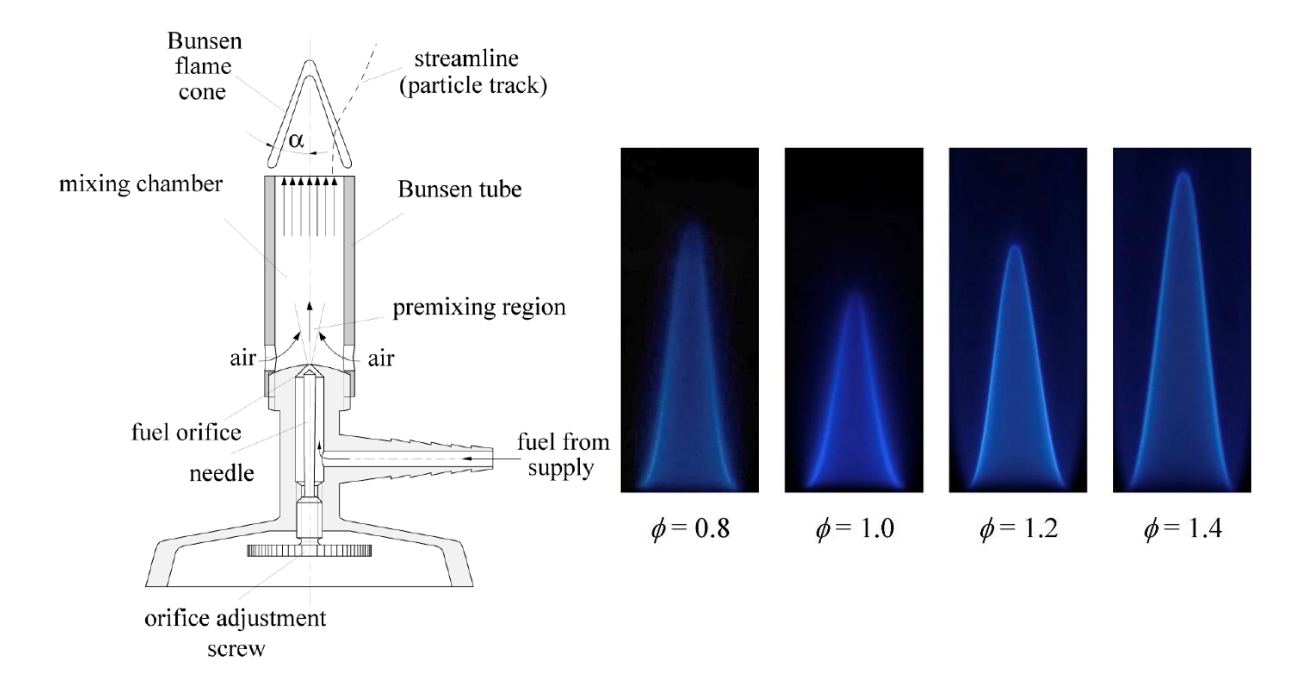


Figure 2-1. Schematic of the Bunsen burner (left [49]) and premixed biogas-hydrogen blending fuel Bunsen flames at different equivalence ratios (right [50]).

Flame front instability problems faced in the Bunsen flames can be resolved with stagnation flames. In late 1980's, Law and coworkers [11, 51] proposed to measure the laminar burning velocity from two symmetric (twin), laminar, steady, and planar stagnation flames with the same chemical composition in a counter-flow flame configuration (Figure 2-2). In the counter-flow method, laser diagnostics techniques, such as particle image velocimetry (PIV) and laser Doppler velocimetry, are used to obtain the axial velocity profile. The minimum flow velocity is specified as the reference flame speed whereas the strain rate is assumed to be the absolute maximum value of the derivative of the axial velocity [45]. By varying the burners flow rates, different reference flame speeds can be obtained for different strain rates. Subsequently, the laminar burning velocity is calculated by extrapolating the reference flame speed to zero strain rate.

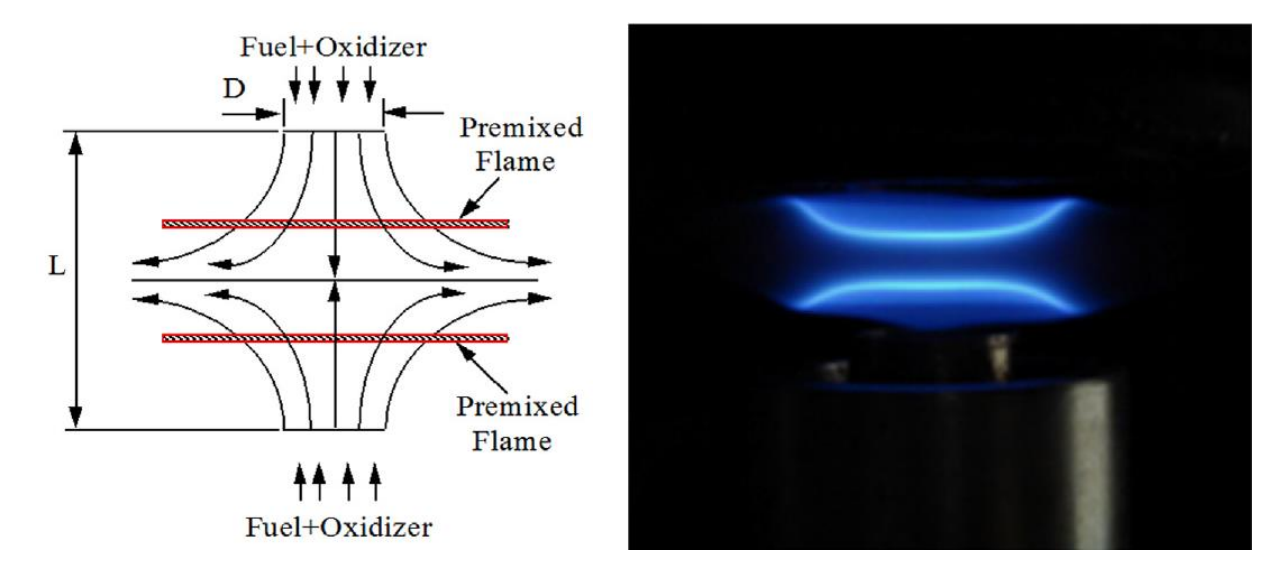


Figure 2-2. Twin counter-flow/stagnation flames, retrieved from [13].

Although counter-flow flames can generally be assumed adiabatic due to the symmetry, the heat loss to the burner nozzle increases at low pressures or low stretch rates, which leads to stabilization problems [13]. At high pressures or high stretch rates, the flame thickness becomes too small to detect with laser diagnostics techniques [13]. Therefore, the method is limited to low burning velocities and low pressures (typically less than 10 bar) due to the unstable flow/flame at high Reynolds numbers (Re) [13].

The heat flux method proposed by de Goey et al. [52] is based on Botha and Spalding's flat flame approach [53], in which the laminar burning velocity is deduced from the relation between the heat loss of the burner stabilized flame and burner flow rate using a porous or perforated plate. Different than the flat flame technique, de Goey et al. [52] heated the reactants externally to solve the heat loss problem and achieve a nearly adiabatic flame (Figure 2-3). Therefore, in the heat flux method, it is assumed that the radial temperature profile depends on the unburned gas velocity and the uniform radial temperature distribution can be achieved when the unburned gas velocity is equal to the unstretched and adiabatic laminar flame speed [54]. In other words, the laminar burning velocity is determined by varying the burner flow rate while screening

the radial plate temperature distribution. Due to radical loss and flow induced instabilities at high burner flow rate and pressure, the heat flux method is limited to low burning velocities and low pressures (typically less than 10 bar), similar to the counter-flow method [13].

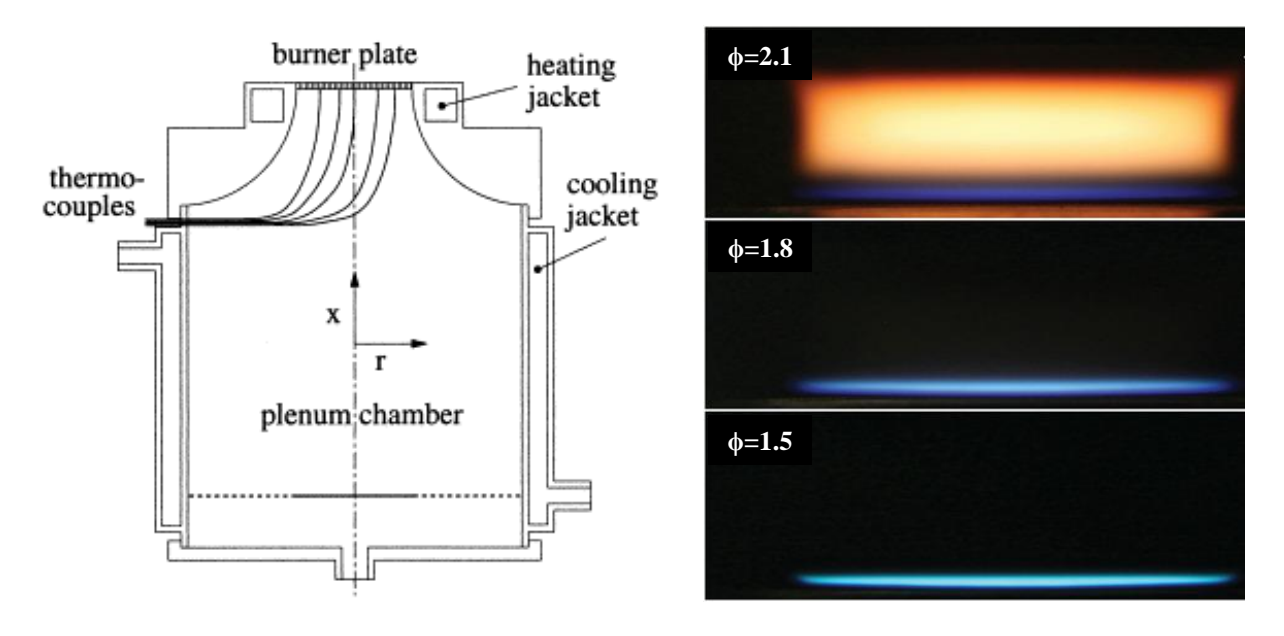


Figure 2-3. Schematic of the heat flux burner (left [55]) and premixed ethylene/air flat flames at different equivalence ratios (right [56]).

Laminar burning velocity measurements at high pressures can be conducted only with freely propagating flames [13]. Rallis and Garforth [44] listed the methods for propagating flames as the cylindrical tube method [57], flame kernel method [58], soap-bubble method [59], and spherically expanding flame method [60]. Among the propagating flame approaches, the advantages of the spherically expanding flame method stand out compared to the inevitable wall interaction effect in the cylindrical tube method, experimental difficulties and low success rate of firing in the flame kernel method, and the need of a water-based soap solution in the soap-bubble method [44]. Therefore, spherically expanding flames are commonly utilized to measure the laminar burning velocity in the entire pressure range except for sub-atmospheric pressures, where the critical ignition radius is large [13]. Finally, laminar flame speed measurement techniques are

compared in Table 2-1 and the theory of spherically expanding flames are discussed in the next section in detail.

Table 2-1. Comparison of laminar burning velocity measurement techniques.

Measurement Technique		Advantages	Disadvantages	
Stationary Flames	Bunsen Burner Method	• The apparatus is inexpensive, versatile, and easy to use [44].	• Main flame surface is negatively stretched [13].	
			• There is a strong curvature effect at the flame tip [13].	
			• The stretch effect cannot be neglected [45].	
			• The Bunsen flames can exhibit severe instabilities at small and large Le [13].	
			• The flame cone is distorted due to flame thrust and not fully adiabatic due to the air entering the flame cone base [61].	
	Counter-Flow Method	 The flame can generally be assumed adiabatic due to the symmetry [45]. Flame front instability problems faced in the Bunsen flames can be resolved with this method [13]. 	• The heat loss to the burner nozzle increases at low pressures or low stretch rates, which leads to stabilization problem [13].	
			• At high pressures or high stretch rates, the flame thickness becomes too small to detect with laser diagnostics techniques [13].	
			• The method is limited to low burning velocities and low pressures [13].	
	Heat Flux Method	 The method is simple and does not need a complicated diagnostics [13]. The flame is not affected by stretch [52]. 	• The porous plate utilized for the flame stabilization causes flame front instabilities [53].	
			The flame speed determined with this method can be slower than the actual flame speed due the best loss from the flame.	
			to the heat loss from the flame [62].	
			• The method is limited to low burning velocities and low pressures [44].	

Table 2-1 (cont'd)

Propagating Flames	Cylindrical Tube Method	• It is a simple method [57].	• The method suffers from wall interaction and vibration effects, which cause a deformed flame front [44].
	Flame Kernel Method	 The flame curvature and thickness treatments are not required [44]. There is no ignition electrode effect on the flame [44]. 	 The flame kernel has a complex flame front shape [44]. Two flame kernels measurements are subjected to spark synchronization problem [44]. Experimental difficulties cause low success rate of firing [44].
	Soap-Bubble Method	 It is a simple method [59]. The method can be used for a wide range of pressure [44]. 	 At high flame speeds, the flame surface is deformed due to inertial effects [63]. Dry mixtures cannot be tested due to the need of water-based soap solution [64]. The method is limited to a narrow range of temperature [44].
	Spherically Expanding Flame Method	• The method is simple and can be utilized for a wide range of pressure and temperature [60].	 It is difficult to ignite the mixture at sub-atmospheric pressures [65]. Ignition electrode effect is significant at low pressures [13]. Flame instabilities are observed at high pressures [66].

2.2 Theory of Spherically Expanding Flames

For spherically expanding flames, the fuel/oxidizer mixture is generally ignited in the center of a constant volume combustion chamber by a spark generated between two ignition electrodes (Figure 2-4-left) or a laser ignition system [67]. Following the spark, the flame starts to grow spherically towards the vessel walls, first at constant pressure and then the pressure begins to build up rapidly with the increase in the flame radius as shown in Figure 2-4 (right).

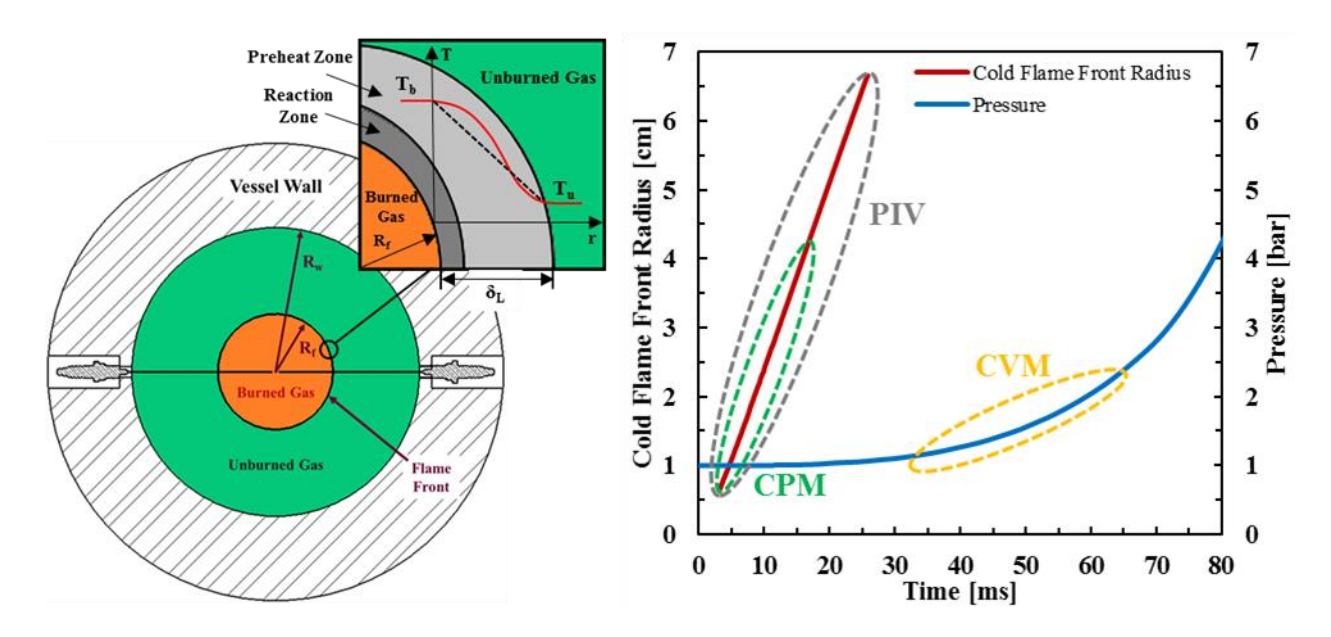


Figure 2-4. Spherical flame propagation inside a constant volume combustion chamber (left) and cold flame front radius and pressure history for a methane/air mixture at 1 bar, 298 K and ϕ =1.0 after spark.

Since the self-sustaining flame propagates subsonically, the pressures of the burned and unburned gases must be equal, and high gradients in temperature and species concentration across the flame suggest a thin flame thickness [4]. In fact, typical flame thicknesses are on the order of a millimeter [4]. With an infinitely thin flame front assumption, the continuity equation can be written as Equation 2-1. In this equation, and in the rest of this dissertation, the subscript u refers to the unburned gas mixture (reactants) while the subscript b stands for the burned gases (products).

$$\rho_{\mathbf{u}}S_{\mathbf{u}} = \rho_{\mathbf{b}}S_{\mathbf{b}}$$
 2-1

A relation between the cold flame front radius (R_f) and the flame speed (S) can be obtained from a kinetic balance at the flame front (Equation 2-2). The unburned gas/flow velocity (V_u) can be written in terms of the cold flame front radius, pressure, and burned and unburned gas thermodynamic properties with the help of the conservation of mass equation for the combustion chamber, i.e. Equation 2-3, and the consumption rate of reactants (dm_u/dt) proposed by Bradley et al. [68], i.e. Equation 2-4. The definition of burned gas mass (m_b), i.e. Equation 2-5, should be

substituted into Equation 2-3 together with Equation 2-4. The resulting S_u expression is given in Equation 2-6. By comparing Equations 2-2 and 2-6, V_u can be found as Equation 2-7.

$$\frac{dR_f}{dt} = V_u + S_u$$
 2-2

$$m_t = m_b + m_u \longrightarrow \frac{dm_t}{dt} = 0 \longrightarrow \frac{dm_u}{dt} = -\frac{dm_b}{dt}$$
 2-3

$$\frac{dm_{u}}{dt} = -4\pi R_{f}^{2} \rho_{u} S_{u}$$
 2-4

$$m_b = \frac{4}{3}\pi R_f^3 \rho_b \longrightarrow \frac{dm_b}{dt} = 4\pi R_f^2 \rho_b \frac{dR_f}{dt} + \frac{4}{3}\pi R_f^3 \frac{d\rho_b}{dt}$$
 2-5

$$S_{u} = \frac{\rho_{b}}{\rho_{u}} \left(\frac{dR_{f}}{dt} + \frac{R_{f}}{3\rho_{b}} \frac{d\rho_{b}}{dt} \right)$$
 2-6

$$V_{\rm u} = \left(1 - \frac{\rho_{\rm b}}{\rho_{\rm u}}\right) \frac{\mathrm{d}R_{\rm f}}{\mathrm{d}t} - \frac{R_{\rm f}}{3\rho_{\rm u}} \frac{\mathrm{d}\rho_{\rm b}}{\mathrm{d}t}$$
 2-7

Under the assumptions of ideal burned and unburned gas mixtures and isentropic compression during the flame propagation (Equation 2-8), the second term of Equation 2-6 can be expressed with pressure (P) rather than density (ρ). The final resulting expressions of S_u , i.e. Equation 2-9, are often used to calculate the laminar burning velocity from spherically expanding flames.

$$\frac{d\rho_b}{\rho_b} = \frac{dP}{\gamma_b P}$$
 2-8

$$S_{u} = \frac{\rho_{b}}{\rho_{u}} \left(\frac{dR_{f}}{dt} + \frac{R_{f}}{3\gamma_{b}P} \frac{dP}{dt} \right)$$
 2-9

Equation 2-9 is important because the unstretched flame speed of the unburned gases (S_u^o) is defined as the laminar flame speed or laminar burning velocity (S_L) . While some researchers describe the laminar burning velocity as the unstretched flame speed of the burned gases (S_u^o) and use S_u^o for the laminar flame speed, the unstretched flame speed of the unburned gases (S_u^o) of

various fuel/oxidizer mixtures has been frequently published as both the laminar flame speed and laminar burning velocity. Thus, in this document, flame speed and burning velocity terms are used interchangeably.

By comparing Equations 2-1 and 2-9, an expression for the burned gas flame speed (S_b) can be derived (Equation 2-10). In Equation 2-10, the time rate of change of the cold flame front radius (dR_f/dt) is defined as the flame propagation speed and it is equal to S_b in constant pressure measurements. Therefore, the flame propagation speed is sometimes called the burned gas flame speed by researchers employing the constant pressure method.

$$S_{b} = \frac{dR_{f}}{dt} + \frac{R_{f}}{3\gamma_{b}P} \frac{dP}{dt}$$
2-10

In the spherically expanding flame approach, there are three main methods to determine the laminar flame speed. The first and oldest method is the constant volume method (CVM), which calculates the laminar flame speed from the pressure measurements with the help of Equation 2-9 [17, 69-76]. At the early stage of the flame propagation, the pressure rise is negligible and therefore, the constant volume method measurements start at relatively large flame radii (Figure 2-4-right). With this method, there is no direct need for flame visualization and the stretch effect is not severe at high radii. Consequently, high-pressure measurements can be conducted without concern for flame stretch and a low-cost windowless combustion chamber can be used. However, this method might not take into account the effect of flame-front cellular instabilities on the flame speed due to the lack of visual observation.

After the establishment of the concept of flame stretch by the mid-1980s [13], the laminar burning velocity has most often been measured through the observation of the flame radius in the constant pressure region together with Equation 2-9 (Figure 2-4-right) [3, 10, 16, 21, 23-24, 66, 77-97]. This method is implemented in an optically accessible combustion chamber, which is

called the constant pressure method (CPM), and is supported with either schlieren or shadowgraph imaging techniques.

Recently, direct measurement of unburned gas/flow velocity (V_u) from PIV images and calculation of the laminar flame speed directly from the flame front observation was proposed by Balusamy et al. [98] and further improved by Varea et al. [99]. The PIV method enables the elimination of the use of thermodynamic properties of the burned gas and offers a wider range of data sampling as long as a clear vision of the flame front is possible (Figure 2-4-right). However, the PIV method is very difficult to implement in experiments and for this reason has not been used extensively [13].

2.2.1 Constant Volume Method

In the constant volume method, the laminar burning velocity is calculated from the pressure history and burned mass fraction instead of the cold flame front radius. Therefore, there is no need for a window in the vessel, which facilitates laminar flame speed measurements at high pressures and temperatures (engine-relevant conditions). Although the laminar burning velocities for a given mixture over a wide range of pressures and temperatures can be determined from a single test, the inception of flame instabilities cannot be identified without optical observation [13, 100]. Therefore, spherical constant volume combustion chambers used for laminar burning velocity measurements with the constant volume method have begun to be equipped with fused quartz/sapphire windows in order to detect flame-front cellular formation by schlieren/shadowgraph techniques, e.g. [101-104]. However, this modification in the vessel design causes the constant volume method to lose its ability to measure laminar burning velocities at very high pressures and temperatures.

As the flame radius increases and the pressure builds up, the flame stretching gets weaker. Since the constant volume method measurements start at relatively large flame radii, it is usually assumed that the measurements are not affected by the flame stretch. Recent studies [105-107] showed that when the relative pressure rise is above 20%, the stretch effect on the flame speed is less than 10% and this effect can be considered insignificant for measurements starting at pressures 2.5 times the initial pressure [108]. Nevertheless, the inception of cellularity is usually observed before the pressure within the chamber reaches 2.5 times the initial pressure [66] and consequently, stretch-free operation may not be possible all the time for the constant volume method.

Laminar burning velocity calculation with the constant volume method is based on Equation 2-9, which is applicable to an infinitely thin smooth flame front, ideal burned and unburned gas mixtures, and isentropic compression during the flame propagation without any buoyancy effect. Since the cold flame front radius (R_f) is not measured in the constant volume method, the burned mass fraction (x) is defined as Equation 2-11 and it is used to find an expression for R_f in terms of R_w , x, y_u , P and P_i , i.e. Equation 2-12 [109]. By substituting Equation 2-12 into Equation 2-9, the final equation for S_u is achieved as Equation 2-13 [110-111]. Equation 2-13 is very important and widely utilized to calculate the laminar burning velocity in the constant volume method.

$$x = \frac{m_b}{m_i} \longrightarrow x = 1 - \frac{m_u}{m_i} = 1 - \frac{\frac{4}{3}\pi(R_w^3 - R_f^3)\rho_u}{\frac{4}{3}\pi R_w^3 \rho_i}$$
 2-11

$$\begin{split} R_f &= R_w \left[1 - (1-x) \left(\frac{P_i}{P} \right)^{1/\gamma_u} \right]^{1/3} \text{ where } \frac{\rho_i}{\rho_u} \\ &= \left(\frac{P_i}{P} \right)^{1/\gamma_u} \text{ for isentropic compression} \end{split}$$

$$S_{u} = \frac{R_{w}}{3} \left(\frac{P_{i}}{P}\right)^{1/\gamma_{u}} \left[1 - (1 - x)\left(\frac{P_{i}}{P}\right)^{1/\gamma_{u}}\right]^{-2/3} \frac{dx}{dt}$$
2-13

The last step of the laminar burning velocity calculation with the constant volume method is the determination of the burned mass fraction (x) as a function of pressure because x is the only unknown in Equation 2-13. This can be achieved by two-zone or multi-zone burned mass fraction models, which divide the vessel inner volume into two regions as burned and unburned gas mixtures and perform equilibrium calculations for each time step.

Since the laminar burning velocities of a given mixture over a wide range of pressures and temperatures can be determined from a single test, laminar flame speed calculations in the constant volume method are sometimes followed by the designation of a correlation for the laminar burning velocity, which shows the dependency of S_L on pressure, temperature, and equivalence ratio (ϕ) [70, 72, 105, 112].

Finally, if some or all of the pressure data utilized for the calculation of S_L is less than 2.5 times the initial pressure, where the stretch effect is still significant [108] and therefore $S_L = S_u^o \neq S_u$, then the stretch treatment should be applied to the S_u values to obtain accurate laminar burning velocities. The stretch treatment is explained in the Stretch Correlations sub-section in the Constant Pressure Method section since the flame stretch is most important in the early stage of combustion, where the pressure is constant or almost constant.

2.2.1.1 Burned Mass Fraction Models

While the two-zone burned mass fraction models assume constant properties throughout the burned gas mixture, the multi-zone models divide the burned gas into layers and make the same assumption within each layer but allow the gas properties to vary from layer to layer. It has been numerically [100] and experimentally [113] shown that in the early stage of combustion (before

approximately 15 ms) the two-zone model assumption holds true since the temperature gradient in the burned gas is relatively small.

Instead of solving the conservation equations throughout the burned gas mixture (multizone model [73, 113]), the two-zone models represent the burned mass fraction (x) with correlations. The most well-known and commonly used correlation was proposed by Lewis and Von Elbe [111] and is shown in Equation 2-14. In this equation, P_m represents the theoretical maximum combustion pressure, which is higher than the maximum pressure experienced in experiments. Therefore, this value can be determined from chemical equilibrium calculations for well-known single component fuels. For the other fuels and fuel surrogates, a correction compensation factor can be determined between the numerical and experimental maximum pressures of known fuels and applied to the experimental data of other fuels [114]. By substituting Equation 2-14 into Equation 2-13, an expression for S_u depending only on pressure, R_w and γ_u can be achieved, i.e. Equation 2-15.

$$x = \frac{P - P_i}{P_m - P_i}$$
 2-14

$$S_{u} = \frac{R_{w}}{3} \left(\frac{P_{i}}{P}\right)^{1/\gamma_{u}} \frac{1}{P_{m} - P_{i}} \left[1 - \left(\frac{P_{m} - P}{P_{m} - P_{i}}\right) \left(\frac{P_{i}}{P}\right)^{1/\gamma_{u}} \right]^{-2/3} \frac{dP}{dt}$$
2-15

Although the approach of Lewis and Von Elbe [111], and therefore Equation 2-15, is frequently used [115-116], Luijten et al. [117] claimed that this approach violated the integral energy equation and provided inaccurate results especially for small burned mass fraction values. By following a different derivation procedure, Luijten et al. [117] came up with a two-zone model, which is identical to another expression of Lewis and Von Elbe [118] for the multi-zone model, i.e. Equation 2-16.

$$x = \frac{P - P_i * f(P)}{P_m - P_i * f(P)} \quad \text{where} \quad f(P) = \left(\frac{\gamma_b - 1}{\gamma_u - 1}\right) + \left(\frac{\gamma_u - \gamma_b}{\gamma_u - 1}\right) \left(\frac{P}{P_i}\right)^{(\gamma_u - 1)/\gamma_u}$$
 2-16

O'Donovan and Rallis [109] proposed Equation 2-17 for burned mass fraction. In this expression, $\overline{T_b}$ is the mass-averaged burned temperature for multi-zone model with the theoretical maximum value of $\overline{T_m}$, which is observed at P_m . In order to find $\overline{T_b}$, first the unburned temperature of each layer/shell is calculated from isentropic compression and the burned gas temperature is obtained from energy conservation for a layer at uniform constant pressure [117]. Then, $\overline{T_b}$ can be calculated from mass-based averaging. $\overline{T_m}$ may be determined with the same approach except by using P_m , i.e. chemical equilibrium calculations.

$$x = \frac{\overline{T_m}}{\overline{T_b}} \left[\frac{P - P_i * \left(\frac{P}{\overline{P_i}}\right)^{(\gamma_u - 1)/\gamma_u}}{P_m - P_i * \left(\frac{\overline{T_m}}{\overline{T_b}}\right) * \left(\frac{P}{\overline{P_m}}\right)^{(\gamma_u - 1)/\gamma_u}} \right]$$
2-17

Since the determination of $\overline{T_b}$ is difficult as prescribed in O'Donovan and Rallis [109], Oancea et al. [119] proposed Equation 2-18 for $\overline{T_b}$ by using the same burned mass fraction expression as O'Donovan and Rallis [109], i.e. Equation 2-17. In Equation 2-18, $T_{adb,p}$ and $T_{adb,v}$ represent the adiabatic flame temperatures for isobaric and isochoric combustion. These two temperature values can be easily calculated using chemical equilibrium software for well-known fuels. Rallis and Tremeer [120] further simplified Equation 2-17 by assuming $\overline{T_b} = \overline{T_m}$, which suggests that mass averaged burned gas temperature does not vary over time and results in Equation 2-19.

$$\frac{\overline{T_m}}{\overline{T_b}} = \left(\frac{P_m}{P}\right)^{(\gamma^* - 1)/\gamma^*} \quad \text{where } \gamma^* = \ln\left[\frac{P_m}{P_i}\left(1 - \frac{T_{adb,p}}{T_{adb,v}}\right)\right]$$
 2-18

$$x = \frac{P - P_i * \left(\frac{P}{P_i}\right)^{(\gamma_u - 1)}/\gamma_u}{P_m - P_i * \left(\frac{P}{P_i}\right)^{(\gamma_u - 1)}/\gamma_u}$$
2-19

Although there are other burned mass fraction correlations, such as Rallis and Garforth [44] and Nagy et al. [121], it was shown that they are not as accurate as the ones mentioned above [100, 117]. Consequently, the burned mass fraction discussion is limited to the correlations of Lewis and Von Elbe [111], Luijten et al. [117], O'Donovan and Rallis [109], Oancea et al. [119], and Rallis and Tremeer [120] for brevity.

Before comparing the performances of the burned mass fraction correlations, the calculation of the burned and unburned gas heat capacity ratios (γ_b and γ_u) should be discussed. Until the inception of flame front cellularity, γ_u for each individual reactant can be calculated from its definition, i.e. Equation 2-20, by assuming isentropic compression and the resulting heat capacity ratio of unburned gases can be determined with simple averaging according to mole fractions. On the other hand, a constant value is mostly used for the heat capacity ratio of burned gases, which is called the frozen heat capacity ratio and assumed to be around 1.25 for hydrocarbon/air mixtures [100, 117]. However, Faghih and Chen [100] proposed Equation 2-21 for γ_b together with a value of $\gamma_{b,shift}$ =1.17 for hydrocarbon/air mixtures due to the influence of chemical equilibrium shifting on burned gases. Another correlation for γ_b was suggested by Omari and Tartakovsky [122], which is shown in Equation 2-22. Numerical studies of Faghih and Chen [100] show that most accurate results can be achieved with Equation 2-21 among these three approaches.

$$\gamma_u = \frac{c_p(T)}{c_p(T) - \frac{R_u}{MW}} \quad \text{where} \quad T = T_i \left(\frac{P}{P_i}\right)^{(\gamma_u - 1)/\gamma_u}$$
 2-20

$$\gamma_b = 8\gamma_{b,shift} - 8$$
 where $\gamma_{b,shift} = 1.17$

$$\gamma_b = 2\gamma_{b,shift} - 1$$
 where $\gamma_{b,shift} = 1.17$

Studies of Faghih and Chen [100] and Luijten et al. [117] showed that among all burned mass fraction correlations available today, Oancea et al.'s approach [119] (Equation 2-17 and Equation 2-18) and Luijten et al.'s approach [117] (Equation 2-16 with γ_b =1.25) are the most accurate. However, Faghih and Chen [100] also noted that the accuracy of Luijten et al.'s approach [117] could be further improved by using Equation 2-21 instead of γ_b =1.25. Rallis and Tremeer's approach [120] (Equation 2-19) has been shown to have the worst performance due to the assumption of $\overline{T_b} = \overline{T_m}$.

For clarity, all burned mass fraction correlations explained above are summarized in Table 2-2. As a result of this literature review on the constant volume method, Equations 2-13, 2-16, 2-20 and 2-21 are suggested for calculating the laminar burning velocity with the constant volume method.

Table 2-2. Burned Mass Fraction Models.

Reference	Burned Mass Fraction Models	
Lewis and Von Elbe [111]	$x = \frac{P - P_i}{P_m - P_i}$	
Luijten et al. [117]	$\begin{split} x = \frac{P - P_i * f(P)}{P_m - P_i * f(P)} \text{where} f(P) = \left(\frac{\gamma_b - 1}{\gamma_u - 1}\right) + \left(\frac{\gamma_u - \gamma_b}{\gamma_u - 1}\right) \left(\frac{P}{P_i}\right)^{(\gamma_u - 1)/\gamma_u} \\ \gamma_b = 8\gamma_{b, shift} - 8 \text{where} \gamma_{b, shift} = 1.17 \end{split}$	
O'Donovan and Rallis [109]	$x = \frac{\overline{T_m}}{\overline{T_b}} \left[\frac{P - P_i * \left(\frac{P}{P_i}\right)^{(\gamma_u - 1)/\gamma_u}}{P_m - P_i * \left(\frac{\overline{T_m}}{\overline{T_b}}\right) * \left(\frac{P}{P_m}\right)^{(\gamma_u - 1)/\gamma_u}} \right]$	

Table 2-2 (cont'd)

Oancea et al. [119]
$$x = \frac{\overline{T_m}}{\overline{T_b}} \left[\frac{P - P_i * \left(\frac{P}{P_i}\right)^{(\gamma_u - 1)/\gamma_u}}{P_m - P_i * \left(\frac{\overline{T_m}}{\overline{T_b}}\right) * \left(\frac{P}{P_m}\right)^{(\gamma_u - 1)/\gamma_u}} \right]$$
 where
$$\frac{\overline{T_m}}{\overline{T_b}} = \left(\frac{P_m}{P}\right)^{(\gamma^* - 1)/\gamma^*} & \& \gamma^* = \ln\left[\frac{P_m}{P_i}\left(1 - \frac{T_{adb,p}}{T_{adb,v}}\right)\right]$$

$$x = \frac{P - P_i * \left(\frac{P}{P_i}\right)^{(\gamma_u - 1)/\gamma_u}}{P_m - P_i * \left(\frac{P}{P_i}\right)^{(\gamma_u - 1)/\gamma_u}}$$

2.2.2 Constant Pressure Method

In the constant pressure method, the cold flame front radius of a spherically expanding flame is generally measured by a schlieren or shadowgraph optical technique in order to calculate the laminar burning velocity. Calculations are based on Equation 2-9, which is derived under the assumptions of an infinitely thin smooth flame front, ideal burned and unburned gas mixtures, and isentropic compression during the flame propagation without any buoyancy effect. Since the measurements are limited to the constant pressure region as shown in Figure 2-5, which is the initial stage of combustion, the second term of Equation 2-9 equals zero, which implicitly suggests that the time rate of change of the burned gas density is zero and the burned gas flame speed is equal to the time rate of change of the cold flame front radius. The resulting simplified laminar burning velocity expression becomes Equation 2-23.

$$S_{u} = \frac{\rho_{b}}{\rho_{u}} \frac{dR_{f}}{dt} = \frac{\rho_{b}}{\rho_{u}} S_{b}$$
2-23

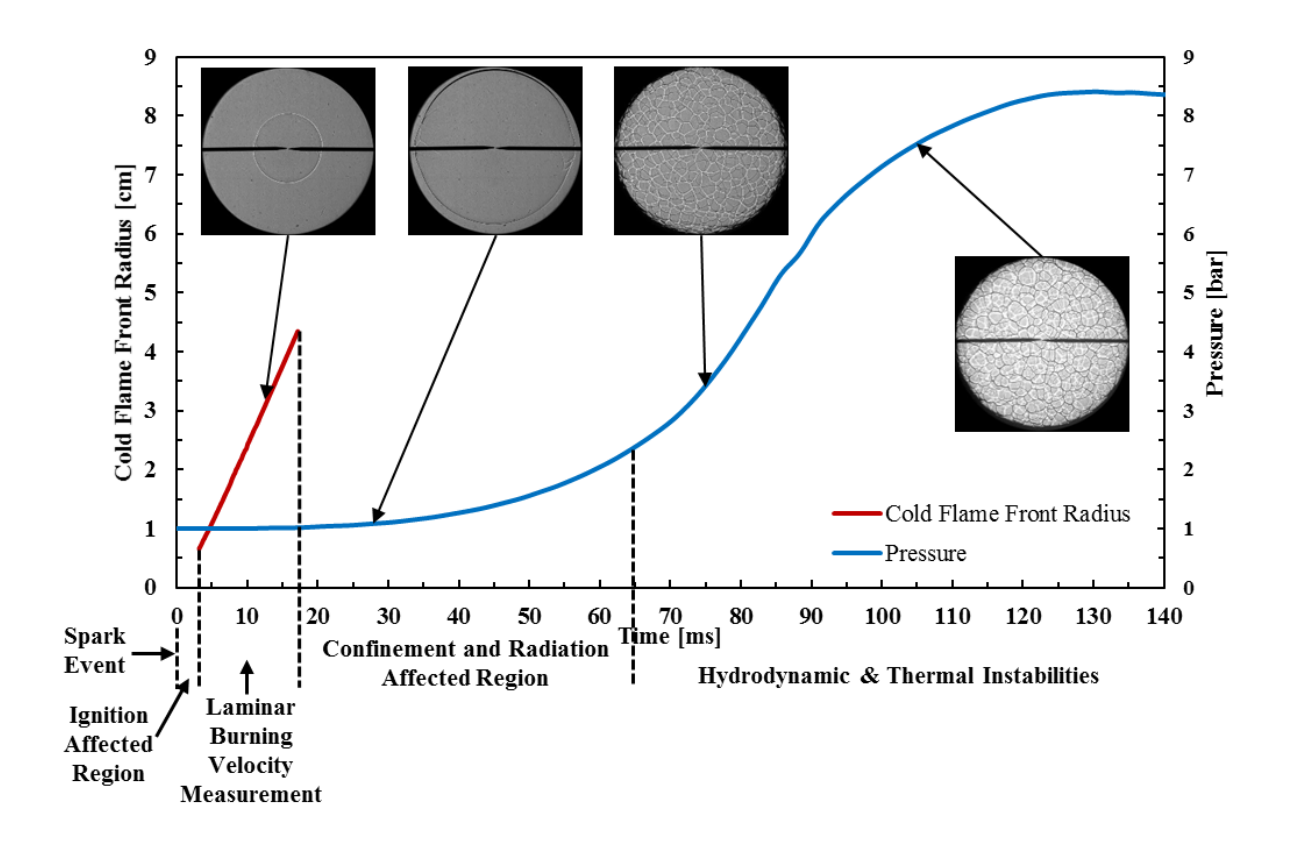


Figure 2-5. Cold flame front radius growth and pressure history for a methane/air mixture at 1 bar, 298 K, and φ=1.0 showing the constant pressure region that is used for the laminar burning velocity measurements.

For Equation 2-23 to hold true, upper and lower limits are applied to the measured cold flame front radius (R_f). The lower radius bound is chosen to avoid the effect of ignition and to obtain a flame structure that obeys linear or non-linear stretch correlations. This limit was found to be 6 mm by Bradley et al. [68] who investigated flame propagations of methane/air mixtures ignited with different ignition energies. However, it has been shown that the ignition effect gets stronger for large Lewis numbers and Markstein lengths [107, 123-124], which can be numerically quantified with the help of the Karlovitz number.

While the influence of the ignition event on the laminar burning velocity decreases at high initial temperatures and pressures due to higher flame propagating speed and thinner flame thickness, respectively, the increase in fuel carbon number magnifies the effect of ignition and

nonlinear stretch behavior by decreasing fuel mass diffusivity, which increases Lewis number and Markstein length [124-125]. Therefore, beginning measurements at $R_f > 6$ mm does not always guarantee negligible ignition effects for different mixtures under different conditions. The best way to determine the lower limit for R_f can be to conduct consecutive experiments with different ignition energies close to the minimum ignition energy of the mixture at the same initial conditions, since varying the spark energy over a wide range from the minimum ignition energy has no significant effect on the flammability limits and burning velocity [126]. Then, the lower limit for R_f can be established where the S_b vs. R_f curves first converge for all experiments at the same test conditions.

Similarly, an upper limit should also be defined for R_f to reduce the effects of buoyancy, flame instability, confinement, and radiation. The influence of radiation and confinement on the laminar burning velocity can be explained by the thermal effect, which is the change in burned or unburned gas temperature, and the flow effect, which is the inward flow of burned gas induced by radiation or compression [127]. Previous studies [125, 127-128] showed that the strength of the radiation and confinement effects depend on the initial thermodynamic conditions of the mixture and the measurement range. For instance, while the radiation induced cooling effect decreases with increasing initial temperature due to faster flame propagation speeds, it increases at higher initial pressures because the laminar flame speed reduces [124]. These examples show that the thermal effect of radiation heavily depends on the flame propagation speed because the burned gases have more time to cool down at low laminar burning velocities [128]. The fuel carbon number has no significant influence on this effect so that the radiation induced cooling effect is nearly fuel-independent [124]. However, the thermal radiation effect gets stronger for equivalence ratios that vary from stoichiometry, especially near the lean and rich flammability limits. The laminar burning

velocity can be reduced by up to 4-6% at the lean and rich flammability limits and 3% near stoichiometric conditions due to the thermal effect of radiation [124, 127]. With numerical simulations of methane, propane, and iso-octane flames, Yu et al. [129] proposed that the reduction in the S_L due to radiation induced cooling is no more than 5% for $S_L \ge 12$ cm/s and 2% for $S_L \ge 26$ cm/s.

Another parameter affecting the influence of radiation and confinement on the laminar burning velocity is the measurement range. The radiation and confinement induced inward flow effects increase with flame radius [107, 129-130]. Burke et al. [131] and Chen [124] suggested that the reduction in the S_L caused by these two effects is around 2-3% at $R_f/R_w<0.25$, where R_w is the equivalent radius for a cylindrical vessel. However, whenever cellular formation or buoyancy effect are observed before the upper limit, measurements should be stopped, and the laminar burning velocity calculations should be limited to the images before the inception of cellular formation.

Jayachandran et al. [125] suggested that the displacement speed should be measured relative to the fresh gases, $S_u = \frac{dR_f}{dt} - V_u$ from Equation 2-2, in order to prevent errors in the laminar burning velocity associated with radiation. In fact, several researchers have attempted to measure the time rate of change of the cold flame front radius and the unburned gas/flow velocity with Particle Image Velocimetry (PIV), which has resulted in the PIV method for measuring the laminar burning velocity from spherically expanding flames [98-99, 132-135]. Although the radiation and confinement induced inward flow effects can be avoided with this approach [125], the effect of heat loss through particle radiation and conduction and the uncertainty in flow speed measurement can affect the accuracy of the laminar burning velocity measurements [124].

Furthermore, the PIV method is very difficult to implement in experiments and for this reason has not been used extensively [13].

For cases when the PIV method is not preferred, the upper limit for the cold flame front radius in the constant pressure method is not satisfied, or if further improvements in accuracy are desired, the variation in the burned gas density can be estimated with several correlations. Self-sustaining flames have high gradients of temperature and species concentration, which suggests that the flame thickness should be very small. In fact, typical flame thicknesses are on the order of a millimeter and decrease with increasing pressure [4]. Consequently, many scientists neglect the burned gas density variation within the flame thickness and burned gases, and evaluate the burned gas density at chemical equilibrium or use the ideal gas law by assuming the burned gas density as constant [130], i.e. Equation 2-24, in which T_b is usually assumed to be the constant pressure adiabatic flame temperature and n corresponds to the mole number. However, curvature and preferential diffusion effects in the early stage of combustion and radiation and confinement effects in the latter stage of combustion affect the evolution of the flame and the burned gas temperature [21, 130]. Therefore, utilization of the mean density of the burned gases ($\overline{\rho_b}$) can lead to more accurate results [13], i.e. Equation 2-25.

$$S_{u} = \frac{\rho_{b}}{\rho_{u}} \frac{dR_{f}}{dt} = \frac{\rho_{b}}{\rho_{u}} S_{b} = \frac{n_{u} T_{u}}{n_{b} T_{b}} S_{b}$$
 2-24

$$S_{u} = \frac{\overline{\rho_{b}}}{\rho_{u}} \frac{dR_{f}}{dt} = \frac{\overline{\rho_{b}}}{\rho_{u}} S_{b}$$
2-25

If the variation in temperature within the burned gases is neglected and the burned gas temperature is assumed to be the adiabatic flame temperature, the calculated burned gas density (ρ_b) should be less than the actual value, which causes lower laminar burning velocities.

Consequently, Andrews and Bradley [46] proposed Equation 2-26 to account for the variation in burned gas density.

$$\overline{\rho_b} = \frac{3}{R_f^3} \int_0^{R_f} \rho_b r^2 dr$$
 2-26

Actual temperature variation, leading to density variation at constant pressure conditions, may be obtained from burner measurements or theoretical calculations can be used [46]. Due to the difficulties in the determination of a temperature profile within the burned gases, Andrews and Bradley [136] assumed constant temperature, therefore constant density, throughout the burned gases and evaluated the mean gas density by using measured temperature vs. flame thickness data together with Equation 2-27. In this expression, δ_L represents the laminar flame thickness. Gulder [69] and Wang et al. [137] further simplified the calculations and used linear temperature profiles within the flame thickness with Equation 2-27. In the absence of measured temperature and flame thickness data, linear temperature profile assumption is reasonable.

$$\frac{\overline{\rho_b}}{\rho_u} = \left(\frac{n_u T_u}{n_b T_b}\right) \frac{1}{R_f^3} \left[(R_f - \delta_L)^3 + 3T_b \int_{R_f - \delta_L}^{R_f} \frac{r^2}{T_r} dr \right]$$
 2-27

Lastly, an alternative approach was proposed by Bradley et al. [68] for the expansion ratio as shown in Equation 2-28. Although Equation 2-28 is an empirical correlation derived from the laminar burning velocity results of methane/air mixtures at normal temperature and pressure (NTP), the same expression was also shown applicable for iso-octane/air [138] and butanol/air [139] mixtures.

$$\frac{\overline{\rho_b}}{\rho_u} = \frac{\rho_b}{\rho_u} \left\{ 1 + 1.2 \left[\frac{\delta_L}{R_f} \left(\frac{\rho_u}{\rho_b} \right)^{2.2} \right] - 0.15 \left[\frac{\delta_L}{R_f} \left(\frac{\rho_u}{\rho_b} \right)^{2.2} \right]^2 \right\}$$
 2-28

In the constant pressure method, the cold flame front radius (R_f) is generally detected by schlieren or shadowgraph techniques. Bradley et al. [68] proposed an empirical relationship (Equation 2-29) between the cold flame front radius and the radius detected by schlieren photography (R_{sch}) by using the definition of the flame stretch rate. Since the laminar flame thickness depends on the laminar burning velocity ($\delta_L = \nu_u / S_u^o$), which cannot be found before R_f , R_f can be first assumed as R_{sch} and subsequently Equation 2-29 can be adopted to give actual R_f [137]. Alternatively, another definition of laminar flame thickness [$\delta_L = (T_{adb,p} - T_u)/(dT/dr)_m$] can be utilized to eliminate the iterative procedure. However, Bradley et al. [68] also showed that the flame speed is almost independent of the chosen isotherm, which is associated with the flame speed to identify the cold flame front radius. This suggests that the flame front definition has almost no influence on the flame propagation speed and stretch rate [129]. Therefore, Equation 2-30 is mostly preferred in the constant pressure method rather than Equation 2-29.

$$\frac{\frac{2}{R_f} \frac{dR_f}{dt}}{\frac{2}{R_{sch}} \frac{dR_{sch}}{dt}} = 1 - 1.95 \frac{\delta_L}{R_f} \sqrt{\frac{\rho_u}{\rho_b}} \longrightarrow R_f = R_{sch} + 1.95 \delta_L \sqrt{\frac{\rho_u}{\rho_b}}$$
2-29

$$\frac{dR_f}{dt} = \frac{dR_{sch}}{dt} \longrightarrow S_u = \frac{\rho_b}{\rho_u} \frac{dR_{sch}}{dt}$$
2-30

One way to approximate the derivative of the cold flame front radius in Equation 2-30 is to use central differencing as a finite difference method. With this method, there is no difference between the definitions of cold flame front radius with respect to R_{sch}, i.e. Equations 2-29 and 2-30, because the second term of Equation 2-29 can be assumed constant in the early stage of the combustion where the pressure is constant. Using the central difference method to obtain the derivative can lead to noise in experimental data. Alternatively, a second- [140] or third-order [90]

polynomial can be fit to the radius-time history and differentiated to obtain the flame speed of the burned gases under constant pressure conditions (S_b) . However, some errors are introduced during the polynomial fit and derivative operations.

Before discussing the stretch correlations, some important combustion parameters, such as laminar flame thickness (δ_L), activation energy (E_a), Zeldovich number (Ze), and Lewis number (Le), should be discussed since they are frequently used in flame stretch discussions. First, there are two widely preferred flame thickness definitions, which are shown in Equations 2-31 and 2-32. Equation 2-31 comes from kinetic analysis and contains thermal diffusivity. Equation 2-32 is derived from the gradient method. Although some researchers prefer Equation 2-31 over the gradient method, such as Wang et al. [137] and Lamoureux et al. [141], others believe it does not yield reliable results due to the arbitrariness of the temperature at which the thermal conductivity of the unburned gas (λ_u) and the constant pressure specific heat of the unburned gas $(c_{p,u})$ are evaluated [142]. Some researchers evaluate $\lambda_u/c_{p,u}$ at the unburned gas temperature, but Lapalme et al. [143] suggested that the average of the unburned gas and adiabatic flame temperatures should be used for the evaluation of λ_u and $c_{p,u}$ due to the increase in gas mixture temperature in the preheat zone of the flame thickness (Figure 2-4-left). Furthermore, Equation 2-31 contains laminar flame speed (S_u^0) , which prevents the independent nature of the flame thickness in characterizing the flame behavior [142]. Due to the concerns stated above, Jomass et al. [142] and Law and Sung [144] recommend Equation 2-32 for calculating laminar flame thickness. In this expression, T_b is mostly assumed to be the adiabatic flame temperature and the maximum temperature gradient can be derived from experimental data in the literature or chemical equilibrium calculations for wellknown fuels.

$$\delta_{\rm L} = \frac{\lambda_{\rm u}}{\rho_{\rm u} c_{\rm n,u} S_{\rm u}^{\rm o}}$$
 2-31

$$\delta_{\rm L} = \frac{T_{\rm b} - T_{\rm u}}{\left(\frac{\rm dT}{\rm dr}\right)_{\rm m}}$$
2-32

Activation energy (E_a) represents the sensitivity of the laminar burning velocity to the flame temperature variation and can be expressed as Equation 2-33, which is also called the activation temperature. The activation temperature can be found by computing $\rho_u S_u^0$ at the desired initial conditions, and then slightly changing the concentration of, for instance, nitrogen with inert argon while keeping the pressure and equivalence ratio unchanged [142-143, 145]. This approach is easily applicable to numerical analysis, however can cause noteworthy errors in experimental studies due to the accuracy limitations of absolute/gauge pressure transducers. An alternative approach is to derive the activation time from the plot of $\ln(\rho_u S_u^0)$ vs. $^1/T_b$ for a given pressure but at slightly different equivalence ratios, in which the activation time is assumed unchanged [137]. However, it should be noted that activation energy strongly depends on φ . A dimensionless form of activation energy is designated as the Zeldovich number (Equation 2-34), whose inverse represents a dimensionless flame thickness.

$$\frac{E_{a}}{R_{u}} = -2 \left[\frac{\partial [\ln(\rho_{u} S_{u}^{o})]}{\partial \left(\frac{1}{T_{b}} \right)} \right]$$
 2-33

$$Ze = \frac{E_a}{R_u T_b^2} (T_b - T_u)$$
 2-34

The Lewis number is defined as the ratio of the thermal diffusivity to the mass diffusivity, i.e. Le $=\frac{\alpha_u}{D_u}=\frac{\lambda_u}{\rho_u c_{p,u} D_u}$. Although the Lewis number depends on unburned gas properties, many intermediate species emerge in the preheat zone and influence the Lewis number with their

different diffusivities, which makes Lewis number calculation complicated [143]. Therefore, the Lewis number can be extracted from the flame response to stretch, i.e. Markstein length (L_b or L_u) which is on the order of the flame thickness [146].

The Markstein length is a constant value representing the influence of flame stretch on the flame speed [146]. After integral analysis of the stretch flame, Law and Sung [144] came up with Equation 2-35 [143]. Bechtold and Matalon [147] followed the asymptotic theory and proposed Equation 2-36, which is valid near stoichiometric conditions [143]. Chen [148] used Equation 2-37, which was originally proposed for counter flow flames, in order to calculate the Lewis number. Lapalme et al. [143] investigated the accuracy of these methods and concluded that Equation 2-36 yielded the best results for hydrogen/air and carbon monoxide/air mixtures, whereas Equation 2-37 showed superior performance for methane/air mixtures. This suggests that it is difficult to determine the most accurate Lewis number definition, which is valid for all mixtures at all conditions.

$$\begin{split} Le &= 1 + \frac{2 \left(1 - \frac{\rho_b}{\rho_u}\right)}{Ze \left(\frac{\rho_b}{\rho_u}\right) (1 - \overline{\alpha})} \left[\frac{L_u}{\delta_L} + \left(1 - \frac{\rho_b}{\rho_u}\right) - \left(\frac{1 - \overline{\alpha}}{1 - \frac{\rho_b}{\rho_u}}\right) \right] \quad \text{where} \\ \overline{\alpha} &= 1 + \ln \left[\frac{\rho_b}{\rho_u} + \left(1 - \frac{\rho_b}{\rho_u}\right) \exp(-1) \right] \quad \text{and} \quad L_u = \frac{\rho_b}{\rho_u} L_b + \left(\overline{\alpha} - \frac{\rho_b}{\rho_u}\right) \delta_L \end{split}$$

$$Le = 1 + \left[\frac{L_b}{\delta_L} - \frac{2}{\sqrt{\rho_u/\rho_b} + 1} \right] \left\{ \frac{2 * Ze}{(\rho_u/\rho_b - 1)} \left[\sqrt{\frac{\rho_u}{\rho_b}} - 1 - \ln\left(\frac{1}{2}\left(\sqrt{\frac{\rho_u}{\rho_b}} + 1\right)\right) \right] \right\}^{-1}$$
 2-36

$$Le = \left[\frac{L_b}{(\rho_u/\rho_b)\delta_L} - \frac{Ze}{2}\right]^{-1} \left(1 - \frac{Ze}{2}\right)$$
 2-37

2.2.2.1 Stretch Correlations

Flame propagation in the early stage of the combustion where the pressure is constant can be divided into three distinctive regions, (1) the ignition affected region, (2) the quasi-steady stretched flame region, which is suitable for the laminar burning velocity calculations with the constant pressure method, and (3) the confinement and radiation affected region, as seen in Figure 2-5 [140]. The flame stretch rate (κ) is defined as the normalization of the rate of change of the flame surface area and is shown in Equation 2-38, which is valid for spherically growing flames [68].

$$\kappa = \frac{1}{A} \frac{dA}{dt} = \frac{2}{R_f} \frac{dR_f}{dt}$$
 2-38

The extrapolation of the stretch correlations is often used to remove the stretch effect from the experimental data, i.e. the experimental stretch model extrapolation method, and to find the unstretched flame speed of the unburned gases (S_u^o), which is the true definition of the laminar burning velocity (S_L). Among various correlations between the stretch rate and the flame speed, the linear flame stretch model based on the local stretch rate proposed by Matalon and Matkowsky [149], Equation 2-39 - designated as LS in Table 2-3, is most commonly used [150-154]. In this expression, L_b and L_u refer to the burned and unburned Markstein lengths, which indicate the effect of flame stretching on the local flame speed and the flame instability due to preferential diffusion [155-156]. In fact, a smaller Markstein length means there is a smaller influence of flame stretch on flame speed and an earlier onset of instabilities [21, 157]. Furthermore, the Markstein length is used as a physicochemical input parameter for some premixed turbulent combustion models [148, 158].

$$S_b = S_b^o - L_b \kappa \quad \& \quad S_u = S_u^o - L_u \kappa$$
 2-39

By normalizing Equation 2-39 with the unstretched flame speed, Equation 2-39 can be expressed in terms of the Markstein number (Ma) and the Karlovitz number (Ka), which characterize the flame stretch, i.e. Equation 2-40. Based on asymptotic theory, the LS model was developed under the assumption of a near unity Lewis number and a weakly stretched flame [159].

Wu et al. [160] and Courty et al. [161] asserted that the LS model overpredicts the laminar flame speed for mixtures with Le far from unity due to preferential diffusion between the fuel and oxidizer causing nonequidiffusion of heat and mass, which results in a considerable change in the burning velocity.

$$\frac{S_u}{S_u^o} = 1 - Ma * Ka$$
 where $Ma = \frac{L_u}{\delta_L} \& Ka = \kappa \frac{\delta_L}{S_u^o}$ 2-40

By assuming a quasi-steady flame propagation to eliminate the acceleration term, Kelley and Law [140] obtained a nonlinear model, Equation 2-41 - designated as NQ in Table 2-3, from the asymptotic analysis of Ronney and Sivashinsky [162] for adiabatic spherical flames. The NQ model is based on a weakly stretched flame and enables the S_L calculation of mixtures with arbitrary Le [160]. Therefore, the model has been used frequently in the past few years and has showed superior performance to Equation 2-39 [163-166]. Nevertheless, the assumption of quasi-steady flame propagation is only valid when the flame radius is reasonably large [159] since the non-linearity of the relationship between the stretch rate and the flame speed not only depends on the Lewis number, but also on the Karlovitz number, which corresponds to the normalized stretch rate [167].

$$\frac{S_b}{S_b^o} \ln \left(\frac{S_b}{S_b^o} \right) = -\frac{2L_b}{R_f} \quad \text{or} \quad \left(\frac{S_b}{S_b^o} \right)^2 \ln \left(\frac{S_b}{S_b^o} \right)^2 = -\frac{2L_b \kappa}{S_b^o}$$
 2-41

Recently, Chen [148] revisited the linear correlation between the flame speed and the flame curvature, Equation 2-42 - designated as LC in Table 2-3, which was first proposed by Markstein [168]. Under the assumption of a large spherical flame radius, the LC model accounts for effects of strong flame stretching and non-unity Le, and has been claimed to show better performance than the previously mentioned correlations for mixtures with Le greater than unity, i.e. positive Markstein length [159-161]. On the other hand, the NQ model has been alleged to show the best

performance for mixtures with Le less than unity, i.e. negative Markstein length [159-161]. Despite these findings, the LC model has not been commonly utilized yet [82, 169].

$$S_{b} = S_{b}^{o} - S_{b}^{o} L_{b} \frac{2}{R_{f}}$$
 2-42

Kelley et al. [159] solved the instability problem of the unstable weakly stretched flame relationship of Matalon and Bechtold [170] differently and suggested its expanded version in terms of the inverse power of the cold flame front radius, i.e. Equation 2-43 - designated as NE in Table 2-3. Wu et al. [160] tested this model and concluded that it provides reasonable laminar burning velocity results. However, currently, the NE model is very rarely used. Finally, for clarity, all stretch models mentioned in this document are summarized in Table 2-3.

$$\frac{S_b}{S_b^o} \left[1 + \frac{2L_b}{R_f} + \frac{4L_b^2}{R_f^2} + \frac{16L_b^3}{3R_f^3} \right] = 1$$
 2-43

Table 2-3. Stretch models.

Model	Formulation	Comments
		• It is the most well-known and commonly used correlation [150-154].
LS [149]	$S_b = S_b^o - L_b \kappa \& S_u = S_u^o - L_u \kappa$	 It was derived under the assumption of near unity Le and weakly stretched flame [159].
		 It overpredicts S_u^o and L_b for mixtures with Le appreciably different from unity [161].
NQ [140]	$\frac{S_b}{S_b^o} \ln \left(\frac{S_b}{S_b^o} \right) = -\frac{2L_b}{R_f} \text{or}$	• It is only valid when the flame radius is reasonably large [159].
	$\left(\frac{S_b}{S_b^o}\right)^2 \ln \left(\frac{S_b}{S_b^o}\right)^2 = -\frac{2L_b\kappa}{S_b^o}$	• It has a superior performance than the other correlations at Le<1 [159-161].

Table 2-3 (cont'd)

LC [148]	$S_b = S_b^o - S_b^o L_b \frac{2}{R_f}$	 It is only valid when the flame radius is reasonably large [159]. It includes the effects of strong stretch and Lewis number and has been proven to show best performance at Le>1 [159-161].
NE [159]	$\frac{S_b}{S_b^o} \left[1 + \frac{2L_b}{R_f} + \frac{4L_b^2}{R_f^2} + \frac{16L_b^3}{3R_f^3} \right] = 1$	 It is the expansion version of weakly stretch flame relationship proposed by Matalon and Bechtold [170] in terms of inverse power of flame radius. It is not commonly used.

After determining the proper stretch correlation for the desired test condition under the guidance of the above discussion, there are three common ways to calculate the unstretched flame speed of the unburned gases, i.e. laminar burning velocity. The first and most commonly used method is the experimental stretch model extrapolation. For example, linear extrapolation of the LS model can be employed on the plot of S_b vs. κ . The y-intercept of this extrapolation line is S_b^o while its slope corresponds to (-L_b). Subsequently, the laminar burning velocity (S_u^o) can be calculated from Equation 2-24 or 2-25. Although the NQ and LS models are nonlinear with respect to the flame stretch rate, the same linear extrapolation procedure can be applied to the plot of $\ln(S_b)$ vs. $2/(S_bR_f)$ for the NQ model and to the plot of S_b vs. $2/(S_bR_f)$ equals $\ln(S_b^o)$ and the y-intercept of S_b vs. $2/(S_bR_f)$ equals $\ln(S_b^o)$ and the y-intercept of S_b vs. $2/(S_bR_f)$ equals $\ln(S_b^o)$

Tahtouh et al. [90] claimed that extrapolation of the stretch correlations using the burned flame speed (S_b) to find the laminar burning velocity is sensitive to the quality of the experiments and to the methodology used to obtain the temporal evolution of the flame front propagation speed and introduces noise with the differentiation process. Alternatively, these stretch correlations can

be integrated with respect to time since S_b and κ can be written in terms of R_f , and R_f depends only on time. Then, S_b^o and L_b can be derived using linear regression [92, 171]. While this approach seems more accurate than the previous approach since there is no differentiation, it is not easy to integrate the extrapolation correlations except the LS model, which is less accurate than the other stretch models. If the integral approach is followed for the LS model, the resulting expression becomes Equation 2-44 [92, 171].

$$R_f = S_b^0 t - 2L_b \ln(R_f) + constant$$
 2-44

Recently, Egolfopoulos and coworkers [172-174] introduced another approach, direct numerical simulation (DNS) mapping, to perform a DNS-assisted extrapolation of stretch correlations. Xiouris et al. [108] stated that a finite uncertainty is introduced no matter which method (experimental stretch model extrapolation, integral, or DNS-mapping) is utilized to subtract the effect of stretch, owing to the lack of knowledge of the actual S_b-κ behavior and assumptions made for these approaches. For instance, while the experimental stretch model extrapolation ignores differential diffusion effects [175], the DNS-mapping suffers from transport and kinetic model uncertainties, especially for large hydrocarbon fuels [125, 176]. Despite all of the assumptions, numerical, theoretical, and experimental studies of Chen [148] and Gong et al. [176] showed that results of both approaches are in good agreement at most of the experimental conditions, but under strong nonlinearity, the accuracy of the experimental stretch model extrapolation method strongly depends on the stretch correlation choice and the range of the flame radius used in the S_L calculation. In fact, Gong et al. [176] demonstrated that the experimental stretch model extrapolation accuracy approaches that of the DNS-mapping with increasing lower flame speed measurement limit for highly nonlinear S_b - κ behavior.

Finally, although the stretch effect and extrapolation uncertainty decrease with increasing pressure due to thinner flame thickness and smaller Markstein length [177], the flame stretch rate still affects the laminar burning velocity until the combustion pressure exceeds 2.5 times the initial pressure [108]. Therefore, the flame stretch is important for all spherically expanding flame speed measurements conducted under 2.5P_i.

2.2.3 PIV Method

In the constant volume and constant pressure methods, the laminar burning velocity depends on the thermodynamic properties of the burned gas, which are estimated with assumptions of an ideal gas, isentropic compression, and adiabatic and equilibrium conditions. However, recently, Balusamy et al. [98] established the PIV method with enhanced post-processing algorithms for direct measurement of local instantaneous laminar flame speed by using Equation 2-45, which is nothing but the rewritten version of Equation 2-2.

$$S_{u} = \frac{dR_{f}}{dt} - V_{u}$$
 2-45

Although the laminar burning velocity calculations seem quite straightforward with respect to the formulation, this approach has not been widely used due to the difficulty of the unburned gas/flow velocity (V_u) measurement near the preheat zone of the flame front, whose thickness is less than a millimeter [13]. Balusamy et al. [98] defines V_u as the maximum of the unburned gas velocity profile within the pre-heat zone of the laminar flame thickness, which characterizes the beginning of the heat diffusion influence on the unburned gas velocity. Standard PIV techniques are not capable of detecting V_u ; consequently, Balusamy et al. [132] developed an algorithm using an adaptive interrogation window scheme by considering the local topologies of the flow and flame front.

With this method, the local flame propagation speed (dR_f/dt) is measured from the distance between two successive flame positions in a sub-pixel level [98]. Subsequently, the laminar burning velocity can be calculated using one of the stretch correlations explained above since the laminar flame speed measurements are still affected by stretch due to the fact that PIV measurements are conducted in the early stages of combustion until there is no longer a clear view of the spherical flame.

This approach has been further developed by Varea et al. [99] with a new post-processing algorithm that accounts for the overall topology of the flame front, assuming that the flame is homogeneous, which therefore enables the detection of global Vu values. The improved PIV method of Varea et al. [99] was used to measure laminar burning velocities of methane/air [99, 133], ethanol/air [99, 134], iso-octane/air [99, 134], and hydrogen/air [135] mixtures. Results of these studies show that laminar burning velocities calculated by the PIV method are generally higher than those derived with the constant volume and constant pressure methods. This may be explained with the findings of Jayachandran et al. [125], which suggest that radiation-induced flow effect can be avoided with the PIV method while it is inevitable for the constant volume and constant pressure methods at some stage of combustion. However, heat loss through particle radiation and conduction and uncertainty in the flow speed measurement still need to be addressed for the validity of this method [124]. Finally, methods to measure the laminar burning velocity from spherically expanding flames are compared in Table 2-4.

Table 2-4. Comparison of methods to measure the laminar burning velocity from spherically expanding flames.

Measurement Technique	Advantages	Disadvantages
Constant Volume Method	 S_L measurements at high pressures and temperatures (engine-relevant conditions) are possible with a windowless chamber which is inexpensive and easy to use. 	The inception of flame instabilities and effects of flame stretch cannot be identified with a windowless chamber.
	 S_L values for a given mixture over a wide range of pressures and temperatures can be determined from a single test. 	• If the apparatus is modified for the optical observation, engine-relevant conditions cannot be tested.
		 S_L values of mixtures with negative L_b cannot be measured due to the early onset of the cellularity.
Constant Volume Method	• The effect of flame stretching is milder than other two methods.	 Inaccuracies are introduced due to burned mass fraction models.
		 Thermodynamic properties of the burned gas are used to calculate the S_L.
Constant Pressure Method	 The method is well established and commonly used for S_L calculations. Since the measurements are limited to the early stage of combustion, the method is not noteworthily affected by flame front instabilities. 	 Thermodynamic properties of the burned gas are used to calculate the S_L. Measurements can be severely affected by the flame stretch.
PIV Method	 This method directly measures the unburned flame speed, therefore the thermodynamic properties of the burned gas are not used. The radiation-induced flow effect can be avoided [125]. 	 Heat loss through particle radiation and conduction and uncertainty in the flow speed measurement still need to be investigated for the validity of this method [124]. The method is difficult to implement in experiments and has a complex post-processing [13]. Measurements can be severely

2.3 Flame Front Instabilities and Cellularity

Apart from external disturbances, such as turbulence and confinement, spherically expanding flame stability is mainly governed by two inherent sources, namely hydrodynamic

(Darrieus-Landau) and thermal-diffusive (preferential-diffusion) instabilities [62]. These instabilities wrinkle the smooth spherical flame front and induce cellularity due to a small flow perturbation, such as a solid body, pressure pulses, or acoustic oscillations [157], and therefore, increase the flame surface area and the flame propagation speed [178]. Continuous development of cellular structure on the flame surface can lead to the possibility of self-acceleration and deflagration-to-detonation transition [179]. Characteristic length of preferential cell size is of the order of the flame thickness, which is smaller than that of the hydrodynamic cells [180], as shown in Figure 2-6.

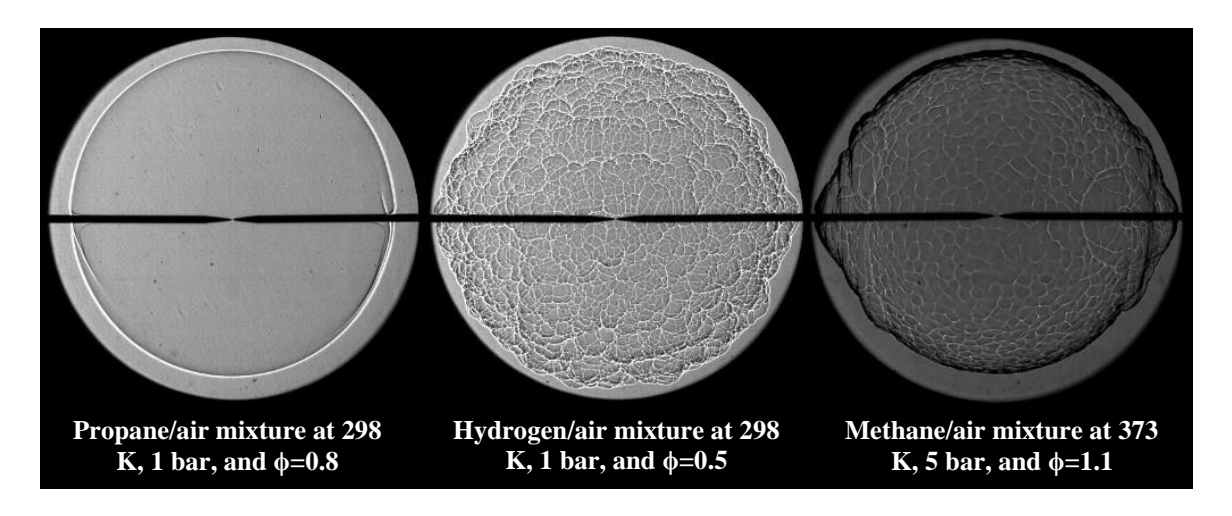


Figure 2-6. Schlieren images showing the cellular formation on the flame surface (left – stable flame, middle – thermal-diffusive cellularity, right – hydrodynamic cellularity).

The hydrodynamic (Darrieus-Landau) instability is a consequence of hydrodynamic perturbations induced by the thermal expansion of gases at the flame front which is a result of the heat release during combustion [181]. The Darrieus-Landau instability is governed by the flame thickness and expansion ratio. For flames with thicknesses thinner than the hydrodynamic scale of the flow field, the Darrieus-Landau instability is more profound [179]. On the other hand, increasing expansion ratio suppresses the hydrodynamic cellularity because the Darrieus-Landau instability intensifies with sudden and severe density change across the flame front [180].

At low pressures, the hydrodynamic cellular formation is not observed until the late stage of combustion so that it does not interfere with flame speed measurements as its wavelength exceeds the length scales of most experiments [4]. However, increasing pressure leads to an earlier onset of the hydrodynamic cellularity due to enhanced combustion reaction, which results in a reduced laminar flame thickness [182].

The hydrodynamic cellularity arises from wrinkles on the flame surface which is a result of small flow disturbances [181]. Convergence (divergence) in the convex (concave) part of the flame wrinkles with respect to the burned gas boosts (curbs) the local thrust, which is induced by the local acceleration of the flow due to the thermal expansion of gases at the flame front [4]. As a result, the flame wrinkling is improved. Subsequently, convex parts of the flame surface evolve and combine while concave parts of the flame fade out so that the hydrodynamic cells are formed with sharp ridges along the lines of neighboring cells, as shown in Figure 2-6 [4, 183].

The thermal-diffusive (preferential-diffusion) instability is a consequence of the preferential diffusion of mass compared to heat within the flame, which causes a change in local equivalence ratio and flame speed, and is observable when the mass diffusivity of the deficient reactant is adequately greater than the thermal diffusivity of the mixture, i.e. the Lewis number of the deficient reactant is less than unity [183]. Therefore, the thermal-diffusive instability is governed by the Lewis number and the preferential cellularity is suppressed for the mixtures with the Lewis number greater than one [180]. Although the hydrodynamic cellular formation generally occurs at high pressures and in the late stage of combustion at low pressures, where combustion pressure builds up, the preferential cells can be formed on the early flame kernel surface at any pressure and temperature.

When small flow disturbances cause wavelike deformation on the flame surface, i.e. flame wrinkling, at convex parts of the flame wrinkles with respect to the unburned gas, the conductive heat flux diverges towards the unburned gas and concentration gradients of the reactant species converge [157]. If the Lewis number of the combustible mixture is less than unity, the enthalpy and local flame speed at convex parts of the flame wrinkles increase, and vice versa at concave parts of the flame wrinkles [157]. Consequently, the convex parts start propagating faster than the concave parts of the flame wrinkles so that the preferential cells are formed on the flame surface. For mixtures with the Lewis number greater than unity, an opposite circumstance happens and, therefore, the thermal-diffusive instability is suppressed together with the stabilization effect of the flame stretch [157].

It is well established that premixed laminar flames exhibit Darrieus-Landau and preferential-diffusion instabilities at elevated pressures and temperatures due to reduced laminar flame thickness and burned gas Marsktein length [66, 71, 184]. Moreover, even at low pressures and temperatures, the preferential cellular formation can commence at small radii of the spherically expanding laminar premixed flames for rich large hydrocarbon fuel/air mixtures, such as propane/air and iso-octane/air, and for lean light fuel/air mixtures, such as hydrogen/air and methane/air [66, 93, 97, 183]. The early onset of the cellular formation sets up a limit for laminar flame speed measurements. One way of extending this limit is to replace some or all the nitrogen in the oxidizer with another diluent gas to increase the laminar flame thickness and Lewis number [184].

3 EXPERIMENTAL APPARATUS AND PROCEDURE AND COMBUSTION MODELING

3.1 Design and Hardware

To measure the laminar burning velocities of various fuel/oxidizer mixtures with the constant pressure method of the spherically expanding flame approaches, a 22.24-liter optically accessible constant volume combustion vessel was designed and constructed. Although the confinement (asymmetric flow) effect can be encountered in cylindrical chambers relative to spherical chambers, a cylindrical vessel geometry was chosen due to its relative ease in manufacturing, sealing, assembly, and disassembly compared to spherical chambers.

It should be noted that the confinement effect increases for small cylinder diameter relative to the length due to the larger flow motion in the axial direction compared to the radial direction [13, 131] and for this reason the diameter to length ratio of the chamber designed for this study was maintained at unity. Burke et al. [131] showed that for a cylindrical vessel having a length to diameter ratio of 1.5, the flame speed calculated at a flame radius of 0.5 times the wall radius could be as low as 15% of the real value even at constant pressure, due to the confinement effect, while the effect of confinement could be neglected for flame radii less than 0.3 times the wall radius, within 3% accuracy [131].

The asymmetric flow effect can be significantly reduced with larger cylindrical vessels and maintaining the unity aspect ratio for the inner cylinder volume [13, 131]. Therefore, the diameter and height of the chamber used in this study were both designed to be 30.48 cm to minimize the confinement effect [131] and improve the fidelity in the extraction of the laminar flame speed from the spherically expanding flames [140]. Furthermore, the upper limit of the cold flame front radius (R_f) for laminar burning velocity measurements with the constant pressure method was set as 4.36

cm (29% of the inner wall radius), which equals to 0.25R_w, where R_w is the equivalent radius of a cylindrical vessel, in order to maintain the confinement effect on the laminar flame speed within 3% [124]. By taking these precautions, the experimental set-up and methodology enabled the laminar burning velocity measurements to be relatively unaffected by the confinement effect.

The vessel was fabricated from 304 stainless steel, which was chosen for its high strength and anti-corrosion properties. Although other less expensive and easier to machine materials, such as aluminum alloys, also have comparable ultimate tensile strengths to that of stainless steel at room temperature, the maximum allowable stresses of the aluminum alloys drop dramatically with increasing temperatures [4]. However, the maximum allowable stress of the 304 stainless steel decreases only from 1380 bar to 899 bar when the temperature is increased from 298 K to 523 K (2015 ASME Boiler and Pressure Vessel Code (BPVC) - Section II – Part D – Table 1A [185]), which is the maximum temperature that the chamber can attain.

The maximum pressure that the vessel should withstand was determined to be 130 bar by taking into account the conditions during H₂/air combustion at 30 bar and 523 K. Subsequently, the thickness of the vessel was determined according to the design procedure set by 2015 ASME BPVC - Section VIII - Division 1 [185], which provides requirements applicable to the design, fabrication, inspection, testing, and certification of pressure vessels operating at either internal or external pressures exceeding 1 bar.

For internally pressurized vessels, if the thickness exceeds one-half of the inside radius, which is the case for the vessel designed for this work, then two constraints are proposed for the chamber thickness in Appendix 1 - 1.2 Cylindrical Shells [185], namely the circumferential stress constraint (Equation 3-1) and the longitudinal stress constraint (Equation 3-2). In Equations 3-1 and 3-2, the maximum pressure (P_m) was set to be 130 bar. In these equations, σ_m represents the

maximum allowable stress value and was assumed to be 899 bar for 304 stainless steel at 523 K since the material properties can be assumed as constant during combustion due to the fact that the entire combustion phenomenon happens in only a few milliseconds. E stands for the joint efficiency for, or the efficiency of, the appropriate joint in cylindrical or spherical shells, or the efficiency of ligaments between openings, whichever is less [185]. In this case, E=1 for the experimental set-up because the main cylindrical body of the chamber was manufactured from one-piece.

$$P_{\rm m} = \sigma_{\rm m} * E * \ln \left(\frac{R_{\rm w} + \text{thk}}{R_{\rm w}} \right)$$
 3-1

$$P_{\rm m} = \sigma_{\rm m} * E * \left[\left(\frac{R_{\rm w} + thk}{R_{\rm w}} \right)^2 - 1 \right]$$
 3-2

The longitudinal stress constraint required a thickness (thk) of 1.07 cm and the circumferential stress constraint suggested a minimum thickness of 2.37 cm; therefore, after incorporating a safety factor of 3.75, the thickness of the main cylindrical body of the chamber was designed to be 8.89 cm. In order to prevent over pressurization of the chamber, a Nickel Alloy 200 rupture disk was installed, as pressure relief valves do not have a fast enough response for this combustion application. The rupture disk is set to burst at 130 bar at 523 Kelvin and at 145 bar for ambient temperatures.

As shown in Figure 3-1, the constant volume combustion chamber consists of a main cylindrical body, whose outer diameter (OD), inner diameter (ID), and length are 48.26 cm, 30.48 cm, and 45.72 cm, respectively. Two bolted end caps connect to each end of the main body and each contains a fused quartz window, whose diameter and thickness is 20.32 cm and 6.35 cm, respectively, which is secured with a window cap (OD=30.48 cm, ID=15.24 cm, and length of 5.08 cm). Technical drawings of the vessel parts are presented in Appendices A through D.

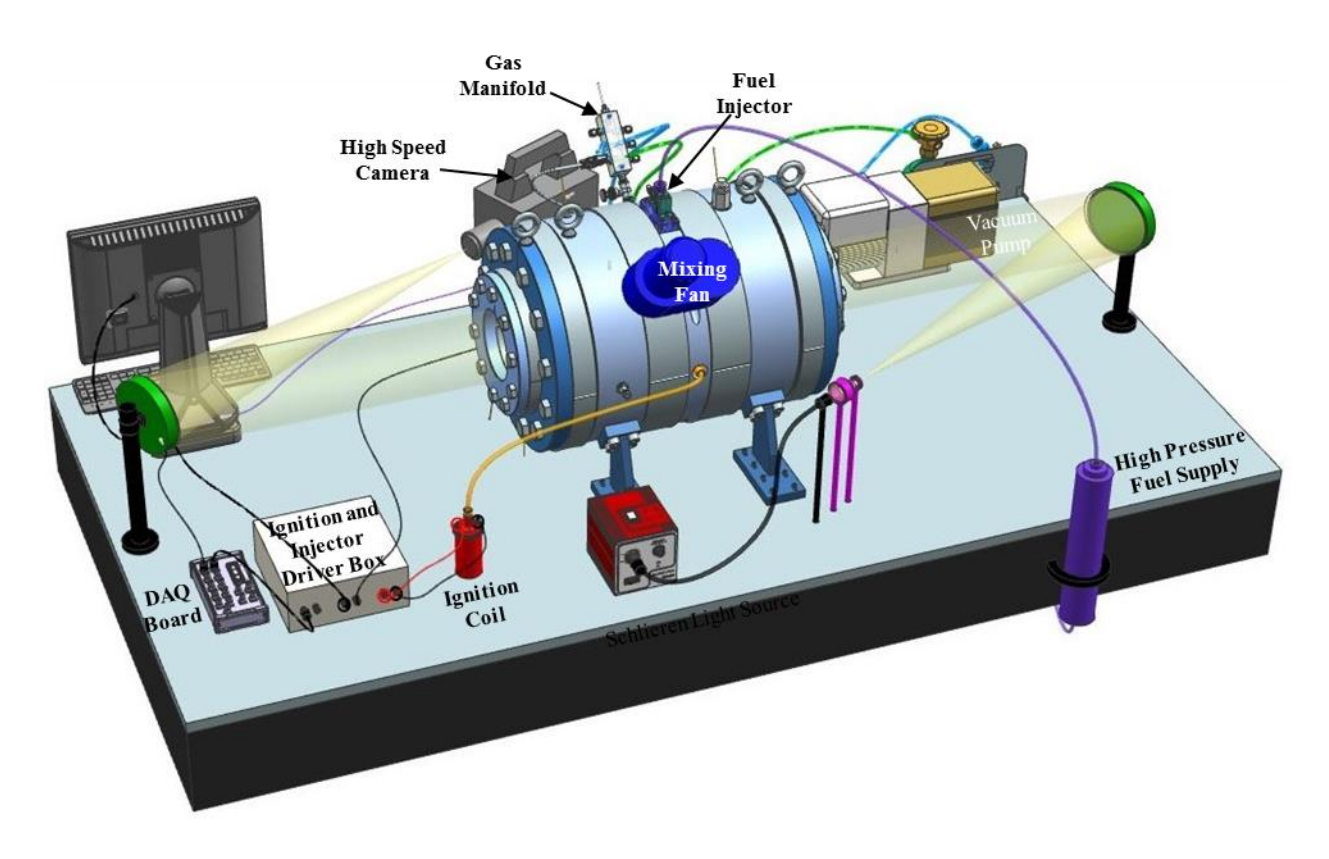


Figure 3-1. Schematic of the optically accessible constant volume combustion chamber showing the schlieren imaging setup.

Each end cap was fastened to the main cylindrical body with 12 zinc yellow-chromate plated hex head screws (grade 8 steel, 1"-8 thread size, 12.70-cm long, partially threaded) with grade 8 steel washers (black ultra-corrosion-resistant coated, 12.54-cm screw size, 6.35-cm OD). Sealing between the main body and the bolted end cap was achieved with a 452 chemical-resistant Viton fluoroelastomer O-ring and a 456 chemical-resistant Viton fluoroelastomer O-ring (details in Appendix A to B). Therefore, the effective area that the maximum inner combustion pressure acting on the end caps is 0.073 m^2 (= π *0.1524²). According to Table 8-7 in [186] and Figure 3-2 below, the effective grip (L'_G), threaded length (L_T), length of useful unthreaded portion (l_d), and length of useful threaded portion (l_t) of the screws between the main body and end caps can be calculated from Equations 3-3, 3-4, 3-5, and 3-6. In Equation 3-3, h and d are the thickness of the washer and clamped material and the diameter of the bolt, respectively.

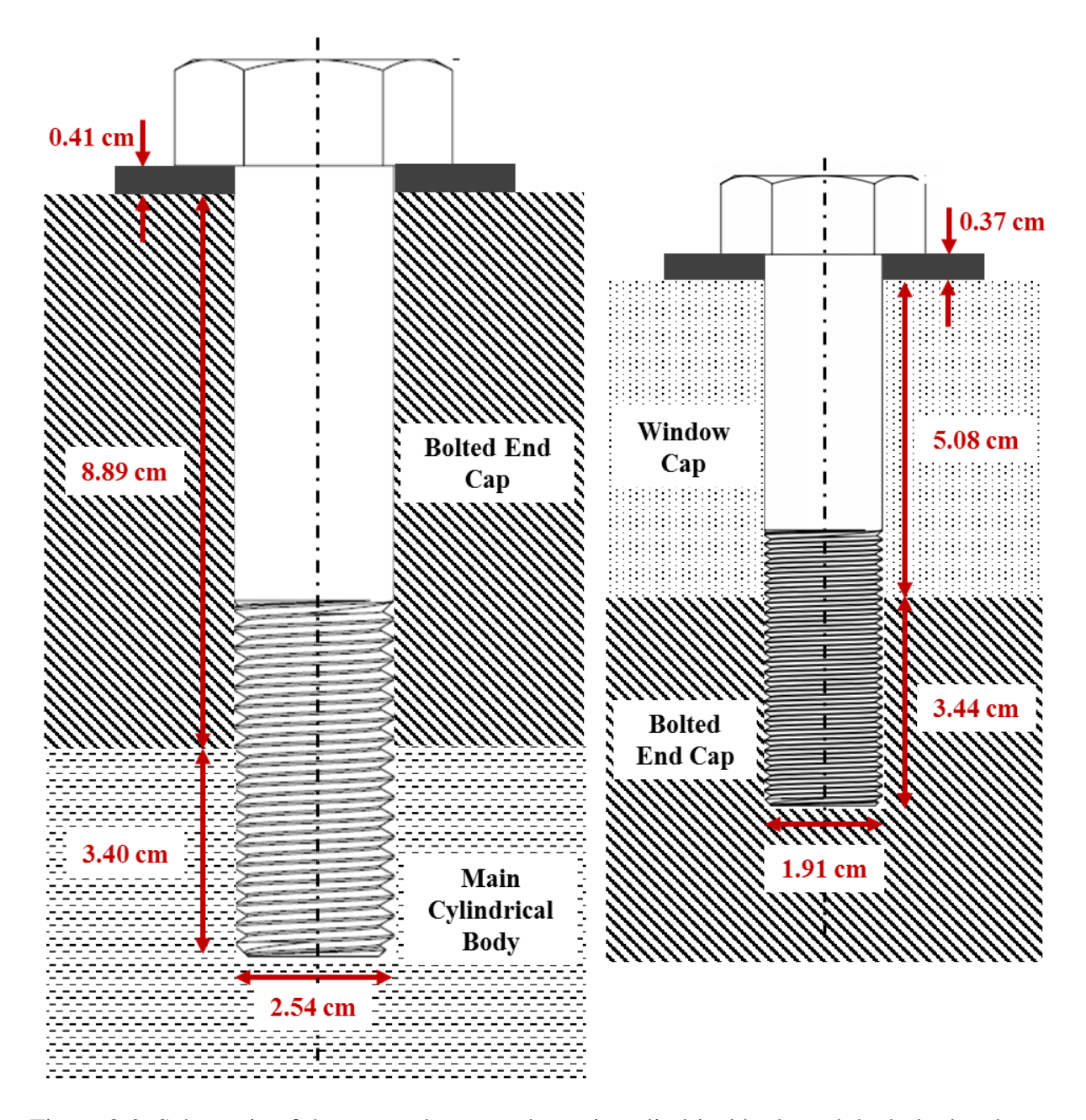


Figure 3-2. Schematic of the screws between the main cylindrical body and the bolted end cap (left) and between the bolted end cap and the window cap (right).

$$L'_{G} = h + \frac{d}{2} = 9.30 + \frac{2.54}{2} = 10.57 \text{ cm}$$
 3-3

$$L_T = 2d + 0.635 = 2 * 2.54 + 0.635 = 5.715 \text{ cm}$$
 3-4

$$l_d = l - L_T = 12.700 - 5.715 = 6.985 \text{ cm}$$
 3-5

$$l_t = L_G' - l_d = 10.570 - 6.985 = 3.585 \text{ cm}$$
 3-6

The estimated effective stiffness of the bolt or cap screw in the clamped zone (k_b) can be calculated with Equation 3-7 [186]. Shigley et al. [186] proposed Equation 3-8 for joint-member stiffness (k_m). In Equation 3-7, the major-diameter area of the screw (A_d) was calculated as 5.067 x 10^{-4} m² (= $\pi/4*0.0254^2$). The tensile-stress area of the fastener (A_t) and the elastic modulus of the steel bolts, washers, and members (EM) are obtained from Tables 8.2 and 8.8 in [186]. Equation 3-8 is a modified version of Equation 8.21 in [186], which was derived under the assumption of the fact that the washer outer diameter is equal to one and a half of the bolt nominal diameter. However, in this clamp, the washer outer diameter is 6.35 cm while the nominal diameter of the bolt is 2.54 cm. Therefore, Equation 8.22 in [186] takes the form of Equation 3-8.

$$\begin{split} k_b &= \frac{A_d*A_t*EM}{A_d*l_t + A_t*l_d} = \frac{5.067 \text{x} 10^{-4}*3.910 \text{x} 10^{-4}*2.068 \text{x} 10^{11}}{5.067 \text{x} 10^{-4}*0.03585 + 3.910 \text{x} 10^{-4}*0.06985} \\ &= 9.01 \, \text{x} \, 10^8 \frac{N}{m} \\ k_m &= \frac{0.5774*\pi*EM*d}{2 \ln \left(2.33 \frac{0.5774*l + 1.5*d}{0.5774*l + 3.5*d}\right)} = \frac{0.5774*\pi*2.068 \text{x} 10^{11}*0.0254}{2 \ln \left(2.33 \frac{0.5774*0.127 + 1.5*0.0254}{0.5774*0.127 + 3.5*0.0254}\right)} \\ &= 1.01 \, \text{x} \, 10^{10} \frac{N}{m} \end{split}$$

The resultant load on the connected members (F_m) equals the fraction of the external load carried by the members $((1-C)*F_{ext})$ subtracted by the clamp load or preload of the fastener (F_p) , i.e. Equation 3-9 [186]. To ensure a safe joint, the external load is required to be smaller than the load needed to cause the joint to separate. If separation does occur, then the entire external load will be imposed on the bolt, i.e. $F_m=0$ in Equation 3-9. The maximum external load, which can be handled by one of the screws, was calculated from Equation 3-9 by using a clamp force of 242,539 N [187]. By considering 12 of the grade 8 steel 1"-8 threaded hex head screws with grade 8 steel

washers and the pressure rating of the chamber, the safety factor for the clamp between the main body and end caps was calculated as 3.34 from Equation 3-10.

$$F_{m} = (1 - C) * F_{ext} - F_{p} \xrightarrow{separation(F_{m}=0)} F_{ext} = \frac{F_{p}}{(1 - C)} = \frac{242539}{(1 - 0.08)}$$

$$= 2.64 \times 10^{5} \text{ N}$$
3-9

where
$$C = \frac{k_b}{k_b + k_m} = \frac{9.01 \times 10^8}{9.01 \times 10^8 + 1.01 \times 10^{10}} = 0.08$$

Safety Factor =
$$\frac{12 * F_{\text{ext,m}}}{P_{\text{m}} * A_{\text{eff}}} = \frac{12 * 2.64 \times 10^5}{1.3 \times 10^7 * 0.073} = 3.34$$

A 20.32-cm diameter fused quartz window was fitted into each of the bolted end caps, locked by a window cap bolted to the end cap and sealed with two Galloup Graphonic gaskets (OD 20.32 cm, ID 15.24 cm, 0.3175-cm thick) on both sides of the window. Therefore, the effective area on which the axial load due to the inner pressure acted is 0.0324 m^2 (= π *0.1016²). This axial load is compensated by 10 zinc yellow-chromate plated hex head screws (grade 8 steel, 3/4"-16 thread size, 8.89-cm long, partially threaded) together with grade 8 steel washers (black ultra-corrosion-resistant coated, 1.905-cm screw size, 5.08-cm OD), which clamped the window caps to the bolted end caps as shown in Figure 3-2. Details of the safety factor calculation for this clamp is presented in Appendix E.

Fused quartz was used for the windows due to its strength and wide range of light transmission [4]. Although the laminar burning velocity measurements are stopped at a flame front diameter of 8.72 cm, optical observation up to a flame diameter of 15.24 cm is enabled with the window cap design to observe flame instabilities over a wider range.

The maximum stress (σ_m) on a uniformly loaded window can be expressed with Equation 3-11 [188] with respect to the vessel inner pressure (P), unsupported diameter of the window (d_{un}), window thickness (thk), and an empirical constant. The empirical constant value of either 0.75

[188-189] or 0.99 [190-191] is commonly used for clamped fused quartz windows. In the following calculations, 0.99 was chosen to consider the worst-case scenario since using the empirical constant value of 0.99 yields thicker windows.

$$\sigma_{m} = \frac{constant}{4} * P * \frac{d_{un}^{2}}{thk^{2}}$$
3-11

The maximum allowable stress for the fused quartz discs is 482.6 bar [188-191]. Maximum pressure inside the vessel was already determined as 130 bar and the unsupported diameter of the window is 15.24 cm as shown in Figure 3-3. From this information, the required minimum thickness of the windows was calculated as 3.935 cm by rewriting Equation 3-11 as Equation 3-12. The thickness of the fused quartz side windows was chosen to be 6.35 cm with the incorporation of a safety factor of 1.61. However, the edges of the windows were still critical since higher stress concentrations are usually faced around the edges; therefore, radiuses were machined on the edges of the fused quartz windows.

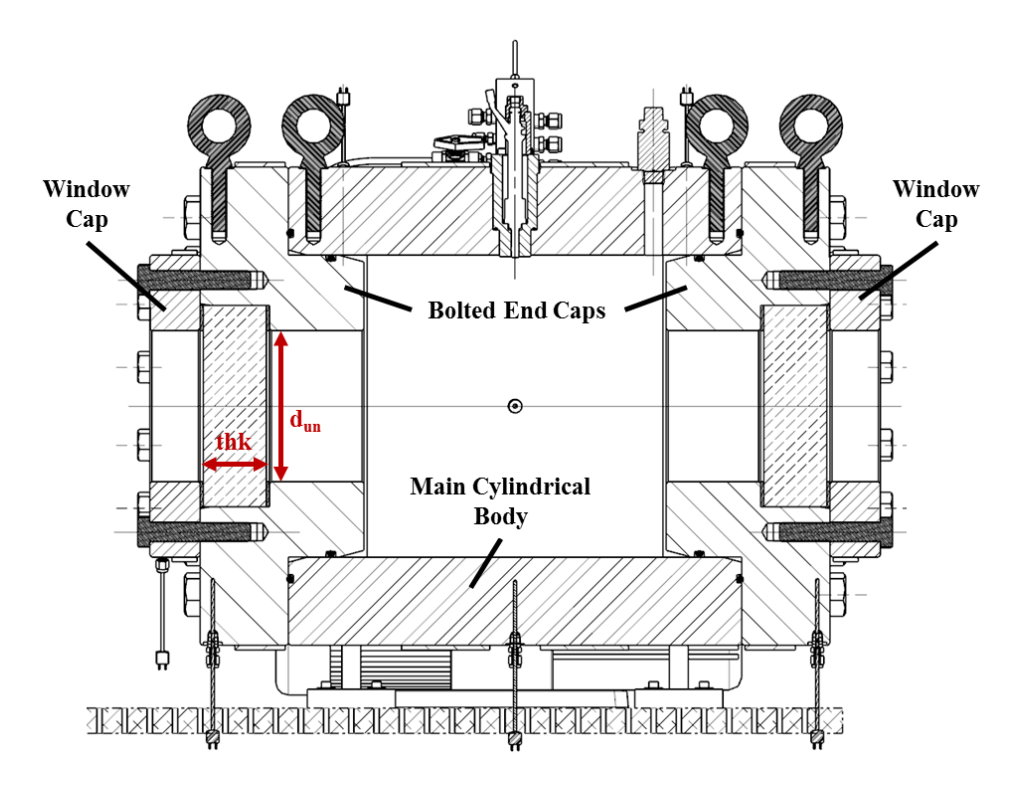


Figure 3-3. Middle cross section of the constant volume combustion chamber.

thk =
$$\frac{d_{un}}{\sqrt{\frac{4 * \sigma_m}{P_m * constant}}} = \frac{15.24}{\sqrt{\frac{4 * 482.6}{130 * 0.99}}} = 3.935 \text{ cm}$$
3-12

A 1/4" stainless steel Swagelok tube fitting with pressure rating of 551 bar at ambient temperature was attached to a 1/4" NPT port on the vessel for gas sampling with a syringe. The homogeneity of the gas mixture inside the vessel, the complete evaporation of liquid fuels injected into the chamber, and the fuel decomposition/cracking can be tested with the samples collected from this port by using gas chromatography–mass spectrometry (GC-MS) [192].

With the help of 4 shouldered steel eyebolts 5/8"-11 thread size, 6.35-cm thread length (two on the main body and one on each end cap), the chamber assembly was placed on four legs, which were bolted to the vessel with 16 zinc-plated alloy steel socket head screws (5/8"-11-thread size, 6.35-cm long). Each leg, whose technical drawing is provided in Appendix F, was fixed onto a ST-48-8 Newport – SmartTable with 8 x zinc-aluminum-coated alloy steel socket head screws (1/4"-20-thread size, 4.445-cm long). Finally, the whole experimental set-up was shielded by a lexan blast wall for safe operation.

3.2 Charge Preparation

Before the charge preparation, the vessel was heated up to the desired temperature with six heating bands ranging from 0.35 kW to 1.75 kW, as shown in Figure 3-1. The heating bands are controlled with a heating unit, which has integrated cascade and hi-limit controllers [193], based on the temperature data collected from six Omega type-T thermocouples installed in the vessel, each with an accuracy of +/- 0.75% [194]. These thermocouples were inserted into 75% of the vessel thickness; therefore, they do not directly read the temperature of the unburned gas mixture inside the chamber.

Another thermocouple was placed in the middle section of the main cylindrical part of the vessel all the way through to the inner wall of the chamber. Although the difference in the temperature readings of all seven thermocouples is negligible for the initial temperatures less than 373 K, it was observed that the unburned gas mixture temperature, which is measured by the thermocouple in the middle section, could be up to 20 K greater than the temperature reading from the six thermocouples inserted into 75% of the vessel thickness. Consequently, the desired initial temperature of the unburned gas mixture inside the vessel was adjusted by taking the temperature readings of the middle section thermocouple as a base.

In this study, measurements were performed at 298-473 K. Insulation jackets were used to significantly reduce the heating time, as it can take more than 10 hours to reach 473 K without insulation jackets. Throughout the experiments, temperature fluctuations were kept to within +/-3.0 K with the help of 3.81-cm thick fiberglass insulating blankets. Numerical studies of Chen [124] on methane/air flames at room temperature suggest a +/- 2% accuracy in the laminar burning velocity calculations for +/- 3.0 K initial temperature fluctuations.

The deviations in the laminar flame speed and adiabatic flame temperature with \pm 3.0 K fluctuation in the initial temperature were computed numerically for fuel/oxidizer mixtures tested in the present study at various pressures, temperatures, and equivalence ratios. Results presented in Table 3-1 showed that maximum deviations in the laminar burning velocity and adiabatic flame temperature are 1.75% and \pm 2.12 K, respectively, at numerically investigated points. Minimum percentile change in the \pm 3L was observed at the equivalence ratio where the peak flame speed is attained, away from which the percentile change in the \pm 3L increases. Minimum deviation in the \pm 3L was detected around stoichiometry.

Table 3-1. Numerically calculated changes in the laminar flame speed and adiabatic flame temperature due to \pm 3.0 K fluctuation in the initial temperature.

Fuel/Air Mixture	Pressure	Temperature	Equivalence Ratio	Change in S_L due to +/- 3.0 K fluctuation in T_u	$\begin{array}{c} Change \ in \ T_{adb} \ due \\ to \ +/\text{-} \ 3.0 \ K \\ fluctuation \ in \ T_u \end{array}$
			0.8	<u>+</u> 2.87 cm/s (<u>+</u> 1.70%)	<u>+</u> 2.12 K
Hydrogen/Air	1 bar	298 K	1.0	<u>+</u> 3.51 cm/s (<u>+</u> 1.53%)	<u>+</u> 1.56 K
			1.2	$\pm 3.95 \text{ cm/s } (\pm 1.45\%)$	<u>+</u> 2.03 K
			0.8	$\pm 0.47 \text{ cm/s } (\pm 1.75\%)$	<u>+</u> 2.03 K
		298 K	1.0	$\pm 0.59 \text{ cm/s } (\pm 1.58\%)$	<u>+</u> 1.48 K
			1.2	± 0.55 cm/s ($\pm 1.65\%$)	<u>+</u> 1.99 K
			0.8	$\pm 0.61 \text{ cm/s } (\pm 1.51\%)$	<u>+</u> 2.01 K
	1 bar	373 K	1.0	$\pm 0.73 \text{ cm/s } (\pm 1.36\%)$	<u>+</u> 1.45 K
			1.2	± 0.68 cm/s ($\pm 1.41\%$)	<u>+</u> 1.97 K
			0.8	± 0.83 cm/s ($\pm 1.30\%$)	<u>+</u> 1.97 K
Methane/Air		473 K	1.0	± 0.95 cm/s ($\pm 1.17\%$)	<u>+</u> 1.42 K
			1.2	$\pm 0.89 \text{ cm/s } (\pm 1.19\%)$	<u>+</u> 1.95 K
			0.8	$\pm 0.40 \text{ cm/s } (\pm 1.59\%)$	<u>+</u> 2.09 K
	3 bar	373 K	1.0	$\pm 0.51 \text{ cm/s } (\pm 1.44\%)$	<u>+</u> 1.55 K
			1.2	$\pm 0.47 \text{ cm/s } (\pm 1.59\%)$	<u>+</u> 2.04 K
			0.8	$\pm 0.31 \text{ cm/s } (\pm 1.62\%)$	<u>+</u> 2.08 K
	5 bar	373 K	1.0	$\pm 0.41 \text{ cm/s } (\pm 1.48\%)$	<u>+</u> 1.60 K
			1.2	$\pm 0.37 \text{ cm/s } (\pm 1.68\%)$	<u>+</u> 2.04 K
			0.8	$\pm 0.47 \text{ cm/s } (\pm 1.70\%)$	<u>+</u> 1.98 K
Propane/Air	1 bar	298 K	1.0	± 0.61 cm/s (± 1.54%)	<u>+</u> 1.41 K
			1.2	± 0.61 cm/s (± 1.53%)	<u>+</u> 1.93 K

Table 3-1 (cont'd)

		373 K	0.8	$\pm 0.56 \text{ cm/s } (\pm 1.49\%)$	<u>+</u> 1.98 K
	1 bar —		1.0	$\pm 0.73 \text{ cm/s } (\pm 1.35\%)$	<u>+</u> 1.40 K
Les Octobre /Air			1.2	<u>+</u> 0.76 cm/s (<u>+</u> 1.35%)	<u>+</u> 1.96 K
Iso-Octane/Air			0.8	<u>+</u> 0.77 cm/s (<u>+</u> 1.29%)	<u>+</u> 1.94 K
		473 K	1.0	<u>+</u> 0.95 cm/s (<u>+</u> 1.17%)	<u>+</u> 1.36 K
		•	1.2	<u>+</u> 0.98 cm/s (<u>+</u> 1.16%)	<u>+</u> 1.91 K

Table 3-1 also demonstrates that, at the same initial conditions, percentile change in the S_L for different fuels are very similar, which suggests that the finding of Chen [124], i.e. +/- 2% accuracy in the laminar burning velocity calculations for +/- 3.0 K initial temperature fluctuations, can be valid for all fuel/oxidizer mixtures. Lastly, according to the numerical results in Table 3-1, percentile deviations in the laminar flame speed and adiabatic flame temperature diminish with increasing unburned gas temperature.

The experimental set-up is equipped with an Edwards RV5 vacuum pump to evacuate the system before and after flushing the chamber with bottled dry air after each test in order to ensure removal of residual volatile materials, as specified in the ASTM standard [195]. The reactant mixtures are prepared inside the combustion chamber using the method of partial pressures. A mixing tank was not used due to the risk of thermal decomposition of the fuel, especially for high molecular weight compounds, during batch premixture preparation and testing at high temperatures for several hours. An additional drawback of the mixing tank approach is condensation in the lines connecting the mixing tank to the test chamber.

As schematically shown in Figure 3-4, the gases fuels, air, and inert gases (CH_4 – minimum 99.99% ultra-high purity, H_2 – 99.995% very high purity, C_3H_8 – minimum 99.5% of purity, dry

air - <10 ppm H₂O, N₂ - 99.998% very high purity, and CO₂ - minimum 99.8% purity) are fed into the system through a heated gas manifold, which has a 1/8" NPT port for thermocouple and 9 x 1/4" NPT ports (details in Appendix G). One of the 1/4" NPT ports on the gas manifold was used to connect the manifold to the main cylindrical part of the vessel with a stainless steel severe service high-pressure union bonnet needle valve (pressure rating of 512 bar at 505 K). This valve is always closed before combustion since the gas manifold cannot withstand high combustion pressures (higher pressures than 30 bar).

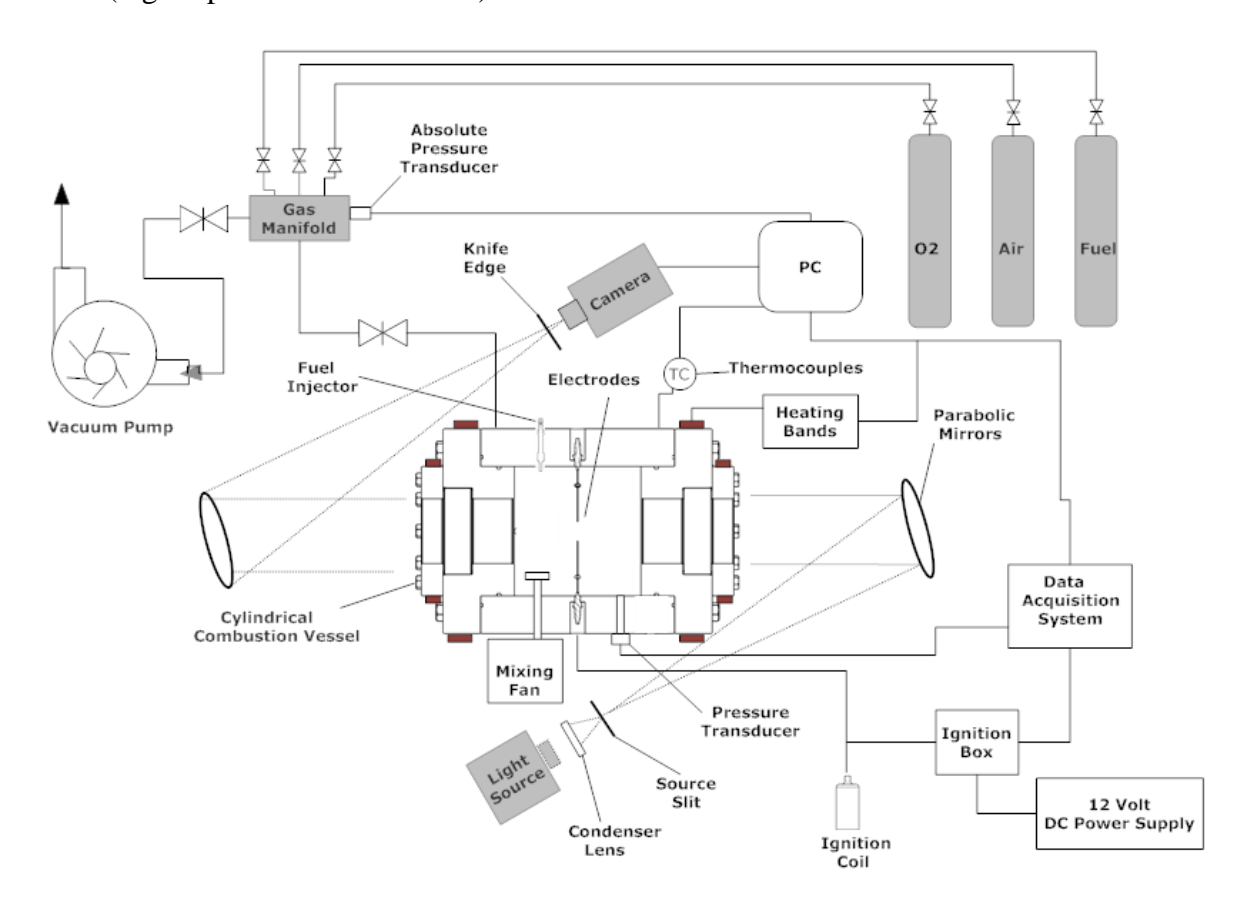


Figure 3-4. Schematic view of the experimental set-up used for the laminar burning velocity measurements.

The liquid fuels, such as high/low RON gasoline and iso-octane – 99.8% of purity, and water are injected directly into the vessel with a calibrated high-pressure gasoline direct injector (Motorcraft CM5220), which is connected to a high-pressure piston assembly. While the upper

side of the piston was filled with the desired liquid, the lower part was pressurized with nitrogen.

Technical drawings of the fuel injector assembly are provided in Appendix H.

The injector was calibrated before the experiments according to the injected liquid fuel/water volume/mass and pressure increase due to the injection. Excellent agreement was observed between the intended volume/mass injection and the corresponding pressure increase by screening the absolute pressure readings during the injection. At the end of the experiments, the injector calibration procedure was repeated to confirm that calibration constants were unchanged.

The partial-pressure charge preparation process started with filling the reactant with the lowest concentration followed by the reactants of higher concentrations to increase the accuracy of the method of partial pressures [13]. The partial pressures before the combustion event were recorded with two absolute pressure transducers, namely an Omega MM series sensor and a Setra ASM AccuSense sensor, connected to the gas manifold to protect the sensors from high combustion temperatures. Both sensors have an accuracy in the 5-bar full scale better than +/- 0.05% and a total error band less than 0.25%. Thus, the systematic uncertainty in absolute pressure readings is less than +/- 0.0025 bar for the experiments conducted at room temperature and less than +/- 0.0063 bar for the experiments conducted at higher temperatures.

Resulting uncertainties in the equivalence ratio for fuel/oxidizer mixtures tested in the present study at various pressures, temperatures, and equivalence ratios are presented in Table 3-2 together with corresponding deviations in the laminar flame speed and adiabatic flame temperature, which were numerically computed. Uncertainty in the equivalence ratio increases with increasing carbon number of the fuel because even a small change in the partial pressure of large hydrocarbon fuels yields a large variation in the equivalence ratio. The main reason behind this is that only a small amount of a large hydrocarbon fuel is needed for the stoichiometric air/fuel

ratio so that slight deficiency/excess of the large hydrocarbon fuel has a significant impact on the equivalence ratio, and therefore, on the laminar burning velocity and adiabatic flame temperature.

Table 3-2. Numerically calculated changes in the laminar flame speed and adiabatic flame temperature due to uncertainty in ϕ .

Fuel/Air Mixture	Pressure	Temperature	Equivalence Ratio	Change in S _L due to uncertainty in φ	Change in T _{adb} due to uncertainty in φ
	1 bar	298 K	0.8 ± 0.0021 (± 0.27%)	$\pm 0.74 \text{ cm/s } (\pm 0.44\%)$	<u>+</u> 3.05 K
Hydrogen/ Air			1.0 ± 0.0024 (± 0.24%)	$\pm 0.62 \text{ cm/s } (\pm 0.27\%)$	<u>+</u> 1.29 K
			1.2 ± 0.0027 (± 0.22%)	$\pm 0.45 \text{ cm/s } (\pm 0.17\%)$	<u>+</u> 1.01 K
		298 K	0.8 ± 0.0056 (± 0.70%)	$\pm 0.41 \text{ cm/s } (\pm 1.54\%)$	<u>+</u> 8.43 K
			1.0 ± 0.0058 (± 0.58%)	$\pm 0.15 \text{ cm/s } (\pm 0.39\%)$	<u>+</u> 2.92 K
			1.2 ± 0.0060 (± 0.50%)	$\pm 0.46 \text{ cm/s } (\pm 1.40\%)$	<u>+</u> 4.84 K
	1 bar	373 K	0.8 ± 0.0140 (± 1.75%)	$\pm 1.39 \text{ cm/s } (\pm 3.46\%)$	<u>+</u> 20.51 K
			1.0 ± 0.0146 (± 1.46%)	$\pm 0.48 \text{ cm/s } (\pm 0.90\%)$	<u>+</u> 7.53 K
			$1.2 \pm 0.0151 \ (\pm 1.26\%)$	$\pm 1.48 \text{ cm/s } (\pm 3.07\%)$	<u>+</u> 11.81 K
Methane/		473 K	$0.8 \pm 0.0140 \ (\pm 1.75\%)$	$\pm 1.88 \text{ cm/s } (\pm 2.94\%)$	<u>+</u> 19.34 K
			$1.0 \pm 0.0146 \ (\pm 1.46\%)$	$\pm 0.57 \text{ cm/s } (\pm 0.70\%)$	<u>+</u> 6.89 K
			1.2 ± 0.0151 (± 1.26%)	<u>+</u> 1.86 cm/s (<u>+</u> 2.51%)	<u>+</u> 11.18 K
		373 K	0.8 ± 0.0140 (± 1.75%)	± 1.00 cm/s (± 4.02%)	<u>+</u> 21.13 K
-	3 bar		1.0 ± 0.0146 (± 1.46%)	± 0.38 cm/s (± 1.08%)	<u>+</u> 8.34 K
			1.2 ± 0.0151 (± 1.26%)	<u>+</u> 1.43 cm/s (<u>+</u> 4.86%)	<u>+</u> 12.29 K
		373 K	0.8 ± 0.0140 (± 1.75%)	<u>+</u> 0.83 cm/s (<u>+</u> 4.30%)	<u>+</u> 21.30 K
	5 bar		1.0 ± 0.0146 (± 1.46%)	<u>+</u> 0.31 cm/s (<u>+</u> 1.11%)	<u>+</u> 8.90 K
			1.2 ± 0.0151 (± 1.26%)	<u>±</u> 1.25 cm/s (<u>±</u> 5.70%)	<u>+</u> 12.37 K

Table 3-2 (cont'd)

Propane/ Air			0.8 ± 0.0127 (± 1.59%)	$\pm 1.00 \text{ cm/s } (\pm 3.61\%)$	<u>+</u> 19.69 K
	1 bar	298 K	1.0 ± 0.0129 (± 1.29%)	$\pm 0.48 \text{ cm/s } (\pm 1.21\%)$	<u>+</u> 7.02 K
			1.2 ± 0.0131 (± 1.09%)	$\pm 0.58 \text{ cm/s } (\pm 1.47\%)$	<u>+</u> 10.09 K
		373 K	$0.8 \pm 0.0765 \ (\pm 9.56\%)$	\pm 7.81 cm/s (\pm 20.76%)	<u>+</u> 120.80 K
Iso- Octane/ Air			1.0 ± 0.0770 (± 7.70%)	$\pm 5.14 \text{ cm/s } (\pm 9.56\%)$	<u>+</u> 55.95 K
	1 1		1.2 ± 0.0775 (± 6.46%)	$\pm 5.11 \text{ cm/s } (\pm 9.09\%)$	<u>+</u> 59.13 K
	1 bar	473 K	0.8 ± 0.0765 (± 9.56%)	± 10.96 cm/s (± 18.41%)	<u>+</u> 114.41 K
			1.0 ± 0.0770 (± 7.70%)	\pm 6.90 cm/s (\pm 8.47%)	<u>+</u> 50.47 K
			$1.2 \pm 0.0775 \ (\pm 6.46\%)$	<u>±</u> 6.28 cm/s (<u>+</u> 7.39%)	<u>+</u> 54.98 K
· · · · · · · · · · · · · · · · · · ·		•	•	·	

Uncertainty in the equivalence ratio is greater at elevated temperatures compared to that at room temperature due to zero and span temperature offsets of the absolute pressure transducer. However, at temperatures above room temperature, percentile changes in the S_L and deviations in the T_{adb} due to the uncertainty in the ϕ decrease with increasing unburned gas temperature. On the contrary, the initial pressure increase leads to greater percentile changes in the S_L and deviations in T_{adb} due to the uncertainty in ϕ .

Percentile fluctuations in the equivalence ratio due to the inaccuracy in the partial pressure readings increase from rich mixtures to lean mixtures. Minimum changes in the S_L and T_{adb} due to the uncertainty in the ϕ were observed at the equivalence ratio, where the flame speed peaks. Therefore, while deviations in the S_L and T_{adb} due to the uncertainty in the ϕ are considerably small for small hydrocarbon or non-hydrocarbon fuels at normal temperature and pressure (NTP), they can be significantly large for large hydrocarbon fuels at high temperatures and pressures and close to the flammability limits, as shown in Table 3-2.

The effect of the absolute pressure transducer inaccuracy on the initial pressure was also investigated numerically. Maximum change in the S_L due to this effect was less than 0.07% and no change was observed in the T_{adb} . Thus, uncertainty in the initial pressure due to the inaccuracy of the absolute pressure transducer has almost no impact on the accuracy of the S_L and T_{adb} as no sub-atmospheric pressures have been tested.

In the present study, laminar flame speeds of diluted methane/air mixtures were measured at various pressures and temperatures. For this reason, uncertainty in dilution ratio due to the absolute pressure transducer inaccuracy and its impact on the laminar flame speed and adiabatic flame temperature of methane/air mixtures were examined numerically and results are presented in Table 3-3, where the percentage of the diluent inside the reactants is particularized as the dilution ratio.

Table 3-3. Numerically calculated changes in the laminar flame speed and adiabatic flame temperature of methane/air mixtures due to uncertainty in dilution ratio.

Diluent	Pressure	Temperature	Equivalence Ratio	Dilution Ratio	Change in S _L due to uncertainty in dilution ratio	Change in T _{adb} due to uncertainty in dilution ratio
CO ₂ 11		473 K	0.8	5% ± 0.13%	$\pm 0.41 \text{ cm/s } (\pm 0.92\%)$	<u>+</u> 2.92 K
				10% ± 0.13%	$\pm 0.32 \text{ cm/s } (\pm 0.99\%)$	<u>+</u> 2.73 K
				15% ± 0.13%	$\pm 0.23 \text{ cm/s } (\pm 1.05\%)$	<u>+</u> 2.68 K
			1.0	5% ± 0.13%	$\pm 0.52 \text{ cm/s } (\pm 0.90\%)$	<u>+</u> 3.02 K
	1 bar			10% <u>+</u> 0.13%	<u>+</u> 0.41 cm/s (<u>+</u> 1.00%)	<u>+</u> 2.67 K
				15% <u>+</u> 0.13%	$\pm 0.30 \text{ cm/s } (\pm 1.05\%)$	<u>+</u> 2.69 K
			1.2	5% <u>+</u> 0.13%	$\pm 0.54 \text{ cm/s } (\pm 1.03\%)$	<u>+</u> 3.17 K
				10% <u>+</u> 0.13%	$\pm 0.39 \text{ cm/s } (\pm 1.09\%)$	<u>+</u> 2.93 K
				15% <u>+</u> 0.13%	$\pm 0.27 \text{ cm/s } (\pm 1.14\%)$	<u>+</u> 2.79 K

Table 3-3 (cont'd)

H ₂ O			0.8	15% <u>+</u> 0.13%	$\pm 0.24 \text{ cm/s } (\pm 0.80\%)$	<u>+</u> 2.15 K
	1 bar	473 K	1.0	15% <u>+</u> 0.13%	$\pm 0.30 \text{ cm/s } (\pm 0.72\%)$	<u>+</u> 2.09 K
			1.2	15% <u>+</u> 0.13%	$\pm 0.30 \text{ cm/s } (\pm 0.86\%)$	<u>+</u> 2.23 K
N ₂			0.8	15% <u>+</u> 0.13%	$\pm 0.20 \text{ cm/s } (\pm 0.50\%)$	<u>+</u> 1.79 K
	1 bar	473 K	1.0	15% <u>+</u> 0.13%	$\pm 0.24 \text{ cm/s} (\pm 0.44\%)$	<u>+</u> 1.67 K
			1.2	15% <u>+</u> 0.13%	$\pm 0.24 \text{ cm/s } (\pm 0.52\%)$	<u>+</u> 1.89 K
9.50% CO ₂ + 19.01% H ₂ O + 71.49% N ₂			0.8	15% <u>+</u> 0.13%	$\pm 0.21 \text{ cm/s } (\pm 0.61\%)$	<u>+</u> 1.94 K
	1 bar	473 K	1.0	15% <u>+</u> 0.13%	$\pm 0.26 \text{ cm/s} (\pm 0.56\%)$	<u>+</u> 1.85 K
	1 bar		1.2	15% <u>+</u> 0.13%	$\pm 0.26 \text{ cm/s} (\pm 0.65\%)$	<u>+</u> 2.07 K
		373 K	1.0	15% <u>+</u> 0.13%	$\pm 0.18 \text{ cm/s } (\pm 0.62\%)$	<u>+</u> 1.94 K
	3 bar	373 K	1.0	15% ± 0.38%	$\pm 0.38 \text{ cm/s} (\pm 2.21\%)$	<u>+</u> 5.98 K

Although greater fluctuations were observed in the S_L due to the uncertainty in dilution ratio at low diluent levels, percentile changes in the S_L are greater at high diluent levels as the laminar flame speed gets smaller with increasing dilution ratio. On the other hand, an increase in dilution ratio leads to smaller fluctuations in the T_{adb} . Similar to the change in the S_L and T_{adb} due to the uncertainty in equivalence ratio, minimum fluctuations in these two fundamental combustion parameters due to the uncertainty in the dilution ratio were detected around stoichiometry, where the S_L and T_{adb} peak.

Among tested diluents, CO_2 has the highest impact on the percentile changes in the S_L and fluctuations in T_{adb} and it is followed by H_2O and then N_2 . The main product concentrations from stoichiometric methane/air combustion, i.e. 71.49% $N_2 + 19.01\%$ $H_2O + 9.50\%$ CO_2 , caused the percentile changes in the S_L and fluctuations in T_{adb} to always lie between the ones diluted with N_2 and H_2O . Reduction in the unburned gas temperature slightly increases the percentile change in

the S_L and fluctuations in T_{adb} , but it should be noted that all above mentioned errors in the S_L and T_{adb} due to the uncertainty in dilution ratio are very small, especially compared to the errors due to the uncertainty in equivalence ratio and initial temperature. However, at elevated pressures, errors in the S_L and T_{adb} due to the uncertainty in dilution ratio can be as high as +/-2.21% and +/-5.98 K, respectively, as shown in Table 3-3.

After the introduction of the reactants to the system, a mixing fan driven by an electric motor was turned on for at least five minutes at 400 rpm to ensure complete mixing and to attain thermal equilibrium, as suggested in the ASTM standard [195]. The mixing fan was turned off at least two minutes prior to ignition to avoid any perturbation during the experiments. Sufficient mixing and fuel decomposition/cracking were qualitatively and quantitatively assessed by Schlieren photography and GC-MS tests [192].

3.3 Ignition System

After the charge preparation, the homogenous and stationary reactant mixtures were ignited in the center of the vessel with two 3.0-mm diameter tungsten electrodes, which were forged to the central electrodes of two modified spark plugs on opposite sides of the chamber. The ground electrodes, as well as a 25% of the threaded portion, were removed from each spark plug in order to expose the center electrode and press-fit a ~15-cm long tungsten electrode extension to the end of the center electrode, as shown in Figure 3-5. Although the size and shape of the electrodes do not significantly alter the minimum ignition energies for electrode gaps larger than the quenching distance [196], the electrode tips were filed down to create a pointed end to generate a stronger electric field between the extension electrodes [101]. For convenience in the forging process, DENSO J16AR-U11 spark plugs were chosen as they have an extended central electrode. The

modified spark plugs were positioned directly across from each other, which enabled spark generation between a specified gap width in the center of the vessel.

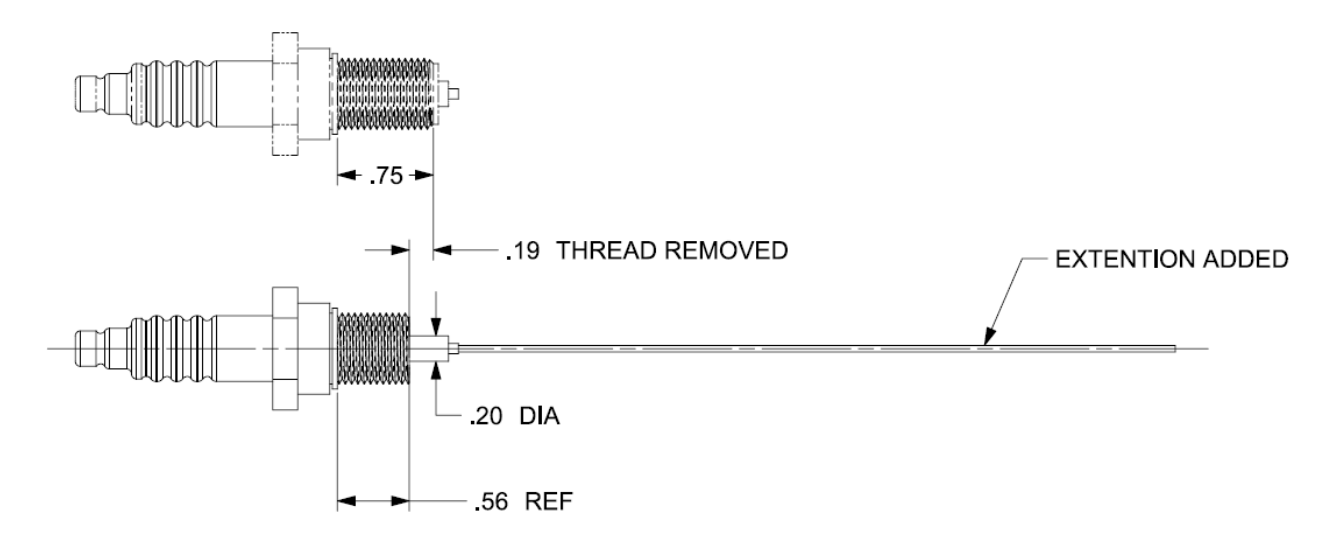


Figure 3-5. Modified spark plug geometry with tungsten electrode extension.

An appropriate electrode gap is defined as slightly greater than the quenching distance, since for smaller gaps, the electrodes may behave like a heat sink and more spark energy may be required for ignition due to heat removed from the developing flame kernel [197-198]. In fact, the minimum ignition energy decreases with increasing electrode gap until the quenching distance, beyond which the minimum ignition energy remains almost constant over a wide range of the distance between the electrodes and then increases linearly with further increases of the gap [199].

The quenching distance is defined here as the minimum spark gap that enables both ignition and the propagation of a premixed laminar flame, with the lowest energy loss to the electrodes [196]. Since the quenching distance is a function of pressure, temperature, flow velocity, and the reactant mixture composition [199], the size of the electrode gap was chosen according to the fuel used in that experiment, as well as the initial test conditions, i.e. temperature and pressure. For instance, an electrode gap of 2 mm was used for the laminar burning velocity measurements of iso-octane/air mixtures at 1 bar and 373 K and 473 K [24]. This value was chosen based on the

quenching distance studies completed by Ferguson et al. [200] and Friedman et al. [201]. The distance between the tips of the electrodes, i.e. electrode gap, was adjusted by either adding or removing copper washers with various thicknesses to the spark plug ports. For methane/air/diluent mixtures at 1-5 bar and 373-473 K, the electrode gap was lowered to 1 mm based on the quenching distance research of Harris et al. [202].

While one of the modified spark plugs serves as ground, the other is connected to an MSD Blaster 2 ignition coil. The spark is generated by a conventional inductive ignition system, shown in Figure 3-6, consisting of a 14 Volt DC power supply, ignition control box, ballast resistor, and ignition coil. On the contrary to capacitive ignition systems, inductive systems enable the initiation of combustion with spark energies that are appreciably higher than the minimum ignition energy while also supplying the approximate value of the minimum ignition energy when specified to do so. This feature of inductive ignition system is later used to determine the minimum limit for the cold flame front radius (R_f) in the laminar burning velocity measurements with the constant pressure method in order to eliminate the effect of ignition on the laminar flame speed.

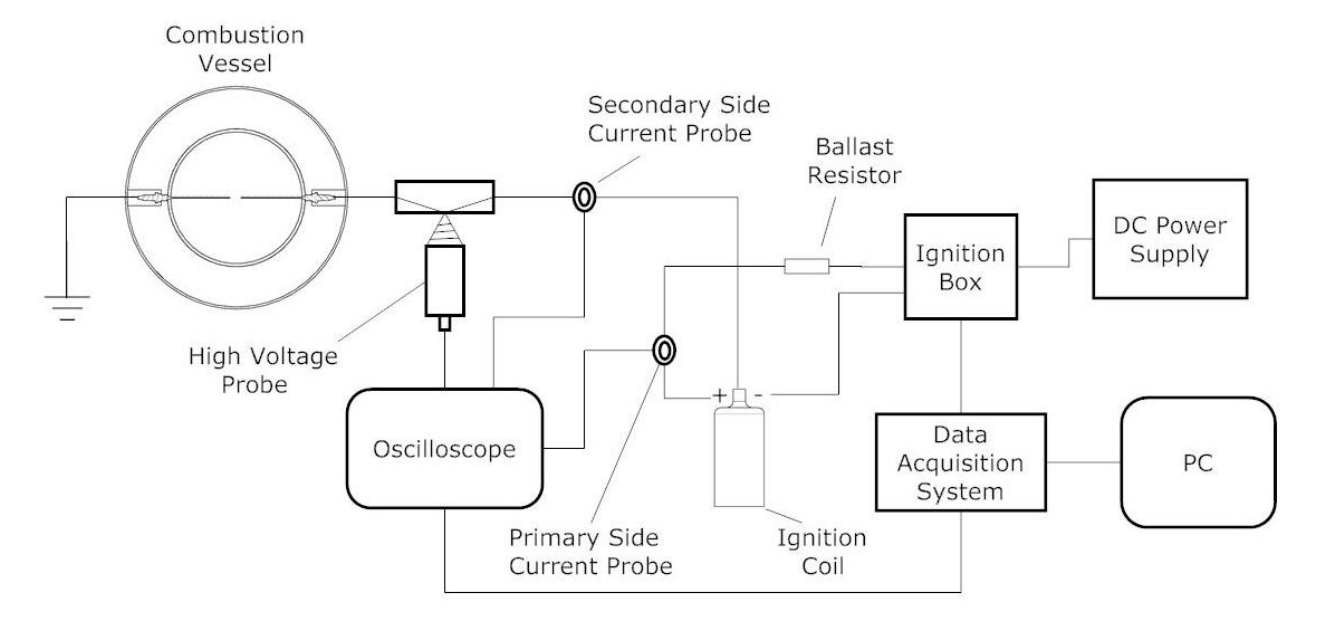


Figure 3-6. Schematic of the inductive ignition system and the discharge energy measurement system.

Ignition is initiated by a trigger signal from an in-house LABVIEW program. The same signal is also sent to a Photron SA5 high-speed camera to start imaging simultaneously and to an oscilloscope to prompt the electronic signal processing. The spark energy was varied by changing the dwell time of the trigger signal, and thus the charging time of the ignition coil. The longer the ignition coil is charged, the longer current is allowed to flow from the power supply to the primary side of the coil and, as a result, more energy is stored within the resulting magnetic field in the core [203]. The amount of current in the primary side of the coil, which is measured by Teledyne LeCroy CP031A 100 MHz high sensitivity current probe, increases with the dwell time until it plateaus at the saturation limit. The maximum dwell time before the saturation is approximately 12 ms for the MSD Blaster 2 ignition coil and corresponds to the point where the maximum discharge can be achieved. Further increase in electrical energy in the primary side of the coil does not lead to an increase in discharge energy [101].

The minimum ignition energy for the specific initial conditions is approximated by choosing initially short dwell times (beginning with an arbitrary value and then adjusting it accordingly in subsequent tests) that are expected to not sufficiently charge the coil and result in a poor spark. By increasing the dwell time in small increments, the approximate minimum ignition energy is found on the iteration where the voltage generated between the electrodes equals the breakdown voltage, and the reactant mixture is ignited. Between any two consecutive discharges, 15-20 s should pass to dissipate the supplied energy by the previous attempt [204].

Contrary to the conventional approach, which suggests always igniting the unburned gas mixture with the minimum ignition energy, in this study, the mixtures at the desired test points were ignited with different spark energies close to the minimum ignition energy of the mixture at that particular initial condition. Then, to eliminate the effect of ignition on the laminar flame speed,

the lower limit for R_f was established where the R_f vs. S_b curves for all experiments at the same test point first converged, as shown in Figure 3-7. This new approach is easier to implement with the inductive ignition system rather than the capacitive system since the inductive systems provide more control over the amount of energy discharged for ignition. On contrary to the generally accepted idea that the laminar flame speed measurements from spherically expanding flames at constant pressure should be initiated at $R_f = 0.6$ cm to prevent the effect of excessive ignition energy [68], Figure 3-7 suggests that beginning measurements at $R_f = 0.6$ cm does not always assure negligible ignition effects, especially for mixtures with the Le appreciably different than unity. Similar conclusions were drawn by other researchers [107, 123-125], recently.

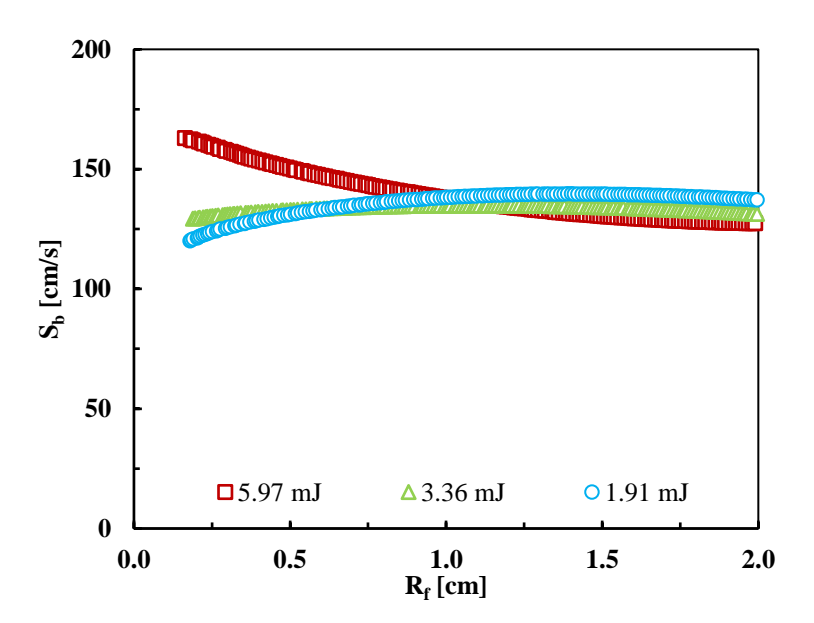


Figure 3-7. Burned gas flame speeds of propane/air mixtures at 1 bar, 298 K, and φ=1.5 ignited with different spark energies against the cold flame front radius.

The spark energy is measured with a Cal Test CT4028 high voltage oscilloscope probe and a Pearson 4100C current transducer on the secondary side of the MSD Blaster 2 ignition coil as shown in Figure 3-6. Although the efficiency of the spark plug assembly should be included in the calculation of the spark energy, it was not considered in this study as the spark plugs were modified with electrode attachments, and attempting to determine a legitimate value for this efficiency

would be impractical. The current and voltage measurements on the secondary side of the coil are sent as electronic signals to the oscilloscope, where their numerical values are recorded after each experiment. Subsequently, the spark discharge energy is calculated by using the product of the numerical values recorded by the oscilloscope until the end of the discharge phase; the product of the secondary side voltage and current yields the amount of electrical power, which is then integrated to give the total amount of spark energy. An example of the oscilloscope readings and calculated ignition power are presented in Figure 3-8. In this study, depending on the initial conditions of the mixtures, the discharge energy was varied from 1.5 to 20 mJ throughout the experiments, which is also suggested by Tse et al. [192] to minimize effects of initial flame acceleration by excessive spark energies.

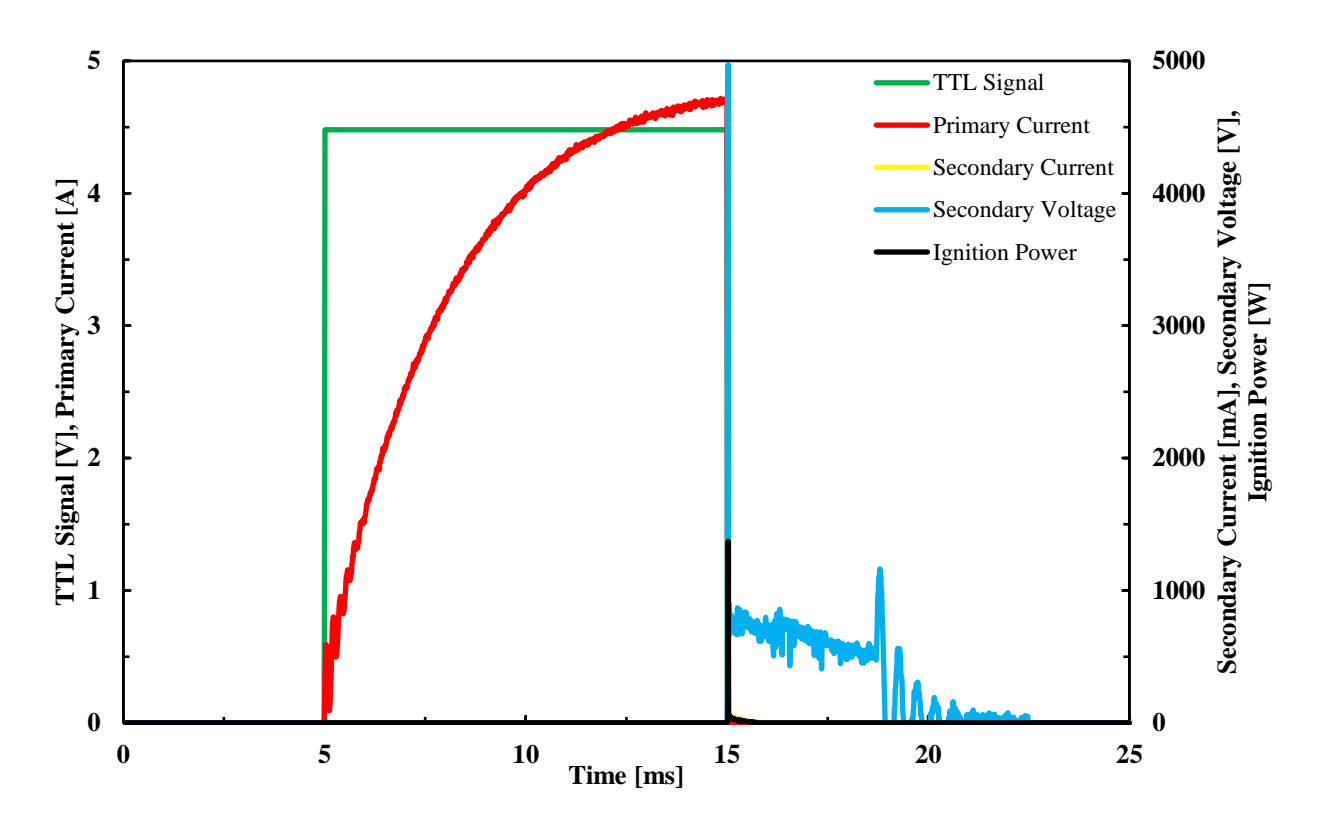


Figure 3-8. Measured oscilloscope data and calculated spark power for the ignition of propane/air mixture at 1 bar, 298 K, and ϕ =0.7 ignited with the discharge energy of 17.69 mJ (dwell time of 10 ms).

3.4 Optical Diagnostics and Image Processing

Due to the poor visibility of the laminar flame front by combustion chemiluminescence, as well as the tendency of normal photography to yield incorrect radii results during the initial stages of combustion [44], schlieren imaging was employed to objectively determine the flame boundary by detecting changes in the density gradient through the test section. In addition, schlieren photography easily detects cellularity, and allows larger flame diameters to be measured as long as the diameter of the vessel window is sufficiently large. Thus, a diameter of 15.24 cm was chosen as the window diameter.

A horizontal axis z-type schlieren system as shown in Figure 3-1 and Figure 3-4 was constructed due to its ability to reduce optical aberrations such as coma and astigmatism, shown in Figure 3-9, that can alter the clarity of images gathered in other schlieren formations [205] and to detect the buoyancy effect on the flame front, shown in Figure 3-10. Coma, which is when magnification is a function of the image location and causes a focal point to be spread apart [206], can be eliminated from a z-type schlieren system by using identical mirrors that are placed on the same plane and arranged at the same angle [205]. Astigmatism, which results from the difference in foci length within a mirror's tangential and normal planes [207], cannot be completely eliminated in the z-type schlieren formation, but can be rendered negligible by choosing mirrors with large f-numbers and minimizing the angle at which the mirrors are oriented [205].

The schlieren set up began by adjusting all optical elements onto the same optic plane, 30.48 cm above the ST-48-8 Newport – SmartTable, so that all elements facilitate a pathway of light that was directly in line with the center of the vessel windows, and thus the test section. A Thorlabs OSL2 fiber optic illuminator with variable intensity control was chosen as the light source, as it contains a 150 W halogen lamp that can generate a high-intensity light output. A light

source such as this one enables the camera to effectively capture the schlieren images at a rate of 12,000 frames per second, as a high-shutter speed can lead to underexposed images if proper lighting is not provided, which would ultimately cause a loss of digital information.

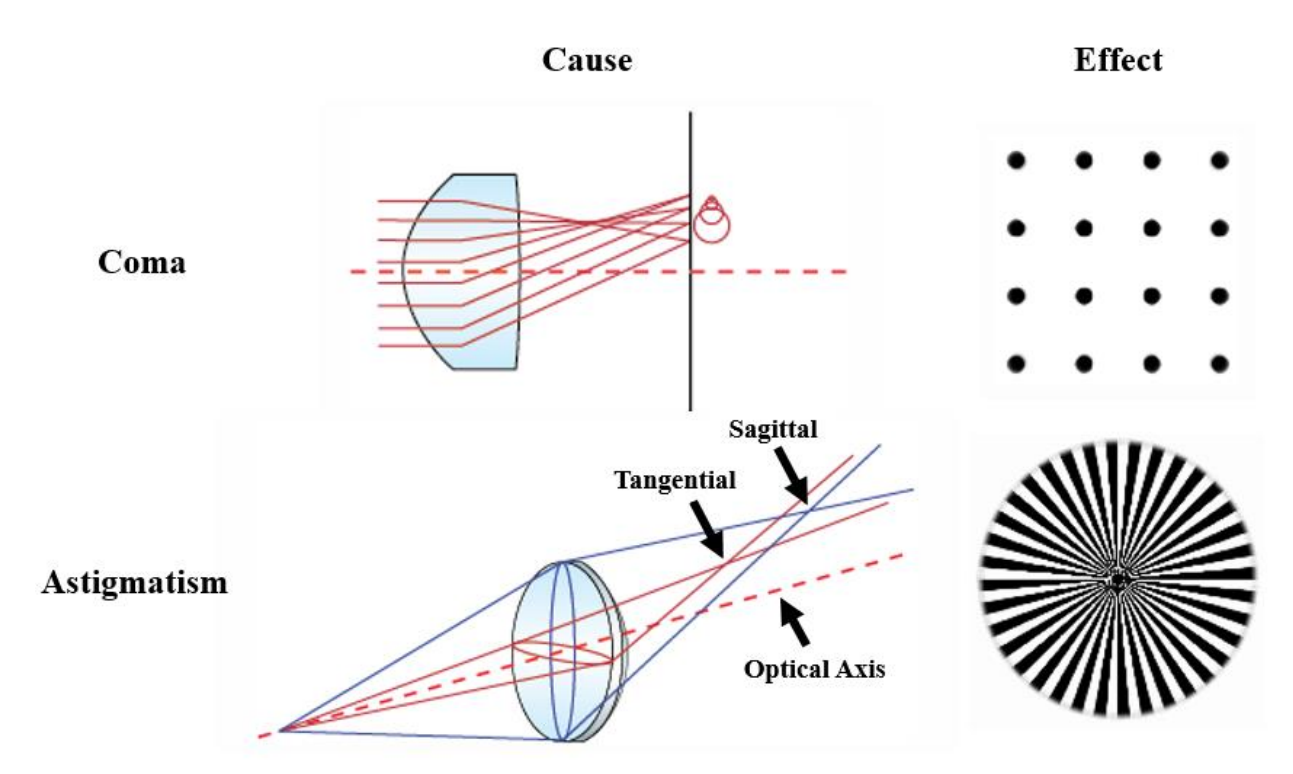


Figure 3-9. Coma and astigmatism, retrieved from [208].

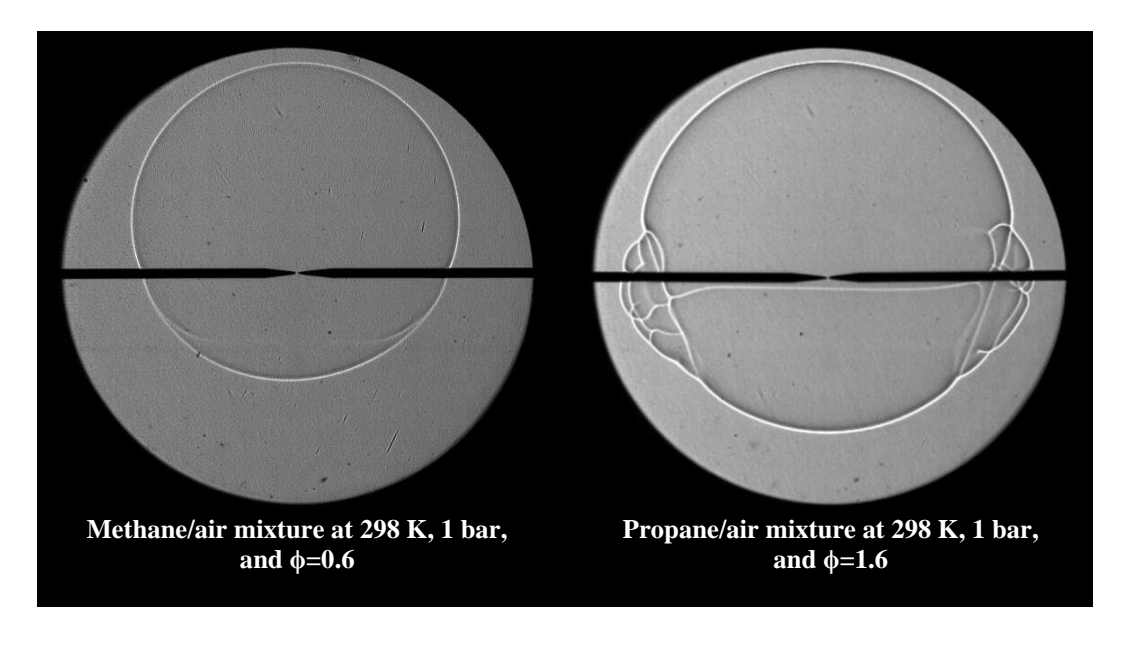


Figure 3-10. Schlieren images showing the buoyancy effect on the flame front.

The point source at the end of the illuminator's fiber bundle was placed approximately at the focal length of an aspherized achromatic condenser lens, 25 mm in diameter with an effective focal length of 30 mm, where the diverging light is collected and converted into a converging beam. An achromatic lens allows white light to be focused to the same focal point, by not separating it by wavelength, and thus reduces chromatic aberrations caused by the polychromatic light generated by the illuminator, while the aspherical feature corrects against spherical aberration [209].

The light from the lens was focused onto an adjustable iris, placed precisely at the focal length of the first mirror as well as the focal length of the lens, and was responsible for intensifying contrast [210] and ultimately creating a sharper final image. If spherical aberrations in the condenser lens were to go unchecked, a final image with uneven lighting would occur as result of a fuzzy image being focused onto the iris [205]. The iris corresponds to the shape of the circular aperture used as the knife edge at the end of the optical set-up, as Toepler [211] found that as long as the source cut-off corresponds to at least one edge of the knife-edge, its shape is immaterial.

Light passes through the iris and onto the first 15.24-cm-diameter spherical concave mirror that has a focal length of 1524 mm. The mirror diameter and focal length yield a relatively large f-number of 10. The mirror's surface accuracy of $\lambda/8$, and a protective aluminum coating allow for effective light redirection [101]. The first mirror was adjusted at the smallest possible angle toward the vessel, directing uninterrupted collimated light through the vessel windows and onto a second identical mirror. The two mirrors were positioned in opposite directions from the optical centerline at equal minimum angle magnitudes. The second mirror allows the passing light to converge away from the vessel and toward a high-speed Photron SA5 camera, with its lens positioned at the second mirror's focal length. The camera lens includes a variable diaphragm that serves as a circular knife

edge, which has been shown to yield a more uniform image with higher sensitivity for flame radius detection, versus conventional straight-edge cut-offs [4].

The Photron Fastcam SA5 offers an ISO light sensitivity of 10,000 in black and white and can provide 1024 x 1024 pixel resolution at frame rates of 7,000 fps and below; with reduced resolution, it can obtain up to 930,000 fps [212]. In this study, images were captured at 12,000 fps in order to capture the combustion process with maximum accuracy while still retaining a high resolution of 896 x 704 pixels. A Nikon UV-105 lens is used with the camera, as it allows a wide range of light transmission of wavelengths between 220-900 nm. It has a focus distance of 105 mm and an adjustable diaphragm within the lens that yields sharp images that are free from aberrations over the entire variable aperture range. The aperture was adjusted prior to experiments until a focused, sufficiently illuminated background image was achieved; this occurred with smaller f-numbers.

Images are processed through an in-house image processing code, until a substantial rise in the total chamber pressure is detected by Kistler 6125C piezoelectric pressure sensor. With negligible buoyancy effects, the flame generated in the center of the vessel propagates outward as an approximate sphere, visualized as a 2D circle with schlieren imaging. The code extracts the rate of 2D radial growth of the spherically propagating flame over time so that the laminar flame speed can be calculated.

To extract the flame boundary, or foreground, the initial background frame of each image set, i.e. the first frame with no spark or flame present, is subtracted from each frame. Before the background subtraction process, a median filter was applied to each image for smoothing and noise reduction, while preserving edge sharpness [213]. The resulting image from the subtraction process is then converted to binary, where the foreground is represented by white pixels assigned

a value of 1, and the background consists of all black pixels, represented by a value of 0. The subtraction process is depicted in Figure 3-11.

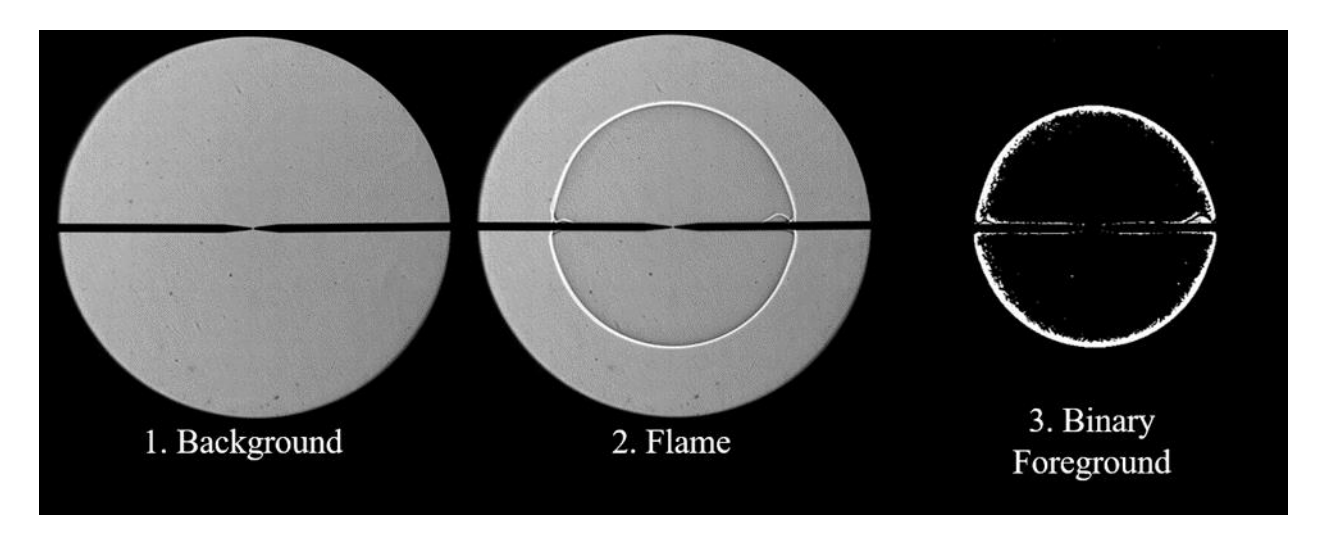


Figure 3-11. Background subtraction/foreground extraction steps of image processing.

Further noise that appears as a result of the subtraction process is removed by carefully setting a lower limit on the area a group of connected pixels makes up; this removes relatively small groups of pixels while effectively avoiding pixels that make up the flame boundary. If wrinkles develop in the flame boundary and segment some boundary pixels into small groups, as shown in Figure 3-12, the lower limit is decreased so that vital pixels will not be deleted.

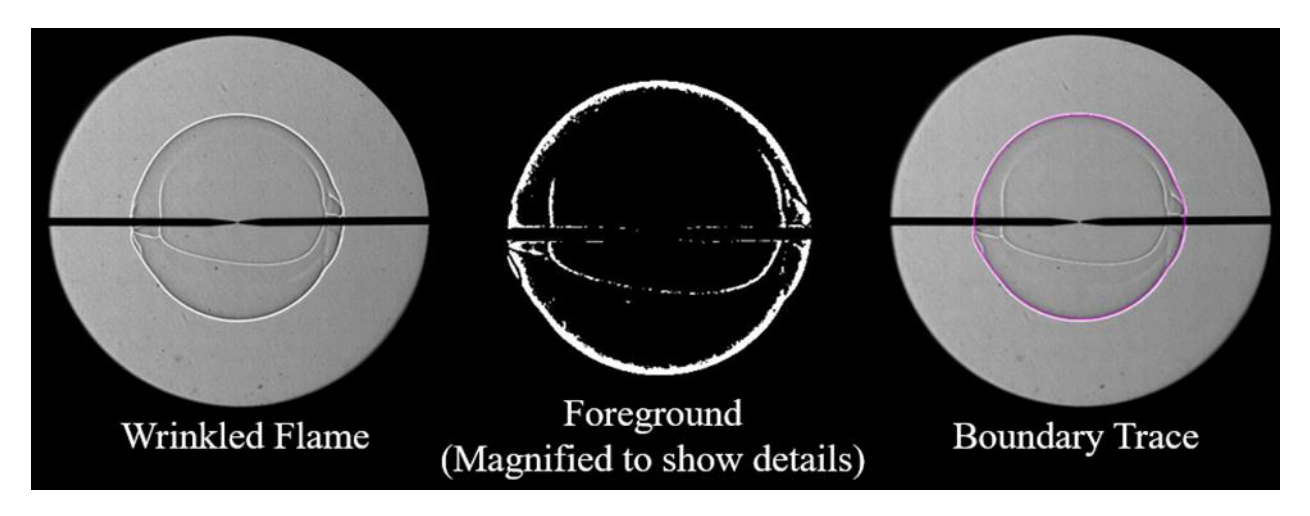


Figure 3-12. Wrinkled flame with segmented pixel groups in flame boundary.

In the special case that large pixel groups of noise exist and are surrounding a wrinkled flame with segmented boundary pixels, simply decreasing the lower limit does not suffice, as large groups of pixel noise will not be removed. In this case, an ellipse mask is creating to segment the outside noise from the flame boundary; all pixels outside the ellipse boundary are set to 0, while all pixels within the ellipse boundary are kept the same. Then, the lower area limit is able to take the small segmented boundary pixels into account, without leaving any pixel noise present. If this occurs in several images in a row, an ellipse that is made for one image can be used on a number of preceding images, as long as the ellipse is placed close enough to the flame boundary that it removes all pixel noise close to the preceding images' flame boundaries.

As a result of the background subtraction process, gaps are formed in the flame boundary due to electrode removal, as shown in the rightmost frame (step 3) in Figure 3-11. A morphological structure is used to close these gaps, based on the diameter of the electrodes. Other morphological operations exists, such as eroding and dilating, where erosion is the action of reducing the foreground by removing all of the outermost boundary pixels of an object and dilation is conversely expanding the foreground by adding a layer of 1 pixel thickness to the boundary. Great care must be used with these operations as they both change the area of the flame boundary and can easily lead to inaccurate results. For that reason, it is recommended that they not be used alone, but can be very helpful when used in succession.

Closing, or dilation immediately followed by erosion, allows one to close gaps in the boundary, like those caused by the electrodes, when used with an appropriate morphological structuring element, as seen in the leftmost image (step 4) of Figure 3-13. Performing dilation directly followed by erosion while using the same structuring element essentially cancels out the effect each of these operations have on the initial flame boundary area; although the closing

operation does add some area to the foreground by filling in the electrode gaps, the net number of pre-existing pixels in the flame boundary does not change. In other words, the boundary thickness does not change from step 3 to step 4 during the closing operation.

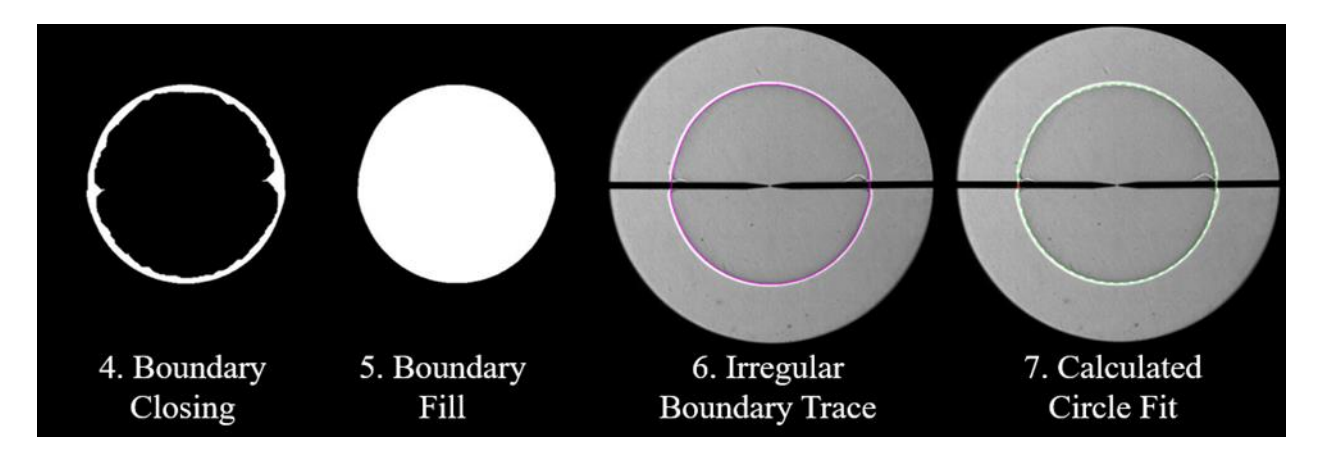


Figure 3-13. Final stages of image processing.

Upon closing, the resulting boundary is then able to be filled with white pixels and the filled surface area can be calculated. The default unit of measure for surface area in the coding software used was pixels². To convert to a useable unit of measure, a known reference length is needed for conversion. It is reasonable to use the known diameter of the frame of view, which should ideally be equal to the exposed diameter of the vessel windows, 15.24 cm. By using the measurement of the flame's surface area, the radius is calculated and used to create a circle of best fit around the flame's centroid. A circle fit can then be superimposed on the original image of the flame for a visual check, as seen in step 7 of Figure 3-13.

Once again using the surface area of the circle, the 'calculated perimeter' can be derived using simple circle geometry. Step 6 of Figure 3-13 shows a pink boundary trace of the flame's irregular boundary, which is used to extract an 'actual perimeter' value. Taylor [214] used the ratio of two similar perimeter values as a circularity reference to account for the fact that flames do not grow in perfect isometric fashion, even in controlled experiments. The closer the ratio is to unity,

the closer the flame is to a perfect sphere. Furthermore, the reference of circularity allows the ability to decide whether the buoyancy effect exits or not.

3.5 Data Acquisition System

Data is collected through a National instruments BNC-2120 connector block, or data acquisition (DAQ) board, which facilitates communication between the system and the lab PC and a PCI-6251 high-speed multifunction DAQ card. The card offers 16-Bit resolution, 16 analog inputs with a ±10 V range. In addition, this particular card has a high accuracy with fast sampling rates of ~1.25 MS/s for one channel and 1 MS/s if several channels are used. It facilitates both digital and analog triggering, and is able to work with several operating systems. An in-house LABVIEW code is used to control triggering signals together with the DAQ card.

Both the absolute (Omega MM series sensor and Setra ASM AccuSense sensor) and differential (Kistler 6125C piezoelectric sensor) pressure transducers, as well as the middle section thermocouple were connected to the DAQ board, which allows the pressures and a temperature reference to be displayed on the PC. By visualizing the absolute pressure within the vessel, it is possible to observe the amount of each reactant that entered the vessel, controlled manually by valves, and use the method of partial pressures to calculate equivalence ratio. In experiments where liquid fuel or water is used, the DAQ system is used to generate the signal for the injection of fuel/water with the help of the LABVIEW code. Simultaneous triggering of spark ignition, camera imaging, and oscilloscope measurements is also provided with signaling-output ports of the DAQ system.

The sampling rate for the trigger signal and the differential pressure (readings of Kistler 6125C piezoelectric sensor) during combustion is 12 kHz, which is equal to the rate of imaging of the Photron SA5 camera, i.e. 12,000 fps. 12 kHz was chosen for easy synchronization of pressure

and cold flame front radius data. However, pressure measurements are initiated earlier than the trigger signal for the baseline calculation until the end of the trigger signal, which is subsequently used for noise reduction in pressure measurements. The rising edge of the trigger signal serves as a reference for offsetting the pressure readings with respect to the schlieren images.

3.6 Laminar Burning Velocity Calculation Methodology

In the present study, spherically expanding flames under constant pressure were employed to measure the laminar burning velocity and burned gas Markstein length since, after the formation of the concept of flame stretch, the laminar burning velocity has most widely been determined by observing the radius of the flame within a region of constant pressure [13]. Experiments were performed in an optically accessible constant volume combustion chamber, with detailed information available in previous sub-chapters.

The pressure built-up inside the chamber during combustion was measured with a Kistler 6125C piezoelectric pressure transducer to ensure that the pressure was constant during the measurements. In fact, a maximum pressure increase of 1.2% was recorded at the upper measurement limit, where the flame occupied 25% of the total chamber volume, i.e. R_f =0.25 R_w =4.36 cm, which yields a maximum of 2-3% inaccuracy in the S_L due to the radiation and confinement induced inward flow effects [124, 131]. If cellularity was detected before R_f =4.36 cm, which sometimes happened at high pressures or away from stoichiometry due to the diffusional-thermal and hydrodynamic instabilities, only the schlieren images before the inception of cellular formation were included in the laminar flame speed calculations. Moreover, the slowest laminar burning velocity measured in the present study is 15.58 cm/s and all test points are appreciably away from the flammability limits, which suggests that the reduction in the S_L due to radiation induced cooling effect is within 2-3% [124, 129] and the buoyancy effect is eliminated

[126]. Therefore, inaccuracy in the laminar flame speed calculations due to the confinement and radiation effects was estimated as less than 5%.

Due to the utilization of the constant pressure method, the measurements were limited to the early stage of combustion, where the flame stretching is more intense. Since there is no change in the pressure within the measurement range, the second term of Equation 2-10 equals zero, which suggests that the flame speed of the burned gases becomes equal to the flame propagation speed, i.e. $S_b=dR_f/dt$. A central differencing scheme was employed to calculate the rate of radial growth, i.e. burned gas flame speed, from R_f data obtained by the image processing of schlieren images. The stretched S_b values were treated using the experimental stretch model extrapolation method to calculate the unstretched burned flame speed. Subsequently, the unstretched unburned flame speed, i.e. the laminar burning velocity or laminar flame speed, was calculated from the mass flow balance at an infinitely thin flame front, i.e. Equation 2-23, which is valid also for unstretched flame speeds. The expansion ratio (ρ_b/ρ_u) in Equation 2-23 was obtained from the results of numerical analysis conducted with the Chemkin-Pro software [215].

3.6.1 Assessment of Accuracies of Stretch Extrapolation Methods

In the early stage of combustion, where spherical flames grow at constant pressure, the stretch effect is severe. Therefore, accuracies of the stretch extrapolation methods play an important role in the uncertainty of experimental flame speed values deduced from spherically expanding flames at constant pressure. Despite the large scatter in the S_L due to the utilization of different stretch models and the obscurity in the stretch model limitations, studies on the accuracies of the stretch methods are scarce.

By investigating hydrogen/air mixtures, Chen et al. [167] revealed that there is a critical flame radius above which the stretch models are valid. This critical flame radius strongly depends

on the Le and it is generally greater than the lower radius limit for S_L calculations (R_L) determined by Bradley et al. [68] to avoid the ignition effect, i.e. 6 mm. Halter et al. [165] compared laminar flame speeds obtained by the extrapolation of LS and NQ models in Table 2-3 for methane and iso-octane flames at 1 bar and 300-400 K and concluded that experimental S_L values from both models converge when R_L is increased.

With detailed numerical simulations and theoretical analysis on methane/air mixtures at 1 bar and 298 K, Chen [148] found that accuracies of the stretch models in Table 2-3 depend on the Le and demonstrated that the LC model shows better performance for mixtures with Le greater than unity, i.e. positive burned gas Markstein length (L_b), while the NQ model is the most accurate for mixtures with Le less than unity, i.e. negative L_b. Similarly, Karpov et al. [216] showed that the LC model performed much better than the LS model for highly curved rich hydrogen flames characterized by a large Le. Numerical results of Li et al. [217] also supported the findings of Chen [148] by stating that the NQ model is the most appropriate stretch correlation for Le<1. However, Cai et al. [218] concluded that the accuracies of the stretch models in Table 1 are almost identical when Le<1. Cai et al. [218] also stated the critical lower flame radius depends strongly on the Le and pressure, and increases linearly with the absolute value of the L_b.

Wu et al. [160] tested the performances of the stretch correlations in Table 2-3 for hydrogen and n-heptane flames by comparing results of laminar flame speed experiments and direct numerical simulations with computation results of the 1-D planar flame using detailed chemistry without including radiation loss and absorption. After observing a large discrepancy between the stretch models and numerical results over a wide range of equivalence ratios, Wu et al. [160] suggested adjusting the Le to close to unity, i.e. L_b~0, by diluting the fuel/oxidizer mixture with inerts to reduce extrapolation error.

Lipatnikov et al. [219] and Huo et al. [220] investigated the effect of the upper and lower bounds of the flame radius range used to calculate S_L , on the accuracies of the stretch methods for mixtures with $L_b>0$. Lipatnikov et al. [219] remarked that the LC model fits the experimental data well for a wider range compared to the LS and NQ models. Huo et al. [220] showed that the flame radius range is the controlling parameter for the model errors and the model errors can be decreased by increasing the upper and lower bounds of the flame radius range. Recently, Beeckmann et al. [221] also studied the effect of lower and upper measurement limits for S_L of methane flames with Le moderately away from unity to highlight the importance of the LS model.

The lack of information about the proper S_L measurement range for the mixtures with different L_bs has caused inaccurate flame speed vs. flame stretch trends predicted by the stretch models. As mentioned above, in recent years, Chen et al. [167], Halter et al. [165], Lipatnikov et al. [219], Hou et al. [220], and Beeckmann et al. [221] have found out that R_L is the controlling parameter for the model errors, which can be reduced by increasing R_L . However, these researchers were unable to capture the general trend of the critical R_L above which the stretch models are valid because Chen et al. [167] only investigated hydrogen/air flames which have a small variation in the L_b and suffer greatly from hydrodynamic and thermal instabilities. Halter et al. [165] and Beeckmann et al. [221] only increased the R_L up to 2.0 cm due to limitations of their experimental setups. Lipatnikov et al. [219] and Hou et al. [220] only tested mixtures with $L_b>0$, for which the critical R_L is relatively high.

The stretch models in Table 2-3 were derived from asymptotic analysis based on various assumptions [160]. From the theoretical point of view, the LS and LC models should yield similar results for small L_b/R_f values or for S_b values close to S_b^o [216]. Similarly, the LS, NQ, and LC models were shown to provide analogous results for weakly stretched flames, i.e. when the stretch

rate tends to zero [159]. In the early stage of the flame kernel, the nonlinear stretch effect is generally severe [216]. As the flame radius increases, the flame stretching gets weaker, the L_b/R_f becomes smaller, and the S_b approaches S_b^o . Consequently, in light of the studies mentioned above, there should be a critical R_L ($R_{L,critical}$) for each Ma_b , where all S_L and L_b values obtained by the extrapolation of the stretch models in Table 2-3 converge to the same S_L and L_b values.

To test the validity of this statement for a wide range of Le, L_b , and Ma_b , and to provide a measurement range for spherically expanding flames where the flame stretch is weak and, therefore, the LS, NQ, and LC models yield the same results, the effect of R_L on the extrapolation results of the stretch models in Table 2-3 were investigated for four different fuel/oxidizer mixtures with -0.48 mm $\leq L_b \leq 1.23$ mm by including both the Lewis number and laminar flame thickness (δ_L) effects. The values of S_L and L_b were experimentally calculated from spherically expanding methane/air flames at 1 bar, 298 K, ϕ =0.7-1.1, hydrogen/air flames at 1 bar, 298 K, ϕ =0.7-4.0, propane/air flames at 1 bar, 298 K, ϕ =0.7-1.4, and iso-octane/air flames at 1 bar, 373 K, ϕ =0.8-1.5 for R_L =0.6, 1.0, 2.0, and 3.0 cm to reveal the general trend of the R_L critical across a wide range of Ma_b .

3.6.1.1 Effect of Lower Radius Limit on the S_L and L_b

The four test fuels (methane, hydrogen, propane, and iso-octane) were chosen to account for both hydrocarbon and non-hydrocarbon fuels with different evolutions in L_b when ϕ is increased so that the universality of the findings of the present study would increase. While the lower radius limit for the S_L calculation was varied from 0.6 cm to 3.0 cm, the upper radius limit (R_{up}) was kept constant at 4.36 cm, which is the maximum value used in order to keep the experimental data minimally affected by confinement [131] and radiation [124], as long as there is no early onset of cellular formation since the flame stretch effect gets weaker at higher radii of

a spherically expanding flame and the stretch models in Table 2-3 depend on a weakly stretched flame assumption.

Some of the S_L and L_b results are plotted against the R_L in Figure 3-14. To find the $R_{L,critical}$, where all S_L and L_b values obtained by the extrapolation of the LS, NQ, and LC stretch models in Table 2-3 converge to the same S_L and L_b , third order polynomials were fit to S_L and L_b results of each stretch model at R_L =0.6, 1.0, 2.0, and 3.0 cm, as shown in Figure 3-15. Then, the intersection points of the S_L and L_b curves were determined by solving for R_L , where the differences between the results of S_L curves and L_b curves were minimized, i.e. the $R_{L,critical}$. It was observed that the intersection points of the S_L curves and L_b curves coincide with each other and the deviations in the results of the S_L curves and L_b curves at these points are always smaller than the random uncertainty in S_L and L_b data at the corresponding test conditions. In fact, the maximum deviations in the results of S_L curves and L_b curves at the intersection points are 1.20 cm/s and 0.14 mm, respectively.

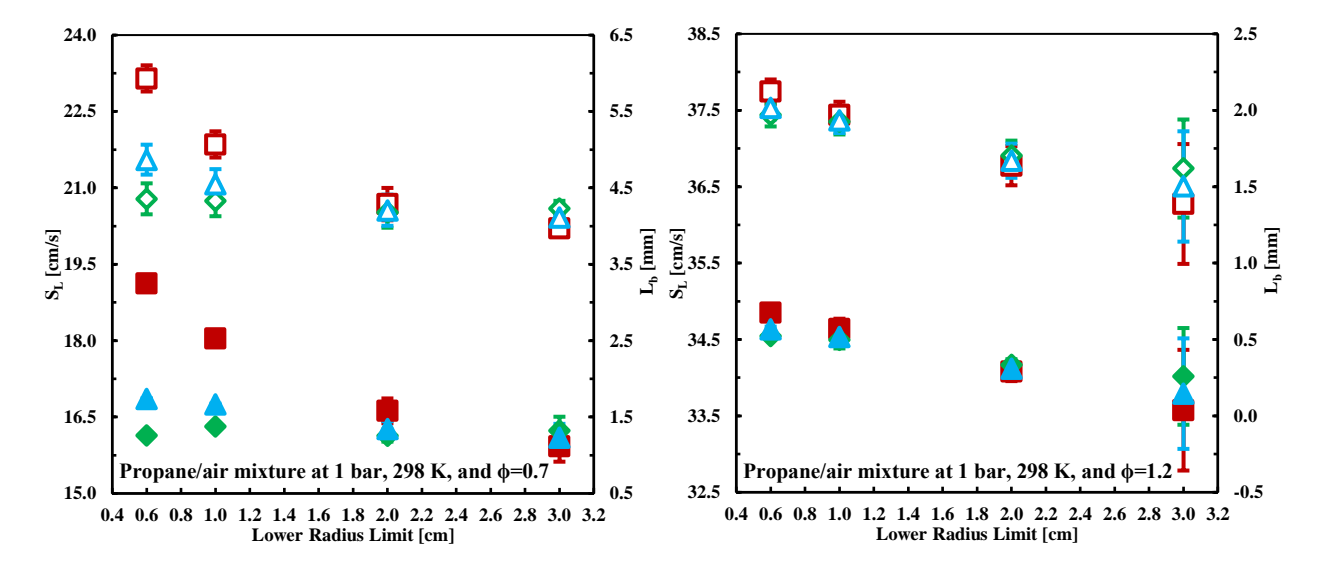
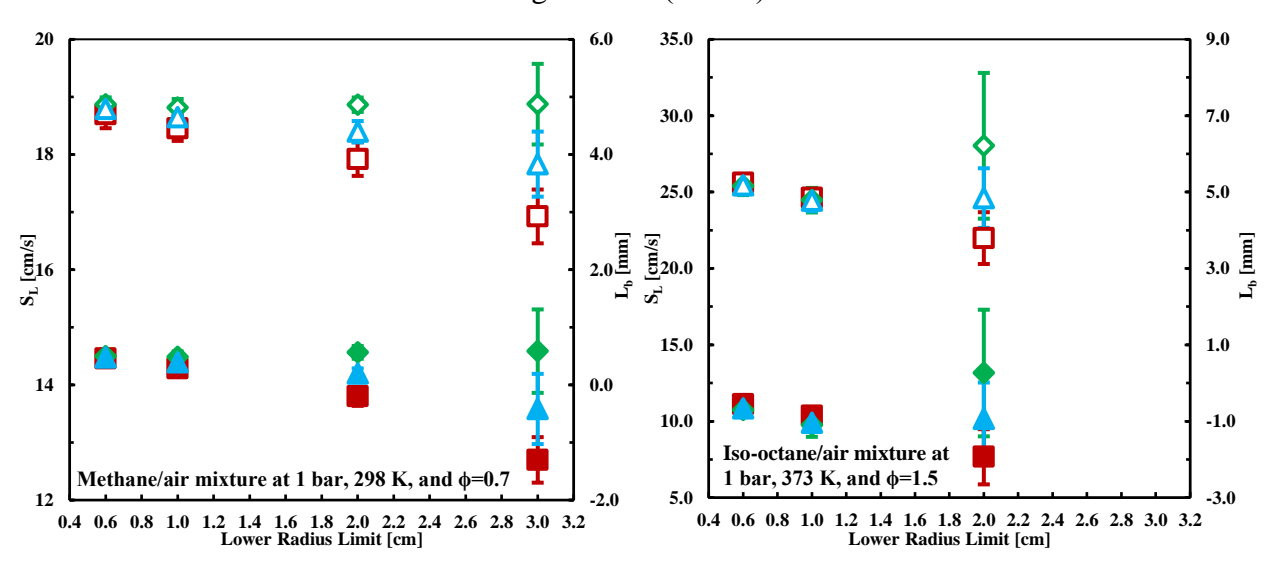


Figure 3-14. Variation in the S_L and L_b across the lower measurement limit on the R_f. (squares results obtained by the LS model [149], diamonds - results obtained by the NQ model [140], triangles - results obtained by the LC model [148], unfilled markers - S_L, and filled markers - L_b)

Figure 3-14 (cont'd)



It was observed that the $R_{L,critical}$ changes with L_b , see Figure 3-14 and Figure 3-15, and the convergence points of the S_L curves and L_b curves can be shifted to R_L values smaller than 0.6 cm for very small L_bs , see the methane/air mixture at 1 bar, 298 K, and ϕ =0.7 in Figure 3-14 and the hydrogen/air mixture at 1 bar, 298 K, and ϕ =0.8 in Figure 3-15. However, no stretch extrapolation calculation was made for R_L <0.6 cm to prevent the laminar flame speed calculations from being affected by the initial energy deposit due to the spark [68]. Therefore, the S_L and L_b splines were extrapolated to R_L =0 cm to detect the intersection points of the S_L curves and L_b curves for $R_{L,critical}$ <0.6 cm, as shown for the hydrogen/air mixture at 1 bar, 298 K, and ϕ =0.8 in Figure 3-15.

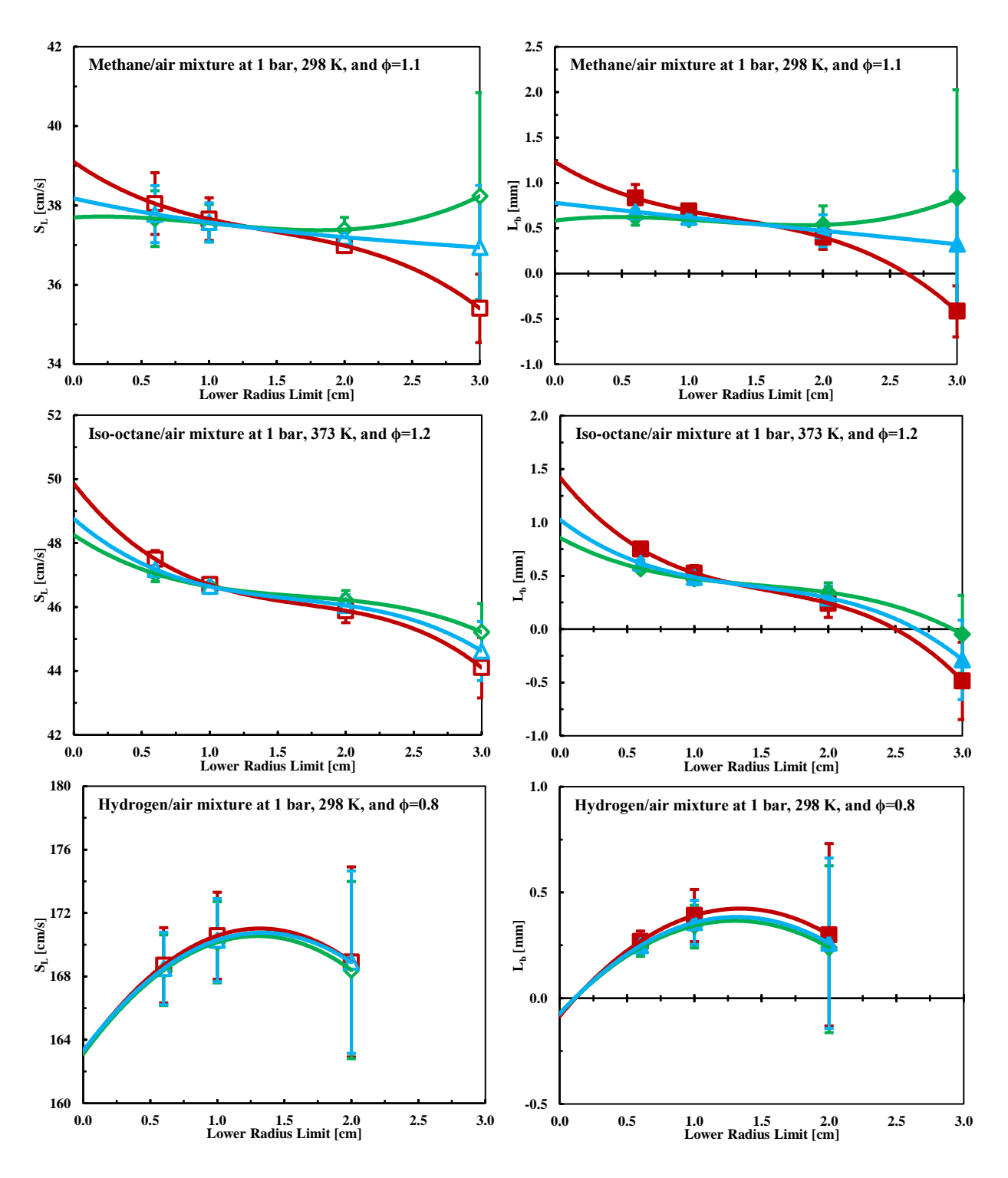


Figure 3-15. Polynomial fitting for S_L and L_b results of each stretch model and determination of the intersection points of S_L curves and L_b curves, i.e. the $R_{L,critical}$ (squares - results obtained by the LS model [149], diamonds - results obtained by the NQ model [140], triangles - results obtained by the LC model [148], unfilled markers - S_L , and filled markers - L_b)

Figure 3-14 and Figure 3-15 show that there is an $R_{L,critical}$, where all S_L and L_b values obtained by the extrapolation of the LS, NQ, and LC stretch models in Table 2-3 converge to the same S_L and L_b . Therefore, the choice of the extrapolation expression plays no role in the stretch model accuracy as long as the measurements are started at the $R_{L,critical}$ presented in this study. This finding is a potential remedy to the scattered experimental S_L data due to the utilization of different stretch models for the same mixtures. Figure 3-14 and Figure 3-15 demonstrate that the value of the $R_{L,critical}$ strongly depends on L_b , and therefore on Le. The convergence points of the S_L and L_b values coincide with each other and generally shift to higher radii for higher L_b and vice versa for lower L_b , see Figure 3-14 and Figure 3-15.

Contradicting Halter et al. [165] and Hou et al. [220], who concluded that stretch extrapolation errors can be decreased by increasing R_L , Figure 3-14 and Figure 3-15 suggest that further increases in R_L after the critical value causes a deviation in the results of the stretch models due mainly to the increased random error with a smaller number of experimental points used for the extrapolation. In fact, as shown in the current study, having the largest/smallest range of data for extrapolation does not ensure high stretch model accuracy. Rather, starting the S_L measurements with the $R_{L,critical}$ is crucial for the stretch model accuracy. The range of data for extrapolation can be large or small depending on the L_b and δ_L . The difference between the findings of the present study and those of Halter et al. [165] may be attributable to the fact that Halter et al. [165] increased R_L up to only 2.0 cm. The $R_{L,critical}$ can be higher than 2.0 cm for strongly stretched flames, e.g. $R_{L,critical}$ =2.75 cm for propane/air mixture at 1 bar, 298 K, and ϕ =0.7 in Figure 3-14 with L_b =1.23 mm. On the other hand, Hou et al. [220] only tested mixtures with L_b appreciably higher than zero, for which the $R_{L,critical}$ is relatively high, see Figure 3-14 and Figure 3-15.

For strongly stretched flames ($L_b>1$ mm), the $R_{L,critical}$ can be as high as 2.98 cm, see Appendix I. This finding suggests that it may not be possible to accurately measure the laminar flame speeds of the strongly stretched flames with a small vessel, such as the one used by Beeckmann et al. [221]. When L_b decreases, the flame gets less stable and cellular formation is generally observed in the earlier stage of combustion, as shown in Figure 3-16. Therefore, having smaller $R_{L,critical}$ values for small L_b values improves the stretch model extrapolation accuracy by increasing the number of early measurement points even though there is a decrease in later measurement points due to the earlier onset of flame cellularity, e.g. iso-octane flames at 1 bar, 373 K, and ϕ =1.5 in Figure 3-14 and hydrogen flames at 1 bar, 298 K, and ϕ =0.8 in Figure 3-15. For the same reason, R_L =3.0 cm could not be investigated for iso-octane/air mixtures at 1 bar, 373 K, and ϕ =1.4-1.5 and hydrogen/air mixtures at 1 bar, 298 K, and ϕ =0.7-0.8.

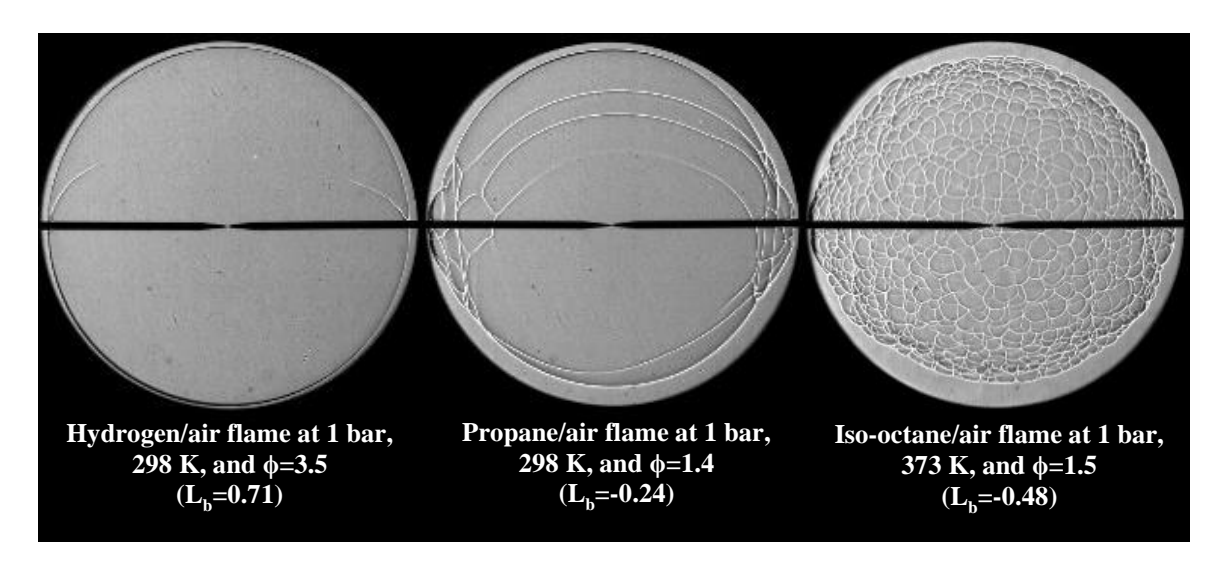


Figure 3-16. Schlieren images of fuel/air mixtures with different L_b values.

When L_b approaches zero, the $R_{L,critical}$ generally penetrates into the ignition-affected region, i.e. $R_{L,critical}$ <0.6 cm [68], see hydrogen/air mixture at 1 bar, 298 K, and ϕ =0.8 in Figure 3-15 ($R_{L,critical}$ =0.26 cm and L_b =0.08 mm). For L_b ~0, i.e. Le~1, choosing R_L as 0.6 cm in order to discard the ignition effect from the experimental data is suggested although the real $R_{L,critical}$ for

 $L_b\sim0$ might be smaller than 0.6 cm. As seen with the methane/air mixture at 1 bar, 298 K, and ϕ =0.7 in Figure 3-14 and the hydrogen/air mixture at 1 bar, 298 K, and ϕ =0.8 in Figure 3-15, choosing a slightly higher R_L (\sim 0.6 cm) than the actual $R_{L,critical}$ (<0.6 cm) for $L_b\sim0$ does not deteriorate the stretch model accuracy remarkably because of the abundance of experimental points used for the extrapolation. At $L_b<0$, i.e. Le<1, the $R_{L,critical}$ evaluation with respect to L_b is similar to the relation between the $R_{L,critical}$ and the absolute value of L_b . For example, $R_{L,critical}$ and L_b values of the methane/air mixture at 1 bar, 298 K, and ϕ =0.7 and the iso-octane/air mixture at 1 bar, 373 K, and ϕ =1.5 in Figure 3-14 are 0.50 cm and 0.51 mm, and 0.47 cm and -0.48 mm, respectively.

3.6.1.2 Effect of Upper Radius Limit on the R_{L,critical}

In order to find out whether the $R_{L,critical}$ depends on the upper radius limit for the S_L measurement (R_{up}), an additional R_{up} value other than 4.36 cm was considered for four different cases with very different L_b (0.08-0.54 mm) and $R_{L,critical}$ (0.26-1.58 cm) values. First, the $R_{L,critical}$ for an iso-octane/air mixture at 1 bar, 373 K, and ϕ =1.2 was computed for R_{up} =3.5 cm and almost no change was observed in the $R_{L,critical}$, S_L , and L_b data ($\Delta R_{L,critical}$ =0.03 cm, ΔS_L =0.26 cm/s, and ΔL_b =0.04 mm). Please note that R_L =3.0 cm was not investigated for R_{up} =3.5 cm because the limited number of experimental points at R_f =3.0-3.5 cm would cause poor stretch model extrapolation accuracy.

For a methane/air mixture at 1 bar, 298 K, and ϕ =1.1, altering the R_{up} from 4.36 cm to 3.5 cm changed the $R_{L,critical}$ from 1.58 cm to 1.31 cm, the S_L from 37.34 cm/s to 37.63 cm/s, and the L_b from 0.54 mm to 0.63 mm. The changes in the S_L and L_b (0.29 cm/s and 0.09 mm, respectively) are smaller than the random uncertainty in the S_L and L_b (0.35 cm/s and 0.12 mm, respectively). Similar to the iso-octane/air mixture at 1 bar, 373 K, and ϕ =1.2, the highest lower radius limit

tested for the methane/air mixture at 1 bar, 298 K, and ϕ =1.1 was 2.0 cm for R_{up}=3.5 cm due to large errors in extrapolation of stretch correlations, as shown in Figure 3-17.

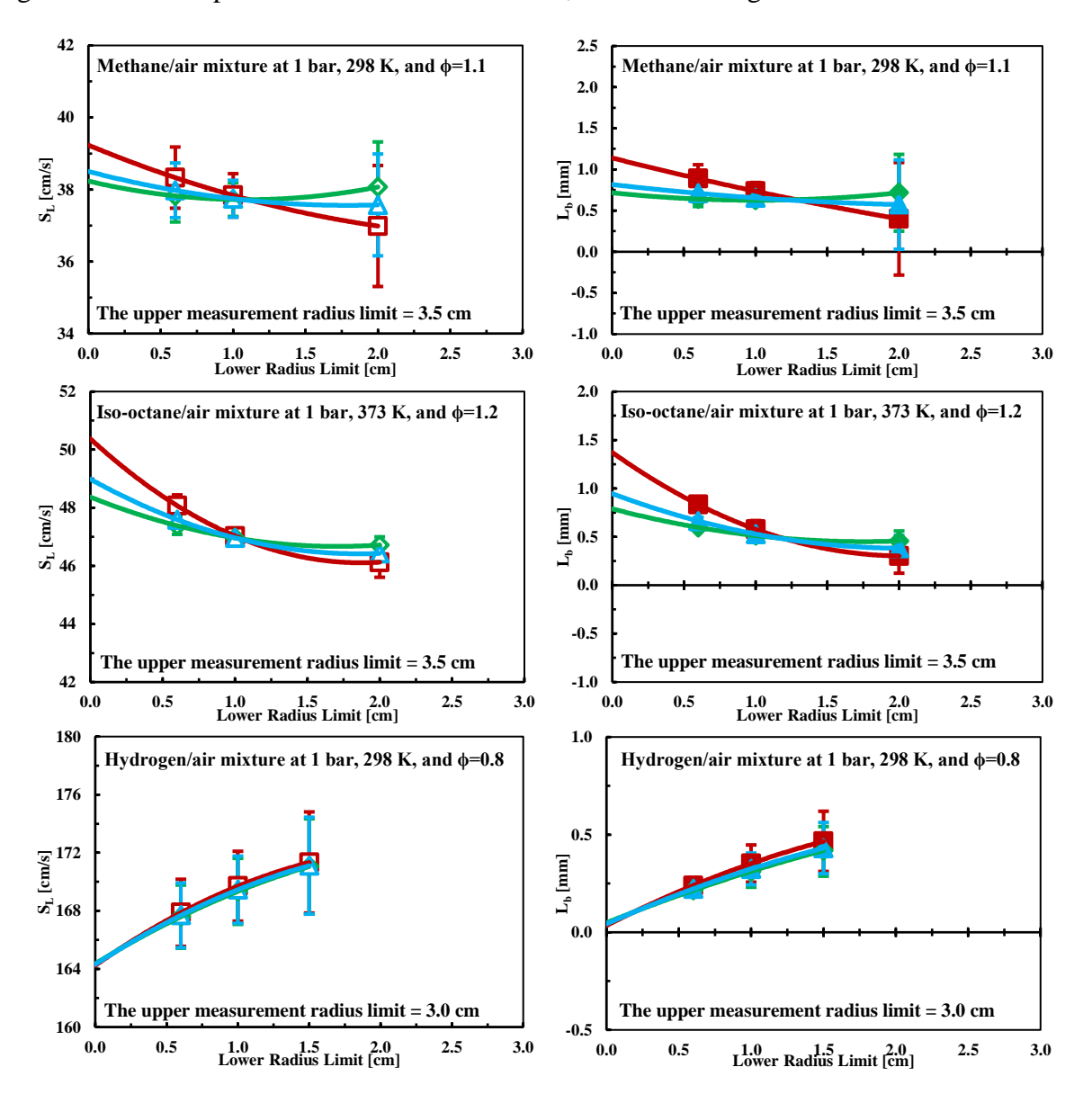
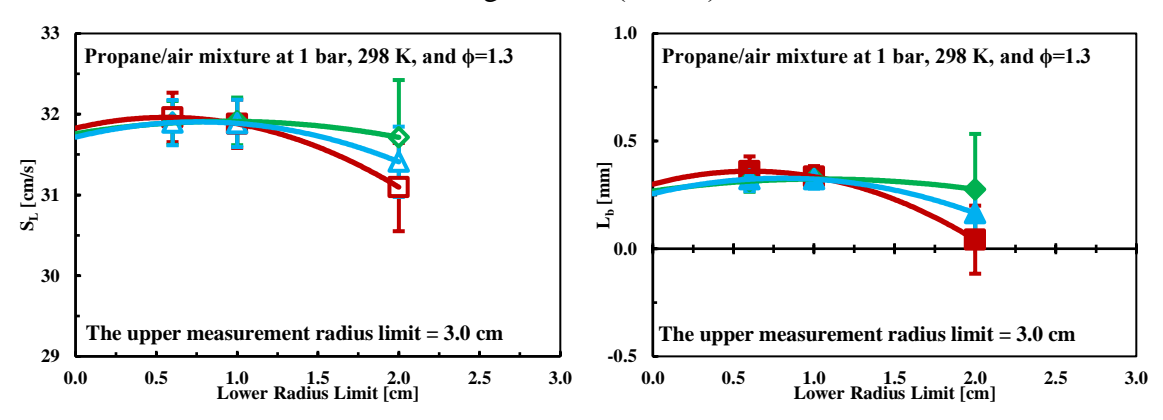


Figure 3-17. Polynomial fitting for S_L and L_b results of each stretch model and determination of the intersection points of S_L curves and L_b curves, i.e. the $R_{L,critical}$, with smaller upper measurement radius limits than 4.36 cm. (squares - results obtained by the LS model [149], diamonds - results obtained by the NQ model [140], triangles - results obtained by the LC model [148], unfilled markers - S_L , and filled markers - L_b)

Figure 3-17 (cont'd)



Even lower R_{up} values (R_{up} =3.0 cm) were tested for the hydrogen/air mixture at 1 bar, 298 K, and ϕ =0.8, and the propane/air mixture at 1 bar, 298 K, and ϕ =1.3. As shown in Figure 3-17, hydrogen and propane laminar flame speeds could not be calculated beyond R_L =1.5 cm and R_L =2.0 cm, respectively, because of deteriorated stretch model extrapolation accuracy. Changing the R_{up} to 3.0 cm did not alter the $R_{L,critical}$, S_L , and L_b values of the hydrogen and propane mixtures significantly. For R_{up} =3.0 cm, the $R_{L,critical}$, S_L , and L_b of hydrogen/air mixture at 1 bar, 298 K, and ϕ =0.8 became 0.25 cm, 165.83 cm/s, and 0.12 mm. Initially, they were 0.26 cm, 165.92 cm/s, and 0.08 mm, respectively. For propane/air mixture at 1 bar, 298 K, and ϕ =1.3, altering the R_{up} from 4.36 cm to 3.0 cm changed the $R_{L,critical}$ from 0.88 cm to 0.97 cm, the S_L from 31.46 cm/s to 31.90 cm/s, and the L_b from 0.23 mm to 0.33 mm.

The effect of the upper radius limit on $R_{L,critical}$, S_L , and L_b is summarized in Table 3-4. For fuel/air mixtures with $R_{L,critical} \le 1.58$ cm, no significant change in the $R_{L,critical}$, S_L , and L_b values was observed when the R_{up} changed from 4.36 cm to 3.0-3.5 cm. Therefore, it can be concluded that the $R_{L,critical}$ does not depend on the R_{up} at these conditions. For smaller R_{up} values ($R_{up} < 3.0$ cm) at these conditions or for more stretched flames with larger $R_{L,critical}$ ($R_{L,critical} > 2.00$ cm) with $R_{up} < 4.0$ cm, determination of the $R_{L,critical}$ can be erroneous because of increased random

uncertainties and poor stretch model extrapolation accuracy as a result of very limited experimental points used for the extrapolation of stretch correlations.

Table 3-4. Effect of upper radius limit on the R_{L,critical}, S_L, and L_b.

Mixture	Rup	R _L ,critical	SL	$\mathbf{L}_{\mathbf{b}}$
Methane/air mixture at 1 bar, 298 K, and φ=1.1	4.36 cm	1.58 cm	37.34 cm/s	0.54 mm
	3.50 cm	1.31 cm	37.63 cm/s	0.63 mm
Propane/air mixture at 1 bar, 298 K, and φ=1.3	4.36 cm	0.88 cm	31.46 cm/s	0.23 mm
	3.00 cm	0.97 cm	31.90 cm/s	0.33 mm
Iso-octane/air mixture at 1 bar, 373 K, and φ=1.2	4.36 cm	1.27 cm	46.43 cm/s	0.43 mm
	3.50 cm	1.24 cm	46.69 cm/s	0.47 mm
Hydrogen/air mixture at 1 bar, 298 K, and φ=0.8	3.50 cm	0.26 cm	165.92 cm/s	0.08 mm
	3.00 cm	0.25 cm	165.83 cm/s	0.12 mm

3.6.1.3 Correlation between Ma_b and R_{L,critical}

Observing the changes in the S_L and L_b across the lower radius limit for the laminar flame speed calculation provided an accurate prediction of the $R_{L,critical}$. It was also possible to capture the general trend of the $R_{L,critical}$ across a wide range of L_b s. However, when the $R_{L,critical}$ values that correspond to different L_b s were compared for all of the tested fuels, a moderate amount of scatter in the $R_{L,critical}$ vs. L_b plot was observed. For instance, although L_b values of methane/air mixtures at 1 bar, 298 K, ϕ =0.7 and ϕ =1.1 and propane/air mixture at 1 bar, 298 K, and ϕ =1.1 are very close to each other (0.51 mm, 0.54 mm, and 0.57 mm, respectively), their $R_{L,critical}$ values are quite different (0.50 cm, 1.58 cm, and 2.18 cm, respectively). Similarly, while the L_b of the propane/air mixture at 1 bar, 298 K, and ϕ =0.7 (1.23 mm) is higher than the L_b of iso-octane/air mixture at 1 bar, 373 K, and ϕ =0.9 (1.01 mm), the $R_{L,critical}$ of the latter mixture (2.98 cm) is greater than that

of the former mixture (2.75 cm). This contradicts the increasing trend of the $R_{L,critical}$ with increasing L_b .

The reason behind these contradictions is that the laminar flame thickness, which is a significant parameter for the flame stretch, was not yet taken into account. Consequently, the data was instead plotted as the burned gas Markstein number ($Ma_b=L_b/\delta_L$) over the $R_{L,critical}$ and presented in Figure 3-18, which includes the absolute value of Ma_b for negative L_b s since it has been shown that the $R_{L,critical}$ evaluation with respect to L_b for $L_b<0$ is similar to the relation between the $R_{L,critical}$ and the absolute value of the L_b .

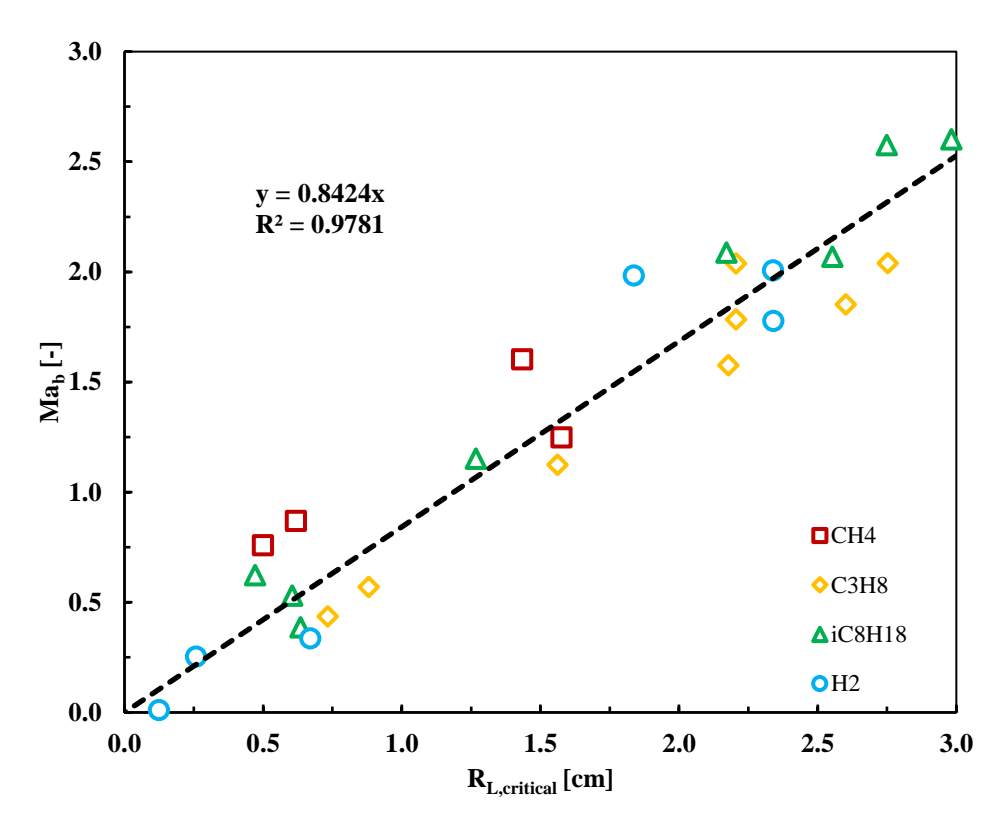


Figure 3-18. Measured Markstein numbers over critical lower radius limit for methane, propane, iso-octane, and hydrogen flames (All S_L and L_b results with experimental uncertainties, $R_{L,critical}$ and Ma_b values are presented in Appendix I).

On the contrary to the L_b dependency of the $R_{L,critical}$, the Ma_b dependency of the $R_{L,critical}$ for all tested fuels was consistent with each other and showed a linear trend (see Figure 3-18), which can be represented as $|Ma_b|$ =0.8424* $R_{L,critical}$ with coefficient of determination (R^2) of

0.9118. This expression provides a lower limit (the $R_{L,critical}$) for a measurement range for spherically expanding flames where the assumptions of the LS, NQ, and LC stretch models are satisfied so that these three models provide the same S_L and L_b values. Therefore, $|Ma_b|=0.8424*R_{L,critical}$ can serve as a reference for choosing the $R_{L,critical}$ for any arbitrary fuel/oxidizer mixture in order to prevent the large scatter in the experimental S_L data due to the utilization of different stretch models.

Including the laminar flame thickness in the $R_{L,critical}$ variation over a wide range of L_bs , i.e. considering the Ma_b dependency of the $R_{L,critical}$, solved the contradictions found earlier in the $R_{L,critical}$ vs. L_b plot. For instance, it was revealed that methane/air mixtures at 1 bar, 298 K, ϕ =0.7 and ϕ =1.1 and propane/air mixture at 1 bar, 298 K, and ϕ =1.1, the L_bs of which are very similar (0.51 mm, 0.54 mm, and 0.57 mm, respectively), have quite different $R_{L,critical}$ values (0.50 cm, 1.58 cm, and 2.18 cm, respectively) because their Ma_bs are 0.759, 1.247, and 1.576, respectively. Similarly, the reason that the iso-octane/air mixture at 1 bar, 373 K, and ϕ =0.9 ($R_{L,critical}$ =2.98 cm) has a greater $R_{L,critical}$ than the propane/air mixture at 1 bar, 298 K, and ϕ =0.7 ($R_{L,critical}$ =2.75 cm), can be explained with the greater Ma_b of the former mixture (2.602) than that of the latter (2.040), despite of the fact that the L_b of the former mixture (1.01 mm) is smaller than that of the latter (1.23 mm).

The initial pressure and temperature change alters the $R_{L,critical}$ as the L_b and δ_L are functions of pressure and temperature [66]. However, the effects of pressure and temperature on the L_b and δ_L are took into account by correlating the $R_{L,critical}$ with Ma_b . In other words, increasing/decreasing the initial pressure of a fuel/air mixture reduces/increases the L_b and δ_L [66], and therefore, the $R_{L,critical}$ changes, but the $|Ma_b|$ =0.8424* $R_{L,critical}$ correlation should still hold true for this mixture because changes in the L_b and δ_L are considered in the Ma_b . To demonstrate this, the $R_{L,critical}$ values

for methane/air mixtures at 3 bar, 373 K and 423 K, and ϕ =1.0, and at 5 bar, 373 K, and ϕ =1.1 were plotted in Figure 3-19 together with the data from Figure 3-18. As seen in Figure 3-19, the $|Ma_b|$ =0.8424* $R_{L,critical}$ correlation holds true for methane/air mixtures at high pressures and temperatures.

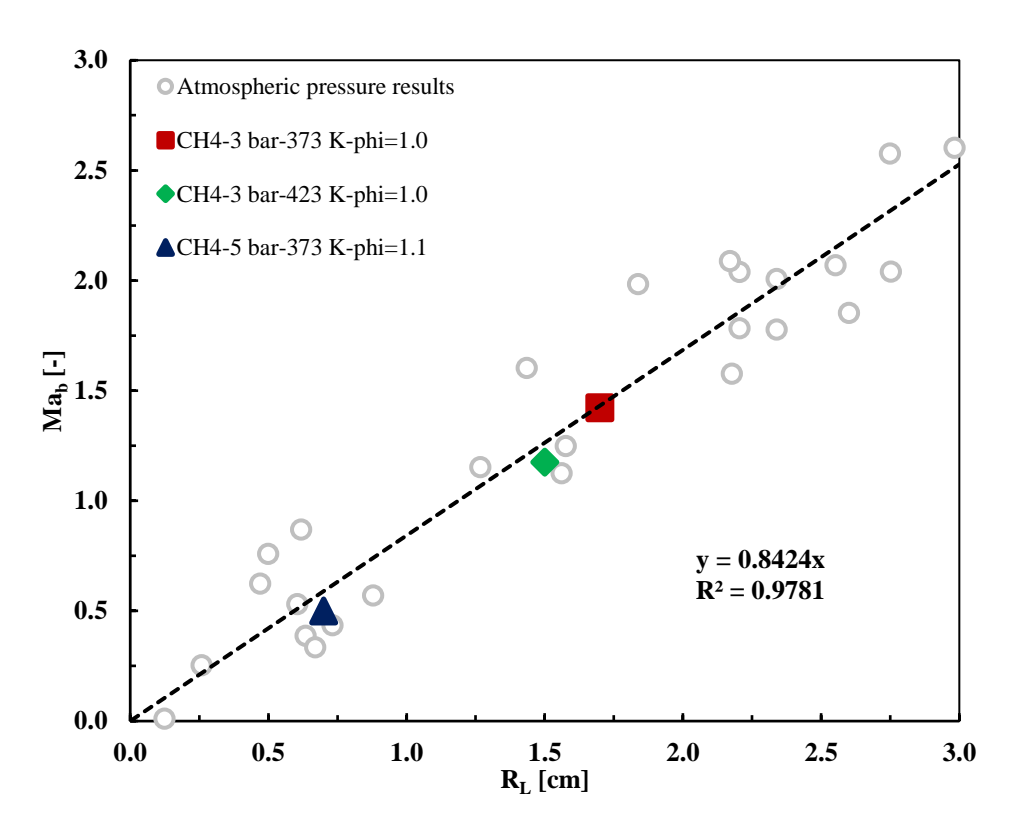


Figure 3-19. R_{L,critical} values of methane/air mixtures at high pressures and temperatures overlayed on the atmospheric pressure results in Figure 3-18.

3.7 Combustion Modeling

Numerical simulations were performed using a freely propagating flame configuration in the Chemkin-Pro software [215], which utilizes a hybrid time-integrating/Newton iteration technique to resolve conservation of species, mass, and energy equations at steady state conditions. A boundary value problem solver, TWOPNT, analyzes the conservation equations for a one-dimensional, freely propagating, premixed, laminar, adiabatic, and planar flame in Chemkin-Pro [215]. Within the code, thermodynamic properties of the species are evaluated, the chemical

mechanism is processed, and mixture averaged transport properties are employed. The flame speed was defined as the unburned gas velocity moving towards the flame [222].

For combustion modeling, the computational domain was fixed from -2.0 cm to 12.0 cm and the initial solution was obtained by establishing a fixed-flame coordinate system [222]. Five continuations followed the initial solution to achieve mesh independency by refining the domain and increasing the number of the grid points until less than a +/- 0.15 cm/s change in the laminar burning velocity was attained between the numerical results of two consecutive continuations, as shown in Figure 3-20. Adaptive grid parameters, namely GRAD and CURV, were varied from 0.5 and 0.5 to 0.005 and 0.01, respectively. The domain of the converged solution, comprising of ~1500-3500 grid points, was large enough to neglect the heat and mass diffusions, i.e. unconstrained by the boundaries of the domain.

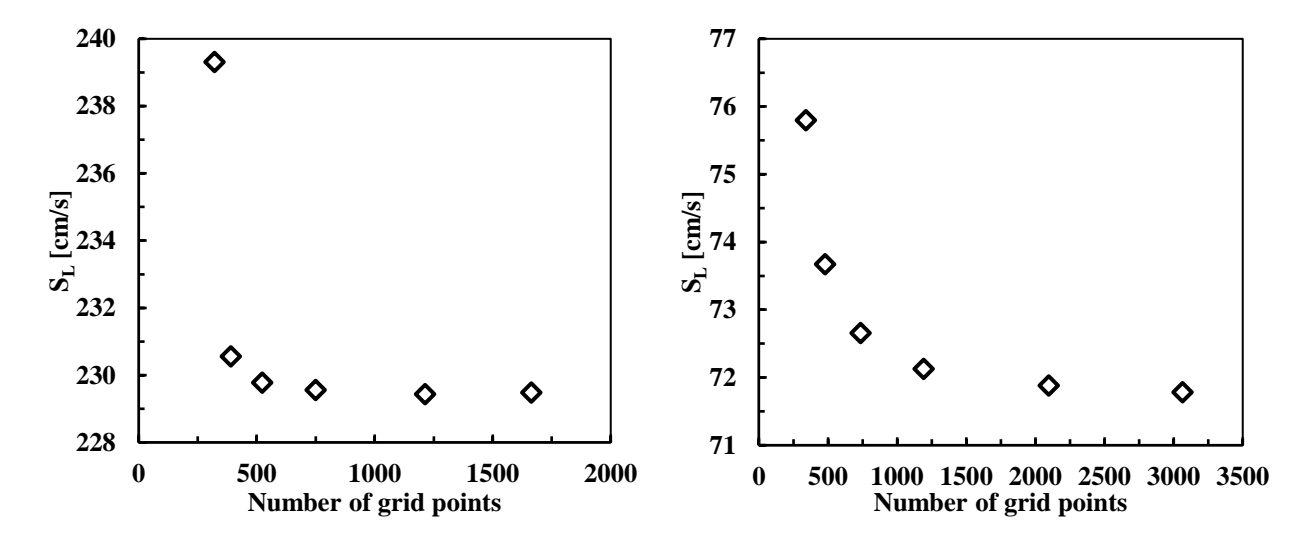


Figure 3-20. Mesh independency studies for the hydrogen/air mixture at 1 bar, 298 K and ϕ =1.0 (left) and the iso-octane/air mixture at 1 bar, 473 K and ϕ =1.0 (right).

Numerical simulations were also used to calculate the laminar flame thickness, adiabatic flame temperature, and expansion ratio. The widely used definition of δ_L , which comes from kinetic analysis, i.e. $\delta_L = \lambda/(\rho_u c_p S_L)$, was not used in the present study due to the arbitrariness of the temperature at which λ/c_p is assessed and the dependence on S_L [143]. Instead, the laminar flame

thickness was calculated with the gradient method [144], i.e. δ_L =(T_b - T_u)/(dT/dr)_m. Burned and unburned gas temperatures, as well as the maximum gradient of temperature, were obtained from the numerical temperature profile solution of a freely propagating flame configuration in Chemkin-Pro [215].

For modeling methane/air/diluent combustion, the GRI-Mech 3.0 [223], comprising 53 species and 325 reactions; USC Mech II [224], comprising 111 species and 784 reactions; San Diego [225], comprising 58 species and 270 reactions; HP-Mech [226], comprising 92 species and 615 reactions; NUI Galway-CH4/DME [227], comprising 113 species and 710 reactions; and AramcoMech 1.3 [228], comprising of 253 species and 1542 reactions, chemical mechanisms were utilized. The rate parameters of 325 reactions in the GRI-Mech 3.0 [223] has been optimized against laminar burning velocities of CH4/air mixtures at 1-20 bar and 300-400 K using experimental studies from Vagelopoulos et al. [229], Vagelopoulos et al. [230], and Egolfopoulos et al. [231]. The GRI-Mech 3.0 kinetic scheme [223] has been shown to have good agreement with the laminar burning velocities of H₂/air, CO/H₂/air, C₂H₄/air, C₂H₆/air, C₃H₈/air, and CH₃OH/air mixtures at a pressure of 1 bar and temperature of 300 K [223].

The USC Mech II kinetic model [224] was developed for high-temperature oxidation of H_2 , CO, and C_1 -C₄ hydrocarbons. The USC Mech II mechanism [224] has been tested against various H_2 /CO/ C_1 -C₄ laminar burning velocity data at 1-5 bar and 300 K [224]. The San Diego detailed kinetic scheme [225] has been tailored for high temperature flames of C_0 -C₄ hydrocarbons. Akram and Kumar [232], Park et al. [233], and Ren et al. [234] showed that the mechanism has good agreement with the experimental laminar flame speed data of methane/air mixtures at 1 bar and 298 K for ϕ <1.0. For rich mixtures, the San Diego mechanism [225] has been shown to underestimate the laminar burning velocity [232-234]. Akram and Kumar [232] also

tested the performance of the mechanism at 500 K for methane/air mixtures and concluded that the San Diego mechanism [225] provided faster laminar flame speeds relative to experimental results.

The HP-Mech [226] is a high-pressure mechanism for C₀-C₂ hydrocarbon fuels with exhaust gas dilution. It uses the elementary reaction rates determined by high level quantum computations and experimental results. The mechanism has shown good performance in the prediction of laminar flame speeds of C₀-C₂ fuels diluted with CO₂ and H₂O at 1-10 bar and flame temperatures between 1600 K and 1800 K [235]. The NUI Galway-CH₄/DME chemical mechanism [227] consists of the H₂/CO sub-mechanism of Kéromnès et al. [236], the C₁-C₂ base sub-mechanism of Metcalfe et al. [228], and the propene mechanism of Burke et al. [237]. The NUI Galway-CH₄/DME [227] has been optimized and validated against ignition delay time and flame speed measurements of methane, dimethylether, and their mixtures at 7-41 bar [227].

The AramcoMech 1.3 detailed kinetic mechanism [228] has been developed in a hierarchical fashion for the characterization of the kinetic and thermochemical properties of C₁-C₄ hydrocarbon fuels. The mechanism has been validated against laminar burning velocity data of methane/air mixtures at a temperature of 298 K and pressure within the range of 1-10 bar, ethane/air mixtures at 295-325 K and 1-5 bar, ethylene/air mixtures at 298-470 K and 1-5 bar, acetylene/air mixtures at 298 K and 1-2 bar, methanol/air mixtures at 298-358 K and 1 bar, and ethanol/air mixtures at 298-453 K and 1 bar [238].

For modeling iso-octane/air/diluent combustion, the chemical mechanisms of Chaos et al. [239], consisting of 107 species and 720 reactions; Kelley et al. [78], consisting of 112 species and 467 reactions; and Jerzembeck et al. [240], consisting of 99 species and 461 reactions, were used. The high temperature chemical kinetic model of Chaos et al. [239] has been developed for the

oxidation of primary reference fuels in a hierarchal manner on a baseline mechanism comprising H₂/O₂ kinetic model of Li et al. [241], C₁-C₄ kinetic model of Zhao et al. [242], and iso-octane oxidation model of Curran et al. [243]. The mechanism of Chaos et al. [239] has been shown to have good agreement with the laminar burning velocities of iso-octane/air mixtures at 1 bar and 298-353 K with a small discrepancy between the model and experimental data at rich conditions [78, 239].

Kelley et al. [78] reduced the original Lawrence Livermore detailed mechanism [243-245] to a skeletal kinetic scheme by comparing ignition delay time, extinction residence time of perfectly stirred reactor, and laminar burning velocity results of the Lawrence Livermore comprehensive mechanism [243-245] and the chemical mechanism of Kelley et al. [78] for iso-octane flames at 600-1800 K, 1-40 bar, and $\phi = 0.5$ -1.5. After testing the kinetic scheme of Kelley et al. [78] for iso-octane flames at 298-353 K and 1-10 bar, Kelley et al. [78] concluded that their chemical mechanism, and therefore the original Lawrence Livermore detailed mechanism [243-245], yields substantially higher laminar burning velocities. This finding can be attributed to the fact that the Lawrence Livermore comprehensive mechanism [243-245] has only been validated through comparison to ignition delay experiments in shock tubes and rapid compression machines.

The high temperature kinetic scheme of Jerzembeck et al. [240] is also based on the Lawrence Livermore comprehensive mechanism [243-245]. The poor performance of the original Lawrence Livermore detailed mechanism [243-245] on the prediction of the laminar flame speed was enhanced with the modification of reaction rates most sensitive to flame propagation, and the Lawrence Livermore comprehensive mechanism [243-245] was reduced to 461 reactions and 99 species. The high-temperature chemical mechanism of Jerzembeck et al. [240] provided laminar

burning velocity values close to experimental findings for iso-octane flames at 298-373 K and 1-25 bar with a notable underestimation at ϕ >1.0 and a slight overprediction at ϕ <1.0 [240].

For modeling hydrogen/air combustion, the chemical mechanisms of Li et al. [241], comprising 13 species and 25 reactions; Konnov [246], comprising 10 species and 33 reactions; and NUI Galway-H₂ [247], comprising 10 species and 21 reactions, were utilized. Li et al. [241] updated the H₂/O₂ kinetic model of Mueller et al. [248] based upon the new thermodynamic data and rate coefficients. Satisfactory agreement between experimental laminar flame speed findings and predictions of the chemical mechanism of Li et al. [241] was observed for H₂/O₂ mixtures with a bath gas of He at 298 K and 1-20 atm and H₂/O₂ mixtures with a bath gas of N₂ or Ar at 298 K and 1 atm.

Konnov [246] revised the H₂/O₂ chemical mechanism of Konnov [249] with reevaluated kinetic data for combustion modeling [250] and for atmospheric chemistry [251] to cover the modeling range of ignition experiments from 950 K to 2700 K and from subatmospheric pressures up to 87 atm; hydrogen oxidation in a flow reactor at temperatures around 900 K from 0.3 atm up to 15.7 atm; flame burning velocities in hydrogen/oxygen/inert mixtures from 0.35 atm up to 4 atm; and hydrogen flame structure at 1 atm and 10 atm. The kinetic mechanism of Konnov [246] provided burning velocities similar to the experimental data for hydrogen/air mixtures at standard temperature and pressure.

Like the chemical mechanism of Li et al. [241], the NUI Galway-H₂ mechanism [247] is also based on the H₂/O₂ kinetic model of Mueller et al. [248]. Conaire et al. [247] modified the kinetic parameters of the model of Mueller et al. [248] so that NUI Galway-H₂ detailed kinetic mechanism [247] can achieve better overall agreement with experimental ignition delay times, flame speeds, and species composition data at the temperature ranged from 298 K to 2700 K, the

pressure from 0.05 atm to 87 atm, and the equivalence ratios from 0.2 to 6.0. The NUI Galway- H_2 mechanism [247] has been validated against H_2/O_2 /air flame speeds at 298 K and 1 atm and H_2/O_2 /He mass burning velocities at 298 K and 1-20 atm.

For modeling propane/air combustion, the USC Mech II chemical mechanism [224], consisting of 111 species and 784 reactions; the San Diego chemical mechanism [225], consisting of 58 species and 270 reactions; and the detailed propane/air kinetic mechanism proposed by Qin et al. [252], consisting of 70 species and 463 reactions, were used. The USC Mech II [224] is based on the H₂/CO kinetic model of Davis et al. [253], the comprehensive ethylene and acetylene reaction models of Wang et al. [254], the C₃ kinetic model of Davis et al. [255], the high temperature 1,3-butadiene kinetic model of Laskin et al. [256], and the GRI-Mech 3.0 kinetic scheme [223]. After the update of several reaction rate parameters, the USC Mech II [224] was validated against various H₂/CO/C₁-C₄ laminar burning velocity data at 1-5 bar and 300 K. Compared to experimental propane laminar flame speeds of Vagelopoulos et al. [229] and Vagelopoulos and Egolfopoulos [230] at 1 atm and 300 K, the USC Mech II [224] provided slightly slower burning velocities for propane rich flames [224].

The San Diego kinetic scheme [225] has been developed with the philosophy of minimizing the number of species and reactions for the scope of combustion rather than being chemically complete. Bramlette and Depcik [257] showed that, among 35 most commonly used propane/air chemical kinetic mechanisms, the detailed San Diego mechanism [225] best matched the experimental ignition delay data across a wide range of initial temperatures and equivalence ratios.

The detailed C_1 - C_3 combustion model of Qin et al. [252] is based on the GRI-Mech 3.0 kinetic scheme [223] for the $C_{<3}$ components and the C_3 kinetic models of Davis and coworkers

[255, 258-259] for the C_3 components. The combined mechanism was optimized for ignition delays and flame speeds of $C_{\leq 3}$ fuels at atmospheric pressure. Laminar burning velocities predicted by the kinetic scheme of Qin et al. [252] for methane, ethylene, ethane, propyne, propene, and propane flames at 1 bar and 298 K showed to have good agreement with experimental findings [252]. Moreover, Akram et al. [260] demonstrated that the chemical mechanism of Qin et al. [252] can accurately predict propane laminar flame speeds at 1 bar and 300-650 K.

3.8 Validation of Experimental Apparatus

For most engineering experiments, three types of errors are considered, namely systematic errors, random errors, and "variable but deterministic" errors [261]. Apart from the uncertainty in initial conditions, the accuracy of laminar burning velocity calculations in the constant pressure method depends on errors in the expansion ratio (ρ_b/ρ_u), cold flame front radius (R_f), and extrapolation of stretch models. In the present study, expansion ratios were calculated using the Chemkin-Pro software [215]. The cold flame front radius was obtained with a z-type schlieren system [205] and an in-house image processing code. The inaccuracies due to the extrapolation of stretch models were minimized with the critical lower radius limit approach, which is explained in 3.6.1 Assessment of Accuracies of Stretch Extrapolation Methods in detail and shown in Figure 3-21. Therefore, the accurate prediction of systematic and "variable but deterministic" errors in the S_L and L_b is not possible and the total uncertainty in the calculation of the S_L and L_b was defined as the random uncertainty.

For the validation of experimental apparatus and procedure, five measurements were performed for each initial condition. The random uncertainty for the S_L and L_b was calculated with the t-distribution method developed by William Sealy Gosset in 1908. In the absence of an outlier, the number of degrees of freedom was four. The confidence level for the Student's t-distribution

was set to be 95%, which yielded a two-sided significance level of 0.01 for four degrees of freedom. The critical value of the Student's t-distribution was computed with the cumulative distribution function for a significance level of 0.01.

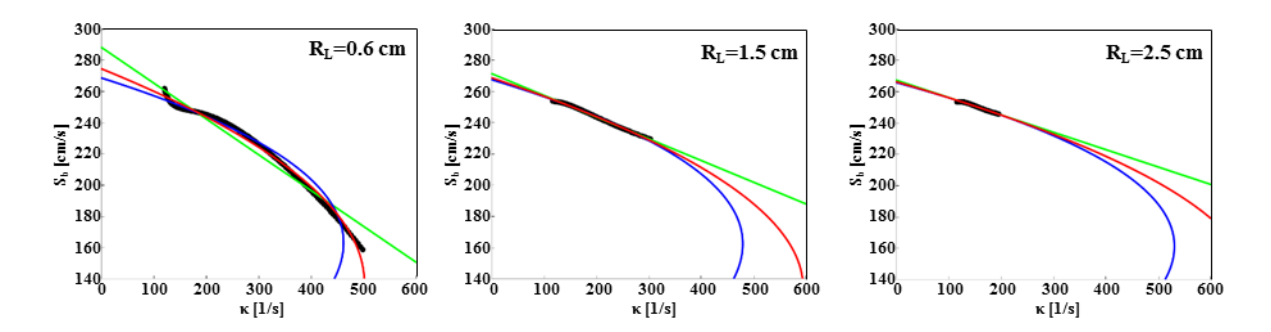


Figure 3-21. Extrapolation of stretch models for different lower radius limits for laminar flame speed calculations of iso-octane/air mixture at 1 bar, 373 K, and ϕ =0.9 (black dots - experimental data, green line - the LS model [149], blue line - the NQ model [140], red line - the LC model [148]).

The two-sided Grubbs' test [262-263], also known as the maximum normed residual test, was used to detect outliers. The critical value for the test was calculated for the critical value of the t-distribution. The null hypothesis (no outlier) was rejected and the outlier was discarded if the Grubbs' test statistic of a test result was greater than the Grubbs' test critical value. Subsequently, the two-sided Grubbs' test was repeated with updated degrees of freedom until no outlier was observed since the test can be used to identify the presence of only one outlier. In the current study, no more than one outlier was observed for any test point. Finally, the random uncertainty, and therefore the total uncertainty, was determined with multiplying the critical t-distribution value by the standard deviation and dividing this multiplication by the square root of the number of measurements. The uncertainty in the S_L and L_b is shown as error bars in the following plots.

Measured S_L and L_b values of methane/air flames at 1 bar and 298 K, hydrogen/air flames at 1 bar and 298 K, propane/air flames at 1 bar and 298 K, and iso-octane/air flames at 1 bar and 373 K were compared with numerical results obtained from several chemical mechanisms as well

as experimental data from the literature. Due to noteworthy advancement in laminar flame speed calculations in last 20 years, attention was focused on experimental studies that were published after 2000. All measured S_L and L_b values with experimental uncertainties and numerical S_L results predicted by several chemical mechanisms are provided in Appendix J.

A summary of S_L and L_b results from the current work for methane/air flames at 1 bar and 298 K is plotted in Figure 3-22 with experimental findings of Bosschaart and de Goey [54], Liao et al. [88], Tahtouh et al. [90], and Varea et al. [99] and simulation results using the GRI-Mech 3.0 [223], USC Mech II [224], and San Diego [225] mechanisms over a range of equivalence ratios. Bosschaart and de Goey [54] used a heat flux burner to obtain the flame speed. While Liao et al. [88] and Tahtouh et al. [90] employed spherically expanding flames with the constant pressure method, Varea et al. [99] measured the laminar burning velocity with the PIV approach. Experimental results in Figure 3-22 show good agreement with each other, but current S_L values are slightly faster than experimental findings of Bosschaart and de Goey [54] and Tahtouh et al. [90] generally. The results of Liao et al. [88] are slightly faster than other S_L results in Figure 3-22 for ϕ =0.9-1.2. Varea et al. [99] provided appreciably slower burning velocities for methane/air mixtures with ϕ ≥1.1.

Excellent agreement was observed between the L_b results of Varea et al. [99] and the current work except at ϕ =0.7, where the L_b value of Varea et al. [99] is significantly smaller than other L_b results shown in Figure 3-22. Tahtouh et al. [90] provided similar L_b s to the experimental data for ϕ ≤1.0, but the L_b values of Tahtouh et al. [50] are higher than the present data for rich methane/air flames, especially at ϕ =1.3. Burned gas Markstein lengths reported by Liao et al. [88] are generally greater than the L_b s found in this study.

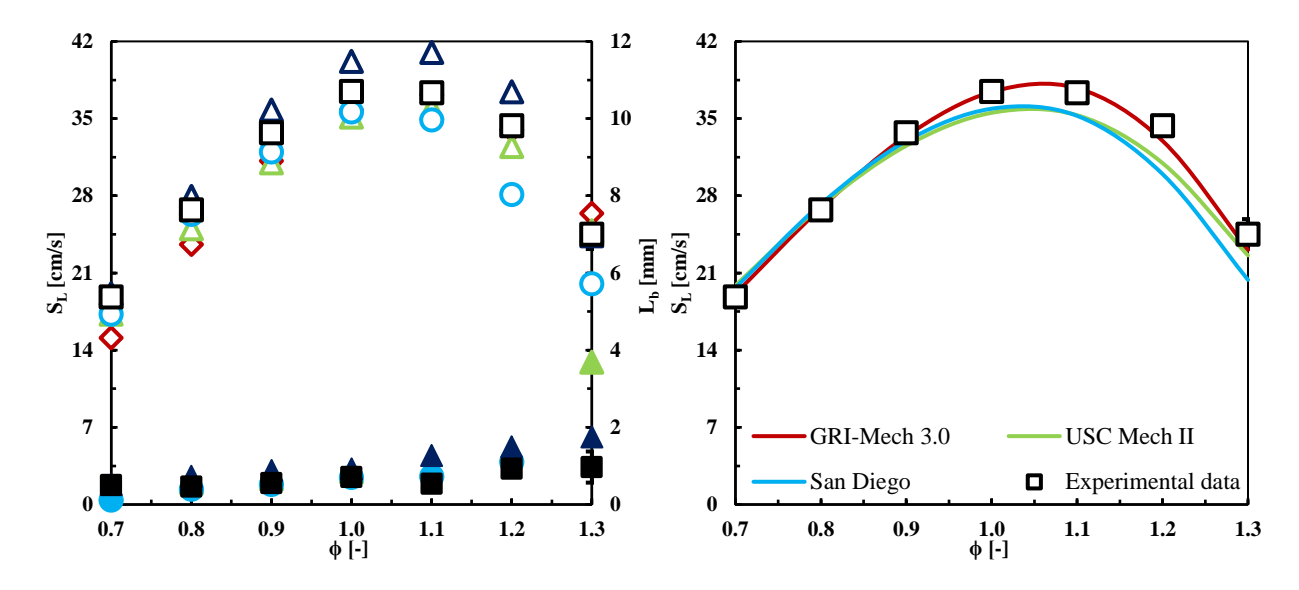


Figure 3-22. Comparison of the experimental and numerical laminar flame speeds and experimental burned gas Markstein lengths of methane/air mixtures at 1 bar and 298 K from the current work with previously published experimental data. (black squares - present data, red diamonds - Bosschaart and de Goey [54], dark blue triangles - Liao et al. [88], light green triangles - Tahtouh et al. [90], light blue circles - Varea et al. [99], unfilled markers - S_L, and filled markers - L_b)

The numerical data predicted by the GRI-Mech 3.0 mechanism [223] and the experimental results from the current work showed excellent agreement over the entire range of equivalence ratio. The USC Mech II [224] and San Diego [225] kinetic schemes showed a similar trend with the GRI-Mech 3.0 [223] for $\phi \le 0.9$. However, the San Diego mechanism [225] predicted slower laminar burning velocities at $\phi > 0.9$ than experimental results and the GRI-Mech 3.0 [223] findings. Akram and Kumar [232], Park et al. [233], and Ren et al. [234] made similar observations. As shown in Figure 3-22, numerical S_L data computed with the USC Mech II [224] are also slightly slower than experimental results at $0.9 < \phi < 1.3$.

S_L and L_b values of hydrogen/air mixtures at 1 bar and 298 K from the current study are plotted against experimental results of Dong et al. [264], Pareja et al. [265], Kuznetsov et al. [116], and Krejci et al. [171] and numerical results obtained with chemical mechanisms of Li et al. [241], Konnov [246], and the NUI Galway-H₂ [247] in Figure 3-23. Kuznetsov et al. [116] and Krejci et

al. [171] deduced the laminar burning velocity from spherically expanding flames at constant pressure while Dong et al. [264] and Pareja et al. [265] used a Bunsen burner to measure hydrogen flame speeds.

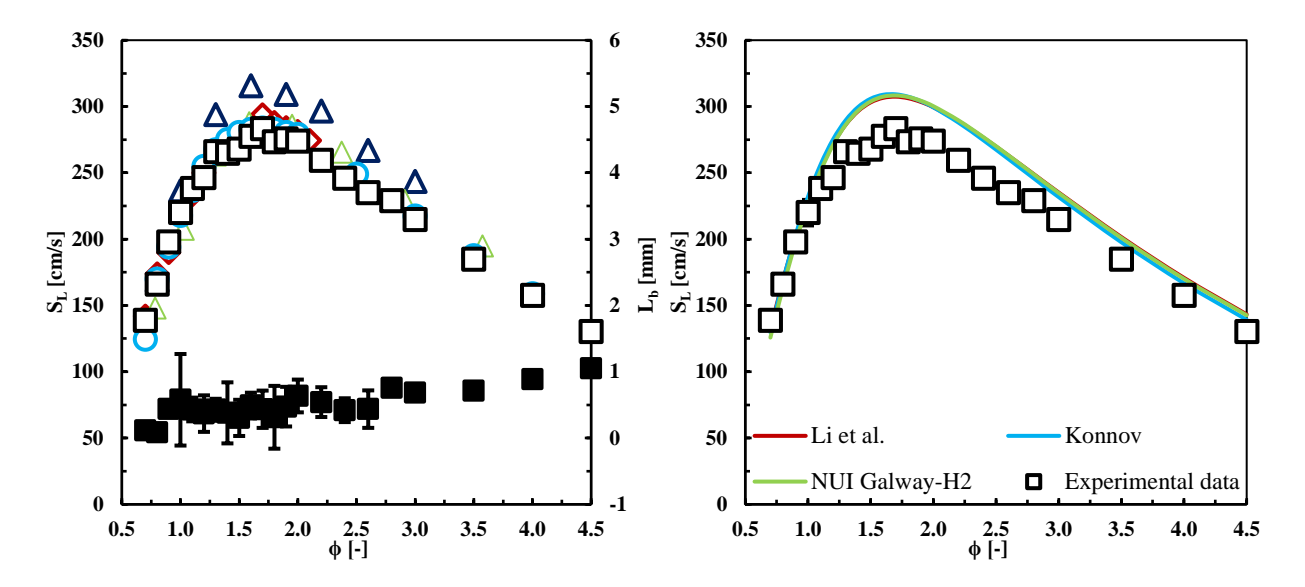


Figure 3-23. Comparison of the experimental and numerical laminar flame speeds and experimental burned gas Markstein lengths of hydrogen/air mixtures at 1 bar and 298 K from the current study with previously published experimental data. (black squares - present data, red diamonds - Dong et al. [264], dark blue triangles - Pareja et al. [265], light green triangles - Kuznetsov et al. [116], light blue circles - Krejci et al. [171], unfilled markers - S_L, and filled markers - L_b)

Findings of Dong et al. [264], Kuznetsov et al. [116], and Krejci et al. [171] are generally consistent with the S_L data from the current work. However, flame speeds obtained by the Bunsen burner studies of Pareja et al. [265] are consistently faster than other results in Figure 3-23 at ϕ =1.0-3.0. Numerical hydrogen/air flame speeds predicted by chemical mechanisms of Li et al. [241], Konnov [246], and the NUI Galway-H₂ [247] are very close to each other over the entire range of equivalence ratio and agree with current experimental findings for ϕ <1.0. Nevertheless, these mechanisms provided faster laminar burning velocities than experimental data for fuel rich hydrogen air flames.

Figure 3-24 presents S_L and L_b values of propane/air flames at 1 bar and 298 K from the current study together with experimental findings of Zhao et al. [266], Dirrenberger et al. [267], Lowry et al. [92], and Miao et al. [268] at 1 bar and 298-300 K and simulation results using the USC Mech II chemical mechanism [224], the San Diego kinetic scheme [225], and the detailed propane/air kinetic mechanism proposed by Qin et al. [252]. Zhao et al. [266] utilized a stagnation jet-wall flame configuration. Dirrenberger et al. [267] performed the measurements in a flat flame adiabatic burner with the heat flux method. Lowry et al. [92] and Miao et al. [268] extracted the S_L values from spherically expanding flames at constant pressure.

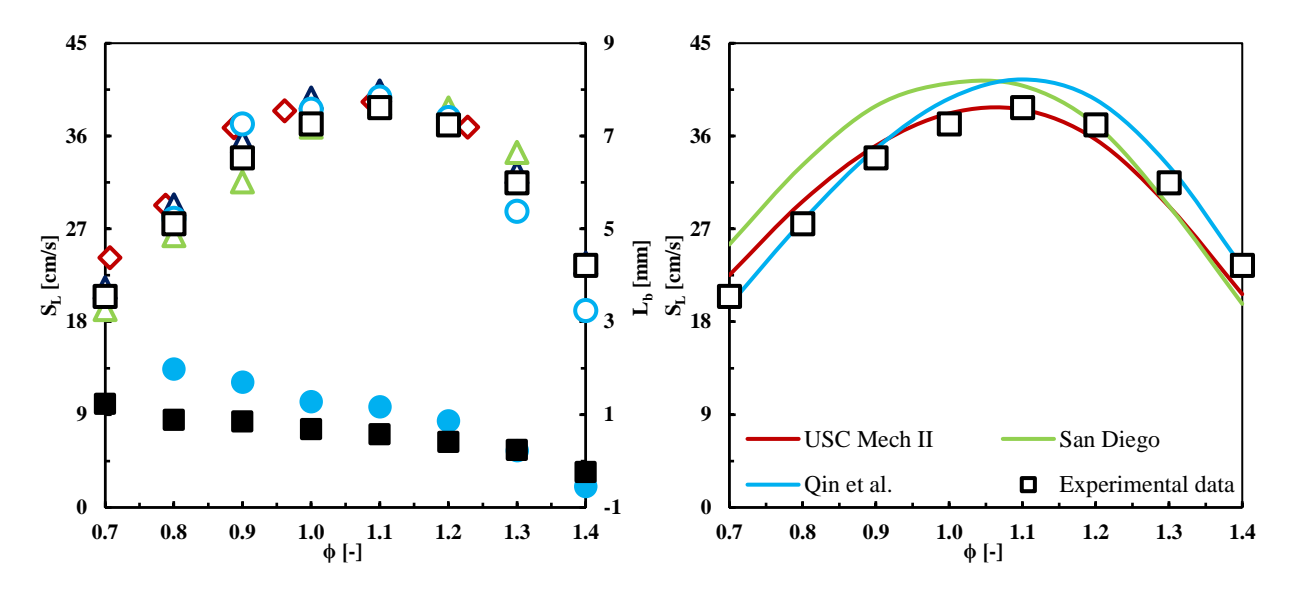


Figure 3-24. Comparison of the experimental and numerical laminar flame speeds and experimental burned gas Markstein lengths of propane/air mixtures at 1 bar and 298 K from the current study with previously published experimental data. (black squares - present data, red diamonds - Zhao et al. [266], dark blue triangles - Dirrenberger et al. [267], light green triangles - Lowry et al. [92], light blue circles - Miao et al. [268], unfilled markers - S_L, and filled markers - L_b)

The general trend of the current data is consistent with the results of former studies although previously published results are slightly scattered. S_L values of Dirrenberger et al. [267] and Miao et al. [268] are slightly higher than the current S_L around stoichiometry. Experimental flame speeds obtained by Miao et al. [268] are slower than the current findings at $\phi \ge 1.3$. Zhao et

al. [266] reported slightly faster burning velocities than the present data for lean propane/air mixtures.

As shown in Figure 3-24, the L_b evolution of propane flames with respect to ϕ is different than those of methane and hydrogen flames, i.e. L_b decreases with increasing ϕ . The L_b values found by Miao et al. [268] are consistently higher than the present data for $\phi \leq 1.2$. At lean and rich conditions, current experimental S_L data match best with numerical results obtained with the chemical mechanism of Qin et al. [252]. Around stoichiometry, the USC Mech II [224] predictions are closest to experimental findings. The San Diego detailed kinetic scheme [225] is unable to capture the general trend of the current experimental results.

Lastly, Figure 3-25 shows a summary of laminar burning velocity results from the current work for iso-octane/air flames at 1 bar and 373 K compared to experimental data of Galmiche et al. [85], Varea et al. [99], Endouard et al. [269], and Hu et al. [270] and numerical results predicted by chemical mechanisms of Chaos et al. [239], Kelley et al. [78], and Jerzembeck et al. [240] over a range of equivalence ratios. While Galmiche et al. [85], Endouard et al. [269], and Hu et al. [270] calculated the S_L with the constant pressure method, Varea et al. [99] utilized the PIV approach. Current iso-octane flame speeds are similar to those of other researchers in Figure 3-25 for $\phi \le 1.0$. However, at rich conditions, findings of Galmiche et al. [85] are consistently slower than others. Similarly, flame speeds obtained by Varea et al. [99] were lower than the present data for $\phi = 1.3$ -1.4.

The L_b trend of iso-octane flames with respect to ϕ is similar to that of propane/air, i.e. L_b decreases with increasing ϕ . L_b values from the present study are consistent with experimental findings of other researchers [85, 99, 270] in Figure 3-25 for ϕ =0.9-1.3. At ϕ =0.8, the L_b value of

Hu et al. [270] is much larger than the findings from the other studies. At ϕ =1.4, L_b values of Galmiche et al. [85] and Varea et al. [99] are smaller than the current data.

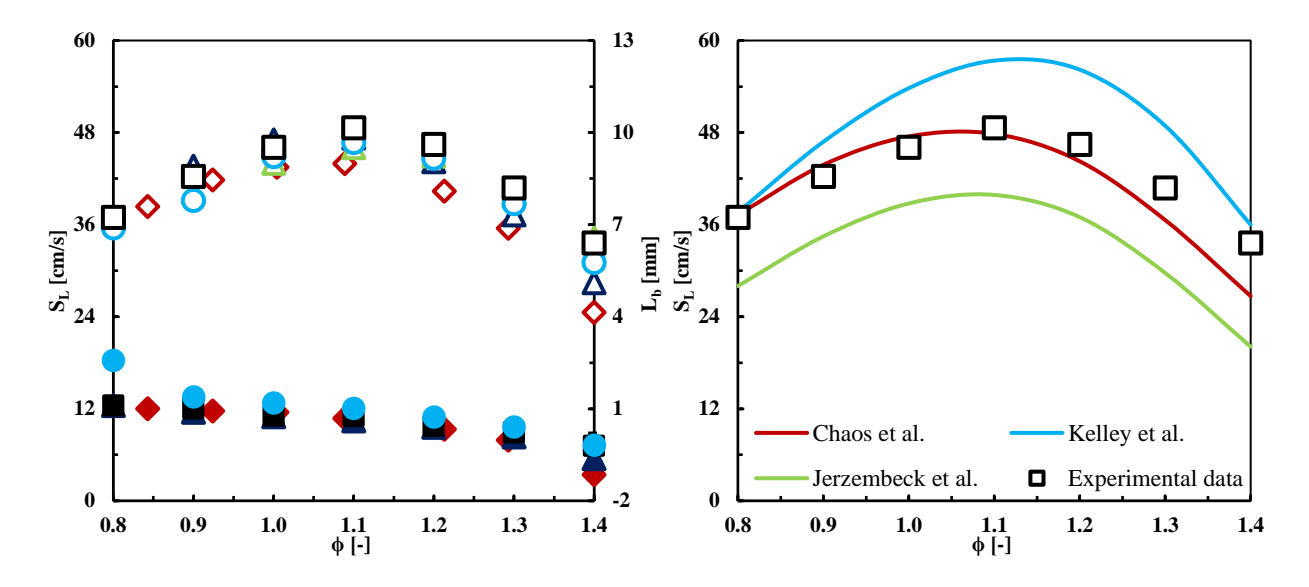


Figure 3-25. Comparison of the experimental and numerical laminar flame speeds and experimental burned gas Markstein lengths of iso-octane/air mixtures at 1 bar and 373 K from the current work with previously published experimental data. (black squares - present data, red diamonds - Galmiche et al. [85], dark blue triangles - Varea et al. [99], light green triangles - Endouard et al. [269], light blue circles - Hu et al. [270], unfilled markers - S_L, and filled markers - L_b)

Figure 3-25 shows that the general trend of the experimental findings is best captured with the chemical mechanism of Chaos et al. [239] with an underestimation of the S_L values for $\phi>1.2$. Chaos et al. [239] and Kelley et al. [78] also concluded that this mechanism provided slower S_L values for rich iso-octane flames compared to experimental data at 1-10 bar and 298-353 K. The kinetic scheme of Kelley et al. [78], and therefore the original Lawrence Livermore detailed mechanism [243-245], provides substantially higher laminar burning velocities except for equivalence ratios of 0.8 and 1.4. Kelley et al. [78] also observed that the kinetic scheme of Kelley et al. [78] significantly overpredicted S_L values of iso-octane at 298-353 K and 1-10 bar. Jerzembeck et al. [240] suggested that the laminar flame speeds predicted by their high temperature kinetic scheme are in good agreement with the experimental data for iso-octane flames at 298-373

K and 1-25 bar with a notable underestimation at ϕ >1.0 and a slight overestimation at ϕ <1.0. However, Figure 3-25 shows the high-temperature chemical mechanism of Jerzembeck et al. [240] underpredicts the laminar burning velocities for iso-octane/air mixtures at 1 bar and 373 K.

4 THE EXHAUST GAS RECIRCULATION EFFECT ON FUNDAMENTAL CHARACTERISTICS OF PREMIXED ISO-OCTANE/AIR AND GASOLINE/AIR FLAMES

4.1 Introduction and Literature Review

The laminar burning velocity is an essential universal parameter of a combustible mixture and enables the prediction of other fundamental combustion features [12]. Due to the proven correlation between engine performance, knocking, and fuel burning velocity, fuels with faster flame speeds can result in better combustion phasing, which yields more efficient energy transfer and improved engine acceleration and performance with decreased knock tendency [271]. Therefore, laminar flame speeds of common components of gasoline surrogate fuel blends, such as isooctane and n-heptane, have been extensively investigated both experimentally and numerically.

One of the earliest studies on laminar burning velocity of iso-octane was published by Gulder [69] who conducted experiments in an optically inaccessible combustion bomb and deduced laminar flame speed data for iso-octane/air mixtures with the constant volume method over the range of 1-8 bar and 300-500 K. Subsequently, Bradley et al. [138] employed the constant pressure method with Schlieren imaging to measure the laminar burning velocities of iso-octane/air mixtures at 1-10 bar and 358-450 K for the equivalence ratios of 0.8 and 1.0.

Since the turn of the century, laminar flame speed measurements of iso-octane have received increased attention. Kwon et al. [77] and Huang et al. [272] focused on experiments at room temperature, with Kwon et al. [77] investigating pressures between 0.5-2.0 bar using the constant pressure method and Huang et al. [272] using a counter-flow configuration at 1 bar. Kumar et al. [273] and Kelley et al. [78] also employed the counter-flame technique for premixed

iso-octane/air mixtures at 1 bar and 298-470 K. Kelley et al. [78] completed additional experiments at 353 K using the spherically expanding flame approach and noted that the counter-flame technique and constant pressure method agreed well.

There are several other studies on laminar burning velocities of iso-octane/air mixtures at 1 bar, which were conducted by Broustail et al.[79] and Li et al. [23] using the constant pressure method at 393 K, van Lipzig et al. [274] using the heat flux method at 298 and 338 K, Sileghem et al. [275] using the heat flux method at 298 and 358 K, Zhang et al. [80] using the constant pressure method at 353 and 433 K, Dirrenberger et al. [276] using the heat flux method at 298, 358, and 398 K, Baloo et al. [81] using the constant pressure method at 363 K, Li et al. [82] using the constant pressure method at 363 K, and Liao and Roberts [15] using the flat flame method at 298-400 K. Recently, Mannaa et al. [83] measured laminar flame speeds of iso-octane/air mixtures up to 6 bar at 358 K with an optically accessible constant-volume spherical vessel.

On the other hand, studies focusing on commercial gasoline are rare. One of the earliest studies on the laminar flame speed of gasoline was conducted by Stanglmaier et al. [277] who measured the S_L values of gasoline flames at 15-25 bar and 550-800 K. Jerzembeck et al. [240] calculated laminar burning velocities of gasoline from spherically expanding flames at 10-25 bar and 373 K. Sileghem et al. [275] and Dirrenberger et al. [276] investigated the laminar flame speed of a commercial gasoline at 1 bar and 298-358 K using a heat flux method. Mannaa et al. [83] extracted laminar burning velocities of high to low research octane number (RON) gasoline fuels up to 6 bar at 358 K from spherically expanding flames.

In an effort to reduce NO_x emissions as well as fuel consumption in internal combustion engines, exhaust gas recirculation (EGR) is commonly used to lower temperatures during combustion while keeping stoichiometry constant, which allows a three-way catalyst to be used.

The introduction of exhaust gases into an engine diminishes the partial-load pumping losses while improving the full-load knock resistance [23]. Nevertheless, exhaust gas recirculation also has an influence on the mixture reactivity and, as a result, the combustion stability [10]. Thus, the interest in the laminar burning velocity of primary reference fuels diluted with post-combustion products has increased.

Metghalchi et al. [70] conducted one of the first studies on this topic and measured the laminar flame speeds of iso-octane/air mixtures at 0.4-50 bar and 298-700 K. In this study, Metghalchi et al. [70] investigated the effect of the combustion products on the laminar burning velocity of a stoichiometric mixture with diluent mass fractions from 0% to 20%. It should be noted that Metghalchi et al. [70] utilized the constant volume method for these experiments and did not have optical access to observe cellular formations and instead assumed that wrinkling did not increase the flame area or decrease the burning velocity by more than a few percent.

More recently, Halter et al. [10] published a study on the effect of N₂, CO₂ and their mixtures on the laminar burning velocities of iso-octane/air mixtures at 1 bar and 300 K using the constant pressure method. With schlieren-aided constant-volume spherical flame measurements, Marshall et al. [17] calculated the S_L values for iso-octane, n-heptane, toluene, ethylbenzene, and ethanol diluted with 0-30% combustion residuals at 310-450 K and 0.5-4 bar. Zhou et al. [84] studied how diluting air with up to 28% volume fraction of CO₂ affected the S_L of iso-octane at 373 K and 1 bar. Subsequently, Galmiche et al. [85] investigated spherically expanding N₂ diluted iso-octane flames at 1-10 bar and 323-473 K with 5% to 25% dilution volume fractions.

Experimental studies focusing on the effect of dilution on the laminar burning velocity of commercial gasoline/air mixtures are rarer. Zhao et al. [278] studied N₂ diluted gasoline/air flames at 1 bar and 353-500 K with up to a 30% dilution ratio. Jerzembeck et al. [279] employed the

spherically expanding flames under a constant pressure approach to understand how laminar burning velocities of standard gasoline at 10-25 bar and 373 K are affected by N_2 dilution. Lastly, Bhattacharya et al. [280] measured the laminar flame speeds of gasoline/air mixtures diluted with N_2 at 423 K and 1 bar with a heat flux burner.

As legislation stemming from environmental concerns requires stricter emissions standards and more efficient operating conditions in internal combustion engines, predicting laminar burning velocities at high temperatures and dilution rates is becoming more and more important. Exhaust gas recirculation is one of the primary methods used by automakers to achieve these emissions standards, but the addition of exhaust gases affects thermodynamic properties and chemical reactivities during combustion [281]. Studies focusing on the impacts of exhaust gases on the laminar burning velocities of commercial gasoline and components of gasoline surrogate fuel blends at high temperatures are scarce. Thus, the CO₂ dilution effect (a major component of exhaust gases) on the S_L and L_b of iso-octane/air and high/low RON gasoline/air mixtures at 1 bar and 373-473 K was examined with 0-15% CO₂ dilution.

Three experiments were conducted to get the dataset of one test point. The uncertainty of the experimental data, which is shown as error bars in the following figures, was defined as the random uncertainty. The dilution ratio is specified as the concentration of CO₂ by mass within the oxidizer. A custom gas mixture with mole percentages of 10.41% CO₂ + 18.81% O₂ + 70.78% N₂ was used for 15% CO₂ dilution tests rather than mixing CO₂ with air in a mixing tank in order to minimize the uncertainty in the dilution ratio. At the experimental test conditions, numerical analyses were conducted with the Chemkin-Pro software [215] using the chemical mechanisms of Chaos et al. [239], Kelley et al. [78], and Jerzembeck et al. [240] to assess the accuracies of the

mechanisms for iso-octane/air mixtures. Numerical analyses were also utilized to quantify the dilution, thermal-diffusion, and chemical effects of CO_2 on the S_L .

4.2 High Temperature Tests

High temperature tests of iso-octane/air and high/low RON gasoline/air mixtures were completed at 373-473 K and 1 bar. The S_L data with random error bars are shown in Figure 4-1. At 373 K and 1 bar, high and low RON gasolines have almost the same S_L for ϕ =1.0-1.1 while laminar flame speeds of iso-octane/air mixtures are slightly slower. The laminar burning velocities of low RON gasoline flames are 2.39 cm/s lower and 4.29 cm/s higher than the S_L values of high RON gasoline at 1 bar, 373 K, and equivalence ratios of 0.85 and 1.3, respectively. Iso-octane has even slower laminar burning velocities at 373 K, 1 bar, and equivalence ratios of 0.85-1.30, so the difference between the laminar flame speeds of iso-octane and commercial gasoline flames can be as high as 9.44%.

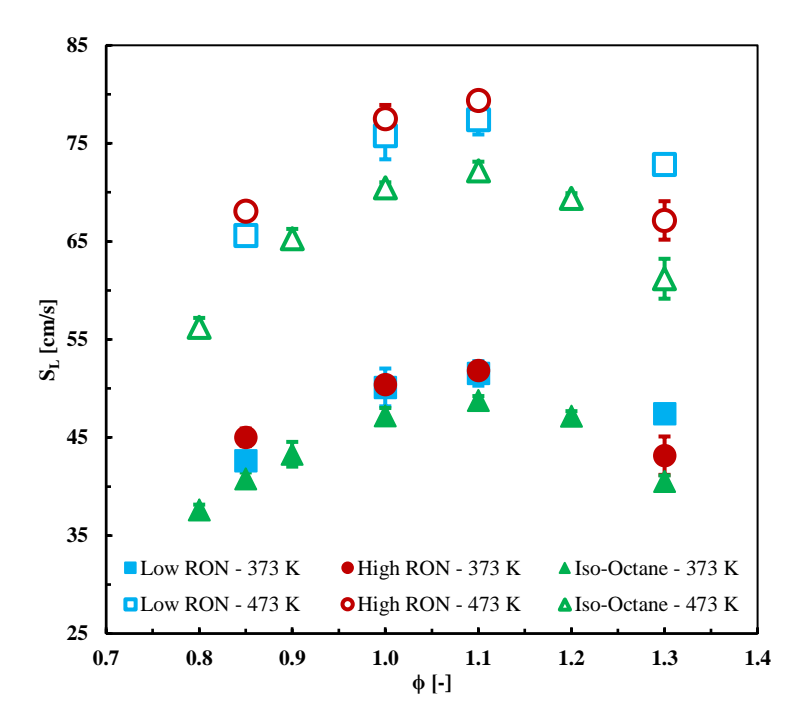


Figure 4-1. Laminar burning velocities of iso-octane/air and high/low RON gasoline/air mixtures at 1 bar and 373-473 K.

The temperature increase by 100 K resulted in a 51-56%, 50-54%, and 48-51% increases in S_L values of high RON gasoline, low RON gasoline, and iso-octane, respectively, over equivalence ratios of 0.85-1.30. The main causes for the increase in the S_L include enhanced dissociation reactions and the higher burned to unburned gas density ratio [85]. High temperatures improved the dissociation reaction rates, which are responsible for increased production of radicals, which initiate combustion reactions [85]. The increase in the initial temperature lowered the unburned gas density more than the decrease in the burned gas density due to the higher combustion temperature. As a result, the ratio of the burned to unburned gas density increased at higher temperatures.

Since high and low RON gasolines experienced similar increases in the laminar burning velocity due to the change in the initial temperature, the general trends in S_L values of both commercial gasolines remained the same. While laminar burning velocities of high and low RON gasolines are very close at ϕ =1.0-1.1, the high RON gasoline has 2.47 cm/s higher and 5.70 cm/s lower laminar burning velocity than the low RON gasoline at 1 bar, 473 K, and ϕ =0.85 and 1.30, respectively. On the other hand, the increase in the laminar burning velocities of iso-octane flames due to the temperature increase by 100 K was less than those for the high and low RON gasolines. Consequently, the difference between the laminar flame speeds of iso-octane and commercial gasoline flames increased at 473 K. The maximum difference in the S_L that was achieved between iso-octane and low RON gasoline was 11.65 cm/s at ϕ =1.3.

Markstein length is an essential indicator of flame stretch and stability [68], and mildly stretched unstable flames have small L_b values [21]. Thus, according to Figure 4-2, iso-octane/air and high/low RON gasoline/air flames get less stable and less prone to the flame stretch at 373 K and 1 bar with increasing ϕ . In fact, earlier onset of the preferential cellularity for very rich iso-

octane flames, L_b of which is less than zero, can be observed in Figure 4-3. As seen in Figure 4-2, burned gas Markstein lengths of high and low RON gasolines are almost the same for ϕ <1.3 while low RON gasoline is slightly more stable than high RON gasoline at ϕ =1.3. Iso-octane/air flames have slightly higher burned gas Markstein lengths than the two commercial gasolines at 1 bar, 373 K, and ϕ <1.1, which suggests that iso-octane is more stable but at the same time more vulnerable to flame stretch at these conditions. However, for ϕ ≥1.1, iso-octane has burned gas Markstein lengths very close to those of the two commercial gasolines.

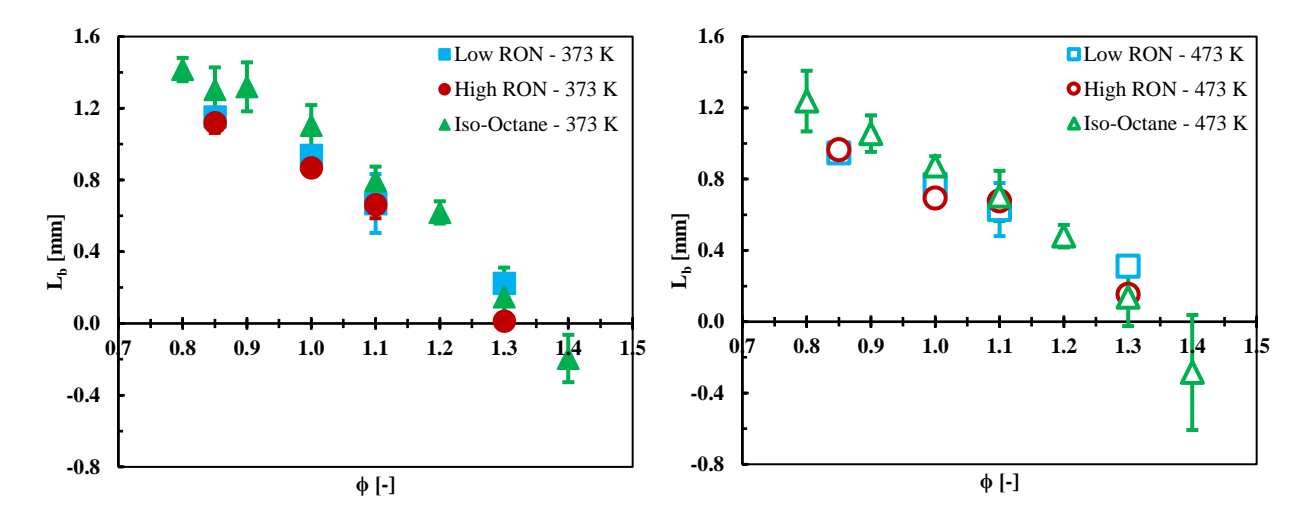


Figure 4-2. Burned gas Markstein lengths for iso-octane/air and high/low RON gasoline/air mixtures at 1 bar and 373-473 K.

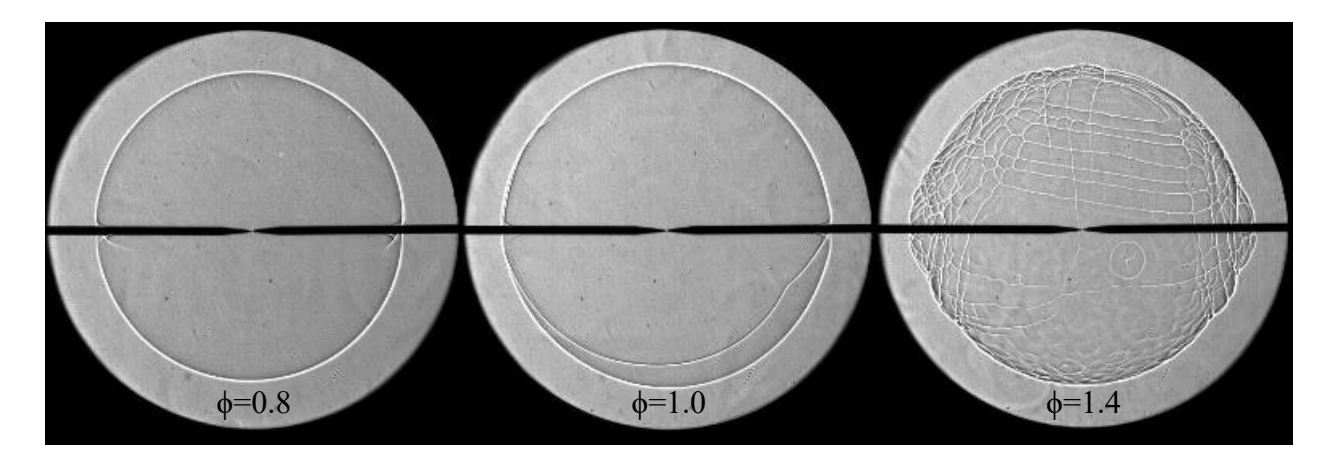


Figure 4-3. Schlieren images of iso-octane/air flames at 1 bar and 373 K.

Shown in Figure 4-2, the initial temperature increase by 100 K does not change the burned gas Markstein lengths of iso-octane/air and high/low RON gasoline/air flames considerably. Burned gas Markstein lengths slightly decrease for $\phi \le 1.0$ and remain almost the same for $\phi > 1.0$ with the 100 K increase in initial temperature. Therefore, it can be concluded that the stability of lean iso-octane/air and high/low RON gasoline/air flames deteriorates slightly while there is almost no change in the flame stability of rich mixtures with increasing temperature. Similar to the 373 K case, high and low RON gasolines have almost the same burned gas Markstein lengths for $\phi < 1.3$, and the burned gas Markstein length of low RON gasoline is slightly higher than that of high RON gasoline for $\phi = 1.3$ at 473 K and 1 bar. L_b values of iso-octane/air flames are consistently higher than those of the high/low RON gasolines for $\phi < 1.0$, whereas the flame stability characteristics of iso-octane are very similar to those of the two commercial gasolines for $\phi \ge 1.0$.

4.3 Numerical Results

Numerical analyses were performed with the Chemkin-Pro software [215] using the chemical mechanisms of Chaos et al. [239], Kelley et al. [78], and Jerzembeck et al. [240] in order to assess the accuracies of the mechanisms for iso-octane flames at the experimentally investigated conditions. Figure 4-4 shows that the general trends of the experimental findings at 373 and 473 K are best captured with the first mechanism with a slight underestimation of the S_L values for ϕ >1.2. The maximum deviation between the kinetic scheme of Chaos et al. [239] and the experimental results is observed as 6.93 cm/s at 373 K and ϕ = 1.4. Chaos et al. [239] and Kelley et al. [78] also noticed similar discrepancies between the model and experimental data and concluded that this mechanism provided slower S_L values for rich iso-octane flames compared to experimental findings at 1-10 bar and 298-353 K.

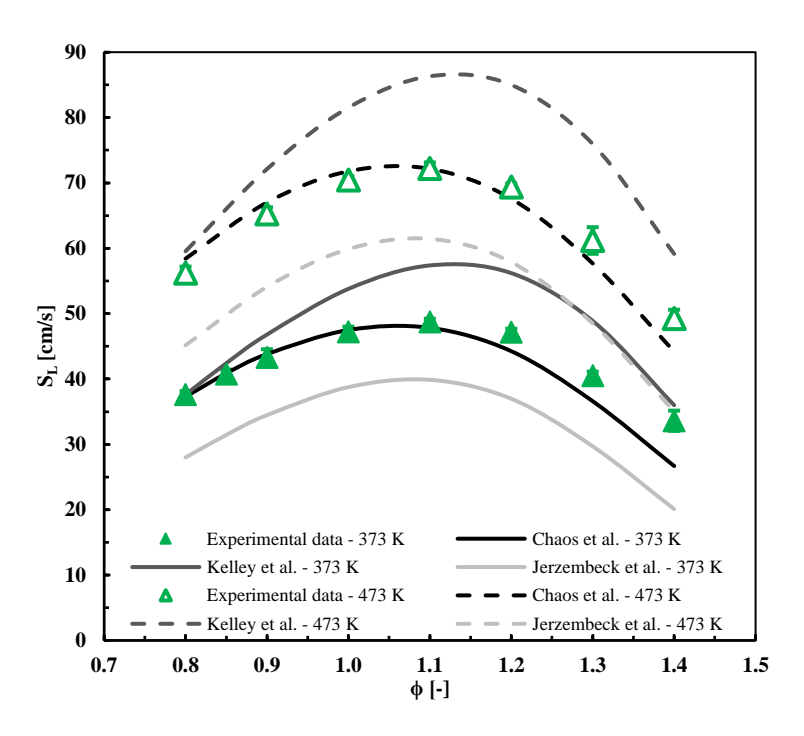


Figure 4-4. Experimental (points) and numerical (lines) laminar flame speeds of iso-octane/air mixtures at 1 bar and 373-473 K.

The kinetic scheme of Kelley et al. [78], and therefore the original Lawrence Livermore detailed mechanism [243-245], provides substantially higher laminar burning velocities for iso-octane/air mixtures at 1 bar and 373-473 K, except for ϕ =0.8-0.9 at 1 bar and 373 K. Differences up to 15.61 cm/s (23%) were obtained between the experimental findings and the laminar burning velocities predicted by the chemical mechanism of Kelley et al. [78] at 473 K and ϕ =1.2. Kelley et al. [78] also observed that the kinetic scheme of Kelley et al. [78] significantly overpredicted S_L values of iso-octane at 298-353 K and 1-10 bar.

Jerzembeck et al. [240] suggested that the laminar flame speeds predicted by their high temperature kinetic scheme are in good agreement with the experimental data for iso-octane flames at 298-373 K and 1-25 bar with a notable underestimation at ϕ >1.0 and a slight overestimation at ϕ <1.0. However, Figure 4-4 shows the high-temperature chemical mechanism of Jerzembeck et al. [240] underpredicts the laminar burning velocities for iso-octane/air mixtures at 1 bar and 373-

473 K relative to the experimental findings over the entire range of equivalence ratios. In fact, the laminar flame speeds predicted by the chemical mechanism of Jerzembeck et al. [240] are 18-40% and 15-29% slower than the present experimental results at 373 and 473 K, respectively.

4.4 The CO₂ Dilution Effect

The exhaust gas recirculation effect on the S_L and L_b was investigated by diluting the high/low RON gasoline and iso-octane mixtures at 473 K and 1 bar with CO_2 (15% by mass within the oxidizer) for ϕ =0.9-1.4. It should be noted that higher dilution levels (30%) and lower temperature conditions (T_u =373K) were tested, but a sustained laminar flame could not be established at these conditions.

Figure 4-5 shows 15% CO₂ dilution decreases the S_L values of high and low RON gasolines by 41-46 and 42-44%, respectively, while the decrease in the S_L of iso-octane/air flames is slightly higher at 46-49%. This causes a difference of 4.41-8.33 cm/s between the laminar burning velocities of the iso-octane and high RON gasoline and a difference of 5.06-10.94 cm/s between the iso-octane and low RON gasoline. CO₂-diluted iso-octane flames are consistently slower than high/low RON gasoline flames at 473 K with 15% CO₂. On the other hand, high and low RON gasoline/air mixtures have almost the same S_L values for ϕ =1.0-1.1 and the laminar flame speeds of low RON gasoline for ϕ =0.9 and 1.3 are slightly faster than those of high RON gasoline.

Numerical results obtained by the chemical mechanisms of Chaos et al. [239], Kelley et al. [78], and Jerzembeck et al. [240] for diluted iso-octane flames at 473 K are also presented in Figure 4-5. Similar to the nondiluted 373 K and 473 K cases, the diluted iso-octane results match best with the laminar burning velocities estimated by the chemical mechanism of Chaos et al. [239] and the discrepancy previously observed between the model and experimental data was observed to be slightly smaller for the dilution case, although the mechanism still underestimates the laminar

flame speeds for ϕ ≥1.2 slightly. The kinetic scheme of Kelley et al. [78] provides laminar burning velocities 11-27% higher than the experimental findings, and the laminar flame speeds predicted by the high temperature kinetic scheme of Jerzembeck et al. [240] are 20-40% slower than the experimental data shown in Figure 4-5.

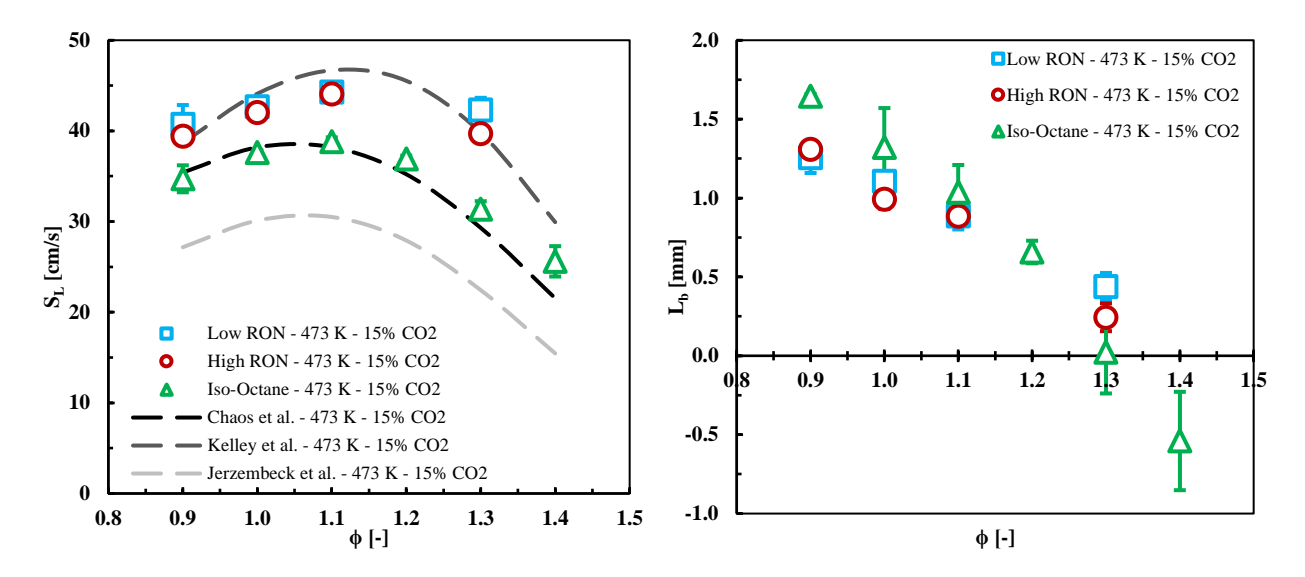


Figure 4-5. Experimental (points) and numerical (lines - iso-octane/air only) laminar burning velocity (left) and burned gas Markstein length (right) results for iso-octane/air and high/low RON gasoline/air mixtures with 15% CO₂ dilution by mass within the oxidizer at 1 bar and 473 K.

The addition of CO_2 lowers the S_L primarily because of the dilution, thermal-diffusion, and chemical effects [282]. The dilution effect is defined as the decrease in the net reaction rate (and thus the laminar burning velocity) due to the reduced fuel/oxidizer concentration in the presence of the diluent [283]. Therefore, the dilution effect gets stronger as the diluent concentration increases [284]. The thermal-diffusion effect is due to the change in thermodynamic properties and thermal/mass diffusivities of the mixture with the addition of a diluent [282]. For instance, the addition of CO_2 as a diluent increases the specific heat capacity of the iso-octane/air mixture, and therefore, decreases the flame temperature, reaction rates, and flame speed by acting like a heat

absorber, which decreases the probability of achieving the activation energy for reactions to occur [283-284].

The chemical, or kinetic, effect is a result of the change in reaction kinetics (and thus the laminar flame speed) due to the participation of the diluent in chemical reactions [282]. Mazas et al. [9] and Xie et al. [19] observed that CO_2 participates in an elementary chain-carrying dissociation reaction $CO_2 + H = CO + OH$ and competes for H radicals with the chain-branching reaction $H + O_2 = O + OH$ and, by doing so, impedes the iso-octane/air combustion. This last reaction is important as it is the dominant reaction that produces reactive radicals, which in part control the laminar flame speed. Halter et al. [10] investigated these three effects and concluded that the CO_2 dissociation becomes less important in decreasing the iso-octane laminar flame speed as the dilution rate is increased.

To quantify the chemical effect alone, iso-octane/air mixtures at 1 bar, 473 K, and φ=0.9, 1.0, and 1.3 were diluted with chemically inactive CO₂, i.e. FCO₂, and the laminar burning velocities of these mixtures were numerically calculated with the Chemkin-Pro software [215] using the chemical mechanism of Chaos et al. [239]. FCO₂ has the same thermal and transport properties as CO₂ but does not participate in any chemical reaction. Therefore, the difference between the numerical laminar burning velocities of iso-octane/air mixtures diluted with CO₂ and FCO₂ indicates the decrease in the laminar flame speed due to the chemical effect of CO₂.

As shown in Figure 4-6, the thermal-diffusion and dilution effects are dominant because of the lower flame temperatures at high dilution rates. The chemical effect of the diluent CO_2 caused a 23-25% reduction in S_L at ϕ =0.9-1.0. Its contribution on the reduction in laminar flame speed decreases from 25% to 15% as the equivalence ratio is increased from 1.0 to 1.3. Due to the more pronounced chemical effect around stoichiometry, and therefore greater reduction in the S_L , the

addition of CO_2 to iso-octane/air mixtures at 1 bar and 473 K flattens the S_L vs. ϕ plot. In fact, while the variation in the S_L for nondiluted iso-octane/air flames at 1 bar and 473 K was 22.96 cm/s, only a 13.19 cm/s difference was observed between the maximum and minimum values of the laminar burning velocity of iso-octane/air mixtures with 15% CO_2 dilution.

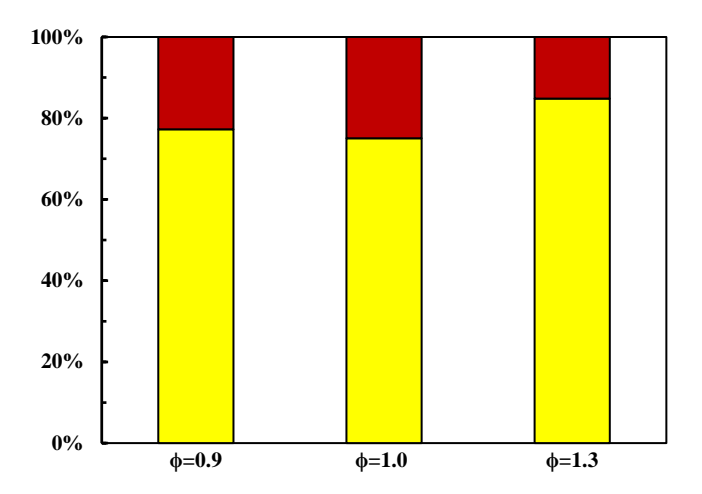


Figure 4-6. Contributions of the dilution and thermal-diffusion effects (yellow) and the chemical effect (red) on the decrease in the laminar burning velocities of iso-octane/air mixtures at 1 bar and 473 K due to the addition of 15% CO₂.

Figure 4-5 shows burned gas Markstein lengths of iso-octane/air and high/low RON gasoline/air mixtures with 15% CO₂ dilution at 473 K and 1 bar. The addition of CO₂ generally raised the L_b , which can be attributable to its thermal-diffusion effect. This suggests that iso-octane and high/low RON gasoline flames are more stable than nondiluted mixtures in terms of the thermal-diffusive instabilities. Similar to nondiluted 373 K and 473 K cases, burned gas Markstein lengths of high and low RON gasolines are almost the same for ϕ <1.3 while the burned gas Markstein length of low RON gasoline is slightly higher than that of high RON gasoline for ϕ =1.3. With higher burned gas Markstein lengths, iso-octane flames appear to be more stretched than high and low RON gasoline flames with 15% CO₂ dilution for ϕ <1.1 at 473 K and 1 bar. Figure 4-5 suggests the flame stability and flame stretch characteristics of iso-octane are very similar to those of the two commercial gasolines for ϕ >1.1.

4.5 Conclusions

The strict regulation of internal combustion engine emissions has pushed vehicle manufacturers to explore alternative fuels and emission reduction techniques. Exhaust gas recirculation technology has been proposed as an effective way of reducing emissions in IC engines. Among main exhaust gases, CO₂ has the greatest influence on the laminar flame speed due to its higher specific heat capacity, lower thermal diffusivity, and active participation in dissociation reaction by competing for the H atom, i.e. CO₂ + H = CO + OH [281, 285-286]. Therefore, in order to investigate effects of EGR on the laminar burning velocity and flame stability of commercial gasolines and iso-octane, a spherically expanding flame approach under constant pressure was employed for iso-octane/air and high/low RON gasoline/air mixtures with and without 15% CO₂ dilution at 1 bar and 373-473 K. All experimental results with uncertainties and numerical data obtained with the Chemkin-Pro software [215] are provided in Appendix K.

High temperature tests showed that the S_L of commercial gasolines does not vary significantly with RON. At 1 bar and 373-473 K, the only noticeable differences between the laminar flame speeds of high and low RON gasolines were observed at very lean conditions where the low RON gasoline has a slightly lower flame speed and at rich conditions where the low RON gasoline has a faster burning velocity. On the other hand, the S_L of iso-octane/air flames is consistently slower than those of the two commercial gasolines. The differences between the S_L values of the iso-octane/air and high/low RON gasoline/air mixtures increase with temperature. This observation is consistent with the findings of Stanglmaier et al. [277], who stated that at high temperatures and pressures the S_L values of iso-octane and gasoline can be appreciably different.

At 1 bar and 373-473 K, earlier onset of thermal-diffusive instabilities was observed as cellular formation for very rich iso-octane/air and high/low RON gasoline/air flames. Increase in

the measurement temperature did not significantly change the L_b values of the experimentally investigated mixtures. High and low RON gasolines have almost the same burned gas Markstein lengths for ϕ <1.3, and the L_b of low RON gasoline is slightly higher than that of high RON gasoline for ϕ =1.3. Iso-octane/air flames have slightly higher burned gas Markstein lengths than the two commercial gasolines at lean conditions and the burned gas Markstein lengths of iso-octane at rich conditions are very close to those of the high/low RON gasoline/air mixtures.

Numerical analysis was performed for iso-octane flames at the experimentally investigated conditions using the kinetic schemes of Chaos et al. [239], Kelley et al. [78], and Jerzembeck et al. [240]. Excellent agreement was observed between the current experimental data and the numerical results of the mechanism of Chaos et al. [239] with slightly slower S_L values observed at φ>1.2. The chemical mechanism of Kelley et al. [78], which is a skeletal kinetic scheme of the Lawrence Livermore detailed mechanism [243-245], predicted significantly higher laminar burning velocities, while the numerical results of the chemical mechanism of Jerzembeck et al. [240] were substantially slower than the experiment's.

The unburned gas temperature increase from 373 K to 473 K at 1 bar yielded 51-56%, 50-54%, and 48-51% increases in the laminar burning velocity of the high and low RON gasolines and the iso-octane, respectively, because of improved dissociation reactions and larger expansion ratios. The addition of 15% CO_2 resulted in 41-46%, 42-44%, and 46-49% decreases in the laminar burning velocities of the high and low RON gasolines and iso-octane, respectively, due to the dilution, thermal-diffusion, and chemical effects of CO_2 . The chemical effect caused 23-25% reduction in the S_L of iso-octane flames at ϕ =0.9-1.0. For ϕ =1.3, where the combustion temperature is lower, it dropped to 15%, which is the cause of the flatter S_L vs. ϕ plot for iso-octane flames with CO_2 .

While the diluted high and low RON gasoline flames have very similar S_L values at ϕ =1.0-1.1, the CO_2 -diluted iso-octane flames are consistently slower. The laminar flame speeds of the low RON gasoline with 15% CO_2 dilution for ϕ =0.9 and 1.3 are slightly faster than those of the high RON gasoline. The addition of CO_2 in iso-octane/air and high/low RON gasoline/air mixtures slightly increased the L_b because of the thermal-diffusion effect of CO_2 . With higher burned gas Markstein lengths for ϕ <1.1, iso-octane flames are more stretched than those of the high and low RON gasolines which have almost the same burned gas Markstein lengths at ϕ <1.3. For ϕ ≥1.1, the burned gas Markstein lengths for the low RON gasoline are slightly higher than those for the high RON gasoline and the flame stability and flame stretch characteristics of iso-octane are very similar to those of the two commercial gasolines.

5 LAMINAR FLAME CHARACTERISTICS OF PREMIXED METHANE/AIR FLAMES DILUTED WITH COMBUSTION RESIDUALS

5.1 Introduction and Literature Review

As the main component of natural gas, methane has drawn attention in flame speed studies because of its usage for power production, heating applications, and internal combustion engines. Therefore, there are many studies on laminar flame characteristics of methane/air mixtures at low temperatures and pressures [21, 86-92, 224, 230, 287-290] while there is only limited information available at higher temperatures and pressures [71, 75-76, 154, 232].

Due to their high load flexibility and air-quality benefits, axial (sequential) stage combustion systems have become more popular among ground-based power gas turbine combustors. However, inert combustion residuals passing from the initial stage onto the secondary stage affect the reactivity and stability of the flame in the second stage of the combustor [10]. Because of this phenomenon, investigating the effect of dilution with post-combustion products on laminar flame characteristics of methane is imperative. In fact, over the years, the dilution effect on laminar burning velocities of methane/oxidizer flames has been examined extensively.

One of the earliest studies was published by Stone et al. [72] who deduced laminar flame speed data from pressure time measurements for methane/air mixtures over the range of 0.5-10.4 bar and 293-454 K. The effect of the diluents CO₂, N₂, and their mixtures was investigated near zero-gravity conditions, but the flame-front cellular instabilities were overlooked due to the lack of visual observation. As a result of their study, Stone et al. [72] proposed a correlation for the S_L values of CH₄/air flames at tested initial conditions. Elia et al. [73] examined the dilution effect of a mixture of CO₂ and N₂ on the S_L of methane/air mixtures at 0.75-70 bar and 298-550 K for combustion residuals at a volume fraction of 0-15% with the constant volume method. Like Stone

et al. [72], Elia et al. [73] also derived an empirical laminar flame speed correlation. For laminar flame speed measurements of methane/air mixtures at 1 bar and 298-388 K, Ponnusamy et al. [74] used the constant volume method. Flue gas recirculation was simulated using dilution with a CO₂ and N₂ mixture.

In the last decade, the dilution effect on laminar flame speeds of methane/oxidizer flames has received increasing attention. Halter et al. [10] studied the effect of CO₂ and N₂ dilution on laminar burning velocities of methane/air mixtures at 1 bar and 300 K with the constant pressure method and concluded that a larger reduction in the S_L can be attained with CO₂ dilution than N₂ due to the higher heat capacity and chemical reactivity of CO₂. Qiao et al. [285] examined Ar and He as diluents, in addition to CO₂ and N₂ for stoichiometric CH₄/air flames at NTP by using the same method. The results of numerical analysis conducted by Qiao et al. [285] showed that the chemical effect of CO₂ is more prominent than that of N₂, Ar, and He. Mazas et al. [9] measured the laminar burning velocities of CH₄/O₂ mixtures diluted with CO₂ and H₂O at 1 bar and 373 K with Bunsen burner flames. By comparing their experimental data with numerical results obtained by GRI-Mech 3.0 [223], Mazas et al. [9] concluded that laminar flame speed values of weakly diluted mixtures (the dilution ratios less than 10%) are underestimated by the GRI-Mech 3.0 mechanism [223].

Galmiche et al. [281] investigated the effect of CO₂, N₂, and H₂O dilution on the laminar flame speed of premixed methane/air flames at 1 bar, 393 K, and stoichiometric conditions. Results of the study [281] pointed out the importance of the heat capacity of the diluent to the reduction of the S_L. Mazas et al. [291] ran Bunsen flame experiments and numerical analysis consisting of water vapor dilution in CH₄ flames enriched with oxygen at 1 bar and 373 K. Mazas et al. [291] observed that H₂O has a noteworthy chemical impact on the S_L due to its high efficiency in third-

body reactions. Hu et al. [292] conducted numerical analysis to quantify the chemical effects of diluents, CO₂, N₂, Ar, and He, on the laminar burning velocity of methane/air mixtures at 1 bar and 303 K. Hu et al. [292] stated that the adiabatic flame temperature plays a significant role in the S_L reduction while the thermal diffusivity of the diluent has less importance for the S_L. Mendieta et al. [283] performed similar numerical simulations to calculate laminar flame speeds of methane/air mixtures with up to 50% CO₂ dilution at 1 bar and 298 K.

Xie et al. [19], Zahedi et al. [282], and Chan et al. [284] investigated the effect of CO₂ dilution on the laminar burning velocity of premixed methane/oxidizer mixtures at 1 bar and 298 K using the constant pressure approach, heat flux method, and flat flame burner, respectively. Khan et al. [286] measured laminar burning velocities of spherically expanding CH₄/O₂ flames diluted with N₂ and CO₂ mixtures at 1 bar and 300 K. Khan et al. [286] explained the reduction in the S_L with decreased energy content of the reactants, increased specific heat capacity, and decreased flame temperature and thermal diffusivity.

As mentioned above, in the past, almost all experimental studies have examined the effect of combustion residuals on laminar flame characteristics of a combustible mixture by using one of the main exhaust gases (N₂, H₂O, and CO₂) or a mixture of two; former experimental studies on the S_L of diluted CH₄/oxidizer mixtures are summarized in Table 5-1. However, N₂, H₂O, and CO₂ have very different thermodynamic properties and chemical reactivities (active participation in elementary reactions and third body reaction efficiency). Therefore, simulating post combustion products, which are used to dilute the fuel/air mixture, with only one or two of the main exhaust gases may cause critical errors in experimental laminar burning velocity data. Almost all of the limited existing studies investigating actual flue gas content (N₂+H₂O+CO₂) is either based on the numerical results or measurements of stoichiometric mixtures at atmospheric pressure.

Table 5-1. Past experiments on laminar flame speed of diluted methane/oxidizer mixtures.

Defeners	0-:4:	P	Т ф		D:14
Reference	Oxidizer	[bar]	[K]	[-]	Diluent
Stone et al. [72]	Air	0.5-10.4	293-454	0.4-1.6	0-15% CO ₂ , N ₂ , and (85% N ₂ +15% CO ₂) dilution by volume
Elia et al. [73]	Air	0.75-70	298-550	0.8-1.2	0-15% (86% N ₂ +14% CO ₂) dilution by volume
Ponnusamy et al. [74]	Air	1	298-388	1.0	0-22% (81.5% N ₂ +18.5% CO ₂) dilution by volume
Halter et al. [10]	Air	1	300	1.0	0-20% CO ₂ , 0-30% N ₂ , and 0-25% (71.6% N ₂ +28.4% CO ₂) dilution by volume
Qiao et al. [285]	Air	1	298	1.0	0-35% He, 0-48% Ar, 0-35% N ₂ , and 0-22% CO ₂ dilution by volume
Mazas et al. [9]	O_2	1	373	0.5-1.5	0-79% CO ₂ and N ₂ dilution by volume within oxidizer + $0-45%$ H ₂ O dilution by volume within reactants
Galmiche et al. [281]	Air	1	393	1.0	0-35% N ₂ , 0-20% CO ₂ , 0-25% H ₂ O, and 0-30% (71.6% N ₂ +18.9% H ₂ O+9.5% CO ₂) dilution by volume
Mazas et al. [291]	Air to O ₂	1	373	0.5-1.5	0-50% H ₂ O dilution by volume
Xie et al. [19]	O_2	1-3	300	0.4-1.6	40-70% CO ₂ dilution by volume within the oxidizer
Zahedi et al. [282]	Air	1-5	298	0.7-1.3	0-20% CO ₂ and N ₂ dilution by volume within the fuel
Chan et al. [284]	Air	1	298	0.8-1.4	0-15% CO ₂ dilution by volume within the fuel
Khan et al. [286]	O_2	1	300	0.6-1.4	30-50% CO ₂ and 50-70% N ₂ dilution by volume

After determination of laminar flame speed data of a fuel/oxidizer mixture at various pressures (P), temperatures (T), and equivalence (ϕ) and dilution (X) ratios with a great amount of experimental or numerical analyses, an empirical correlation can be derived for $S_L(P,T,\phi,X)$ with data fitting. This analytical correlation, which is a single equation depending on pressure,

temperature, and sometimes equivalence and dilution ratios, is quite useful since it enables one to calculate S_L with only one equation within a wide range of pressures and temperatures. Consequently, laminar burning velocity correlations have frequently been used in the numerical analysis of engineering applications in order to evaluate the S_L due to the significant computational effort needed for solving detailed chemical kinetic models.

The most commonly utilized form of S_L correlations is the power law of Metghalchi and Keck [112], i.e. Equation 5-1. In this expression, $S_{L,o}$, α , and β coefficients are determined according to the experimental or numerical results of the investigated fuel/oxidizer mixture. These coefficients can be a function of equivalence ratio or the ϕ effect can be included in the correlation by adding another term for it. While T_u represents the unburned gas temperature, $T_{u,o}$ and P_o are the reference temperature and pressure values, which are usually assumed as 298-300 K and 1 bar-1 atm, respectively.

$$S_{L} = S_{L,o} \left(\frac{T_{u}}{T_{u,o}}\right)^{\alpha} \left(\frac{P}{P_{o}}\right)^{\beta}$$
 5-1

Experimental laminar flame speed findings were highly scattered before establishing the presence of flame stretch in 1985 [13]. Therefore, the attention is focused on S_L correlations for methane/air flames that were published after 1990. With spherically expanding flames propagating at constant pressure, Gu et al. [21] determined the power law coefficients for methane/air mixtures at initial temperatures between 300 and 400 K, pressures between 1 and 10 bar, and equivalence ratios of 0.8, 1.0, and 1.2. $T_{u,o}$ and P_o values were chosen as 300 K and 1 bar. For the calculation of the S_L in cm/s, $S_{L,o}$, α , and β coefficients were found to be 25.9, 2.105, and -0.504 for ϕ =0.8; 36.0, 1.612, and -0.374 for ϕ =1.0; and 31.4, 2.000, and -0.438 for ϕ =1.2, respectively. Han et al. [293] optimized the power law coefficients with spherically expanding flames of stoichiometric methane/air mixtures at constant volume. $T_{u,o}$, P_o , $S_{L,o}$, α , and β values were specified as 298 K, 1

atm, 36.11, 1.5365+0.1165P, and -0.37, respectively, which are valid for T_u =298-473 K and P=1-5 atm.

Instead of the power law, Dirrenberger et al. [267] used the formulation proposed by Gulder [294], i.e. $S_L = W \varphi^{\eta} \exp(-\xi(\varphi - \sigma)^2)$, for methane/air flames at 1 bar, 298 K, and φ =0.7-1.6. The values of coefficients in this expression were deduced from an adiabatic heat flux burner as W=38.638, η =-0.15, ξ =6.2706, and σ =1.1. Moccia and D'Alessio [295] analyzed stoichiometric methane spherically expanding flames at 3-18 bar and 293-305 K with the shadowgraph optical technique. In this study, Metghalchi and Keck's power law [112] was used, but only the pressure dependence was evidenced with β =-0.45 and $S_{L,0}$ equal S_L at 3 bar and 298 K.

Another study employing the power law formulation was conducted by Hu et al. [76], who measured the S_L of methane/air mixtures at 1-5 bar and 298-443 K in a constant volume combustion chamber. Hu et al. [76] noticed that the USC Mech II chemical mechanism [224] showed a high level of agreement with experimental data at stoichiometric conditions. Therefore, the mechanism was used to calculate S_L to represent the experimental data at the extended pressures and temperatures. Subsequently, Hu et al. [76] proposed a power law based on experimental measurements and numerical calculations with $T_{u,o}$ =300 K, P_o =1 bar, $S_{L,o}$ ~37 cm/s, α =1.39+0.0006 T_u , and β =0.226*exp(-P/0.841)-0.511 for stoichiometric methane/air mixtures at 300-700 K and 1-60 bar.

Hinton et al. [296] developed a quartic laminar burning velocity correlation for methane/air mixtures at 394-652 K, 0.64-16.4 bar, and ϕ =0.7-1.4 with the spherically expanding flame approach. Recently, Amirante et al. [297] derived an empirical power law for methane/air mixtures at 1-50 atm, 298-800 K, and ϕ =0.6-1.7 from previously published S_L data in the literature. In this study, the $S_{L,o}$ coefficient was defined with Gulder's exponential formulation [294] with W= 38.85,

 η =-0.20, ξ =6.45, and σ =1.08. Other coefficients were found to be $T_{u,o}$ =298 K, P_o =1 atm, α =4.9199 ϕ ²-10.287 ϕ +6.9258, and β =-1.3712 ϕ ²+2.6808 ϕ -1.7492.

As explained above, there are only a few correlations revealing effects of pressure, temperature, and equivalence ratio on the laminar burning velocity of methane/air mixtures. Analytical correlations taking the dilution effect into account are rarer still. To the best of the author's knowledge, there are only two methane laminar burning velocity correlations accounting for effects of pressure, temperature, equivalence and dilution ratios published in the present literature.

The first correlation was proposed by Stone et al. [72] in 1998. This quartic power law formulation was based on S_L data deduced from spherically expanding flames at constant volume and valid at T_u =295-454 K, P=0.5-10.4 bar, ϕ =0.6-1.4, and X=0-15%. Stone et al. [72] studied the dilution effect with CO_2 , N_2 , and a mixture of 85% N_2 +15% CO_2 . Elia et al. [73] also utilized the constant volume method for S_L measurements since this approach allows for the determination of the S_L over a wide range of temperatures and pressures from a single test. In this study, a power law correlation was developed for the S_L of methane/air flames at T_u =298-550 K, P=0.75-70 atm, ϕ =0.8-1.2, and X=0-15%. Elia et al. [73] used a mixture of 86% N_2 +14% CO_2 for dilution.

Both Stone et al. [72] and Elia et al. [73] assumed a smooth spherical flame front while ignoring the possibility of cellularity on the flame surface, which may lead an overprediction of S_L values. However, in the present study, a severe cellular formation was observed with a mere 2% pressure increase during the stoichiometric methane/air combustion at an initial pressure and temperature of 5 bar and 373 K. Schlieren images presented in Figure 5-1 suggest that increasing the equivalence and dilution ratios suppresses the flame instabilities, whereas earlier onset of the cellularity was observed with increasing pressure. Increasing unburned gas temperature from 373

K to 423 K did not significantly alter the flame front stability of a stoichiometric methane/air mixture at 3 bar.

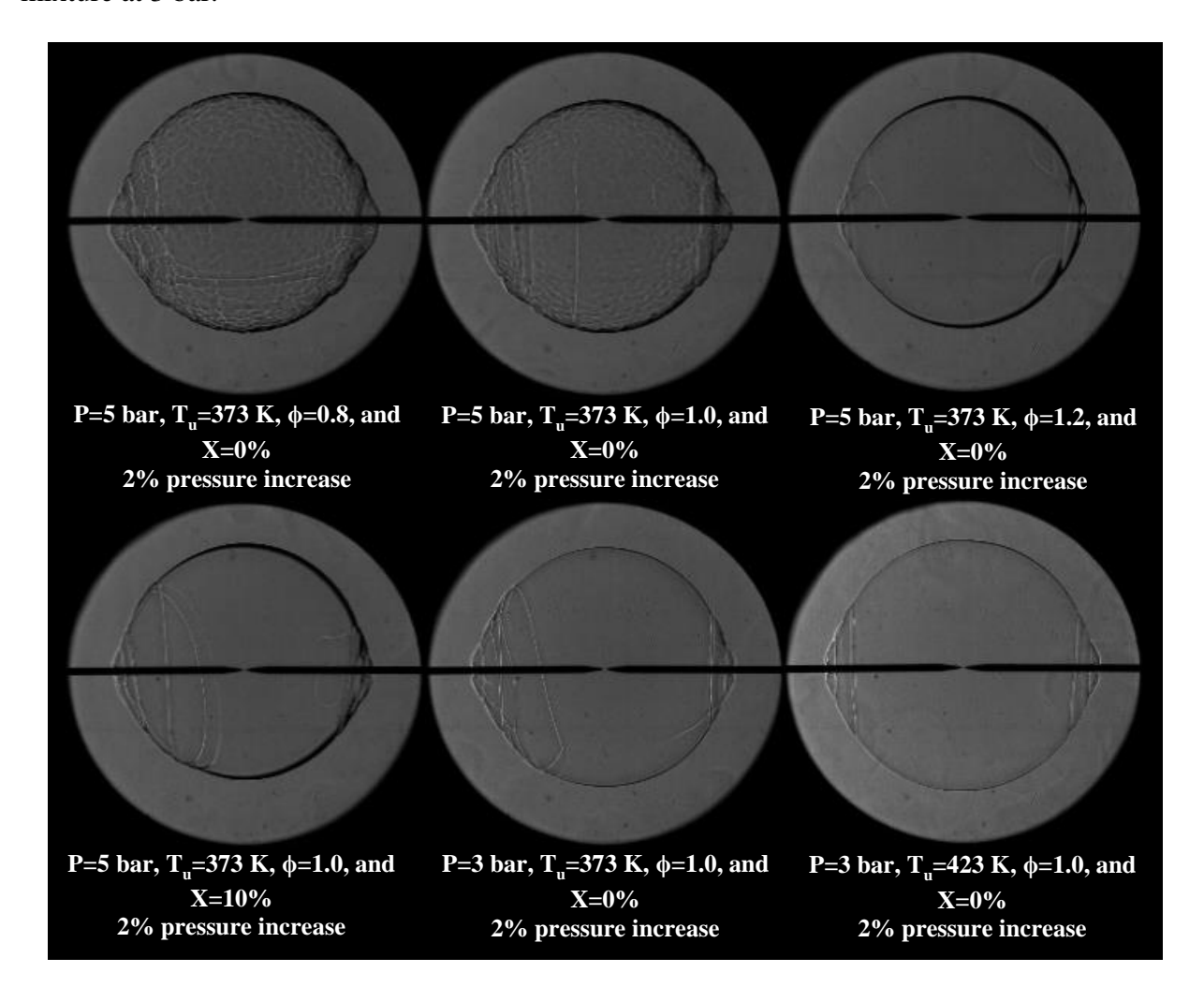


Figure 5-1. Schlieren images showing the flame front instabilities.

Stone et al. [72] also ignored the effect of flame stretch by anticipating its impact on the S_L as less than 1 cm/s. On the other hand, to remove stretch effects from the burning velocity data, Elia et al. [73] used the LS model [149], which has been shown to provide faster S_L for mixtures with a Lewis number appreciably different than one [160-161]. Moreover, instead of real flue gas content ($N_2+H_2O+CO_2$), Stone et al. [72] and Elia et al. [73] utilized a mixture of 85-86% $N_2+15-14\%$ CO_2 for dilution of methane/air mixtures.

In the present study, first, the effects of equivalence ratio, temperature, and pressure on the laminar methane/air flame characteristics, namely laminar flame speed and burned gas Markstein length, were experimentally investigated with spherically expanding flames under constant pressure at 1-5 bar and 373-473 K. A wide range of equivalence ratios was experimentally tested, but only the equivalence ratios where the S_L was greater than 15 cm/s were reported, due to the buoyancy effect limitation [126]. Three measurements were performed for each initial condition. The overall uncertainty in the S_L and L_b , shown as error bars in the following figures, is equivalent to the random uncertainty.

As mentioned above, although simulating combustion residuals with one of the main exhaust gases or a mixture of two can lead to significant errors in the S_L and L_b data due to their different chemical reactivities and thermodynamic and transport properties, almost all studies in the past imitated flue gases with one of N_2 , H_2O , and CO_2 or a mixture of two. To address this problem, the S_L and L_b values of CH_4 /air mixtures diluted with N_2 , H_2O , and CO_2 individually as well as with a mixture of 71.49% N_2 + 19.01% H_2O + 9.50% CO_2 by volume, which corresponds with the percentage of core products that result from stoichiometric CH_4 /air combustion, were measured at 1 bar and 473 K. Dilution ratios of 0%, 5%, 10%, and 15% by mole within reactants were tested.

Experimental results showed that an accurate simulation of the actual combustion residuals with one of the main exhaust gases is impossible. Even using a mixture of two main exhaust gases to mimic combustion residuals by achieving the same expansion ratio may lead to significant error in the laminar burning velocity calculations, as thermodynamic properties and chemical reactivities of the combustion residuals can change considerably with temperature, pressure, and equivalence and dilution ratios.

Subsequently, the S_L and L_b values of methane/air flames diluted with a mixture of 71.49% $N_2 + 19.01\%$ $H_2O + 9.50\%$ CO_2 by volume were deduced at 1-5 bar, 373-473 K, and a dilution level of 0-15% in an optically accessible constant volume combustion chamber in order to develop correlations for the S_L and L_b of methane/air mixtures in the form of Metghalchi and Keck's power law [112] by including extra terms for equivalence and dilution ratios. The diluent level is specified as the concentration of the diluent mixture by mole within reactants.

At experimentally investigated initial conditions, computational analyses were conducted with the GRI-Mech 3.0 [223], USC Mech II [224], San Diego [225], HP-Mech [226], NUI Galway-CH₄/DME [227], and AramcoMech 1.3 [228] mechanisms in the Chemkin-Pro software [215] to assess the performance of these kinetic schemes. Furthermore, the contribution from each of the dilution, thermal-diffusion, and chemical effects on the decrease in the laminar burning velocity due to the combustion residuals was determined with a series of numerical analyses with the GRI-Mech 3.0 [223].

5.2 The Equivalence Ratio Effect

To examine the effect of equivalence ratio on the S_L and L_b of methane/air mixtures, experiments were conducted at 1 bar and 373 K, 423 K, and 473 K; 3 bar and 373 K and 423 K; and 5 bar and 373 K with an increment of 0.1 in the ϕ . The S_L results over a wide range of equivalence ratios were presented in Figure 5-2 and Figure 5-3 for different pressures and temperatures. As shown in these figures, peak laminar burning velocities were observed at ϕ =1.0-1.1, where the adiabatic flame temperature is at a maximum, which yields improved chemical reactivity, and the burned to unburned gas density ratio is at a minimum. The laminar flame speed is slower at both lean and rich conditions.

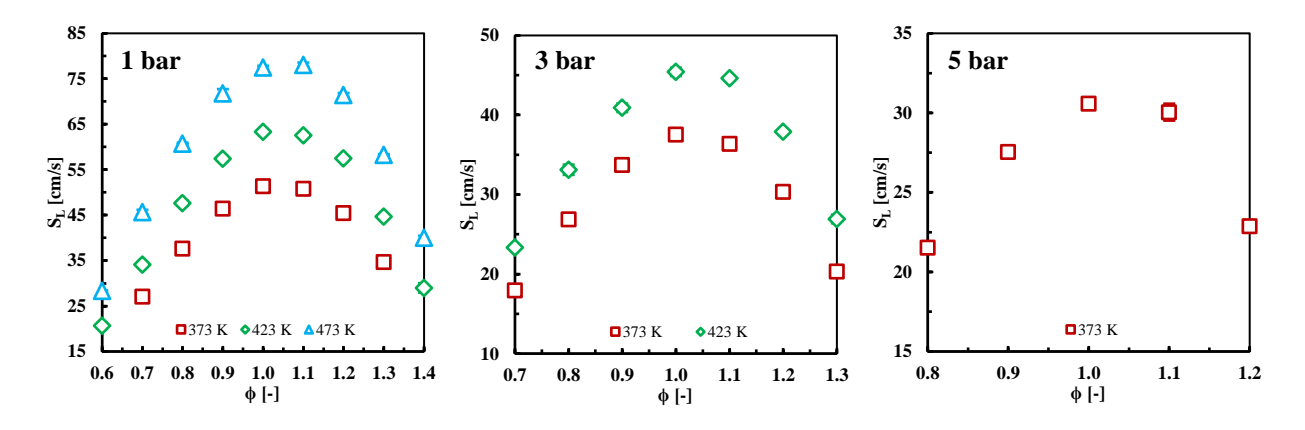


Figure 5-2. Experimental S_L data for methane/air mixtures at 1, 3, and 5 bar.

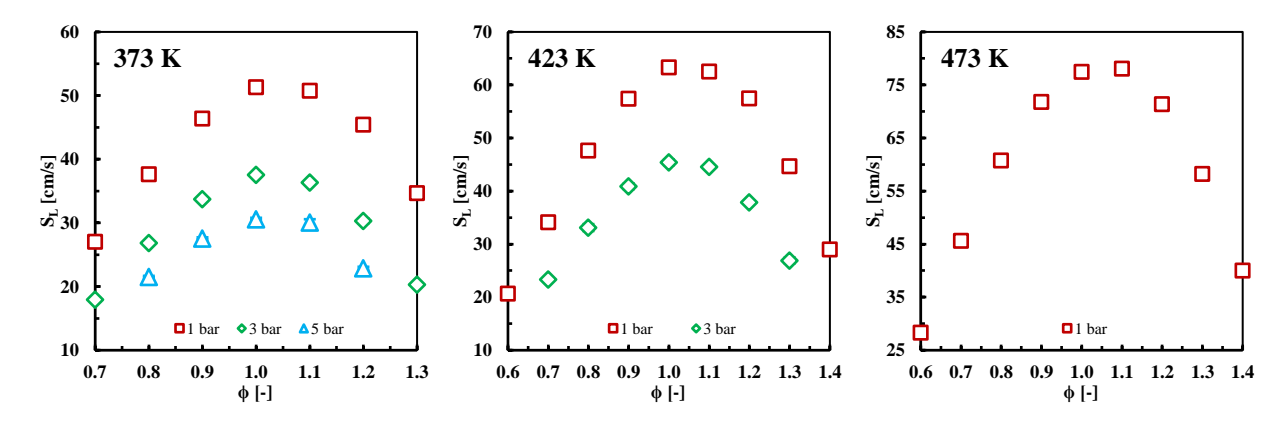


Figure 5-3. Experimental S_L data for methane/air mixtures at 373, 423, and 473 K.

The L_b values for methane/air mixtures were plotted against the equivalence ratio in Figure 5-4 and Figure 5-5 for different pressures and temperatures. The L_b generally grows with increasing equivalence ratio, which suggests that the thermal-diffusive instabilities are less profound for rich methane/air flames, which are also more stretched than lean flames [21]. This phenomenon was observed most clearly at high pressures where some of the L_b s of very lean methane/air flames are negative. Furthermore, enhanced reaction rates around stoichiometry reduce the laminar flame thickness, which fosters the hydrodynamic cellular formation as shown in Figure 5-1.

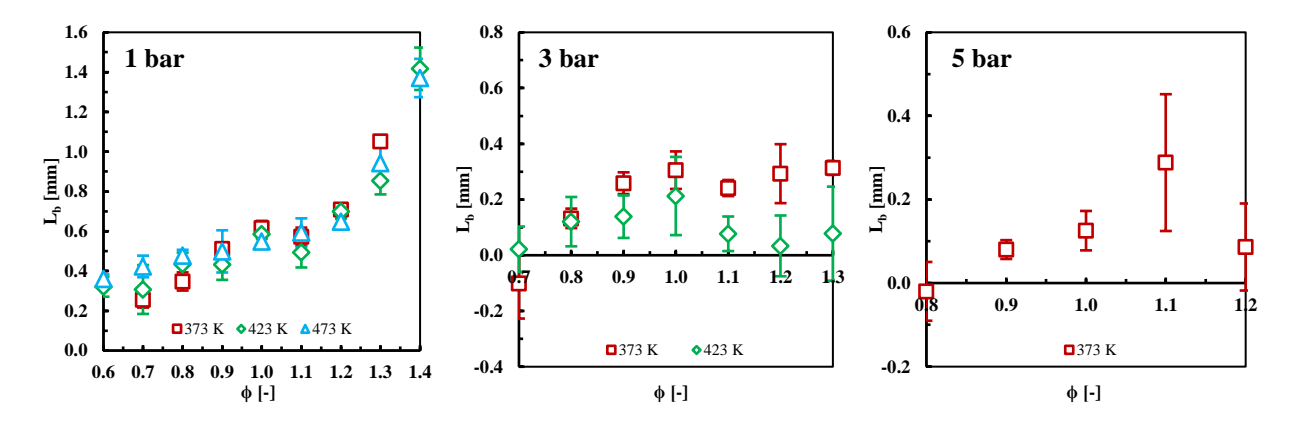


Figure 5-4. Experimental L_b data for methane/air mixtures at 1, 3, and 5 bar.

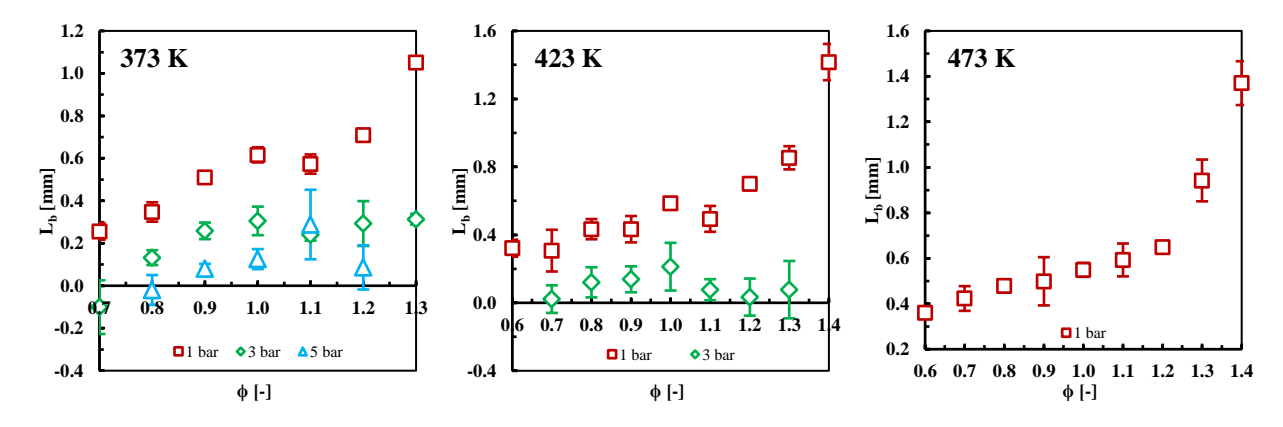


Figure 5-5. Experimental L_b data for methane/air mixtures at 373, 423, and 473 K.

5.3 The Unburned Gas Temperature Effect

Effect of the unburned gas temperature on the S_L and L_b of methane/air mixtures at 1 bar can be observed, together with the equivalence ratio effect, in Figure 5-6, which contains S_L and L_b hill charts. The S_L increased by 23-29% and 22-34% with temperature increases from 373 K to 423 K and from 423 K to 473 K, respectively, due mainly to the enhanced dissociation reactions and higher expansion ratios. Elevated unburned gas temperatures boost the dissociation reaction rates, which augments the radical production and therefore increases the combustion temperature and laminar burning velocity [298]. Increased temperatures of reactants and products decrease burned and unburned gas densities. However, the unburned gas density was lowered more than the

burned gas density, which results in higher expansion ratios. As shown in Figure 5-2, the highest percentile increases in the S_L due to the temperature elevation were seen away from stoichiometry.

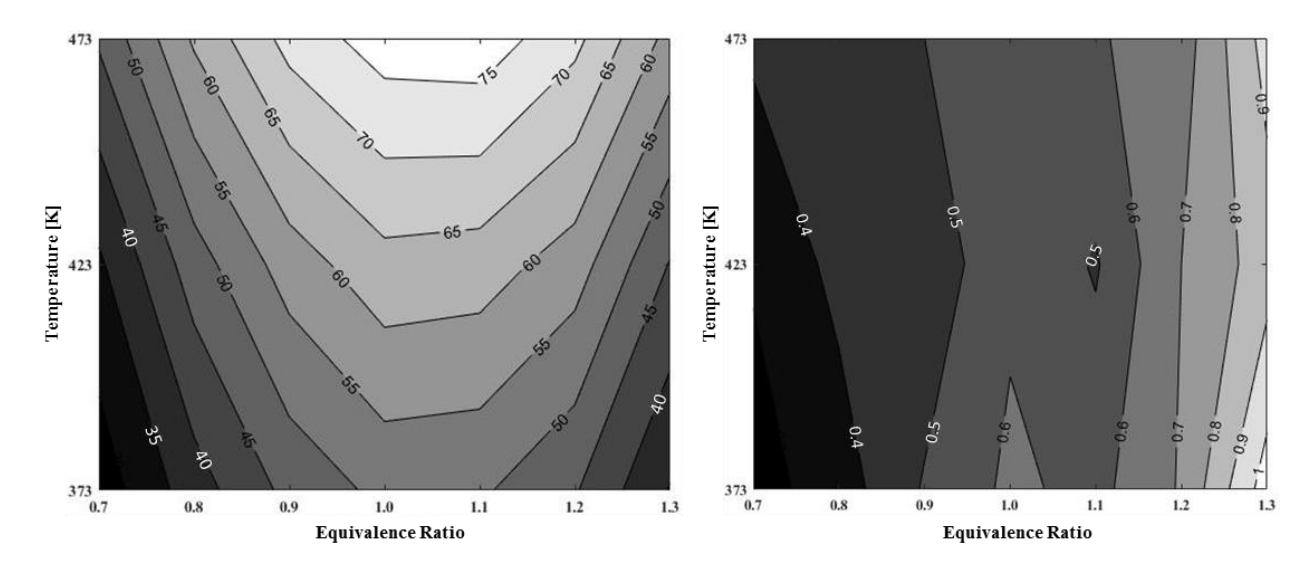


Figure 5-6. Contour plots of the S_L (left) and L_b (right) of methane/air mixtures with respect to temperature and equivalence ratio at 1 bar.

The impact of the unburned gas temperature on the L_b is almost insignificant for methane/air mixtures, see Figure 5-4 and Figure 5-6. Similarly, in the previous chapter, any considerable change in the L_b of iso-octane/air and high/low RON gasoline/air mixtures due the change in initial temperature from 373 K to 473 K could not be detected. The unburned gas temperature increase resulted in a thinner methane flame, which causes more intense hydrodynamic instabilities. On the contrary, higher expansion ratios at elevated unburned gas temperatures suppressed the hydrodynamic instabilities. The earlier onset of the hydrodynamic cellularity at elevated unburned gas temperature suggests that the former effect is more dominant than the latter.

5.4 The Initial Pressure Effect

Effect of pressure on the S_L and L_b of methane/air mixtures at 373 K can be observed, together with the equivalence ratio effect, in Figure 5-7, which contains 2D contour plots of the S_L

and L_b . The S_L lowered by 27-33% and 17-25% with pressure increases from 1 bar to 3 bar and from 3 bar to 5 bar, respectively, due mainly to decreased dissociation. With increasing pressure, $H + O_2 + M = HO_2 + M$ consumes H radicals at a higher rate, inhibits $H + O_2 = O + OH$, and therefore decreases the overall oxidation reaction, which yields slower laminar burning velocities at elevated pressures [298]. As shown in Figure 5-3, the highest percentile decreases in the S_L due to the pressure increase were seen away from the stoichiometry.

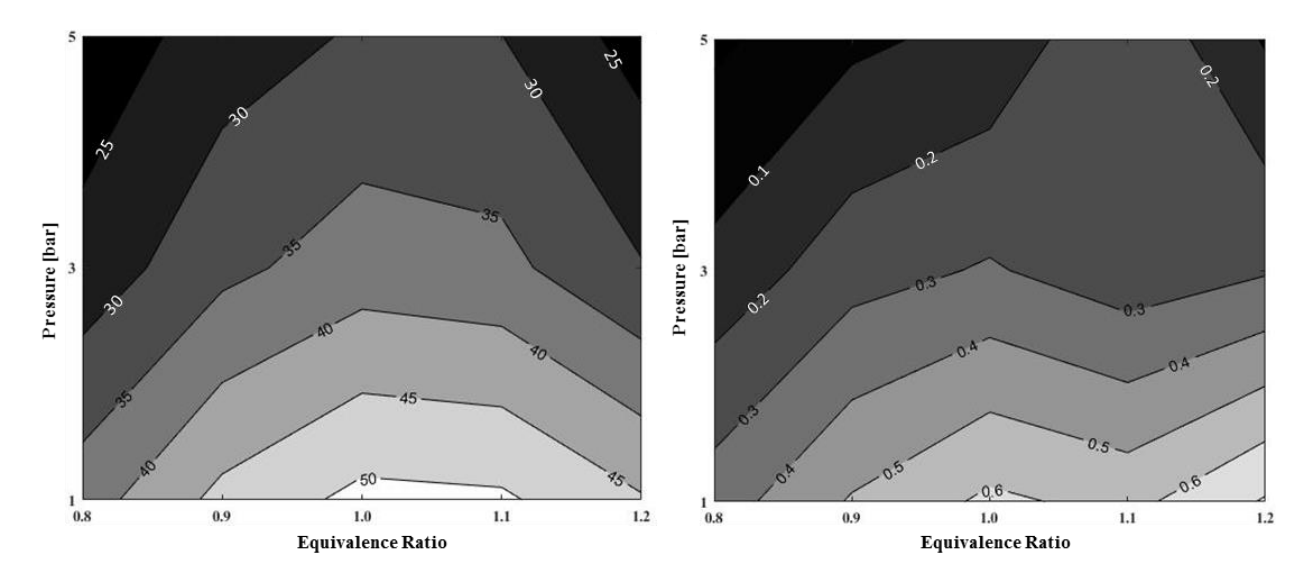


Figure 5-7. Contour plots of the S_L (left) and L_b (right) of methane/air mixtures with respect to pressure and equivalence ratio at 373 K.

The pressure increases from 1 bar to 3 bar and from 3 bar to 5 bar resulted in 0.22-0.42 mm and 0.05-0.21 mm reductions in the L_b, respectively. Smaller L_b values at elevated pressures suggests that methane/air flames are less stable with respect to the thermal-diffusive instabilities and less stretched at high pressures [21]. Moreover, the pressure rise decreases the methane flame thickness and slightly lowers the expansion ratio, which enhances the intensity of the hydrodynamic flame instabilities, see Figure 5-1.

5.5 The Dilution Effect

First, the S_L and L_b values of methane/air mixtures diluted with N_2 , H_2O , CO_2 , and a mixture of 71.49% N_2 + 19.01% H_2O + 9.50% CO_2 by volume, which represents the actual concentrations of the main stoichiometric methane/air combustion residuals, were measured in order to investigate effects of different combustion residuals on the laminar methane flame characteristics at 1 bar and 473 K. Table 5-2 and Figure 5-8 show the decreases in the laminar burning velocities at ϕ =0.8, 1.0, and 1.2 due to the addition of different diluents. The most dramatic reduction in the methane laminar flame speed were observed for CO_2 dilution and H_2O dilution caused larger decreases than N_2 dilution. In fact, the S_L values of methane/air mixtures diluted with 10% H_2O were similar to those diluted with 15% N_2 . For all equivalence and dilution ratios, the reduction in the S_L due to CO_2 dilution was approximately double the reductions caused by N_2 dilution.

Table 5-2. Percentage reduction in laminar burning velocities of methane/air mixtures diluted with N_2 , H_2O , CO_2 , and a mixture of 71.49% N_2 + 19.01% H_2O + 9.50% CO_2 at 1 bar, 473 K, and ϕ =0.8, 1.0, and 1.2.

Dilution Ratio			$ m H_2O$ dilution			CO ₂ dilution			71.49% N ₂ + 19.01% H ₂ O + 9.50% CO ₂ dilution			
	φ=0.8	φ=1.0	φ=1.2	φ=0.8	φ=1.0	φ=1.2	φ=0.8	φ=1.0	φ=1.2	φ=0.8	φ=1.0	φ=1.2
5%	12%	12%	12%	23%	21%	16%	30%	30%	30%	18%	14%	10%
10%	27%	25%	24%	41%	37%	32%	53%	51%	51%	38%	26%	28%
15%	41%	37%	37%	61%	51%	51%	68%	66%	68%	52%	45%	43%

While the percentile reductions for different equivalence ratios at the same dilution ratio did not vary significantly for N_2 and CO_2 dilutions, the percentile reductions of H_2O dilution varied by up to 10%. This similarity is a result of higher reductions in the S_L near stoichiometry, where maximum laminar burning velocity and combustion temperature are achieved. As seen in Figure

5-8, at ϕ =0.8, the laminar burning velocities of methane flames diluted with the actual combustion residuals are slightly faster than the ones with H₂O dilution at 5% and 10% dilution ratios. For 5% and 10% dilution ratios at ϕ =1.0 and 5%, 10%, and 15% dilution ratios at ϕ =1.2, N₂ dilution and actual combustion residuals mixture provided very close S_L values. This can be attributable to high N₂ concentration within the methane/air flue gases (71.49%). While the S_L values for methane/air mixtures diluted with actual combustion residuals always lie between the ones diluted with N₂ and H₂O, the laminar flame speeds of methane flames diluted with CO₂ are considerably slower. This finding is consistent with low CO₂ concentration of the combustion residuals (9.50%).

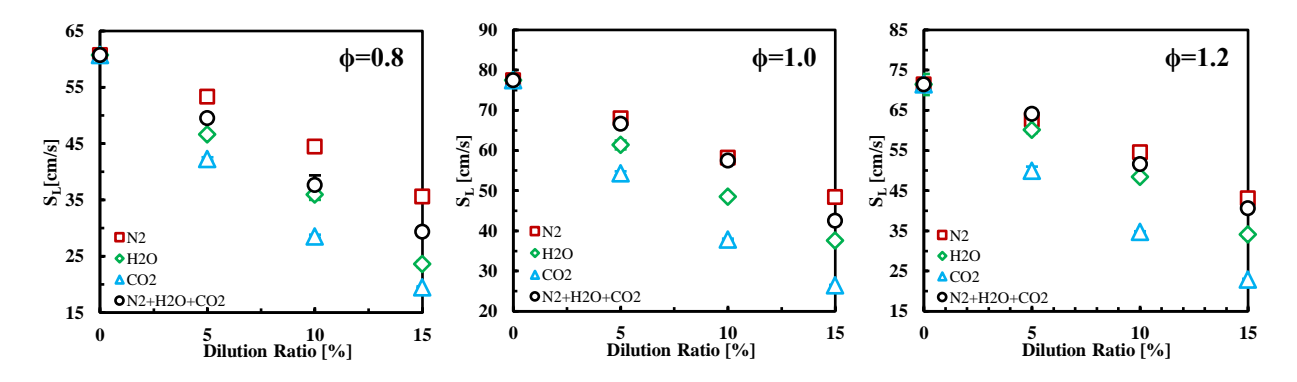


Figure 5-8. Laminar burning velocities of methane/air mixtures diluted with N_2 , H_2O , CO_2 , and a mixture of 71.49% $N_2 + 19.01\%$ $H_2O + 9.50\%$ CO_2 at 1 bar, 473 K, and ϕ =0.8, 1.0, and 1.2.

Regardless of which diluent is used, Figure 5-9 shows that methane flames stabilize with increasing equivalence and dilution ratios and become more susceptible to stretch. The L_b generally increases with diluent addition and increasing equivalence ratio. Although the L_b values for all diluents reported in the present study are similar, CO_2 dilution provided the largest L_b values - as high as 1.31 mm at ϕ =1.2 and 15% dilution. The L_b for 71.49% N_2 + 19.01% H_2O + 9.50% CO_2 mixture is generally very similar to the one for N_2 dilution. This can be attributed to high N_2 concentration within the initial fuel/oxidizer mixture and combustion residuals, which leads to similar thermal and mass diffusivities, and therefore Lewis number, which is the controlling parameter for flame stretch. From the experimental results presented in Figure 5-9, it can be

concluded that the effects of different combustion residuals on the burned gas Markstein length are not significantly distinctive.

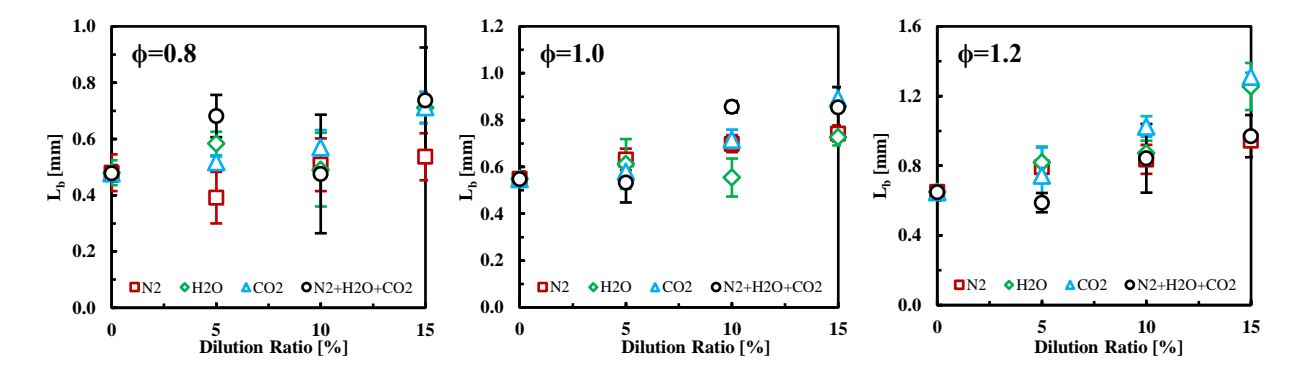


Figure 5-9. Burned gas Markstein lengths of methane/air mixtures diluted with N_2 , H_2O , CO_2 , and a mixture of 71.49% N_2 + 19.01% H_2O + 9.50% CO_2 at 1 bar, 473 K, and ϕ =0.8, 1.0, and 1.2.

As mentioned in the previous chapter, the main reasons for the decrease in the laminar burning velocity attributable to the combustion residuals can be explained through their dilution, thermal-diffusion, and chemical effects [282]. When combustion residuals are introduced into the combustible mixture, the concentration of fuel/oxidizer decreases, which causes a reduction in the S_L [284]; this effect is called the dilution (DI) effect. The use of combustion residuals also causes changes in the mass/thermal diffusivities, and thus the Le, and the mixture's specific heat capacity [282], i.e. the thermal-diffusion (TD) effect. Moreover, the combustion residuals usage introduces CO₂, N₂, and H₂O into the reactant mixture, and in turn alters the reaction kinetics and, thus, the S_L [282]; this phenomenon is called the chemical (CH), or kinetic, effect. The total chemical effect can be viewed as the combination of two factors; the chemical effect due to the active participation of the flue gas components in the dissociation reactions (CH1) and the chemical effect due to the participation of the flue gas components in the third body reactions (CH2).

In order to specify the dilution, thermal-diffusion, and chemical effects individually, four different computational models were used with the GRI-Mech 3.0 chemical mechanism [223], as

shown in Table 5-3. Model 1 consists of the dilution, thermal-diffusion, and chemical effects, as it corresponds to the conventional numerical analysis with actual flue gas content added to methane/air mixtures. In Model 2, the reactants were diluted with chemically inactive diluent with zero third body efficiency. The chemically inactive combustion residuals were added to the chemical mechanism, as well as the thermodynamic and transport datasets in addition to their actual correspondent. Chemically inactive diluent with zero third body efficiency has the same thermal and transport properties as the actual diluent used in Model 1 but it does not participate in any chemical reactions, including the third body reactions. Consequently, Model 2 does not contain the CH1 and CH2 effects and the comparison of the S_L results of Models 1 and 2 yields the decrease in the S_L due to the chemical effect.

Table 5-3. Description of the diluent properties and effects for different computational models.

	Model 1	Model 2	Model 3	Model 4	
Properties of the diluent	Dilution with the actual diluent	Dilution with chemically inactive diluent with zero third body efficiency	Dilution with chemically inactive diluent with actual third body efficiency	Dilution with chemically inactive N ₂ with zero third body efficiency	
Effects of the diluent	DI+TD+CH1+CH2	DI+TD	DI+TD+CH2	DI	

Similar to Model 2, numerical analyses for Model 3 were conducted with CH₄/air mixtures diluted with chemically inactive diluent, which has the same thermal and transport properties as the actual diluent in Model 1. However, in Model 3, the chemically inactive combustion residuals added to the chemical mechanism and thermodynamic and transport datasets have the same third body efficiencies as the actual combustion residuals used in Model 1. This means that while Model 3 has the CH2, DI, and TD effects, Model 2 has only the DI and TD effects. Therefore, the comparison of the S_L results of Models 1, 2, and 3 gives the CH1 and CH2 effects separately. For

Model 4, chemically inactive N₂ with zero third body efficiency was added to the chemical mechanism, as well as the thermodynamic and transport datasets, and used for dilution. By assuming that the transport and thermodynamic properties of the initial CH₄/air mixture were very similar to those of N₂, Model 4 has only the DI effect. In fact, this assumption is highly realistic because the reactants contain 70-73% of N₂. By comparing Models 2 and 4, the reduction in the S_L due to the TD effect can be calculated.

Figure 5-10 presents the percentiles of the reduction in the S_L of methane/air flames due to the DI, TD, CH1, and CH2 effects of different diluents at 1 bar, 473 K, and ϕ =0.8, 1.0, and 1.2. Numerical results in Figure 5-10 reveal that the dilution effect is the most dominant effect for all diluents at all equivalence and dilution ratios. It reaches its maximum of 98% for methane/air flames diluted with 5%, 10%, and 15% N_2 at ϕ =0.8, 1.0, and 1.2. The remaining 2% reduction in the S_L is a result of the chemical effect, which can be attributed to the CH2 effect. 66-71% of the decrease in the S_L values of H_2O -diluted mixtures is because of the dilution effect. In addition, the thermal-diffusion effect lowered the S_L by 10-13% by increasing the specific heat capacity and therefore decreasing the combustion temperature and the reaction rate. The chemical effect of H_2O dilution heavily depends on the participation of H_2O in the third body reactions for ϕ =1.0 and 1.2. At ϕ =0.8, contributions of the CH1 and CH2 effects to the decrease in the S_L are similar.

For methane/air flames diluted with CO_2 , the dilution effect dropped down to 41-46% at ϕ =0.8, 46-51% at ϕ =1.0, and 52-57% at ϕ =1.2. Consequently, the laminar flame speed vs. dilution ratio graphs in Figure 5-8 have a curved shape for CO_2 dilution whereas the same plots for N_2 and H_2O dilutions are almost linear due to the strong dominance of the dilution effect, which scales linearly with increasing dilution ratio. CO_2 has a greater impact on the laminar burning velocity than N_2 and H_2O due to its higher specific heat capacity and lower thermal diffusivity [286], i.e.

the TD effect ranging from 26% to 29%. In fact, CO₂ dilution reduces flame temperature by behaving as a heat sink, which lowers the chance of reaching the activation energy needed for a reaction to take place [284].

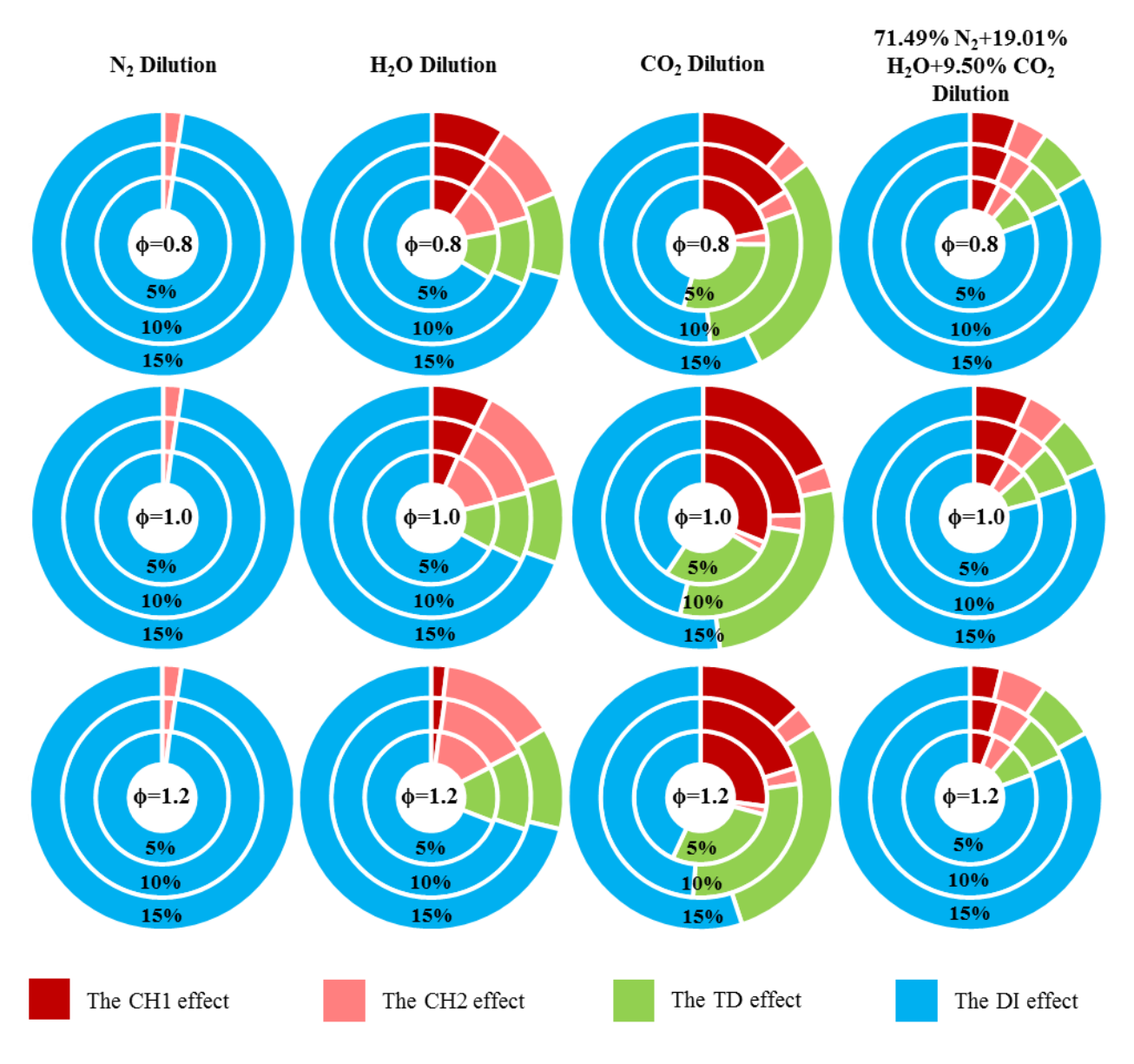


Figure 5-10. Contributions of the dilution, thermal-diffusion, and chemical effects of different combustion residuals to the decrease in the laminar burning velocity of methane/air/diluent mixtures at 1 bar and 473 K.

The chemical effect of 5%, 10%, and 15% CO₂ dilution, which depends mostly on the active participation of CO₂ in dissociation reactions, i.e. the CH1 effect, caused a decrease in the

laminar burning velocity by 25-33%, 20-27%, and 15-22%, respectively. Greater percentile reductions in the S_L due to the chemical effect were observed near stoichiometry and at low dilution ratios because of the higher combustion temperatures at these conditions, which leads to improved elementary dissociation reaction rates.

Detailed sensitivity analysis was performed to gain a better understanding of the most important elementary reactions that affect the burning velocity. The sensitivity analysis showed that CO_2 is involved in an elementary chain-carrying dissociation reaction $CO_2 + H = CO + OH$ and inhibits the combustion of methane/air mixtures by competing for H radicals with the chain-branching reaction $H + O_2 = O + OH$, which is the dominant reaction for the production of reactive radicals that promote the laminar flame speed with the largest positive sensitivity factor as seen in Figure 5-11. With increases in the dilution ratio, the sensitivity coefficients of the elementary reactions shown in Figure 5-11 increase, except for $CO + OH = CO_2 + H$, whose reverse reaction is considered as the main pathway in which CO_2 participates in chemical reactions. This can be attributed to the decreased H radical production due to the excessive CO_2 and also suggests that the chemical effect of CO_2 is less dominant at high dilution ratios.

As shown in Figure 5-10, the most dominant effect of the 71.49% N_2 + 19.01% H_2O + 9.50% CO_2 mixture is the dilution effect with a 79-84% contribution to the methane laminar burning velocity reduction at 1 bar and 473 K. The percentile dilution effect slightly decreases near stoichiometry and at low dilution ratios because of the higher combustion temperatures at these conditions, which leads to an increased chemical effect. The thermal-diffusion effect contributes the least to the decrease in the S_L , which can be attributed to relatively low H_2O and CO_2 concentrations within the combustion residuals of methane/air flames. The variation in the

thermal-diffusion effect relative to the dilution and chemical effects over different equivalence or dilution ratios is negligible. This is similar to the H_2O and CO_2 dilutions shown in Figure 5-10.

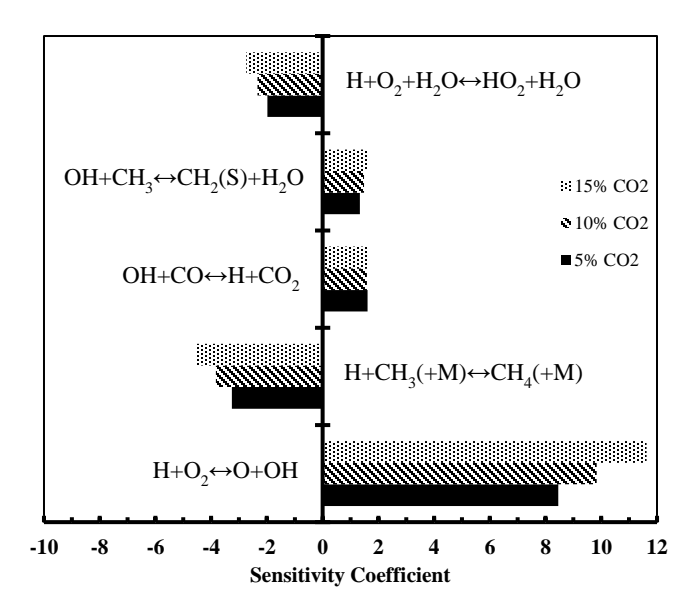


Figure 5-11. Methane sensitivity factors at 1 bar, 473 K, and φ=1.0 for 5%, 10%, and 15% CO₂ dilution.

The chemical effect of the 71.49% $N_2 + 19.01\%$ $H_2O + 9.50\%$ CO_2 mixture is slightly more dominant than the thermal-diffusion effect but gets slightly weaker when the dilution ratio is increased or the equivalence ratio moves away from stoichiometry, due to the lower flame temperatures. For $\phi \le 1.0$, the CH1 effect is slightly more dominant than the CH2 effect, which can be attributed to the high reactivity of CO_2 within the combustion residuals. At fuel rich conditions, the CH1 and CH2 effects have almost the same contributions to the decrease in the S_L , which can be explained by improved chemical activity of H_2O in the third body reactions at $\phi = 1.2$.

In brief, while CO_2 has the strongest CH1 effect due to its active participation in the dissociation reactions and H_2O has the strongest CH2 effect due to the third body reactions, N_2 is the least chemically active main combustion residual resulting from the methane/air combustion. Moreover, CO_2 dilution causes the largest decrease in the laminar burning velocity due to its superior thermal-diffusion effect relative to N_2 and H_2O . The experimental findings in Figure 5-8

and the numerical results presented in Figure 5-10 suggest that N₂, H₂O, and CO₂ have very different thermodynamic properties and chemical reactivities and therefore, simulating post combustion products with only one or two of the main exhaust gases may cause critical errors in experimental laminar burning velocity data. In fact, Figure 5-12 shows that these errors can be as high as 40% for stoichiometric methane/air flames at 1 bar and 473 K with 15% dilution. For the same mixture, Figure 5-12 illustrates that reduction in the laminar burning velocity due to the chemical effect of CO₂ is almost 18 times more than that of N₂.

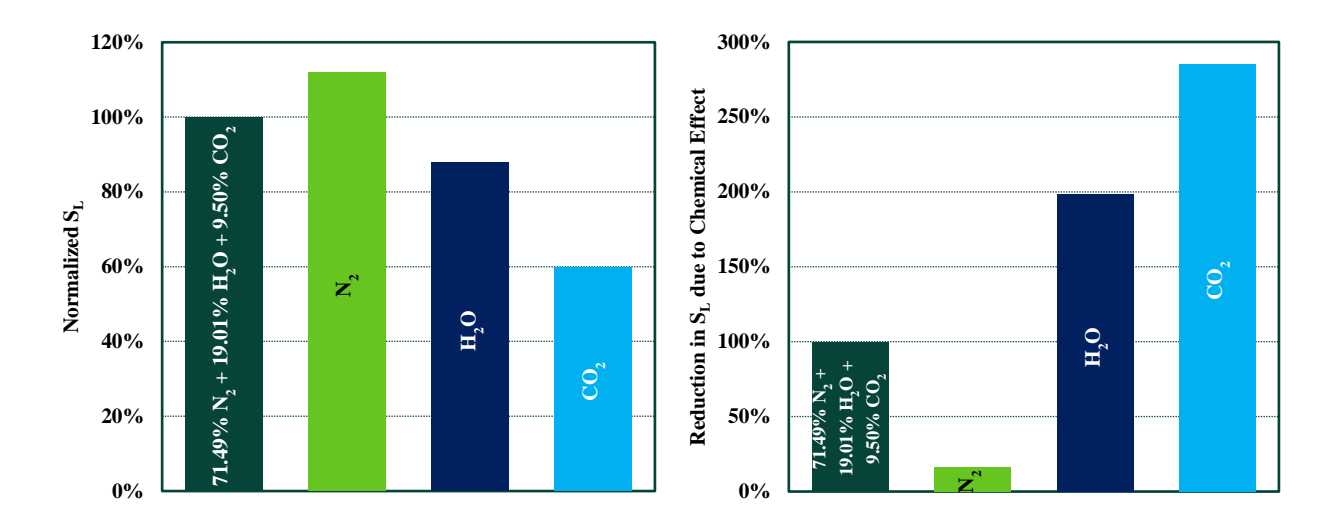


Figure 5-12. Laminar flame speed comparison of stoichiometric methane/air mixtures diluted with different diluents at 1 bar and 473 K with a diluent level of 15%.

After observing significant differences between the laminar flame characteristics of methane/air mixtures diluted with different combustion residuals, the S_L and L_b of methane/air flames diluted with simulated flue gas content were measured at 1 bar and 373 K, 423 K, and 473 K; 3 bar and 373 K and 423 K; and 5 bar and 373 K. The combustion residuals content was simulated by a mixture of 71.49% N_2 + 19.01% H_2O + 9.50% CO_2 by volume, which represents the main post combustion product concentrations of stoichiometric methane/air. 0%, 5%, 10%, and 15% diluent levels were tested.

As shown in Figure 5-13, 5%, 10%, and 15% dilutions led to 5.66-8.85 cm/s, 7.38-8.42 cm/s, and 6.35-7.07 cm/s reductions in the S_L at 1 bar and 373 K; 7.46-11.74 cm/s, 6.20-10.40 cm/s, and 5.81-8.01 cm/s reductions in the S_L at 1 bar and 423 K; 6.78-12.40 cm/s, 9.15-13.61 cm/s, and 8.30-15.00 cm/s reductions in the S_L at 1 bar and 473 K; 6.18-7.78 cm/s, 4.96-6.51 cm/s, and 5.01-5.78 cm/s reductions in the S_L at 3 bar and 373 K; 6.32-8.84 cm/s, 5.78-8.82 cm/s, and 5.75-6.86 cm/s reductions in the S_L at 3 bar and 423 K; and 4.55-7.28 cm/s and 5.47-5.85 cm/s reductions in the S_L (15% dilution was not possible due to the buoyancy effect) at 5 bar and 373 K, respectively, due to decreased methane/air concentration, increased specific heat capacity, and reduced active radicals and effective collisions.

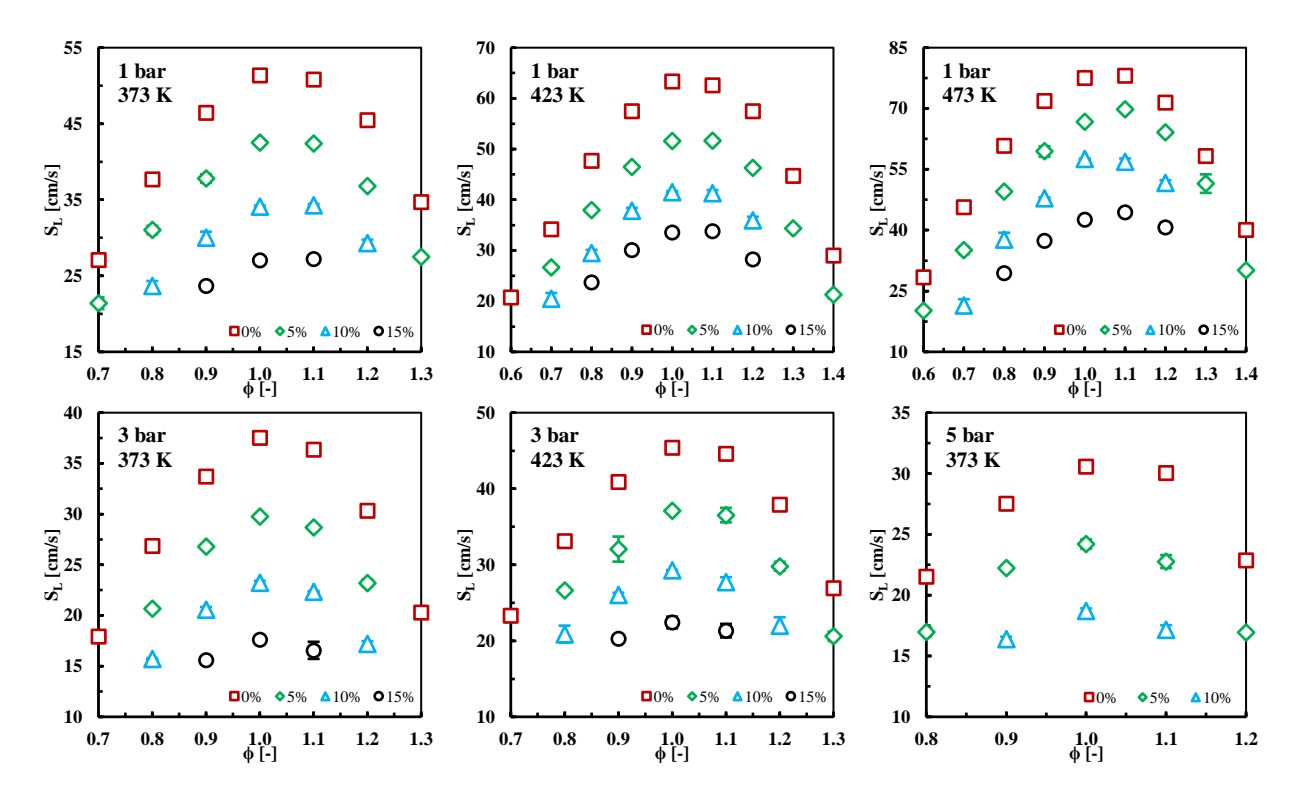


Figure 5-13. Experimental S_L data for methane/air mixtures with 0%, 5%, 10%, and 15% diluent levels.

At each initial condition, the trend of the S_L drop over the dilution ratio is almost linear. This may be due to the large N_2 concentration in the exhaust gas mixture (71.49%) as it was already shown that N_2 is the least chemically-active species among the major flue gas components.

Besides, since thermodynamic properties of N_2 highly resemble those of initial methane/air mixtures, almost the only impact of N_2 on the S_L as a diluent is the reduction of the fuel/oxidizer concentration due to the N_2 addition, which scales linearly with increasing diluent level. However, the decreasing trend of S_L over the dilution ratio is not perfectly linear. In fact, slightly smaller decreases in the S_L were observed at higher diluent levels. This can be attributed to reduced chemical reactivity of CO_2 at high dilution ratios due to lower flame temperatures, which slow down the inhibition of the overall combustion reaction.

While the highest percentile decreases in the S_L because of the dilution were seen away from stoichiometry, percent reductions in the S_L for the same equivalence ratio at different temperatures, pressures, and dilution ratios are very similar. This situation can be explained by the low chemical reactivity of the diluent mixture due to the low concentration of CO_2 within the main exhaust gases (9.50%), which makes the dilution impact of the flue gases the most dominant effect on the S_L reduction. While the chemical effect depends on temperature, pressure, and diluent level, the dilution effect, i.e. the reduction of the fuel/oxidizer concentration, is almost insensitive to these parameters.

The addition of combustion residuals to the methane/air mixtures not only decreases the laminar flame speed but also leads to a flattening of the laminar burning velocity vs. equivalence ratio plots, shown in Figure 5-13, as the dilution rate is increased. This observation is due to a more pronounced decrease in the laminar flame speed near ϕ =1.0 relative to rich and lean conditions, which leads to less variation in the laminar burning velocity over the entire range of equivalence ratios for high dilution rates. Figure 5-10 suggests that the chemical effect is strongest near stoichiometric conditions where the combustion temperature is highest, which results in higher elementary dissociation reaction rates leading to a larger reduction in laminar burning velocity in

the presence of combustion residuals. Consequently, there are greater decreases in the laminar flame speed near stoichiometric conditions compared to rich and lean conditions as the dilution rate is increased.

Figure 5-14 exhibits experimental L_b results of methane/air mixtures at 1-5 bar and 373-473 K with 0%, 5%, 10%, and 15% dilution ratios. The diluent addition changed the Lewis number of the reactants by varying mass as well as thermal diffusivities. As a result, the flame stability and stretch characteristics were changed. Combustion residuals mostly suppressed the thermal-diffusive as well as the hydrodynamic flame instabilities and caused more stretched flames by slightly increasing the L_b and increasing the methane laminar flame thickness and expansion ratio, as shown in Figure 5-1.

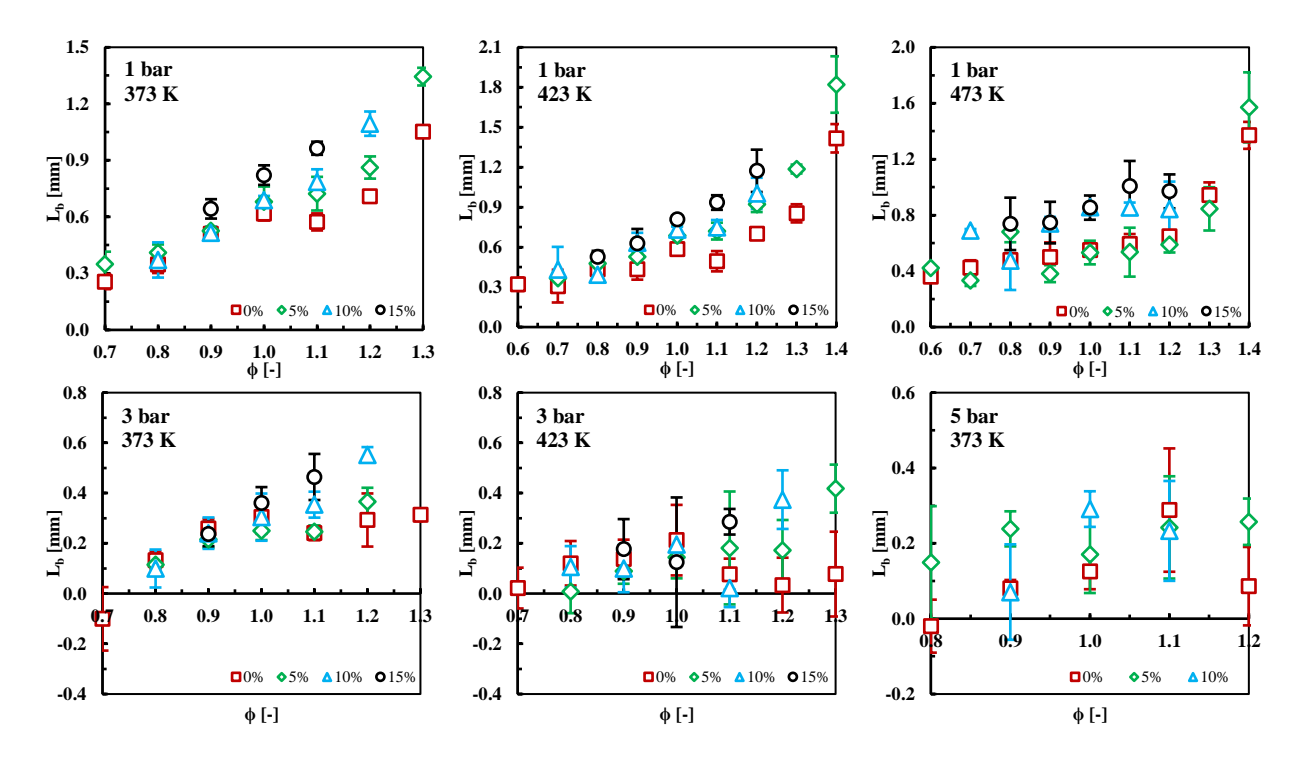


Figure 5-14. Experimental L_b data for methane/air mixtures with 0%, 5%, 10%, and 15% diluent levels.

While there was no significant change in the L_b due to dilution at lean conditions, higher increases in the L_b due to dilution were observed when the equivalence ratio increased. The minor

impact of the flue gases on the L_b is attributable to high N_2 concentrations within the main exhaust gases (71.49%) and the reactants (70-73%). Therefore, the addition of combustion residuals did not change thermal and mass diffusivities of initial methane/air mixtures considerably, which resulted in an only slightly increased Lewis number and L_b . Since N_2 concentration of the reactants reduces with increasing ϕ , greater changes could be seen in the thermodynamic properties of fuel rich mixtures with diluent addition yielding higher increases in the L_b at $\phi>1.0$.

5.6 Laminar Flame Speed Correlation

Semi-empirical S_L correlations, many of which are in the Arrhenius form [297], are based either on Zeldovich and Frank-Kamenetsky's theory for thermal propagation of a flame [299] or on Lewis and von Elbe's diffusion theory [300]. These correlations are very sensitive to the thermodynamic model utilized to compute the adiabatic flame temperature [70]. Moreover, the Arrhenius parameters change with the ϕ irregularly [70]. On the other hand, completely empirical S_L correlations derived from the data fit to experimental or numerical results allow smooth variation of the S_L across temperature and equivalence ratio [297]. Therefore, the most commonly used form of the completely empirical correlations, Metghalchi and Keck's power law [112] - Equation 5-1, was adopted in the present study.

As suggested by Stone et al. [72], additional terms were included for equivalence and dilution ratio effects instead of defining power coefficients as a function of ϕ and X in order to lower errors in the data fitting. For simplicity, quadratic expressions were preferred for ϕ and X dependencies in the initial nonlinear regression model, which is shown in Equation 5-2. T_u and P were nondimensionalized by division with $T_{u,o}$ =298 K and P_o =1 bar. Coefficients of b_1 - b_9 were adjusted to minimize the root mean square error (RMSE).

$$S_{L} = b_{1} * \left(\frac{T_{u}}{T_{u,o}}\right)^{b_{2}} * \left(\frac{P}{P_{o}}\right)^{b_{3}} * (b_{4} + b_{5}\phi + b_{6}\phi^{2}) * (b_{7} + b_{8}X + b_{9}X^{2})$$
5-2

Nonlinear regression model coefficients (b₁-b₉) were initially estimated from the S_L correlation of Elia et al. [73]. The RMSE was defined as the standard deviation of the residuals, which is the difference between the experimental data and the S_L values predicted by the correlation. The model coefficients were optimized with the generalized reduced gradient (GRG) method proposed by Lasdon et al. [301]. The GRG method is an extension of the reduced gradient method by allowing nonlinear constraints and arbitrary bounds on the variables. The method searches for a local optima for an objective variable in the vicinity of the initial estimation by screening partial derivatives. In the present study, the objective variable was set as the root mean square of the residuals. A forward difference formula was used for derivatives. The convergence criteria was defined as a change in the objective variable less than 0.0001 between two consecutive iterations.

As a result of the nonlinear optimization of the model coefficients, a completely empirical S_L correlation with an RMSE of 2.34 cm/s was derived from 133 experimental test points (399 measurements in total). Subsequently, detailed sensitivity analysis was performed for each term/coefficient in the correlation. It was found that S_L values were least sensitive to the quadratic term of the dilution ratio (b_9X^2), which suggests that there is almost a linear relation between the S_L and X. This finding is also consistent with the conclusion drawn from Figure 5-8 and Figure 5-13, which show that the trend of the S_L drop over the dilution ratio is almost linear due to high N_2 concentration within the main exhaust gases. Therefore, the regression model was updated by omitting the quadratic term of the dilution ratio.

Optimization of the model coefficients was repeated and the final S_L correlation, i.e. Equation 5-3, was obtained with an RMSE of 2.40 cm/s. Equation 5-3 is valid at 1 bar and 373-

473 K, 3 bar and 373-423 K, and 5 bar and 373 K for 0-15% dilution ratios (except at 5 bar and 373 K, where the maximum diluent level is 10% due to the buoyancy effect). Like Stone et al. [72] and Hinton et al. [296], a higher degree of polynomials (cubic and quartic) for the φ effect were also investigated, but a significant improvement in the correlation accuracy was not achieved.

$$S_{L} = b_{1} * \left(\frac{T_{u}}{T_{u,0}}\right)^{b_{2}} * \left(\frac{P}{P_{0}}\right)^{b_{3}} * (b_{4} + b_{5}\phi + b_{6}\phi^{2}) * (b_{7} + b_{8}X)$$
5-3

where S_L is in cm/s, T_u in K, P in bar, ϕ - dimensionless, X - dimensionless (e.g. 0.10 – not 10%), $T_{u,o}$ =298 K, P_o =1 bar, b_1 =30.53, b_2 =2.035, b_3 =-0.352, b_4 =-2.686, b_5 =6.778, b_6 =-3.272, b_7 =1.234, and b_8 =-3.997.

The newly proposed S_L correlation, Equation 5-3, has an excellent agreement with current experimental data with an RMSE of 2.40 cm/s. The correlation accuracy is not affected by a change in pressure, temperature, and dilution ratio whereas it slightly deteriorates at very lean conditions. The maximum deviation between the experimental and correlation results was detected as 8.77 cm/s at 1 bar, 473 K, ϕ =0.6, and X=0%. S_L values provided by the correlation were plotted in Figure 5-15 with current experimental findings at 1 bar and 373 K, 1 bar and 473 K, and 5 bar and 373 K to visualize the differences between the S_L results. As seen in Figure 5-15, S_L predictions of the correlation are highly consistent with the experimental data. However, dissimilarities can be observed at very low/high equivalence ratios.

Current measurements and the newly developed correlation were compared with the correlations proposed by Stone et al. [72], Gu et al. [21], Elia et al. [73], Han et al. [293], Hu et al. [292], Amirante et al. [297], and Hinton et al. [296] at the designated test conditions shown in Table 5-4. The RMSE value of each correlation is presented in Table 5-4 together with the RMSE of the current S_L correlation at the given test conditions. The correlations of Gu et al. [21] and Stone et al. [72] were modified so that they provide S_L values in cm/s like the other correlations.

While temperature is in K for all correlations in Table 5-4, the unit of the pressure is either bar or atm depending on the definition of the authors, which can be found in 5.1 Introduction and Literature Review.

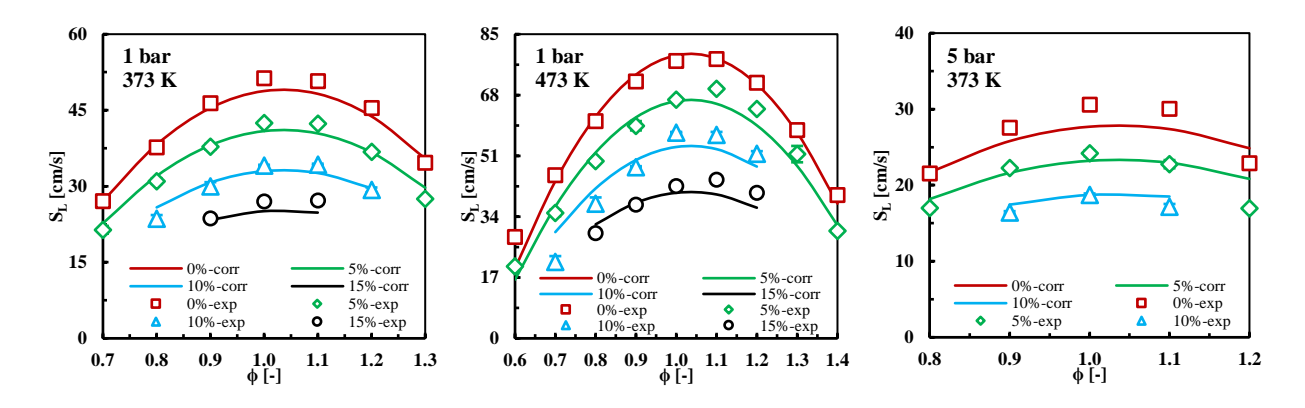


Figure 5-15. Comparison of measured and predicted S_L data for methane/air mixtures.

Only two S_L correlations considering the diluent effect, i.e. Stone et al. [72] and Elia et al. [73], represent the dilution effect with extra terms, which are not linear. However, the present study prove that there is almost a linear relation between the S_L and X as a result of a large N_2 concentration in the exhaust gas mixture. The reason behind Stone et al. [72] and Elia et al. [73] not observing the same trend of the S_L drop over the dilution ratio may be because of the fact that they used a mixture of 85-86% N_2 + 15-14% CO_2 for dilution. The present study revealed that CO_2 is much more chemically active than N_2 and H_2O and it affects thermodynamic properties of initial methane/air mixture more than these two. Therefore, replacing H_2O with N_2 and CO_2 and almost doubling the normal CO_2 concentration within the flue gases can cause a nonlinear relation between the S_L and X, which does not truly represent the effects of combustion residuals on the S_L . Apart from that, high RMSE values of these two correlations can be attributed to ignoring the possibility of cellularity on the flame surface and the improper treatment of the flame stretch.

Table 5-4. Comparison of various S_L correlations against the current experimental results.

Reference	Correlation	Test Conditions	RMSE	RMSE of the Present Correlation
Present Work	$S_L = 30.53* \left(\frac{T_u}{298}\right)^{2.035}* \left(\frac{P}{1}\right)^{-0.352}* \left(-2.686 + 6.778 \varphi - 3.272 \varphi^2\right)* (1.234 - 3.997X)$	 1-5 bar 373-473 K φ=0.6-1.4 X=0-15% 	2.40	2.40
Stone et al. [72]	$\begin{split} S_L &= 100*\left(\frac{T_u}{298}\right)^{1.42-1.98(\varphi-1)} * \left(\frac{P}{1}\right)^{-0.314+0.608(\varphi-1)} \\ * \left[0.376+0.151(\varphi-1)-2.21(\varphi-1)^2-0.458(\varphi-1)^3 \right. \\ &+ 3.58(\varphi-1)^4\right] * \left(1-2.046X^{(0.730+0.447(\varphi-1))}\right) \end{split}$	 1-5 bar 373-423 K φ=0.6-1.4 X=0-15% 	3.34	1.96
Gu et al. [21]	$\begin{split} S_L &= 25.9 \left(\frac{T_u}{300}\right)^{2.105} \left(\frac{P}{1}\right)^{-0.504} & \text{for } \varphi = 0.8 \\ S_L &= 36.0 \left(\frac{T_u}{300}\right)^{1.612} \left(\frac{P}{1}\right)^{-0.374} & \text{for } \varphi = 1.0 \\ S_L &= 31.4 \left(\frac{T_u}{300}\right)^{2.000} \left(\frac{P}{1}\right)^{-0.438} & \text{for } \varphi = 1.2 \end{split}$	 1-5 bar 373 K 	2.84	1.96
Elia et al. [73]	$\begin{split} S_L &= 37.5* \left(\frac{T_u}{298}\right)^{1.857}* \left(\frac{p}{1}\right)^{-0.435}* \left(-5.883 + 14.003\varphi - 7.115\varphi^2\right)\\ &* \left[1 - \left(4.829X - 7.778X^2 + 0.003X^3\right)\right] \end{split}$	 1-5 bar 373-473 K φ=0.8-1.2 X=0-15% 	5.17	2.01
Han et al. [293]	$S_L = 36.11 \left(\frac{T_u}{298}\right)^{1.5365+0.1165P} \left(\frac{P}{1}\right)^{-0.37}$	 1-5 bar 373-473 K φ=1.0 X=0% 	0.87	2.14
Hu et al. [292]	$S_L = 37 \left(\frac{T_u}{300}\right)^{1.39 + 0.0006 T_u} \left(\frac{P}{l}\right)^{0.226 exp(-P/0.841) - 0.511}$	 1-5 bar 373-473 K φ=1.0 X=0% 	5.26	2.14
Amirante et al. [297]	$\begin{split} &S_L\\ &= 38.85 \varphi^{-0.20} exp(-6.45(\varphi\\ &- 1.08)^2) \left(\frac{T_u}{298}\right)^{(6.9258-10.287\varphi+4.9199\varphi^2)} \left(\frac{P}{1}\right)^{(-1.7492+2.6808\varphi-1.3712\varphi^2)} \end{split}$	 1-5 bar 373-473 K φ=0.6-1.4 X=0% 	4.32	2.34
Hinton et al. [296]	$\begin{split} S_L = \left(\frac{T_u}{298}\right)^{2.0879 + 0.17135(\varphi - 1) + 5.4338(\varphi - 1)^2} * \left(\frac{P}{1}\right)^{-0.3463 - 0.0419(\varphi - 1) - 0.9067(\varphi - 1)^2} \\ * \left[30.799 + 1.6141(\varphi - 1) - 241.19(\varphi - 1)^2 \right. \\ - 22.214(\varphi - 1)^3 + 680.84(\varphi - 1)^4 \end{split}$	 1-3 bar 423-473 K φ=0.7-1.4 X=0% 	3.69	1.60

The performance of the correlations proposed by Gu et al. [21] is satisfactory, but using different correlations for different equivalence ratios is not convenient. In addition, these correlations are not valid at high temperatures (higher than 400 K) and for diluted methane/air flames. The power law correlation of Han et al. [293] is the only correlation in Table 5-4 having superior accuracy over the present correlation at designated test conditions. However, it can only be employed for stoichiometric methane/air mixtures without dilution. High RMSE of the

correlation developed by Hu et al. [292] may be a result of using numerical data obtained by the USC Mech II [224] to extend the correlation to elevated pressures and temperatures, which are beyond experimentally tested points. Amirante et al. [297] developed an empirical correlation for non-diluted methane/air mixtures by collecting, comparing, and analyzing previously published experimental S_L data. In their paper, Amirante et al. [297] mentioned the need of a deeper analysis due to scarce data for rich and lean mixtures at elevated initial temperatures and pressures. Finally, the correlation of Hinton et al. [296] shows that using higher order terms for the ϕ effect does not assure a better correlation accuracy.

5.7 Burned Gas Markstein Length Correlation

A similar approach used for the S_L correlation development was employed for data fitting to experimental L_b findings at 1 bar and 373-473 K, 3 bar and 373-423 K, and 5 bar and 373 K for 0-15% dilution ratios (except at 5 bar and 373 K, where maximum diluent level is 10% due to the buoyancy effect). An initial nonlinear regression model was defined as Equation 5-4 in the form of Metghalchi and Keck's power law [112]. T_u and P were nondimensionalized by division with $T_{u,o}$ =298 K and P_o =1 bar. Coefficients of b_1 - b_9 were optimized with the GRG method [301] and the RMSE was minimized to 0.11 mm.

$$L_{b} = b_{1} * \left(\frac{T_{u}}{T_{u,o}}\right)^{b_{2}} * \left(\frac{P}{P_{o}}\right)^{b_{3}} * (b_{4} + b_{5}\phi + b_{6}\phi^{2}) * (b_{7} + b_{8}X + b_{9}X^{2})$$
5-4

Nonlinear optimization of the model coefficients was followed by the detailed sensitivity analysis for each term/coefficient in the regression model. Similar to sensitivity results of the S_L correlation, L_b values were least sensitive to the quadratic term of the dilution ratio (b_9X^2), which suggests that there is almost a linear relation between the L_b and X. Therefore, the regression model was updated by omitting the quadratic term of the dilution ratio. Then, optimization of the model coefficients was repeated and the RMSE value did not change, i.e. RMSE=0.11 mm. Accuracies

of cubic and quartic expressions for the dilution effect were also assessed but no improvement was achieved in the correlation accuracy. On the other hand, adding a cubic term to the expression accounting for the ϕ effect improved the correlation accuracy by 9%, i.e. new RMSE=0.10 mm. A quartic expression was also evaluated for the ϕ effect but the correlation accuracy remained unchanged. In the light of aforementioned investigations, the final L_b correlation was set as Equation 5-5.

$$L_{b} = b_{1} * \left(\frac{T_{u}}{T_{u,o}}\right)^{b_{2}} * \left(\frac{P}{P_{o}}\right)^{b_{3}} * (b_{4} + b_{5}\phi + b_{6}\phi^{2} + b_{7}\phi^{3}) * (b_{8} + b_{9}X)$$
5-5

where L_b is in mm, T_u in K, P in bar, ϕ - dimensionless, X - dimensionless (e.g. 0.10 – not 10%), $T_{u,o}$ =298 K, P_o =1 bar, b_1 =2.848, b_2 =-0.363, b_3 =-1.031, b_4 =-0.738, b_5 =2.816, b_6 =-3.198, b_7 =1.250, b_8 =1.487, and b_9 =5.913.

The L_b values decrease with increasing pressure. Similarly, increasing temperature generally lowers the L_b very slightly. Therefore, both b_2 and b_3 coefficients are negative and b_2 is 35% of b_3 . The newly proposed L_b correlation, Equation 5-5, has good agreement with current experimental data with an RMSE of 0.10 mm. The correlation accuracy is not affected by a change in pressure, temperature, or equivalence and dilution ratios. However, the correlation accuracy slightly deteriorates at 473 K. The maximum deviation between the experimental and correlation results was detected as 0.28 mm at 1 bar, 473 K, ϕ =1.3, and X=5%.

To visualize the performance of the correlation at different equivalence and dilution ratios, L_b values provided by the correlation were plotted at ϕ =0.8, 1.0, and 1.2 for X=0-15% in Figure 5-16 with current experimental findings at 1 bar and 373 K, 1 bar and 473 K, and 3 bar and 373 K. As can be seen in Figure 5-16, the burned gas Markstein length predictions of the correlation are consistent with the experimental data. However, deviation of experimental points from the

linear L_b -vs-X trend line can be observed especially at very lean/rich conditions for high dilution ratios.

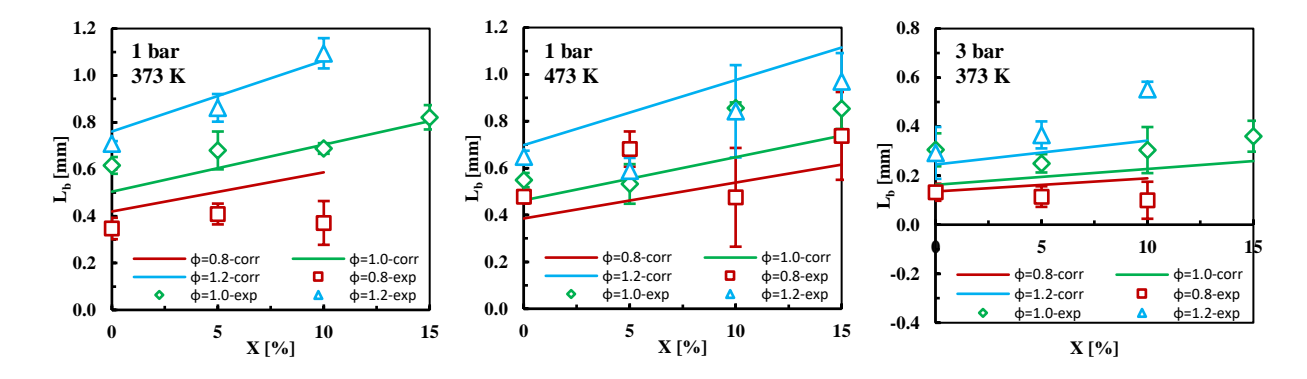


Figure 5-16. Comparison of measured and predicted L_b data for methane/air mixtures.

5.8 Numerical Laminar Flame Speed Results

Initially, numerical analyses were performed in the Chemkin-Pro software [215] with the GRI-Mech 3.0 [223], USC Mech II [224], San Diego [225], HP-Mech [226], NUI Galway-CH₄/DME [227], and AramcoMech 1.3 [228] mechanisms for methane/air mixtures at 3 bar and 423 K with and without dilution. Numerical results were compared with the experimental S_L data to evaluate performances of these chemical mechanisms. As shown in Figure 5-17, The numerical results obtained by the GRI-Mech 3.0 [223] and HP-Mech [226] mechanisms and the current experimental results at 3 bar and 423 K were in excellent agreement overall, yet experimental results differed from those predicted by the HP-Mech [226] by as much as 7% at very rich initial conditions. The biggest discrepancy between GRI-Mech 3.0 [223] and experimental results was 9% for very rich mixtures diluted by 5%.

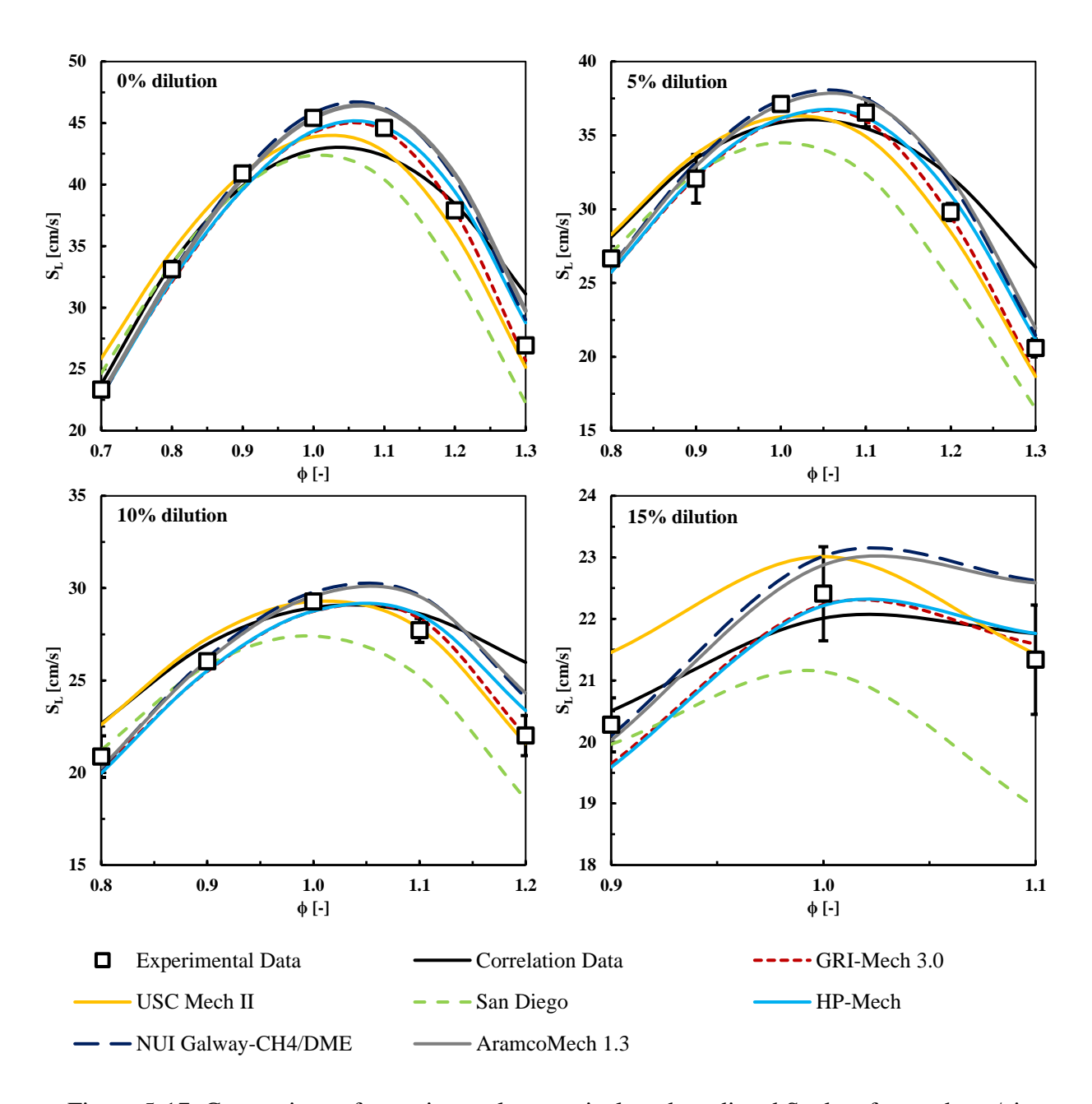


Figure 5-17. Comparison of experimental, numerical, and predicted S_L data for methane/air mixtures at 3 bar and 423 K.

The GRI-Mech 3.0 [223] and HP-Mech [226] provided very close S_L values for mixtures with $\phi \leq 1.0$, which are slightly slower than the experimental findings. Mazas and coworkers made similar observations for CH₄/O₂ mixtures slightly diluted with CO₂ and H₂O at a temperature of 373 K and a pressure of 1 bar [9] and for CH₄/air mixtures diluted with <10% of H₂O at 373 K and 1 bar [291]. Laminar flame speeds obtained with the HP-Mech [226] are consistently faster than

those of the GRI-Mech 3.0 [223] and experimental data at φ>1.0. The average deviations of the S_L data provided by the GRI-Mech 3.0 [223] and HP-Mech [226] mechanisms from current measurements are 2% and 3%, respectively. The accuracy of the HP-Mech [226] in predicting the S_L values of diluted methane/air mixtures is attributable to the fact that it has been tailored for C₀-C₂ hydrocarbon fuels with exhaust gas dilution [235]. As the dilution ratio increases, the GRI-Mech 3.0 accuracy improves, suggesting that the GRI-Mech 3.0 [223] is competent in third body and elementary dissociation reactions of combustion residuals.

Numerical results of the USC Mech II [224], NUI Galway-CH₄/DME [227], and AramcoMech 1.3 [228] mechanisms in Figure 5-17 are in good agreement with experimental findings with an average deviation of 4%. The USC Mech II [224] overpredicted the S_L at lean conditions by as much as 11% and underestimated the S_L for rich mixtures diluted with 0% and 5% of combustion residuals. The USC Mech II [224] was highly accurate in its predictions, except at very lean conditions. This accuracy may be a result of the mechanism undergoing optimization/validation for C1-C4 hydrocarbons at a temperature of 300 K and at pressures in the range of 1-5 bar [224].

The S_L results of the NUI Galway-CH₄/DME [227] and AramcoMech 1.3 [228] mechanisms are almost identical, which makes the NUI Galway-CH₄/DME kinetic scheme [227] more practical than the AramcoMech 1.3 [228] for the S_L prediction of diluted CH₄/air mixtures at 3 bar and 423 K since the NUI Galway-CH₄/DME [227] consists of 710 reactions and 113 species while the AramcoMech 1.3 [228] contains 1542 reactions and 253 species. Both mechanisms performed well at $\phi \leq 1.0$ but started to overpredict the S_L for fuel rich mixtures.

The San Diego detailed kinetic scheme [225] provided flame speed predictions similar to the experimental results in Figure 5-17 for equivalence ratios less than or equal to 0.9, but the mechanism's results differed from experimental data by up to 20% for higher equivalence ratios. Similar to the Figure 5-17 results, Akram and Kumar [232], Park et al. [233], and Ren et al. [234] found that the San Diego mechanism [225] underestimated the S_L for rich CH_4 /air flames at 1 bar and 298 K.

For methane/air mixtures at 3 bar and 423 K with and without dilution, satisfactory agreement was observed between the experimental data and computational results obtained by the GRI-Mech 3.0 [223], USC Mech II [224], HP-Mech [226], NUI Galway-CH4/DME [227], and AramcoMech 1.3 [228] mechanisms. However, the San Diego chemical mechanism [225] showed poor performance in predicting the S_L at these conditions. Furthermore, the AramcoMech 1.3 [228] predicted almost identical S_L values with the NUI Galway-CH4/DME [227], which contains considerably less chemical reactions compared to the AramcoMech 1.3 [228]. Therefore, numerical analyses for methane/air mixtures with 0%, 5%, 10%, and 15% dilution at 1 bar and 373 K, 423 K, and 473 K; 3 bar and 373 K; and 5 bar and 373 K were performed only with the GRI-Mech 3.0 [223], USC Mech II [224], HP-Mech [226], and NUI Galway-CH4/DME [227] chemical mechanisms.

Numerical results were compared with the S_L data provided by experimental measurements and the newly developed correlation in this study, which is summarized in Table 5-5 and visualized for CH₄ flames at 1 bar and 423 K in Figure 5-18. The RMSE_{exp} and RMSE_{corr} values in Table 5-5 represents the RMSE of each mechanism relative to the experimental measurements and the RMSE of each mechanism relative to the newly developed correlation, respectively.

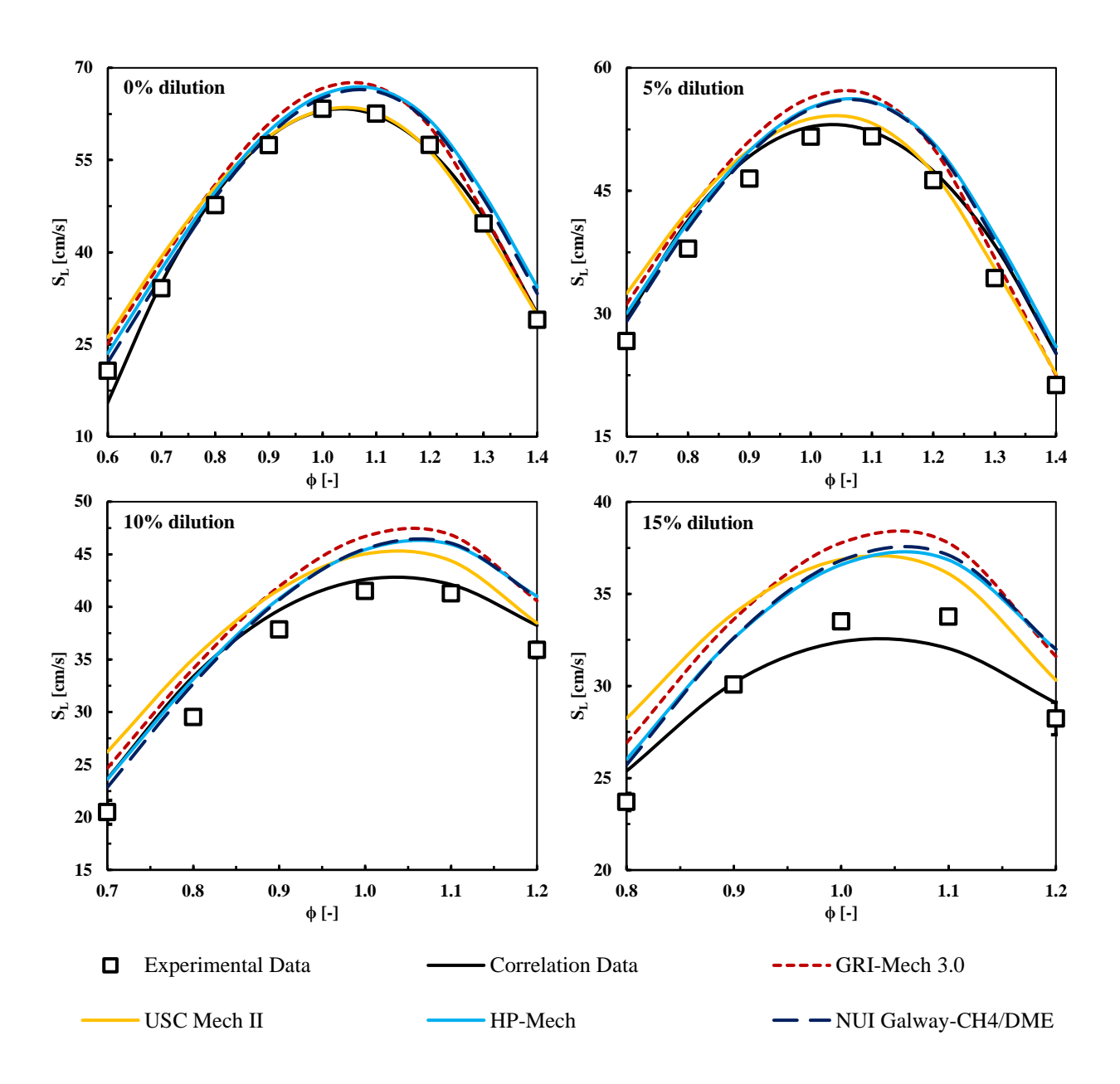


Figure 5-18. Comparison of experimental, numerical, and predicted S_L data for methane/air mixtures at 1 bar and 423 K.

Table 5-5. Comparison of various chemical mechanisms against current experimental results and S_L correlation.

Mechanism	RMSE _{exp}	RMSEcorr	General Trend
GRI-Mech 3.0 [223]	2.74 cm/s	3.20 cm/s	 Overprediction at high temperatures and low pressures Underestimation at high pressures
USC Mech II [224]	2.78 cm/s	2.93 cm/s	 Deteriorated accuracy (overprediction) at lean conditions Slight underestimation at rich conditions
HP-Mech [226]	2.21 cm/s	2.62 cm/s	 Overprediction at high temperatures and low pressures Slight underestimation at high pressures
NUI Galway- CH4/DME [227]	1.82 cm/s	2.38 cm/s	 Deteriorated accuracy (overprediction) at low pressures, low temperatures, and φ≥1.0 Improved accuracy at high temperatures and pressures

The overall trends of the numerical results obtained by testing the four mechanisms are highly consistent with that of the experimental data. The NUI Galway-CH₄/DME kinetic scheme [227] provided the closest S_L values to the experimental findings with an RMSE of 1.82 cm/s. While it overpredicted rich CH₄ laminar burning velocities at low pressures and temperatures, its accuracy improved at elevated initial conditions. The HP-Mech [226] has superior performance over the other three mechanisms at high dilution ratios, which can be attributed to its optimization for the exhaust gas dilution effect on C_0 - C_2 fuels [235]. The mechanism generally overpredicted the S_L at high temperatures and low pressures while it slightly underestimated the S_L at elevated pressures. The GRI Mech 3.0 [223] showed a similar trend to the HP-Mech [226] but its RMSE value is 2.74 cm/s, which is higher than that of the HP-Mech [226], i.e. 2.21 cm/s. The USC Mech II [224] predictions were very similar to experimental data around stoichiometry; however, its accuracy deteriorated when moving further from ϕ =1.0. The USC Mech II [224] overpredicted the S_L at lean conditions and slightly underestimated the S_L for rich mixtures.

5.9 Conclusions

With the increasing role of renewable energy sources in power production, contemporary natural gas-fired power plants should exhibit high load flexibility [25]. Consequently, axial (sequential) stage combustion systems for stationary gas turbines have been gaining in popularity since they can provide lower emissions, higher combined cycle efficiency, and enhanced operational and fuel flexibilities [26]. However, hot inert combustion residuals transferred from the first to second stage of the sequential two-stage combustor affect the flame reactivity and stability [10]. In order to investigate these effects, the S_L and L_b of CH₄/air mixtures with flue gases at 1-5 bar and 373-473 K were measured, as these laminar flame characteristics are associated with the reactivity and stability of the flame [12]. All experimental results with uncertainties and numerical data obtained with the Chemkin-Pro software [215] are provided in Appendices L and M.

Experimental results showed that the S_L at 1 bar increased by 23-29% and 22-34% with temperature increases from 373 K to 423 K and 423 K to 473 K, respectively, which was due mainly to the enhanced dissociation reactions and higher expansion ratios. The S_L at 373 K decreased by 27-33% and 17-25% with pressure increases from 1 bar to 3 bar and from 3 bar to 5 bar, respectively, due mainly to the decreased dissociation. Peak laminar burning velocities were observed at ϕ =1.0-1.1, where the adiabatic flame temperature is at a maximum, which yields improved chemical reactivity, and where the expansion ratio is at a minimum. The S_L reduced at both lean and rich conditions.

Experimental and numerical S_L data of methane/air mixtures diluted with N_2 , H_2O , CO_2 , and a mixture of 71.49% N_2 + 19.01% H_2O + 9.50% CO_2 at 1 bar and 473 K showed that an accurate simulation of the actual combustion residuals with one of the main exhaust gases is

impossible. Even using a mixture of two main exhaust gases to mimic combustion residuals by achieving the same expansion ratio may lead to significant error in the laminar burning velocity calculations, as thermodynamic properties and chemical reactivities of the combustion residuals can change considerably with temperature, pressure, and equivalence and dilution ratios. For instance, while CO_2 has the strongest CH1 effect and H_2O has the strongest CH2 effect, N_2 is the least chemically active main combustion residual resulting from methane/air combustion. CO_2 dilution causes the largest reduction in the S_L as a result of its superior thermal-diffusion effect relative to N_2 and H_2O .

After observing significant differences between the laminar flame characteristics of methane/air mixtures diluted with different combustion residuals, the actual combustion residuals content was simulated by a mixture of 71.49% $N_2 + 19.01\%$ $H_2O + 9.50\%$ CO_2 by volume, which represents the main post combustion product concentrations of stoichiometric methane/air, for the S_L and L_b measurements of methane/air flames at 1-5 bar and 373-473 K. Due to a combination of decreased methane/air concentration, increased specific heat capacity, and reduced active radicals and effective collisions, the combustion residuals addition lowered the S_L almost linearly because of the high N_2 concentration within the main exhaust gases. For the same reason, the percent reduction in the S_L due to the dilution is nearly insensitive to the temperature, pressure, and dilution ratio changes at the same equivalence ratio.

The L_b increased with increasing equivalence ratio and decreased at high pressures, which suggests that rich methane/air flames at low pressures are more stable and stretched than lean ones at high pressures. Moreover, the pressure rise decreased the methane flame thickness and slightly lowered the expansion ratio, which enhances the intensity of the hydrodynamic flame instabilities. The temperature effect on the L_b is almost negligible. Increasing the unburned gas temperature

generally lowered the L_b very slightly and caused a thinner flame thickness and greater expansion ratio. The cellular formation was delayed with the addition of flue gases to the reactants by slightly increasing the L_b and increasing the flame thickness and expansion ratio. The small effect of combustion residuals on the L_b was found to be due to the high N_2 concentrations within the main exhaust gases and reactants.

Due to their easier usage in computational fluid dynamic codes than tabulated data, laminar flame speed correlations are essential for many combustion models [302]. Therefore, in the present study, the S_L and L_b correlations for methane/air mixtures with 0-15% dilution at 1-5 bar and 373-473 K were developed in the form of Metghalchi and Keck's power law [112] with extra terms for equivalence and dilution ratio effects. The newly proposed S_L correlation has an excellent agreement with current experimental data with an RMSE of 2.40 cm/s. The correlation accuracy is not affected by a change in pressure, temperature, and dilution ratio whereas it slightly deteriorates at very lean conditions. A similar approach was followed for the L_b correlation. The newly proposed L_b correlation is consistent with present experimental findings with an RMSE of 0.10 mm. Pressure, temperature, and equivalence and dilution ratios do not have a noteworthy impact on the correlation accuracy. However, the accuracy of the L_b correlation slightly worsens at 473 K.

In combination with the experimental results, the accuracies of the GRI-Mech 3.0 [223], USC Mech II [224], HP-Mech [226], and NUI Galway-CH₄/DME [227] mechanisms were assessed. The general trends of numerical results obtained by the four tested mechanisms are very similar to the experimental findings. The NUI Galway-CH₄/DME [227] was most consistent with the current measurements. The HP-Mech [226] predictions were very similar to experimental data consisting of high dilution ratios. The USC Mech II [224] had superior performance over the other

three mechanisms around stoichiometry. The GRI-Mech 3.0 [223] generally overpredicted the $S_{\rm L}$ at high temperatures and low pressures whereas it slightly underestimated the $S_{\rm L}$ at elevated pressures.

6 SUMMARY AND CONCLUDING REMARKS

The main goal of this research is to advance understanding of fundamental characteristics of fuel/air/diluent flames that occur in modern stationary gas turbine combustors and internal combustion engines. Although conclusions regarding the experimental and numerical results are presented as a part of each chapter, remarks addressing the general aspects of this research are presented as answers to the research questions posed in Chapter 1. Before the concluding remarks, the experimental and modeling research achievements are highlighted.

An optically accessible high pressure and high temperature constant volume combustion chamber was designed and constructed to employ the spherically expanding flame approach. An experimental procedure and a post-processing/data analysis methodology were established for the laminar flame speed measurement. The experimental apparatus and flame speed calculation methodology were validated by comparing current measurements for hydrogen/air, methane/air, propane/air, and iso-octane/air mixtures to previously published experimental data. Numerous high pressure and high temperature experiments (~1000) were completed to examine the dilution effect on laminar flame characteristics of petroleum-derived liquid fuels and natural gas.

A 1-dimensional kinetic model of the combustion reactions occurring in the constant volume combustion chamber was developed using the Chemkin-Pro software [215] in conjunction with several kinetic mechanisms in order to test the performance of these mechanisms at high pressures, temperatures, and dilution ratios. A new chemical kinetic modeling approach was introduced to quantify effects of combustion residuals on the laminar burning velocity reduction separately. Numerous computational simulations (~300) were performed to investigate impacts of a diluent on laminar flame characteristics of petroleum-derived liquid fuels and natural gas.

1. What is the effect of the measurement range on the stretch model accuracy?

The effect of the measurement range on the stretch model accuracy was investigated with spherically expanding flames of methane/air mixtures at 1 bar and 298 K, hydrogen/air mixtures at 1 bar and 298 K, propane/air mixtures at 1 bar and 298 K, and iso-octane/air mixtures at 1 bar and 373 K. Experimental results show that there is a critical lower radius limit for the laminar flame speed calculation (R_{L,critical}), where all S_L and L_b values obtained by the extrapolation of the LS, NQ, and LC stretch models in Table 2-3 converge to the same S_L and L_b. Therefore, the choice of the extrapolation expression plays no role in the stretch model accuracy as long as the measurements are started at the R_{L,critical}.

The value of the $R_{L,critical}$ strongly depends on the L_b and δ_L , i.e. $Ma_b = L_b/\delta_L$, and this dependency can be expressed with $|Ma_b|$ =0.8424* $R_{L,critical}$ for fuel/oxidizer mixtures with -0.62 \leq $Ma_b \leq$ 2.60. The correlation between Ma_b and $R_{L,critical}$ presented in this study provides not only a potential remedy to scattered experimental S_L data due to the utilization of different stretch models and lower radius measurement limits for the same mixtures, but also a lower limit for the measurement range for spherically expanding flames where the flame stretch is weak and the assumptions of the LS, NQ, and LC stretch models are satisfied so that these three models provide the same S_L and L_b values.

The effect of the upper radius limit for the laminar flame speed calculation on $R_{L,critical}$, S_{L} , and L_{b} was also studied. For fuel/air mixtures with $R_{L,critical} \le 1.58$ cm, no significant change in the $R_{L,critical}$, S_{L} , and L_{b} values was observed when the R_{up} changed from 4.36 cm to 3.0-3.5 cm. Therefore, it can be concluded that the $R_{L,critical}$ does not depend on the R_{up} at these conditions.

2. How different are the effects of various diluents on the laminar burning velocity and flame stability of a combustible mixture?

Almost all experimental studies in the past that have examined how combustion residuals affect the laminar flame characteristics of fuel/oxidizer mixtures have only used one or a mixture of two main exhaust gases (N_2 , H_2O , and CO_2). In order to address this problem, S_L and L_b values of methane/air mixtures diluted with N_2 , H_2O , CO_2 , and a mixture of 71.49% N_2 + 19.01% H_2O + 9.50% CO_2 , which corresponds with the percentage of core products that result from stoichiometric CH_4 /air combustion, were measured at 1 bar and 473 K.

Experimental results and numerical analyses show that simulating post combustion products used to dilute a fuel/air mixture with only one or two of the main exhaust gases may result in erroneous data since N_2 , H_2O , and CO_2 have vastly dissimilar thermodynamic properties and chemical reactivities. For instance, CO_2 actively participates in elementary dissociation reactions and H_2O has a high third body collision efficiency. On the other hand, N_2 is the least chemically active main combustion residual resulting from methane/air combustion.

 CO_2 dilution caused the largest reduction in the S_L as a result of its higher specific heat capacity and lower thermal diffusivity relative to N_2 and H_2O . The laminar burning velocity of methane/air mixtures diluted with actual combustion residuals always lie between the ones for N_2 and H_2O dilutions. Post combustion products curbed the hydrodynamic and thermal-diffusive flame instabilities for methane/air mixtures by increasing the L_b and laminar flame thickness. However, the effects of different combustion residuals on the burned gas Markstein length are not significantly distinctive.

3. How do combustion residuals affect the laminar burning velocity and the flame stability of various fuel/oxidizer mixtures at elevated pressures and temperatures?

The effect of combustion residuals on laminar burning velocity and flame stability was analyzed with spherically expanding flames of iso-octane/air, high/low RON gasoline/air, and methane/air mixtures diluted with combustion residuals at high pressures and temperatures. The laminar flame speeds of the high and low RON gasolines and the iso-octane at 1 bar and 473 K decreased by 41-46%, 42-44%, and 46-49%, respectively, due to the EGR. Similar to the experimental results without the diluent, EGR-diluted high and low RON gasolines had almost the same S_L while the S_L of the diluted iso-octane flames was consistently slower than those of the two commercial gasolines. Similarly, the L_b of commercial gasolines did not vary significantly with RON. The EGR improved the flame stability and stretch by increasing the L_b and suppressing the cellular formation.

5%, 10%, and 15% combustion residuals additions to the methane/air mixtures lead to 5.66-8.85 cm/s, 7.38-8.42 cm/s, and 6.35-7.07 cm/s reductions in the S_L at 1 bar and 373 K; 7.46-11.74 cm/s, 6.20-10.40 cm/s, and 5.81-8.01 cm/s reductions in the S_L at 1 bar and 423 K; 6.78-12.40 cm/s, 9.15-13.61 cm/s, and 8.30-15.00 cm/s reductions in the S_L at 1 bar and 473 K; 6.18-7.78 cm/s, 4.96-6.51 cm/s, and 5.01-5.78 cm/s reductions in the S_L at 3 bar and 373 K; 6.32-8.84 cm/s, 5.78-8.82 cm/s, and 5.75-6.86 cm/s reductions in the S_L at 3 bar and 423 K; and 4.55-7.28 cm/s and 5.47-5.85 cm/s reductions in the S_L at 5 bar and 373 K, respectively. Combustion residuals mostly suppressed the thermal-diffusive as well as the hydrodynamic methane/air flame instabilities and caused more stretched methane/air flames by slightly increasing the L_b and increasing the laminar flame thickness and expansion ratio.

4. What are the main causes for the change in the laminar burning velocity and burned gas Markstein length of a combustible mixture due to the diluent addition?

The main causes for the change in the laminar burning velocity and burned gas Markstein length of a combustible mixture due to the diluent addition include (1) the decrease in the net reaction rate due to the reduced fuel/oxidizer concentration in the presence of a diluent, i.e. the dilution effect, (2) the change in the mass/thermal diffusivities and the specific heat capacity of the mixture with the addition of a diluent, i.e. the thermal-diffusion effect, and (3) the change in reaction kinetics because of the participation of a diluent in chemical reactions, i.e. the chemical effect. A series of numerical analyses was performed for diluted methane/air mixtures using the GRI-Mech 3.0 mechanism [223] to quantify each of these effects separately.

Chemical kinetic modeling results show that the primary effect for the decrease in the laminar flame speed is the dilution effect over the entire range of pressure, temperature, and equivalence and dilution ratios. The thermal-diffusion effect of the flue gases contributes the least to the decrease in flame propagation speed. However, it is vital for flame stability and stretch since it alters the thermal and mass diffusivities, and therefore Lewis number. The chemical effect of combustion residuals is slightly stronger than the thermal-diffusion effect and becomes very slightly weaker as the dilution ratio is increased or the equivalence ratio moves away from stoichiometry as a result of lower flame temperatures. The chemical effect of the flue gases can be attributed to the high reactivity of CO_2 within the combustion residuals and the high third body collision efficiency of H_2O .

5. How accurately can currently available chemical mechanisms predict the effect of dilution on the laminar burning velocity at elevated pressures and temperatures?

For diluted iso-octane flames, numerical analyses were conducted at the experimentally investigated conditions using the chemical mechanisms of Chaos et al. [239], Kelley et al. [78], and Jerzembeck et al. [240] in order to test the performance of these mechanisms at high temperatures and dilution ratios. The results from the current experiments and the numerical data obtained by the mechanism of Chaos et al. [239] showed good agreement with slightly slower numerical S_L values at φ>1.2. The chemical mechanism of Kelley et al. [78], which is a skeletal kinetic scheme of the Lawrence Livermore detailed mechanism [243-245], predicted significantly higher laminar burning velocities, while the numerical results of the chemical mechanism of Jerzembeck et al. [240] were substantially slower than the experiment's.

Numerical results for diluted methane/air flames were obtained with the GRI-Mech 3.0 [223], USC Mech II [224], HP-Mech [226], and NUI Galway-CH₄/DME [227] chemical mechanisms and compared with experimental flame speed results. The general trends of numerical results obtained by the four tested mechanisms are very similar to the experimental findings. The NUI Galway-CH₄/DME [227] performed best. The HP-Mech [226] predictions were very close and in good agreement with experimental findings at high dilution ratios. The USC Mech II [224] provided the most accurate simulation of the experimental data around stoichiometry. The GRI-Mech 3.0 [223] generally overpredicted the S_L at high temperatures and low pressures whereas it slightly underestimated the S_L at elevated pressures.

APPENDICES

APPENDIX A: Technical Drawing of Main Cylindrical Body

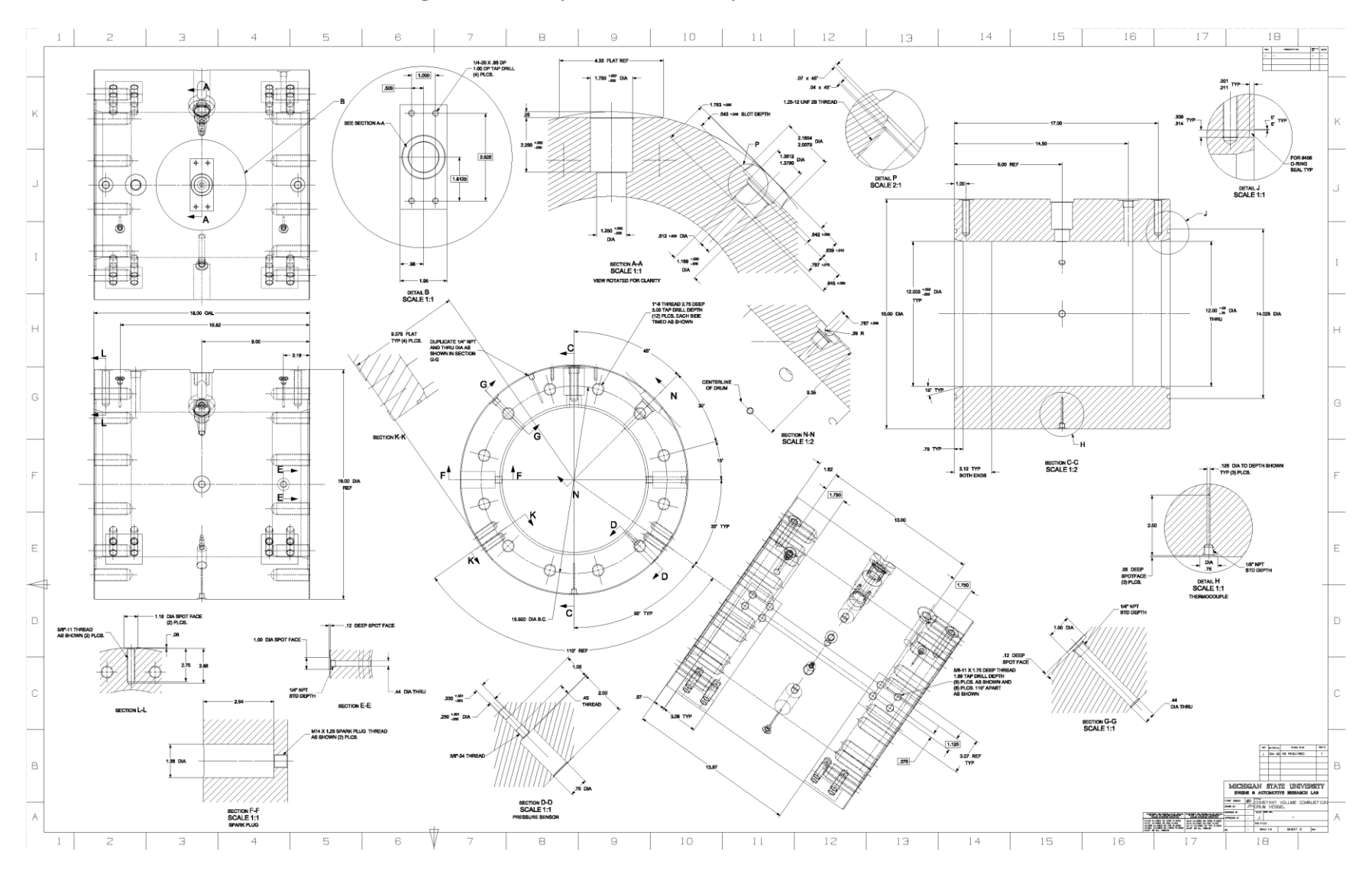


Figure A-1. Technical drawing of main cylindrical body.

APPENDIX B: Technical Drawing of Bolted End Cap

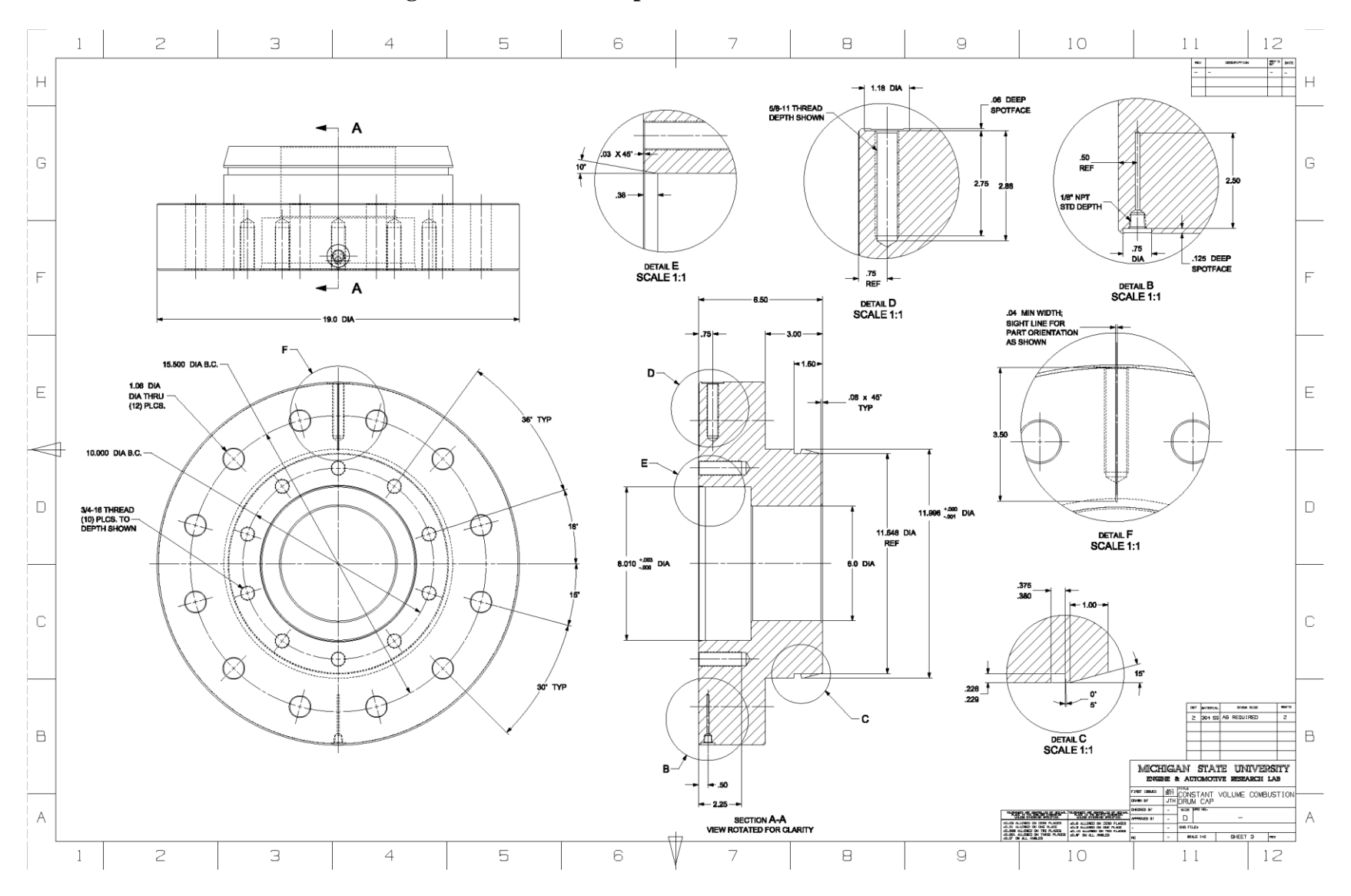


Figure A-2. Technical drawing of bolted end cap.

APPENDIX C: Technical Drawing of Fused Quartz Window

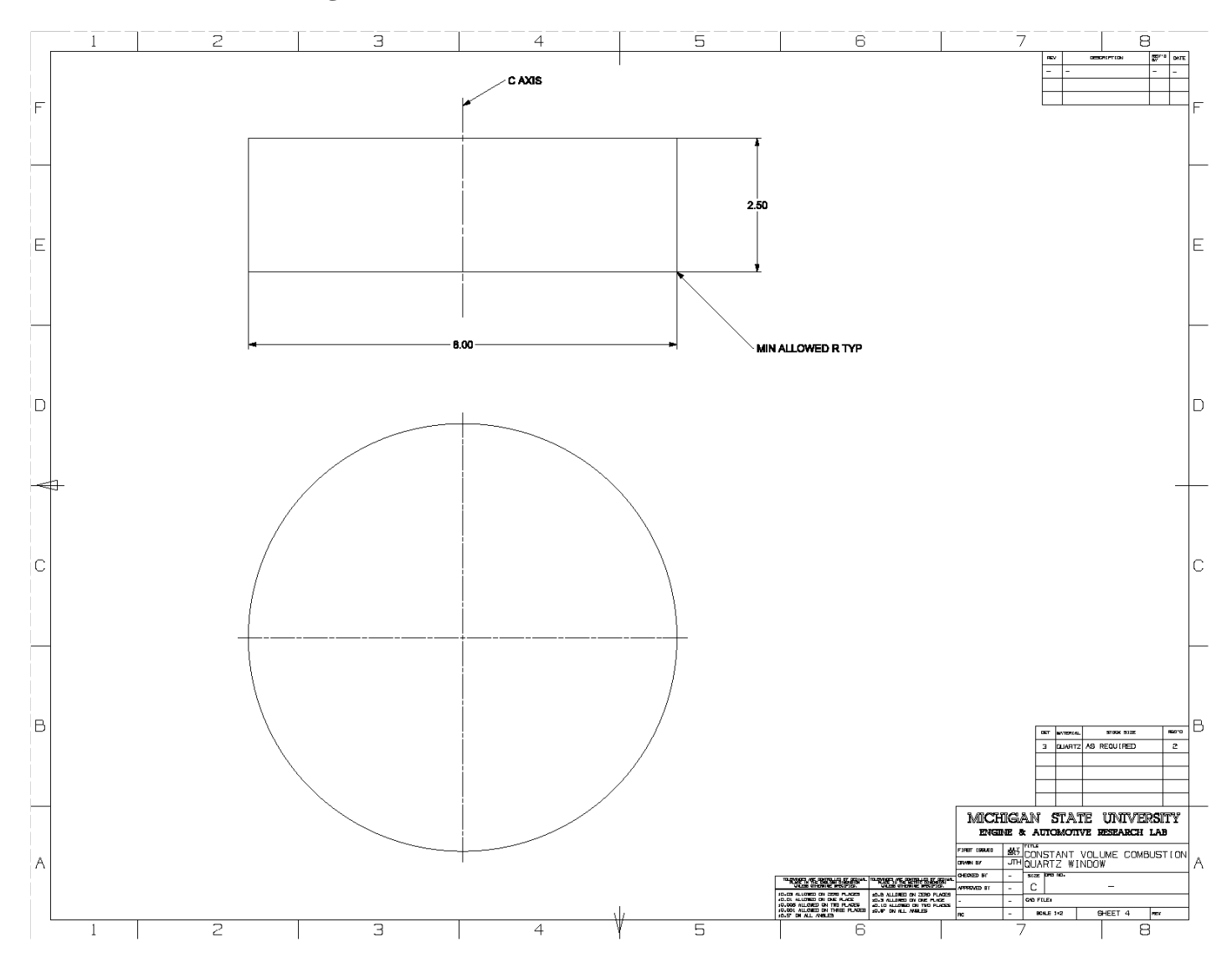


Figure A-3. Technical drawing of fused quartz window.

APPENDIX D: Technical Drawing of Window Cap

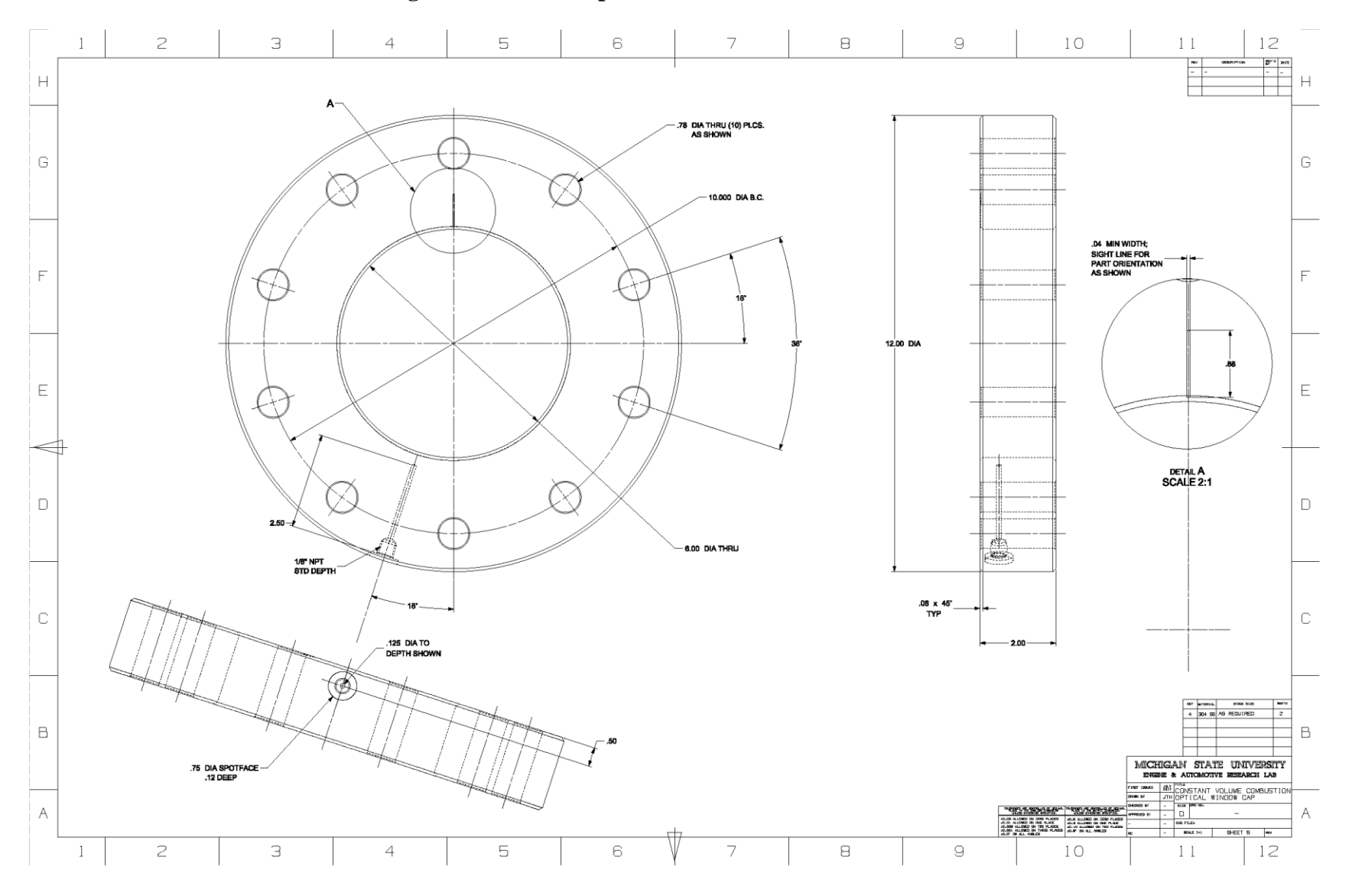


Figure A-4. Technical drawing of window cap.

APPENDIX E: Safety Factor Calculation for the Clamp between Bolted End Cap and Window Cap

According to Table 8-7 in [186] and Figure 3-2, effective grip (L'_G) , threaded length (L_T) , length of useful unthreaded portion (l_d) , and length of useful threaded portion (l_t) of the screws between the bolted end caps and window caps can be calculated as follows.

$$\begin{split} L_G' &= h + \frac{d}{2} = 5.45 + \frac{1.91}{2} = 6.41 \text{ cm} \\ L_T &= 2d + 0.635 = 2 * 1.91 + 0.635 = 4.46 \text{ cm} \\ l_d &= l - L_T = 8.89 - 4.46 = 4.43 \text{ cm} \\ l_t &= L_G' - l_d = 6.41 - 4.43 = 1.98 \text{ cm} \end{split}$$

Estimated effective stiffness of the bolt in the clamped zone (k_b) and joint-member stiffness (k_m) were calculated below [186]. Major-diameter area of the screw (A_d) is 2.865 x 10^{-4} m² (= $\pi/4*0.0191^2$). Tensile-stress area of fastener (A_t) and elastic modulus of steel bolts, washers, and members (EM) are obtained from Tables 8.2 and 8.8 in [186].

$$\begin{split} k_b &= \frac{A_d*A_t*EM}{A_d*l_t + A_t*l_d} = \frac{2.865 \text{x} 10^{-4}*2.406 \text{x} 10^{-4}*2.068 \text{x} 10^{11}}{2.865 \text{x} 10^{-4}*0.0198 + 2.406 \text{x} 10^{-4}*0.0443} \\ &= 8.72 \text{ x} 10^8 \frac{N}{m} \\ k_m &= \frac{0.5774*\pi*EM*d}{2 \ln \left(2.2 \frac{0.5774*l + 1.5*d}{0.5774*l + 3.5*d}\right)} = \frac{0.5774*\pi*2.068 \text{x} 10^{11}*0.0191}{2 \ln \left(2.2 \frac{0.5774*0.0889 + 1.25*0.0191}{0.5774*0.0889 + 2.75*0.0191}\right)} \\ &= 7.87 \text{ x} 10^9 \frac{N}{m} \end{split}$$

Resultant load on the connected members (F_m) equals to fraction of the external load carried by members $((1-C)*F_{ext})$ subtracted by clamp load or preload of the fastener (F_p) [186]. To ensure a safe joint, the external load is required to be smaller than the load needed to cause the

joint separate. If separation does occur, then the entire external load will be imposed on the bolt, i.e. F_m =0. Subsequently, maximum external load, which can be handled by one of the screws, was calculated below by using a clamp force of 149,460 N [303]. By considering 10 of the grade 8 steel 3/4"-16 threaded hex head screws with grade 8 steel washers and pressure rating of the chamber, safety factor for the clamp between the bolted end caps and window caps was calculated as 3.94.

$$F_m = (1 - C) * F_{ext} - F_p$$
 $\xrightarrow{separation(F_m = 0)}$ $F_{ext} = \frac{F_p}{(1 - C)} = \frac{149460}{(1 - 0.10)}$
= 1.66x10⁵ N

where
$$C = \frac{k_b}{k_b + k_m} = \frac{8.72 \times 10^8}{8.72 \times 10^8 + 7.87 \times 10^9} = 0.10$$

Safety Factor =
$$\frac{10 * F_{ext,m}}{P_m * A_{eff}} = \frac{10 * 1.66 \times 10^5}{1.3 \times 10^7 * 0.0324} = 3.94$$

APPENDIX F: Technical Drawing of Riser Support

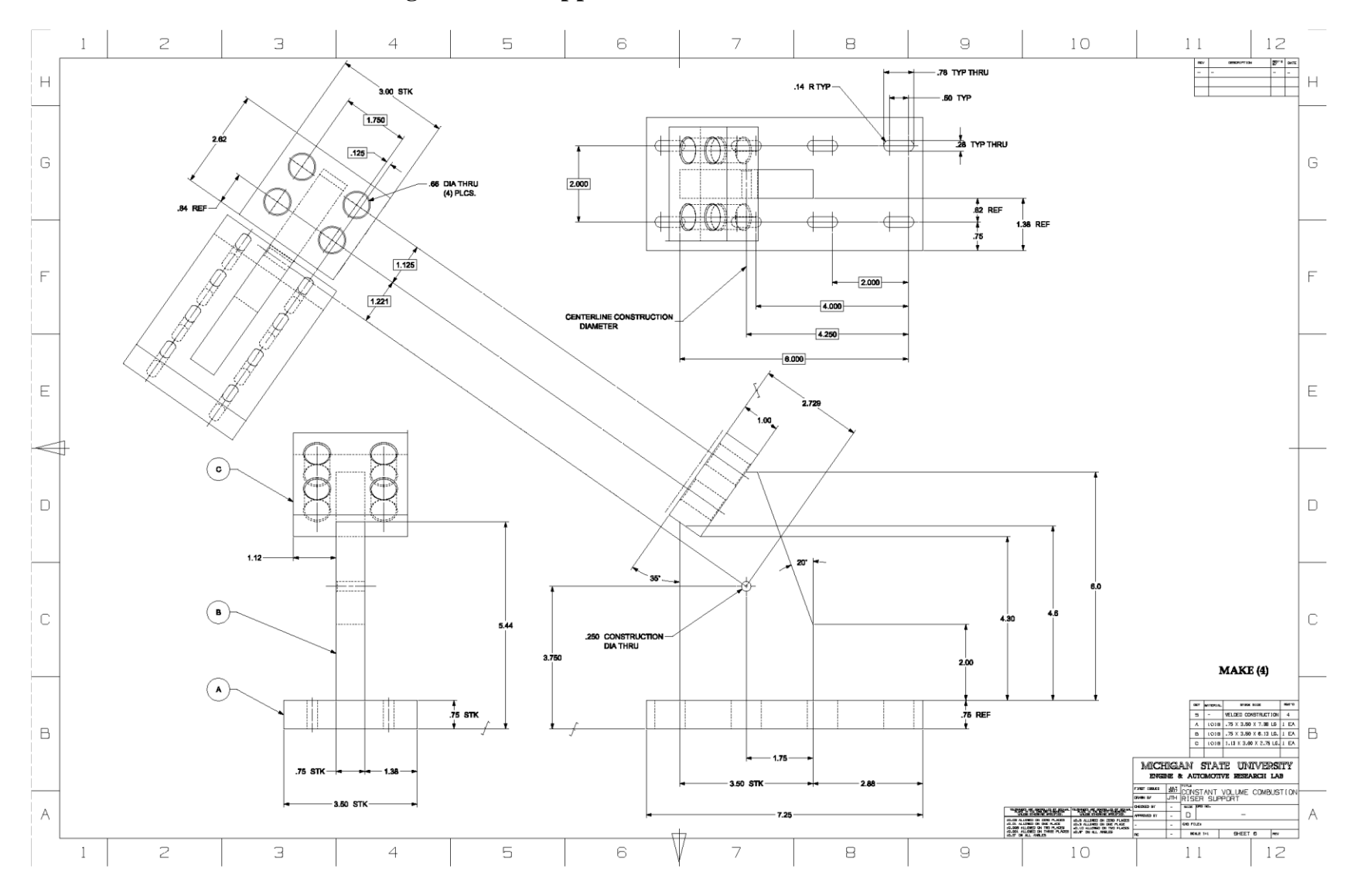


Figure A-5. Technical drawing of riser support.

APPENDIX G: Technical Drawing of Gas Manifold

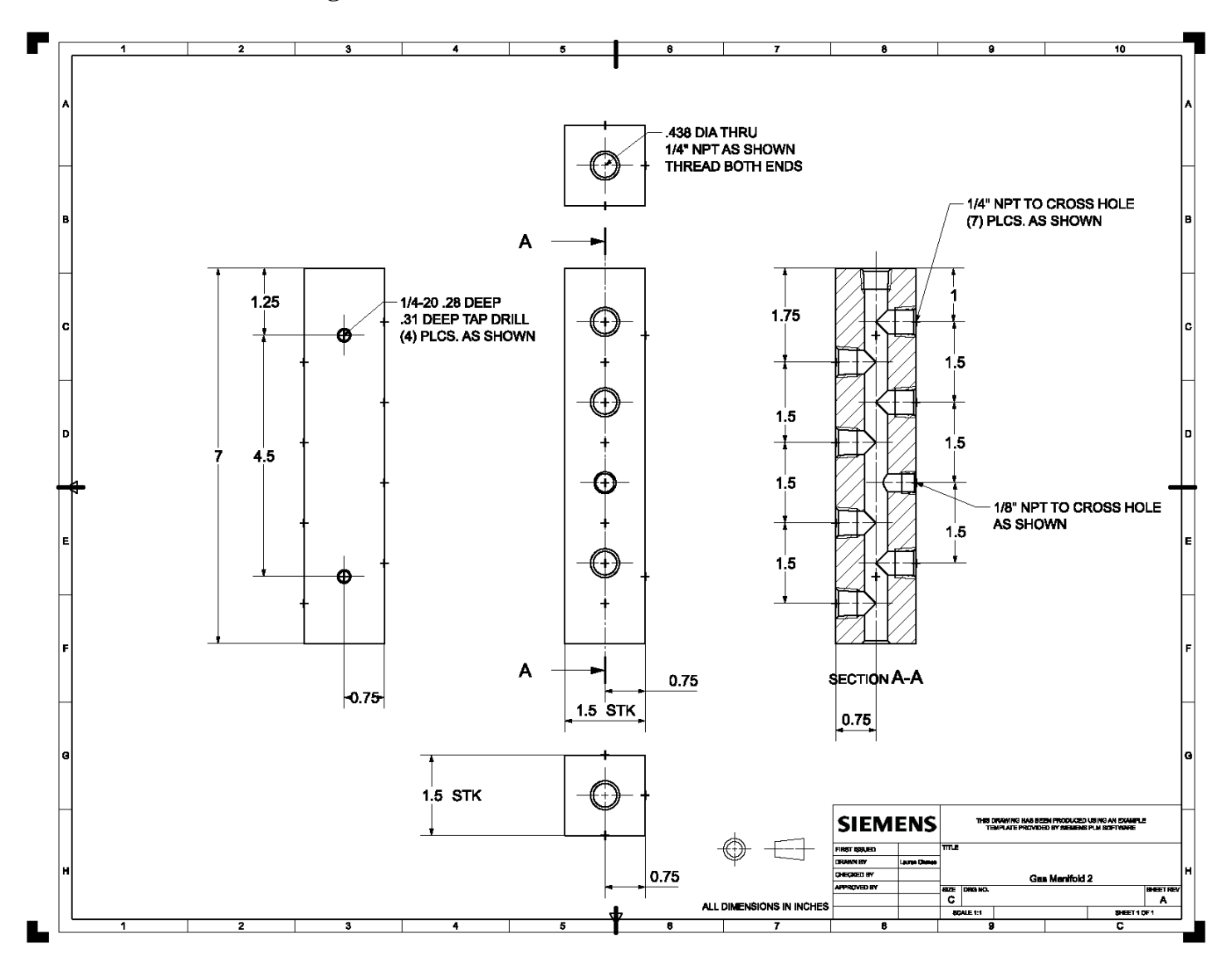


Figure A-6. Technical drawing of gas manifold.

APPENDIX H: Technical Drawings of Fuel Injector Assembly

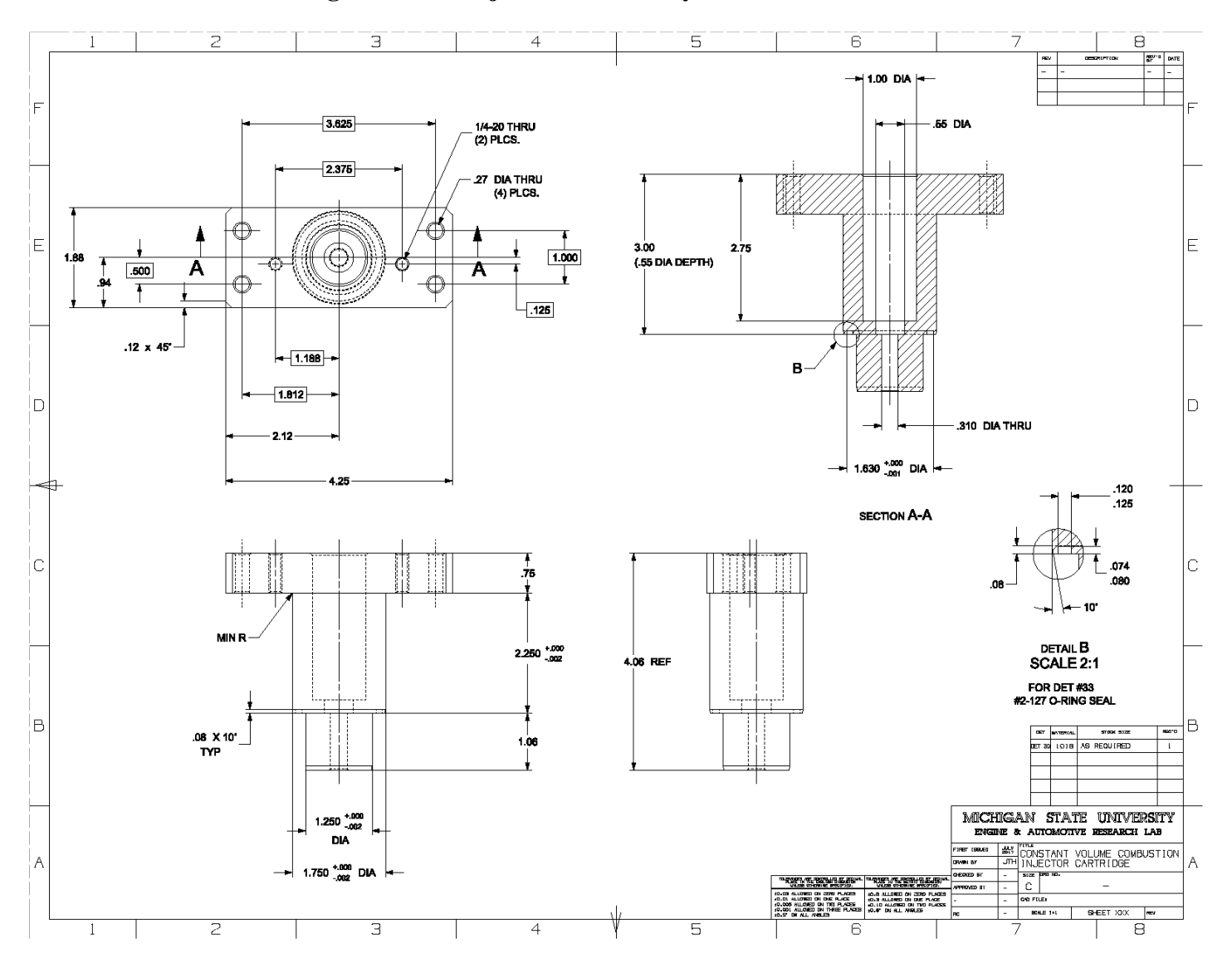


Figure A-7. Technical drawing of fuel injector cartridge.

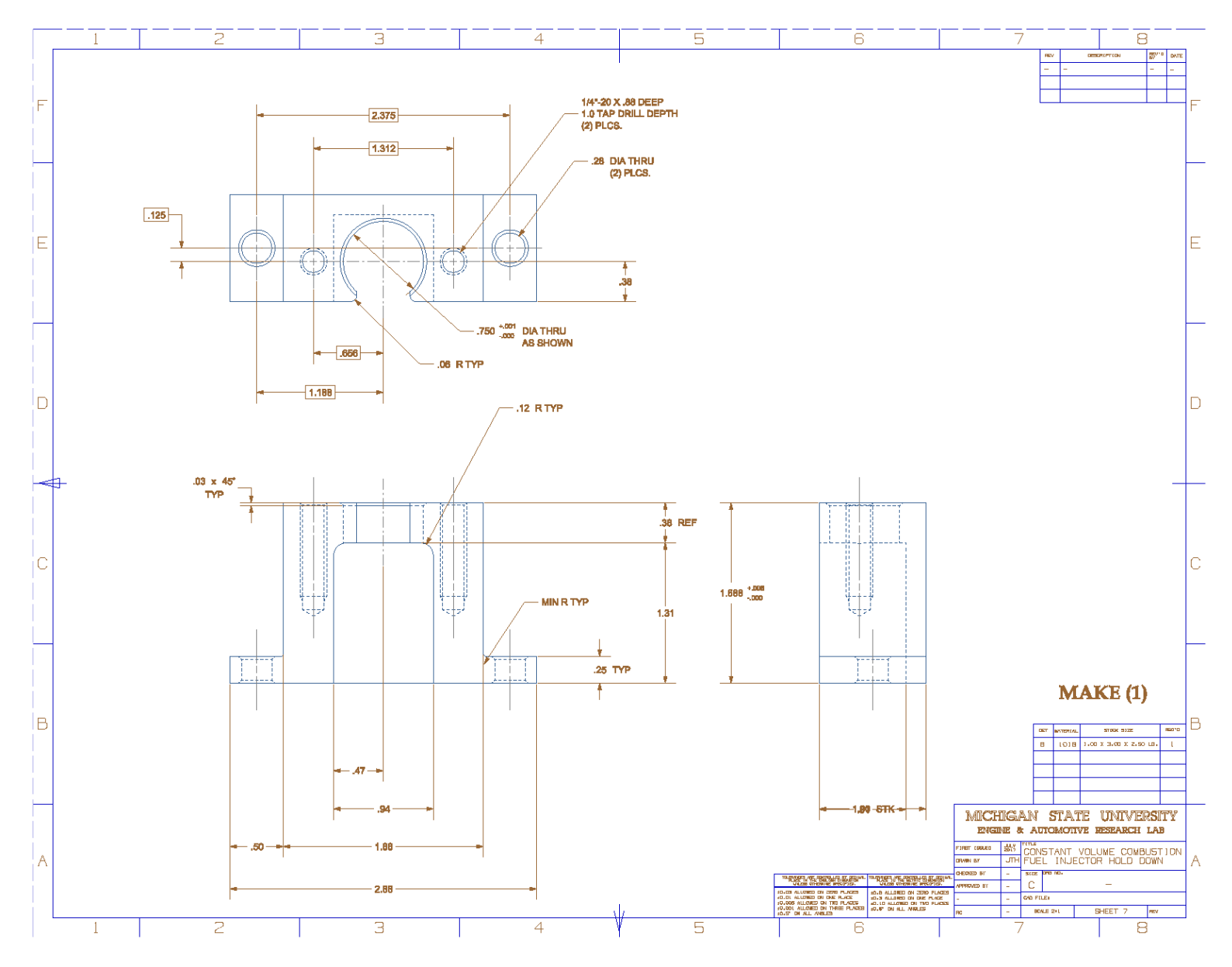


Figure A-8. Technical drawing of fuel injector hold down.

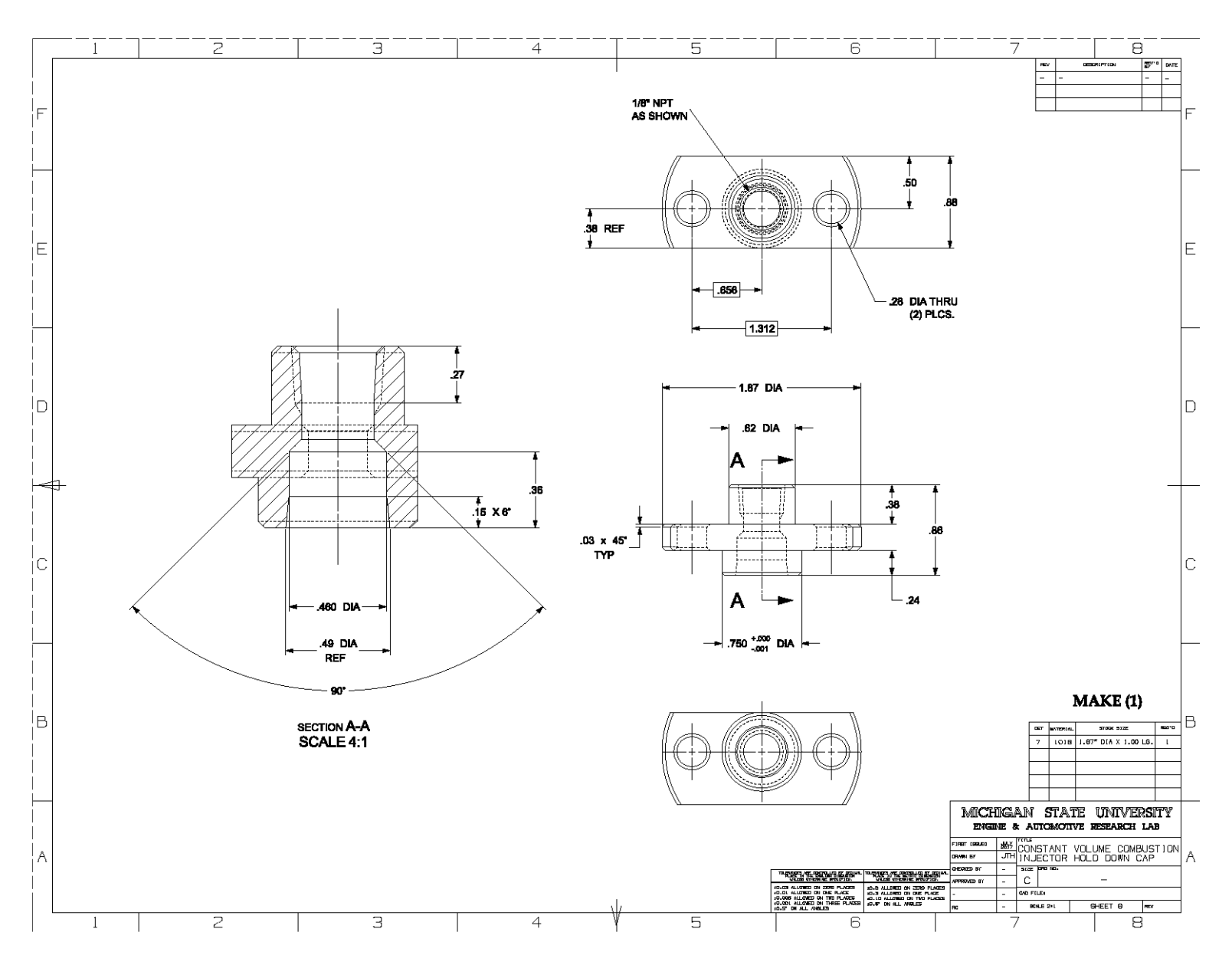


Figure A-9. Technical drawing of fuel injector hold down cap.

APPENDIX I: Laminar flame speeds, burned gas Markstein lengths, burned gas Markstein numbers, and critical lower radius limits for the measurements with uncertainties.

Table A-1. Experimental laminar flame speed, burned gas Markstein length, and burned gas Markstein number data at critical lower radius limit for methane, propane, iso-octane, and hydrogen.

Fuel	P	Т	ф	R _L ,critical	SL	Uncertainty of S _L	L_b	Uncertainty of L _b	Маь
	[bar]	[K]	[-]	[cm]	[cm/s]	[cm/s]	[mm]	[mm]	[-]
			0.70	0.50	18.83	0.18	0.505	0.039	0.759
Mathana	1	200	0.80	0.62	26.72	0.33	0.463	0.074	0.869
Methane	1	298	1.00	1.43	37.45	0.73	0.709	0.204	1.603
			1.10	1.58	37.34	0.35	0.540	0.121	1.247
			0.70	2.75	20.46	0.15	1.229	0.169	2.040
			0.80	2.60	27.48	0.29	0.884	0.139	1.853
			0.90	2.21	33.88	0.28	0.846	0.140	2.038
D	1	200	1.00	2.21	37.15	0.23	0.682	0.101	1.783
Propane	1	298	1.10	2.18	38.76	0.32	0.573	0.138	1.576
			1.20	1.56	37.08	0.20	0.410	0.054	1.124
			1.30	0.88	31.46	0.21	0.234	0.036	0.570
			1.40	0.73	23.45	0.24	-0.237	0.060	-0.435
			0.80	2.75	36.94	0.51	1.101	0.182	2.575
			0.90	2.98	42.28	0.56	1.012	0.214	2.602
			1.00	2.55	46.09	0.72	0.767	0.250	2.069
I 0 /	1	272	1.10	2.17	48.63	0.55	0.761	0.206	2.087
Iso-Octane	1	373	1.20	1.27	46.43	0.24	0.434	0.075	1.152
			1.30	0.61	40.79	1.18	0.226	0.059	0.530
			1.40	0.63	33.59	0.78	-0.210	0.076	-0.386
			1.50	0.47	25.92	0.55	-0.477	0.061	-0.624
			0.70	0.67	138.66	3.13	0.113	0.106	0.335
			0.80	0.26	165.92	2.30	0.084	0.042	0.253
TT 1	4	200	1.30	0.12	256.01	5.19	0.003	0.031	0.010
Hydrogen	1	298	2.00	2.34	273.94	3.24	0.635	0.247	2.006
			3.50	2.34	184.73	1.40	0.713	0.104	1.777
			4.00	1.84	157.55	1.26	0.886	0.076	1.983

APPENDIX J: Experimental and numerical laminar flame speeds and burned gas Markstein lengths for methane/air, hydrogen/air, propane/air, and iso-octane/air mixtures for the validation of experimental apparatus and procedure.

Table A-2. Experimental and numerical laminar flame speed and burned gas Markstein length data of methane/air mixture for the validation of experimental apparatus and procedure.

P	T	ф	S_L	Uncertainty of S _L	L_b	Uncertainty of L _b	SL,GRI-Mech	SL,USC Mech II	S _L ,San Diego
[bar]	[K]	[-]	[cm/s]	[cm/s]	[mm]	[mm]	[cm/s]	[cm/s]	[cm/s]
		0.70	18.83	0.18	0.51	0.04	19.10	19.86	19.64
		0.80	26.72	0.33	0.46	0.07	26.88	27.07	27.25
		0.90	33.71	0.68	0.55	0.17	33.41	32.54	32.96
1	298	1.00	37.45	0.73	0.71	0.20	37.42	35.52	35.89
		1.10	37.34	0.35	0.54	0.12	37.75	35.30	35.24
		1.20	34.36	0.62	0.93	0.17	32.98	30.96	29.97
		1.30	24.53	1.36	0.97	0.40	23.09	22.59	20.37

Table A-3. Experimental and numerical laminar flame speed and burned gas Markstein length data of propane/air mixture for the validation of experimental apparatus and procedure.

P	T	ф	S_L	$\begin{array}{c} \textbf{Uncertainty} \\ \textbf{of } S_L \end{array}$	L_b	Uncertainty of L _b	SL,USC Mech II	S _L ,San Diego	SL,Qin et al.
[bar]	[K]	[-]	[cm/s]	[cm/s]	[mm]	[mm]	[cm/s]	[cm/s]	[cm/s]
		0.70	20.46	0.15	1.23	0.17	22.52	25.49	19.60
		0.80	27.48	0.29	0.88	0.14	29.66	33.19	27.77
		0.90	33.88	0.28	0.85	0.14	35.07	38.91	34.78
1	298	1.00	37.15	0.23	0.68	0.10	38.19	41.11	39.63
1	298	1.10	38.76	0.32	0.57	0.14	38.56	40.89	41.48
		1.20	37.08	0.20	0.41	0.05	35.66	37.09	39.53
		1.30	31.46	0.21	0.23	0.04	29.18	29.22	33.07
		1.40	23.45	0.24	-0.24	0.06	20.67	19.73	23.30

Table A-4. Experimental and numerical laminar flame speed and burned gas Markstein length data of iso-octane/air mixture for the validation of experimental apparatus and procedure.

P	T	ф	S_L	Uncertainty of S _L	L_b	Uncertainty of L _b	SL,Chaos et al.	SL,Kelley et al.	S _L ,Jerzembeck et al.
[bar]	[K]	[-]	[cm/s]	[cm/s]	[mm]	[mm]	[cm/s]	[cm/s]	[cm/s]
		0.80	36.94	0.51	1.10	0.18	37.29	37.61	28.00
		0.90	42.28	0.56	1.01	0.21	43.80	46.80	34.47
		1.00	46.09	0.72	0.77	0.25	47.49	53.79	38.76
1	373	1.10	48.63	0.55	0.76	0.21	47.82	57.38	39.87
		1.20	46.43	0.24	0.43	0.08	44.25	56.20	36.98
		1.30	40.79	1.18	0.23	0.06	36.60	48.88	29.70
		1.40	33.59	0.78	-0.21	0.08	26.69	35.99	20.09

Table A-5. Experimental and numerical laminar flame speed and burned gas Markstein length data of hydrogen/air mixture for the validation of experimental apparatus and procedure.

P	Т	ф	SL	Uncertainty of S _L	L _b	Uncertainty of L _b	SL,Li et al.	SL,Konnov	SL,NUI Galway- H2
[bar]	[K]	[-]	[cm/s]	[cm/s]	[mm]	[mm]	[cm/s]	[cm/s]	[cm/s]
		0.70	138.66	3.13	0.11	0.11	131.68	129.68	125.77
		0.80	165.92	2.30	0.08	0.04	168.56	168.14	163.43
		0.90	197.95	3.01	0.44	0.06	201.35	202.59	197.18
		1.00	219.96	9.62	0.58	0.69	229.50	231.96	226.59
		1.10	238.20	2.22	0.43	0.18	252.98	256.11	251.18
		1.20	246.49	3.95	0.37	0.28	271.83	275.18	271.02
		1.30	265.93	6.46	0.43	0.17	286.25	289.55	286.14
	298	1.40	264.67	6.93	0.38	0.46	296.53	299.62	296.91
		1.50	267.90	3.79	0.30	0.27	303.11	305.87	303.80
1		1.60	277.44	4.34	0.49	0.19	306.56	308.86	307.43
1	290	1.70	283.27	3.98	0.43	0.28	307.43	309.18	308.31
		1.80	273.42	7.26	0.31	0.47	306.24	307.39	307.18
		1.90	275.53	5.07	0.47	0.30	303.48	304.03	304.34
		2.00	273.94	3.24	0.63	0.25	299.45	299.42	300.26
		2.20	259.37	2.39	0.54	0.22	289.00	287.90	289.59
		2.40	245.81	2.48	0.42	0.18	276.48	274.51	276.86
		2.60	235.04	4.37	0.44	0.28	262.96	260.34	263.12
		2.80	229.10	1.22	0.76	0.08	249.08	245.95	248.96
		3.00	214.85	1.62	0.69	0.07	235.16	231.71	234.80
		3.50	184.73	1.40	0.71	0.10	201.55	197.65	200.93

Table A-5 (cont'd)

1	200	4.00	157.55	1.26	0.89	0.08	170.78	166.73	170.06
1	298	4.50	130.25	1.13	1.05	0.11	143.25	139.20	142.59

APPENDIX K: Numerical and experimental laminar burning velocity and burned gas Markstein length results for iso-octane/air and high/low RON gasoline/air mixtures with and without 15% CO₂ dilution at 1 bar and 373-473 K.

Table A-6. Experimental and numerical laminar flame speed and burned gas Markstein length data of iso-octane/air mixture.

P	T	X _{CO2}	ф	S_{L}	Uncertainty of S _L	L_b	Uncertainty of L _b	SL,Chaos et	SL,Kelley et al.	SL,Jerzembeck et al.
[bar]	[K]	[%]	[-]	[cm/s]	[cm/s]	[mm]	[mm]	[cm/s]	[cm/s]	[cm/s]
			0.80	37.60	0.55	1.42	0.07	37.29	37.61	28.00
			0.85	40.76	0.67	1.30	0.12	40.86	42.41	31.43
			0.90	43.29	1.26	1.32	0.14	43.80	46.80	34.47
	373	0	1.00	47.19	0.81	1.10	0.11	47.49	53.79	38.76
	3/3	U	1.10	48.75	0.47	0.80	0.08	47.82	57.38	39.87
			1.20	47.18	0.51	0.62	0.06	44.25	56.20	36.98
			1.30	40.51	0.61	0.15	0.16	36.60	48.88	29.70
			1.40	33.61	1.55	-0.20	0.13	26.69	35.99	20.09
			0.80	56.22	0.98	1.24	0.17	58.41	59.55	45.16
		0	0.90	65.28	0.99	1.06	0.10	67.00	72.12	54.09
1			1.00	70.46	0.57	0.87	0.05	71.78	81.52	59.88
	473		1.10	72.20	0.93	0.71	0.14	72.16	86.31	61.45
			1.20	69.38	0.54	0.48	0.06	67.57	84.99	57.86
			1.30	61.19	2.04	0.14	0.16	57.68	75.96	48.50
			1.40	49.24	1.36	-0.28	0.32	44.18	59.14	35.03
			0.90	34.71	1.49	1.65	0.01	35.41	38.68	27.17
			1.00	37.61	0.27	1.32	0.25	38.18	44.10	30.11
	473	1.5	1.10	38.80	0.48	1.04	0.17	38.20	46.69	30.50
	4/3	15	1.20	36.89	0.38	0.66	0.07	35.22	45.52	27.91
			1.30	31.36	0.88	0.02	0.26	29.30	39.80	22.44
			1.40	25.61	1.68	-0.54	0.31	21.54	29.93	15.46

Table A-7. Experimental laminar flame speed and burned gas Markstein length data of high RON gasoline/air mixture.

P	T	X_{CO_2}	ф	S_{L}	Uncertainty of S _L	L_{b}	Uncertainty of L _b
[bar]	[K]	[%]	[-]	[cm/s]	[cm/s]	[mm]	[mm]
			0.85	45.02	0.90	1.12	0.06
	272	0	1.00	50.41	0.59	0.87	0.02
	373	0	1.10	51.84	0.36	0.66	0.08
			1.30	43.15	1.96	0.01	0.04
	472		0.85	68.07	0.53	0.96	0.05
1		0	1.00	77.50	1.42	0.69	0.05
1	473	U	1.10	79.35	0.53	0.68	0.04
			1.30	67.14	1.96	0.15	0.05
			0.90	39.42	0.68	1.31	0.01
	472	1.5	1.00	42.02	0.35	0.99	0.06
	473	15	1.10	44.05	0.20	0.89	0.04
			1.30	39.69	0.76	0.24	0.09

Table A-8. Experimental laminar flame speed and burned gas Markstein length data of low RON gasoline/air mixture.

P	T	X_{CO_2}	ф	S_L	Uncertainty of S _L	$\mathbf{L}_{\mathbf{b}}$	Uncertainty of Lb
[bar]	[K]	[%]	[-]	[cm/s]	[cm/s]	[mm]	[mm]
			0.85	42.63	0.31	1.15	0.05
	373	0	1.00	50.10	1.93	0.94	0.03
	3/3	U	1.10	51.54	1.25	0.67	0.16
			1.30	47.43	0.20	0.22	0.01
	472		0.85	65.61	0.73	0.95	0.04
1		0	1.00	75.78	2.41	0.77	0.06
1	473	U	1.10	77.40	1.49	0.63	0.15
			1.30	72.84	0.73	0.31	0.05
			0.90	40.70	2.15	1.26	0.10
	472	1.5	1.00	42.67	0.40	1.11	0.03
	473	15	1.10	44.28	0.51	0.89	0.09
			1.30	42.30	1.35	0.44	0.09

APPENDIX L: Dilution effect of different combustion residuals on laminar burning velocities and burned gas Markstein lengths of premixed methane/air mixtures at 1 bar and 473 K.

Table A-9. Experimental laminar flame speed and burned gas Markstein length data of diluted methane/air mixture.

ф	Diluent	X	$\mathbf{S}_{\mathbf{L}}$	Uncertainty of S _L	L_b	Uncertainty o	
[-]	[-]	[%]	[cm/s]	[cm/s]	[mm]	[mm]	
		0	60.75	0.47	0.48	0.07	
	N	5	53.38	0.90	0.39	0.09	
	N_2	10	44.48	1.02	0.51	0.09	
		15	35.62	1.09	0.54	0.08	
		0	60.75	0.42	0.48	0.04	
	H_2O	5	46.68	0.11	0.58	0.04	
	H ₂ O	10	35.98	0.96	0.49	0.13	
0.8		15	23.63	0.53	0.71	0.06	
0.8		0	60.75	0.19	0.48	0.03	
	CO_2	5	42.28	0.30	0.52	0.02	
	CO_2	10	28.56	0.28	0.57	0.06	
		15	19.53	0.15	0.71	0.06	
		0	60.75	0.19	0.48	0.03	
	71.49% N ₂ +	5	49.53	0.06	0.68	0.08	
	19.01% H ₂ O + 9.50% CO ₂	10	37.70	1.68	0.48	0.21	
		15	29.40	0.75	0.74	0.19	
		0	77.51	0.36	0.55	0.00	
	N	5	68.00	0.75	0.63	0.05	
	N_2	10	58.21	0.26	0.70	0.04	
		15	48.46	1.03	0.74	0.03	
		0	77.51	0.78	0.55	0.02	
1.0		5	61.39	1.09	0.61	0.11	
1.0	H_2O	10	48.50	0.16	0.55	0.08	
		15	37.63	0.52	0.73	0.04	
		0	77.51	0.35	0.55	0.03	
	a-	5	54.31	0.52	0.58	0.04	
	CO_2	10	37.81	0.26	0.72	0.04	
		15	26.49	0.10	0.89	0.05	

Table A-9 (cont'd)

		0	77.51	0.35	0.55	0.03
1.0	71.49% N ₂ + 19.01% H ₂ O +	5	66.69	0.22	0.53	0.08
1.0	9.50% CO ₂	10	57.54	0.15	0.86	0.02
		15	42.54	0.73	0.85	0.09
		0	71.43	0.13	0.65	0.00
	N	5	62.67	0.58	0.79	0.03
	N_2	10	54.57	0.60	0.84	0.08
		15	44.99	0.22	0.94	0.02
		0	71.43	2.63	0.65	0.03
	H ₂ O	5	60.18	0.82	0.82	0.09
		10	48.45	0.29	0.87	0.07
1.2		15	35.18	0.82	1.25	0.14
1.2		0	71.43	0.43	0.65	0.03
	CO	5	49.96	1.04	0.74	0.16
	CO_2	10	34.74	0.16	1.03	0.06
		15	22.90	0.18	1.31	0.02
		0	71.43	0.43	0.65	0.03
	71.49% N ₂ + 19.01% H ₂ O +	5	64.10	0.39	0.59	0.06
	9.50% CO ₂	10	51.64	0.66	0.84	0.20
		15	40.66	1.09	0.97	0.12

APPENDIX M: Experimental and numerical laminar flame speed and burned gas Markstein length for diluted methane/air mixtures at 1-5 bar and 373-473 K.

Table A-10. Experimental and numerical laminar flame speed and burned gas Markstein length data of methane/air mixture.

P	Т	X	ф	$S_{L,exp}$	S _{L,exp-error}	L_{b}	L _{b-error}	S _{L,corr}	$L_{b,corr}$	S _{L,GRI} - Mech 3.0	S _{L,USC} Mech II	S _{L,HP} .	S _{L,NUI} Galway- CH4/DME
[bar]	[K]	[%]	[-]	[cm/s]	[cm/s]	[mm]	[mm]	[cm/s]	[mm]	[cm/s]	[cm/s]	[cm/s]	[cm/s]
			0.70	27.07	0.74	0.26	0.04	27.09	0.37	29.56	30.45	28.54	27.58
			0.80	37.67	0.33	0.35	0.05	38.21	0.42	40.08	40.06	39.12	38.41
			0.90	46.42	0.20	0.51	0.03	45.45	0.46	48.59	47.17	47.54	47.08
		0	1.00	51.35	0.12	0.62	0.04	48.79	0.50	53.70	50.96	52.69	52.41
			1.10	50.78	0.29	0.57	0.05	48.24	0.60	54.08	50.61	53.55	53.34
			1.20	45.46	0.16	0.71	0.01	43.79	0.76	48.30	45.14	49.02	48.67
			1.30	34.69	0.50	1.05	0.03	35.46	1.03	35.97	34.47	38.61	37.93
			0.70	21.40	0.76	0.35	0.07	22.70	0.44	23.62	24.83	22.68	21.93
			0.80	31.03	0.55	0.41	0.04	32.02	0.50	32.78	33.33	31.87	31.41
			0.90	37.80	0.57	0.52	0.02	38.09	0.55	40.36	39.70	39.32	39.11
1	272	5	1.00	42.50	0.13	0.68	0.08	40.89	0.60	44.99	43.07	43.88	43.86
1	373		1.10	42.37	0.06	0.72	0.09	40.42	0.72	45.28	42.64	44.52	44.55
			1.20	36.79	0.25	0.86	0.06	36.70	0.91	39.62	37.31	40.07	39.92
			1.30	27.50	0.34	1.34	0.05	29.71	1.23	27.90	27.19	30.28	29.73
			0.80	23.64	0.68	0.37	0.09	25.83	0.59	26.18	27.15	25.36	25.05
		10	0.90	30.01	0.79	0.52	0.03	30.73	0.64	32.77	32.74	31.81	31.78
			1.00	34.08	0.15	0.69	0.02	32.98	0.70	36.88	35.69	35.78	35.94
			1.10	34.25	0.19	0.79	0.07	32.61	0.83	37.04	35.15	36.20	36.38
			1.20	29.28	0.48	1.09	0.06	29.61	1.06	31.48	29.94	31.81	31.78
			0.90	23.67	0.38	0.64	0.05	23.37	0.73	25.91	26.38	25.08	25.14
		15	1.00	27.01	0.32	0.82	0.05	25.08	0.81	29.45	28.89	28.45	28.71
			1.10	27.19	0.21	0.96	0.03	24.80	0.95	29.46	28.22	28.65	28.92
			0.60	20.70	0.58	0.32	0.05	15.59	0.26	25.10	26.15	23.57	22.10
			0.70	34.13	0.33	0.31	0.12	34.99	0.35	38.49	39.30	37.28	36.00
			0.80	47.64	0.60	0.43	0.06	49.36	0.40	51.01	50.61	49.87	48.87
			0.90	57.43	0.53	0.43	0.08	58.70	0.43	60.89	58.84	59.71	58.97
1	423	0	1.00	63.34	0.39	0.58	0.02	63.02	0.48	66.66	63.12	65.63	65.10
			1.10	62.54	0.45	0.49	0.08	62.31	0.57	66.98	62.66	66.60	66.16
			1.20	57.46	0.22	0.70	0.04	56.57	0.73	60.39	56.40	61.45	60.91
			1.30	44.70	0.13	0.85	0.07	45.80	0.98	46.36	44.17	49.57	48.71
			1.40	28.99	1.04	1.42	0.11	30.00	1.36	29.70	29.85	34.31	33.28

Table A-10 (cont'd)

		0.70 0.80	26.67	0.54	0.37	0.04	29.32	0.42	31.18	32.46	30.04	29.06
		0.80	27.02									
		0.00	37.92	0.42	0.48	0.08	41.36	0.48	42.18	42.54	41.08	40.42
		0.90	46.47	0.39	0.53	0.05	49.19	0.52	51.07	49.95	49.86	49.48
	_	1.00	51.61	0.25	0.69	0.07	52.81	0.58	56.36	53.81	55.15	54.97
	5	1.10	51.64	0.44	0.72	0.06	52.22	0.68	56.61	53.25	55.89	55.77
		1.20	46.30	0.35	0.92	0.06	47.40	0.87	50.21	47.19	50.85	50.58
		1.30	34.35	0.27	1.19	0.03	38.38	1.18	36.80	35.54	39.62	38.93
		1.40	21.28	0.66	1.82	0.21	25.14	1.63	22.49	22.66	25.98	25.18
		0.70	20.48	1.14	0.43	0.17	23.65	0.49	24.67	26.21	23.61	22.84
1 423		0.80	29.51	0.62	0.39	0.04	33.37	0.56	34.12	35.06	33.13	32.68
	10	0.90	37.84	0.54	0.63	0.08	39.69	0.61	41.95	41.63	40.79	40.66
	10	1.00	41.51	0.21	0.73	0.02	42.61	0.67	46.70	45.03	45.44	45.52
		1.10	41.28	0.63	0.75	0.05	42.12	0.80	46.85	44.38	45.94	46.06
		1.20	35.90	0.74	1.00	0.12	38.24	1.02	40.58	38.46	41.01	40.91
		0.80	23.70	0.47	0.53	0.05	25.38	0.64	26.91	28.23	26.02	25.71
		0.90	30.08	0.17	0.63	0.11	30.18	0.69	33.62	33.95	32.60	32.61
	15	1.00	33.50	0.23	0.81	0.03	32.40	0.77	37.77	36.87	36.58	36.82
		1.10	33.76	0.12	0.93	0.05	32.03	0.91	37.76	36.10	36.84	37.11
		1.20	28.23	0.88	1.17	0.16	29.08	1.16	31.61	30.31	31.99	31.99
		0.60	28.33	0.12	0.36	0.02	19.56	0.25	33.20	34.30	31.39	29.51
		0.70	45.65	0.53	0.42	0.05	43.92	0.34	49.22	49.81	47.77	46.09
		0.80	60.75	0.19	0.48	0.03	61.96	0.39	63.81	62.87	62.48	61.09
		0.90	71.81	0.93	0.50	0.11	73.68	0.42	75.05	72.21	73.76	72.65
	0	1.00	77.51	0.35	0.55	0.03	79.10	0.46	81.44	76.96	80.46	79.60
		1.10	78.09	0.47	0.59	0.07	78.21	0.55	81.64	76.33	81.50	80.78
		1.20	71.43	0.43	0.65	0.03	71.00	0.70	74.21	69.26	75.71	74.93
		1.30	58.26	0.17	0.94	0.09	57.49	0.94	58.52	55.47	62.36	61.27
4 450		1.40	40.06	0.40	1.37	0.10	37.66	1.31	39.52	38.81	44.61	43.32
1 473		0.60	20.17	0.51	0.42	0.00	16.40	0.30	26.50	27.92	24.81	23.30
		0.70	35.03	0.90	0.33	0.04	36.80	0.41	40.38	41.63	39.03	37.74
		0.80	49.53	0.06	0.68	0.08	51.92	0.46	53.32	53.36	52.03	51.09
		0.90	59.41	1.30	0.38	0.06	61.75	0.50	63.54	61.84	62.17	61.53
	5	1.00	66.69	0.22	0.53	0.08	66.29	0.55	69.44	66.15	68.18	67.78
		1.10	69.76	0.69	0.54	0.17	65.54	0.66	69.60	65.43	69.00	68.69
		1.20	64.10	0.39	0.59	0.06	59.50	0.84	62.43	58.60	63.37	62.93
		1.30	51.48	2.28	0.84	0.15	48.18	1.13	47.38	45.42	50.69	49.84

Table A-10 (cont'd)

			0.70	21.42	1.56	0.69	0.01	29.69	0.47	32.41	34.09	31.15	30.15
			0.80	37.70	1.68	0.48	0.21	41.89	0.54	43.68	44.48	42.47	41.84
		10	0.90	47.82	0.28	0.74	0.05	49.82	0.58	52.77	52.04	51.41	51.12
		10	1.00	57.54	0.15	0.86	0.02	53.48	0.65	58.14	55.88	56.74	56.69
			1.10	56.85	0.84	0.85	0.04	52.88	0.76	58.22	55.08	57.32	57.33
1	473		1.20	51.64	0.66	0.84	0.20	48.00	0.98	51.23	48.44	51.82	51.63
	•		0.80	29.40	0.75	0.74	0.19	31.85	0.61	34.93	36.28	33.84	33.42
			0.90	37.38	0.55	0.75	0.15	37.88	0.67	42.83	42.92	41.60	41.53
		15	1.00	42.54	0.73	0.85	0.09	40.67	0.74	47.59	46.26	46.22	46.39
			1.10	44.38	0.70	1.01	0.18	40.21	0.87	47.53	45.35	46.54	46.75
			1.20	40.66	1.09	0.97	0.12	36.51	1.11	40.71	38.88	41.16	41.11
			0.70	17.94	0.27	-0.10	0.13	18.40	0.12	17.44	19.79	17.13	17.04
			0.80	26.85	0.12	0.13	0.03	25.96	0.14	24.94	27.10	24.98	25.37
			0.90	33.72	0.24	0.26	0.04	30.87	0.15	31.22	32.45	31.35	32.22
		0	1.00	37.54	0.20	0.31	0.07	33.14	0.16	35.16	35.02	35.20	36.40
			1.10	36.37	0.10	0.24	0.03	32.77	0.19	35.25	33.98	35.45	36.70
			1.20	30.32	0.38	0.29	0.11	29.75	0.25	29.40	28.16	30.73	31.59
	-		1.30	20.30	0.13	0.31	0.03	24.09	0.33	19.11	18.89	21.58	21.78
			0.80	20.67	0.12	0.11	0.04	21.76	0.16	19.76	21.92	19.68	19.95
			0.90	26.80	0.18	0.22	0.03	25.87	0.18	25.08	26.54	25.14	25.84
3	373	5	1.00	29.75	0.17	0.25	0.04	27.78	0.19	28.40	28.67	28.40	29.41
			1.10	28.69	0.07	0.25	0.02	27.46	0.23	28.24	27.48	28.39	29.44
	-		1.20	23.21	0.34	0.37	0.06	24.93	0.29	22.44	21.81	23.71	24.39
			0.80	15.71	0.09	0.10	0.08	17.55	0.19	15.25	17.29	15.04	15.20
			0.90	20.59	0.25	0.24	0.06	20.87	0.21	19.64	21.20	19.63	20.16
		10	1.00	23.25	0.17	0.30	0.09	22.41	0.23	22.34	22.89	22.32	23.13
			1.10	22.34	0.07	0.35	0.05	22.16	0.27	21.93	21.59	22.07	22.93
	-		1.20	17.22	0.25	0.55	0.03	20.11	0.34	16.30	16.15	17.46	18.02
			0.90	15.58	0.17	0.24	0.05	15.87	0.23	14.92	16.46	14.83	15.20
		15	1.00	17.63	0.09	0.36	0.06	17.04	0.26	17.03	17.74	16.98	17.61
			1.10	16.56	0.84	0.46	0.09	16.85	0.31	16.39	16.33	16.52	17.20
			0.70	23.33	0.16	0.02	0.08	23.77	0.11	23.03	25.86	22.77	22.70
			0.80	33.12	0.64	0.12	0.09	33.53	0.13	32.11	34.57	32.24	32.75
2	400	0	0.90	40.90	0.53	0.14	0.08	39.88	0.14	39.61	40.88	39.61	40.90
3	423	0	1.00	45.42	0.51	0.21	0.14	42.81	0.16	44.24	43.88	44.36	45.82
			1.10	44.59	0.10	0.08	0.06	42.33	0.18	44.39	42.69	44.71	46.22
			1.20	37.90	0.24	0.03	0.11	38.43	0.23	37.86	36.08	39.42	40.49
			1.30	26.92	0.54	0.08	0.17	31.11	0.32	25.70	25.15	28.78	29.03

Table A-10 (cont'd)

			0.80	26.65	0.38	0.01	0.09	28.10	0.15	25.74	28.28	25.73	26.11
			0.90	32.06	1.65	0.09	0.05	33.42	0.17	32.15	33.75	32.27	33.17
		5	1.00	37.12	0.28	0.14	0.08	35.88	0.19	36.10	36.25	36.15	37.40
		3	1.10	36.53	0.95	0.18	0.22	35.47	0.22	35.98	34.92	36.21	37.50
			1.20	29.81	0.58	0.17	0.12	32.21	0.28	29.50	28.46	30.96	31.84
			1.30	20.60	0.61	0.42	0.10	26.08	0.38	18.78	18.67	21.21	21.45
3	423		0.80	20.87	1.13	0.11	0.08	22.67	0.18	20.14	22.60	19.97	20.23
3	423		0.90	26.03	0.29	0.10	0.09	26.96	0.20	25.49	27.27	25.53	26.23
		10	1.00	29.27	0.04	0.20	0.04	28.95	0.22	28.74	29.28	28.76	29.78
			1.10	27.71	0.65	0.02	0.08	28.62	0.26	28.36	27.81	28.55	29.62
			1.20	22.01	1.09	0.37	0.12	25.98	0.33	22.00	21.58	23.37	24.08
			0.90	20.28	0.44	0.18	0.12	20.50	0.22	19.65	21.46	19.59	20.10
		15	1.00	22.41	0.76	0.12	0.26	22.01	0.25	22.23	23.01	22.22	23.02
			1.10	21.34	0.89	0.29	0.05	21.76	0.29	21.59	21.43	21.76	22.63
			0.80	21.53	0.15	-0.02	0.07	21.69	0.08	19.35	21.57	19.81	19.93
			0.90	27.53	0.19	0.08	0.02	25.80	0.09	24.55	26.04	25.30	25.84
		0	1.00	30.59	0.21	0.13	0.05	27.69	0.10	27.78	27.97	28.52	29.34
			1.10	30.05	0.53	0.29	0.16	27.38	0.11	27.61	26.59	28.44	29.24
			1.20	22.87	0.23	0.09	0.10	24.86	0.14	21.96	20.94	23.63	24.05
			0.80	16.98	0.37	0.15	0.15	18.18	0.10	15.11	17.16	15.28	15.29
5	373		0.90	22.24	0.18	0.24	0.05	21.62	0.10	19.43	20.94	19.93	20.29
		5	1.00	24.20	0.38	0.17	0.10	23.21	0.12	22.05	22.45	22.60	23.21
			1.10	22.76	0.53	0.24	0.14	22.94	0.14	21.62	20.97	22.26	22.90
			1.20	16.95	0.18	0.26	0.06	20.83	0.17	16.23	15.68	17.56	17.93
			0.90	16.40	0.19	0.07	0.13	17.44	0.12	14.97	16.41	15.23	15.43
		10	1.00	18.73	0.19	0.29	0.05	18.72	0.13	17.01	17.53	17.38	17.82
			1.10	17.18	0.35	0.23	0.13	18.51	0.16	16.36	15.99	16.82	17.33

BIBLIOGRAPHY

BIBLIOGRAPHY

- 1. Energy Information Administration. 2017. "International Energy Outlook 2017." Accessed October 31, 2018. https://www.eia.gov/outlooks/ieo/pdf/0484(2017).pdf.
- 2. Boyce, Meherwan. 2012. "10 Combustors." In *Gas Turbine Engineering Handbook*, 427-90. Oxford: Butterworth-Heinemann.
- 3. Duva, Berk Can, Lauren Elizabeth Chance, and Elisa Toulson. 2020. "Effect of CO2 Dilution on the Laminar Burning Velocities of Premixed Methane/Air Flames at Elevated Temperature." *Journal of Engineering for Gas Turbines and Power* 142 (3): 031014. https://doi.org/10.1115/1.4044641.
- 4. De Vries, Jaap. 2009. "A study on spherical expanding flame speeds of methane, ethane, and methane/ethane mixtures at elevated pressures." Doctoral dissertation, Texas A&M University. http://hdl.handle.net/1969.1/ETD-TAMU-2009-05-601.
- 5. Kalghatgi, Gautam. 2018. "Is it really the end of internal combustion engines and petroleum in transport?" *Applied Energy* 225: 965-74. https://doi.org/10.1016/j.apenergy.2018.05.076.
- 6. Saravanamuttoo, Herbert, Gordon Frederick Crichton Rogers, and Henry Cohen. 2001. *Gas Turbine Theory*. Pearson College Div.
- 7. Concawe. 2006. "Motor Vehicle Emission Regulations and Fuel Specifications Part I: 2004/2005 Update." Accessed November 7, 2018. https://www.concawe.eu/wp-content/uploads/2017/01/rpt_06-5_appendix-2006-02031-01-e.pdf.
- 8. DieselNet. n.d. "Emission Standards." Accessed November 7, 2018. https://www.dieselnet.com/standards.
- 9. Mazas, Antoine, Deanna Lacoste, and Thierry Schuller. 2010. "Experimental and Numerical Investigation on the Laminar Flame Speed of CH4/O2 Mixtures Diluted With CO2 and H2O." *Proceedings of the ASME Turbo Expo 2010: Power for Land, Sea, and Air, June 14-18, 2010.* Glasgow, UK. https://doi.org/10.1115/GT2010-22512.
- 10. Halter, Fabien, Fabrice Foucher, Ludovic Landry, and Christine Mounaïm-Rousselle. 2009. "Effect of Dilution by Nitrogen and/or Carbon Dioxide on Methane and Iso-Octane Air Flames." *Combustion Science and Technology* 181 (6): 813-27. https://doi.org/10.1080/00102200902864662.
- 11. Wu, Cheng Kang, and Chung Law. 1985. "On the determination of laminar flame speeds from stretched flames." *Symposium (International) on Combustion* 20 (1): 1941-49. https://doi.org/10.1016/S0082-0784(85)80693-7.
- 12. Turns, Stephen. 2012. *An introduction to combustion: concepts and applications*. New York: McGraw-Hill.

- 13. Egolfopoulos, Fokion, Nils Hansen, Yiguang Ju, Katharina Kohse-Höinghaus, Chung Law, and Fei Qi. 2014. "Advances and challenges in laminar flame experiments and implications for combustion chemistry." *Progress in Energy and Combustion Science* 43: 36-67. https://doi.org/10.1016/j.pecs.2014.04.004.
- 14. Syed, Iltesham, Yeliana Yeliana, Abhijit Mukherjee, Jeffrey Naber, and Donna Michalek. 2010. "Numerical Investigation of Laminar Flame Speed of Gasoline Ethanol/Air Mixtures with Varying Pressure, Temperature and Dilution." *SAE International Journal of Engines* 3 (1): 517-28. https://doi.org/10.4271/2010-01-0620.
- 15. Liao, Ying-Hao, and William Roberts. 2016. "Laminar Flame Speeds of Gasoline Surrogates Measured with the Flat Flame Method." *Energy & Fuels* 30 (2): 1317–24. https://doi.org/10.1021/acs.energyfuels.5b01433.
- 16. Takashi, Hara, and Kimitoshi Tanoue. 2006. "Laminar Flame Speeds of Ethanol, n-Heptane, Iso-Octane Air Mixtures." *FISITA 2006 Student Congress* 19 (2-3): 181-6. https://citeseerx.ist.psu.edu/viewdoc/download?doi=10.1.1.541.9753&rep=rep1&type=pdf.
- 17. Marshall, Steve, Scott Taylor, Richard Stone, Trevor Davies, and Roger Cracknell. 2011. "Laminar burning velocity measurements of liquid fuels at elevated pressures and temperatures with combustion residuals." *Combustion and Flame* 158 (10): 1920–32. https://doi.org/10.1016/j.combustflame.2011.02.016.
- 18. Meher-Homji, Cyrus. 2000. "The Historical Evaluation of Turbomachinery." *Proceedings of the 29th Turbomachinery Symposium, September 18-21, 2000.* Texas, US. https://doi.org/10.21423/R1X948.
- 19. Xie, Yongliang, Jinhua Wang, Meng Zhang, Jing Gong, Wu Jin, and Zuohua Huang. 2013. "Experimental and Numerical Study on Laminar Flame Characteristics of Methane Oxy-fuel Mixtures Highly Diluted with CO2." *Energy & Fuels* 27 (10): 6231-37. https://doi.org/10.1021/ef401220h.
- 20. Lieuwen, Tim, Vincent McDonell, Eric Petersen, and Domenic Santavicca. 2008. "Fuel Flexibility Influences on Premixed Combustor Blowout, Flashback, Autoignition, and Stability." *Journal of Engineering for Gas Turbines and Power* 130 (1): 011506. https://doi.org/10.1115/1.2771243.
- 21. Gu, Xiao-Jun, Zahurul Haq, Malcolm Lawes, and Robert Woolley. 2000. "Laminar burning velocity and Markstein lengths of methane—air mixtures." *Combustion and Flame* 121 (1): 41-58. https://doi.org/10.1016/S0010-2180(99)00142-X.
- 22. Brower, Marissa, Eric Petersen, Wayne Metcalfe, Henry Curran, Marc Füri, Gilles Bourque, Naresh Aluri, and Felix Güthe. 2013. "Ignition Delay Time and Laminar Flame Speed Calculations for Natural Gas/Hydrogen Blends at Elevated Pressures." *Journal of Engineering for Gas Turbines and Power* 135 (2): 021504. https://doi.org/10.1115/1.4007763.

- 23. Li, Qianqian, Jin Fu, Xuesong Wu, Chenglong Tang, and Zuohua Huang. 2012. "Laminar Flame Speeds of DMF/Iso-octane-Air-N2/CO2 Mixtures." *Energy & Fuels* 26 (2): 917-25. https://doi.org/10.1021/ef201638w.
- 24. Duva, Berk Can, Lauren Elizabeth Chance, and Elisa Toulson. 2019. "Laminar Flame Speeds of Premixed Iso-Octane/Air Flames at High Temperatures with CO2 Dilution." *SAE International Journal of Advances and Current Practices in Mobility* 1 (3): 1148-57. https://doi.org/10.4271/2019-01-0572.
- 25. Winkler, Dieter, Weiqun Geng, Klaus Knapp, Geoffrey Engelbrecht, Timothy Griffin, and Peter Stuber. 2014. "Staged combustion concept for increased operational flexibility of gas turbines." *Proceedings of the 1st Global Power & Propulsion Society Forum, January 16-18*, 2014. Zurich, Switzerland.
- 26. Schulz, Oliver, and Nicolas Noiray. 2019. "Combustion regimes in sequential combustors: Flame propagation and autoignition at elevated temperature and pressure." *Combustion and Flame* 205: 253-68. https://doi.org/10.1016/j.combustflame.2019.03.014.
- 27. Bulysova, L. A., A. L. Berne, V. D. Vasil'ev, M. N. Gutnik, and M. M. Gutnik. 2018. "Study of Sequential Two-Stage Combustion in a Low-Emission Gas Turbine Combustion Chamber." *Thermal Engineering* 65 (11): 806-17. https://doi.org/10.1134/S0040601518110010.
- 28. Ciani, Andrea, Mirko Bothien, Birute Bunkute, John Wood, and Gerhard Früchtel. 2019. "Superior fuel and operational flexibility of sequential combustion in Ansaldo Energia gas turbines." *Journal of the Global Power and Propulsion Society* 3: 630-8. https://doi.org/10.33737/jgpps/110717.
- 29. Hayashi, Shigeru, and Hideshi Yamada. 2000. "NOx emissions in combustion of lean premixed mixtures injected into hot burned gas." *Proceedings of the Combustion Institute* 28 (2): 2443-9. https://doi.org/10.1016/S0082-0784(00)80658-X.
- 30. Ahrens, Denise, Michael Kolb, Christoph Hirsch, and Thomas Sattelmayer. 2016. "Influence of Preflame and Postflame Mixing on NOx Formation in a Reacting Premixed Jet in Hot Cross Flow." *Journal of Engineering for Gas Turbines and Power* 138 (8): 081506. https://doi.org/10.1115/1.4032420.
- 31. Wind, Torsten, Felix Güthe, and Khawar Syed. 2014. "Co-Firing of Hydrogen and Natural Gases in Lean Premixed Conventional and Reheat Burners (Alstom GT26)." *Proceedings of the ASME Turbo Expo 2014: Turbine Technical Conference and Exposition, June 16-20, 2014.* Düsseldorf, Germany. https://doi.org/10.1115/GT2014-25813.
- 32. Van Basshuysen, Richard, and Fred Schäfer. 2004. *Internal combustion engine handbook: basics, components, systems, and perspectives*. Warrendale, Pennsylvania: SAE International.

- 33. Toulson, Elisa. 2008. "Applying Alternative Fuels in Place of Hydrogen to the Jet Ignition Process." Doctoral dissertation, The University of Melbourne. http://cat.lib.unimelb.edu.au/record=b3257928
- 34. Heywood, John. 1988. Internal combustion engine fundamentals. New York: McGraw-Hill.
- 35. Meffert, Michael, Denis Lenane, Martin Openshaw, and Joseph Roos. 2000. "Analysis of Nitrous Oxide Emissions from Light Duty Passenger Cars." *SAE International* 2000-01-1952. https://doi.org/10.4271/2000-01-1952.
- 36. Tully, Edward, and John Heywood. 2003. "Lean-Burn Characteristics of a Gasoline Engine Enriched with Hydrogen Plasmatron Fuel Reformer." *SAE International* 2003-01-0630. https://doi.org/10.4271/2003-01-0630.
- 37. Amiridis, Michael, Tiejun Zhang, and Robert Farrauto. 1996. "Selective catalytic reduction of nitric oxide by hydrocarbons." *Applied Catalysis B: Environmental* 10 (1): 203-27. https://doi.org/10.1016/0926-3373(96)00031-8.
- 38. Burch, Robbie, John Breen, and Frederic Meunier. 2002. "A review of the selective reduction of NOx with hydrocarbons under lean-burn conditions with non-zeolitic oxide and platinum group metal catalysts." *Applied Catalysis B: Environmental* 39 (4): 283-303. https://doi.org/10.1016/S0926-3373(02)00118-2.
- 39. Fritz, A., and Veronique Pitchon. 1997. "The current state of research on automotive lean NOx catalysis." *Applied Catalysis B: Environmental* 13 (1): 1-25. https://doi.org/10.1016/S0926-3373(96)00102-6.
- 40. Heck, Ronald, and Robert Farrauto. 2001. "Automobile exhaust catalysts." *Applied Catalysis A: General* 221 (1): 443-57. https://doi.org/10.1016/S0926-860X(01)00818-3.
- 41. Guibet, Jean-Claude. 1999. *Fuels and Engines: Technology, Energy, Environment*. TECHNIP: Institut Français du Petrole Publications.
- 42. Kalghatgi, Gautam. 2014. Fuel/engine Interactions. Warrendale, Pennsylvania: SAE International.
- 43. Gomaa, Mohamed, Ahmad Alimin, and Kamarul Kamarudin. 2011. "The effect of EGR rates on NOX and smoke emissions of an IDI diesel engine fuelled with Jatropha biodiesel blends." *International Journal of Energy and Environment* 2 (3): 477-90. http://www.ijee.ieefoundation.org/vol2/issue3/IJEE_07_v2n3.pdf.
- 44. Rallis, Costa John, and Ashton Garforth. 1980. "The determination of laminar burning velocity." *Progress in Energy and Combustion Science* 6 (4): 303-29. https://doi.org/10.1016/0360-1285(80)90008-8.
- 45. Wang, Ziyu, Sai Yelishala, Guangying Yu, Hameed Metghalchi, and Yiannis Levendis. 2019. "Effects of Carbon Dioxide on Laminar Burning Speed and Flame Instability of

- Methane/Air and Propane/Air Mixtures: A Literature Review." *Energy & Fuels* 33 (10): 9403-18. https://doi.org/10.1021/acs.energyfuels.9b02346.
- 46. Andrews, Gordon, and Derek Bradley. 1972. "Determination of burning velocities: A critical review." *Combustion and Flame* 18 (1): 133-53. https://doi.org/10.1016/S0010-2180(72)80234-7.
- 47. Eberius, H., and T. Kick. 1992. "Stabilization of Premixed, Conical Methane Flames at High Pressure." *Berichte der Bunsengesellschaft für physikalische Chemie* 96 (10): 1416-9. https://doi.org/10.1002/bbpc.19920961013.
- 48. Bouvet, Nicolas, Christian Chauveau, Iskender Gökalp, Seong-Young Lee, and Robert Santoro. 2011. "Characterization of syngas laminar flames using the Bunsen burner configuration." *International Journal of Hydrogen Energy* 36 (1): 992-1005. https://doi.org/10.1016/j.ijhydene.2010.08.147.
- 49. Pitsch, Heinz. 2014. "Laminar Premixed Flames: Kinematics and Burning Velocity." Lecture, CEFRC Combustion Summer School, Princeton University, Princeton, NJ.
- 50. Wei, Zhilong, Haisheng Zhen, Chunwah Leung, Chunshun Cheung, and Zuohua Huang. 2015. "Heat transfer characteristics and the optimized heating distance of laminar premixed biogas-hydrogen Bunsen flame impinging on a flat surface." *International Journal of Hydrogen Energy* 40 (45): 15723-31. https://doi.org/10.1016/j.ijhydene.2015.06.047.
- 51. Law, Chung, Delin Zhu, and Gang Yu. 1988. "Propagation and extinction of stretched premixed flames." *Symposium (International) on Combustion* 21 (1): 1419-26. https://doi.org/10.1016/S0082-0784(88)80374-6.
- 52. De Goey, Philip, A. van Maaren, and R. M. Quax. 1993. "Stabilization of Adiabatic Premixed Laminar Flames on a Flat Flame Burner." *Combustion Science and Technology* 92 (1-3): 201-7. https://doi.org/10.1080/00102209308907668.
- 53. Botha, Johan, and Dudley Brian Spalding. 1954. "The laminar flame speed of propane/air mixtures with heat extraction from the flame." *Proceedings of the Royal Society of London. Series A. Mathematical and Physical Sciences* 225 (1160): 71-96. https://doi.org/10.1098/rspa.1954.0188.
- 54. Bosschaart, Karel Joop, and Philip de Goey. 2004. "The laminar burning velocity of flames propagating in mixtures of hydrocarbons and air measured with the heat flux method." *Combustion and Flame* 136 (3): 261-9. https://doi.org/10.1016/j.combustflame.2003.10.005.
- 55. Bosschaart, Karel Joop, and Philip de Goey. 2003. "Detailed analysis of the heat flux method for measuring burning velocities." *Combustion and Flame* 132 (1): 170-80. https://doi.org/10.1016/S0010-2180(02)00433-9.
- 56. Campbell, Matthew Frederick, Paul Schrader, Leneke Catalano, Olof Johansson, Alexis Bohlin, Nicole Richards-Henderson, Christopher Kliewer, and Hope Michelsen. 2017. "A

- small porous-plug burner for studies of combustion chemistry and soot formation." *Review of Scientific Instruments* 88 (12): 125106. https://doi.org/10.1063/1.5016212.
- 57. Gerstein, Melvin, Oscar Levine, and Edgar Wong. 1951. "Flame Propagation. II. The Determination of Fundamental Burning Velocities of Hydrocarbons by a Revised Tube Method." *Journal of the American Chemical Society* 73 (1): 418-22. https://doi.org/10.1021/ja01145a136.
- 58. Andrews, Gordon, and Derek Bradley. 1973. "Determination of burning velocity by double ignition in a closed vessel." *Combustion and Flame* 20 (1): 77-89. https://doi.org/10.1016/S0010-2180(73)81259-3.
- 59. Linnett, John Wilfrid, H. S. Pickering, and Peter Wheatley. 1951. "Burning velocity determinations. Part IV.—The soap bubble method of determining burning velocities." *Transactions of the Faraday Society* 47: 974-80. https://doi.org/10.1039/TF9514700974.
- 60. Strauss, William, and Rudolph Edse. 1958. "Burning velocity measurements by the constant-pressure bomb method." *Symposium (International) on Combustion* 7 (1): 377-85. https://doi.org/10.1016/S0082-0784(58)80068-5.
- 61. Fristrom, Robert. 1957. "The structure of laminar flames." *Symposium (International) on Combustion* 6 (1): 96-110. https://doi.org/10.1016/S0082-0784(57)80016-2.
- 62. Law, Chung. 2006. Combustion Physics. Cambridge: Cambridge University Press.
- 63. Discussion. 1958. *Symposium (International) on Combustion* 7 (1): 407-14. https://doi.org/10.1016/S0082-0784(58)80072-7.
- 64. Simon, Dorothy, and Edgar Wong. 1954. "An Evaluation of the Soap-bubble Method for Burning Velocity Measurements Using Ethylene-oxygen-nitrogen and Methane-oxygen-nitrogen Mixtures." *NACA Technical Note 3106*. https://ntrs.nasa.gov/citations/19930083831
- 65. Chen, Zheng, and Yiguang Ju. 2007. "Theoretical analysis of the evolution from ignition kernel to flame ball and planar flame." *Combustion Theory and Modelling* 11 (3): 427-53. https://doi.org/10.1080/13647830600999850.
- 66. Duva, Berk Can, Lauren Elizabeth Chance, and Elisa Toulson. 2020. "Correlations for the Laminar Burning Velocity and Burned Gas Markstein Length of Methane-Air Mixtures Diluted with Flue Gases at High Temperatures and Pressures." *Fuel* 281: 118721. https://doi.org/10.1016/j.fuel.2020.118721.
- 67. Peters, Nathan, and Ben Akih-Kumgeh. 2017. "Spark and Laser Ignition of Iso-octane and Ethanol Blends." Paper presented at *10th U.S. National Combustion Meeting, April 23-26, 2017.* College Park, US.
- 68. Bradley, Derek, Philip Gaskell, and Xiao-Jun Gu. 1996. "Burning velocities, markstein lengths, and flame quenching for spherical methane-air flames: A computational study." *Combustion and Flame* 104 (1): 176-98. https://doi.org/10.1016/0010-2180(95)00115-8.

- 69. Gülder, Omer. 1982. "Laminar burning velocities of methanol, ethanol and isooctane-air mixtures." *Symposium (International) on Combustion* 19 (1): 275-81. https://doi.org/10.1016/S0082-0784(82)80198-7.
- 70. Metghalchi, Mohamad, and James Keck. 1982. "Burning velocities of mixtures of air with methanol, isooctane, and indolene at high pressure and temperature." *Combustion and Flame* 48: 191-210. https://doi.org/10.1016/0010-2180(82)90127-4.
- 71. Farrell, John, Robert Johnston, and Ioannis Androulakis. 2004. "Molecular Structure Effects on Laminar Burning Velocities At Elevated Temperature And Pressure." *SAE International* 2004-01-2936. https://doi.org/10.4271/2004-01-2936.
- 72. Stone, Richard, Andrew Clarke, and Paul Beckwith. 1998. "Correlations for the Laminar-Burning Velocity of Methane/Diluent/Air Mixtures Obtained in Free-Fall Experiments." *Combustion and Flame* 114 (3): 546-55. https://doi.org/10.1016/S0010-2180(97)00329-5.
- 73. Elia, Mimmo, Matthew Ulinski, and Mohamad Metghalchi. 2000. "Laminar Burning Velocity of Methane–Air–Diluent Mixtures." *Journal of Engineering for Gas Turbines and Power* 123 (1): 190-6. https://doi.org/10.1115/1.1339984.
- 74. Ponnusamy, Senthilkumar, David Checkel, and Brian Fleck. 2005. "Maintaining Burning Velocity of Exhaust-Diluted Methane/Air Flames by Partial Fuel Reformation." *International Flame Research Foundation Combustion Journal* 200506. https://ifrf.net/research/archive/maintaining-burning-velocity-of-exhaust-diluted-methane-air-flames-by-partial-fuel-reformation/.
- 75. Marshall, Stephen, Richard Stone, Crina Hegheş, Trevor Davies, and Roger Cracknell. 2010. "High pressure laminar burning velocity measurements and modelling of methane and n-butane." *Combustion Theory and Modelling* 14 (4): 519-40. https://doi.org/10.1080/13647830.2010.500021.
- 76. Hu, Erjiang, Xiaotian Li, Xin Meng, Yizhen Chen, Yu Cheng, Yongliang Xie, and Zuohua Huang. 2015. "Laminar flame speeds and ignition delay times of methane—air mixtures at elevated temperatures and pressures." *Fuel* 158: 1-10. https://doi.org/10.1016/j.fuel.2015.05.010.
- 77. Kwon, Oh Chae, Mohamed Hassan, and Gerard Faeth. 2000. "Flame/Stretch Interactions of Premixed Fuel-Vapor/O/N Flames." *Journal of Propulsion and Power* 16 (3): 513-22. https://doi.org/10.2514/2.5598.
- 78. Kelley, Andrew, Wei Liu, Yuxuan Xin, Andrew Smallbone, and Chung Law. 2011. "Laminar flame speeds, non-premixed stagnation ignition, and reduced mechanisms in the oxidation of iso-octane." *Proceedings of the Combustion Institute* 33 (1): 501-8. https://doi.org/10.1016/j.proci.2010.05.058.
- 79. Broustail, Guillaume, Fabien Halter, Patrice Seers, Gladys Moréac, and Christine Mounaïm-Rousselle. 2013. "Experimental determination of laminar burning velocity for butanol/iso-

- octane and ethanol/iso-octane blends for different initial pressures." *Fuel* 106: 310-7. https://doi.org/10.1016/j.fuel.2012.10.066.
- 80. Zhang, Xinyi, Chenglong Tang, Huibin Yu, Qianqian Li, Jing Gong, and Zuohua Huang. 2013. "Laminar Flame Characteristics of iso-Octane/n-Butanol Blend–Air Mixtures at Elevated Temperatures." *Energy & Fuels* 27 (4): 2327-35. https://doi.org/10.1021/ef4001743.
- 81. Baloo, Mahdi, Bijan Mollaei Dariani, Mehdi Akhlaghi, and Iman Chitsaz. 2015. "Effect of iso-octane/methane blend on laminar burning velocity and flame instability." *Fuel* 144: 264-73. https://doi.org/10.1016/j.fuel.2014.11.043.
- 82. Li, Qianqian, Wu Jin, and Zuohua Huang. 2016. "Laminar Flame Characteristics of C1–C5 Primary Alcohol-Isooctane Blends at Elevated Temperature." *Energies* 9 (7): 511. https://doi.org/10.3390/en9070511.
- 83. Mannaa, Ossama, Morkous Mansour, William Roberts, and Suk Chung. 2015. "Laminar burning velocities at elevated pressures for gasoline and gasoline surrogates associated with RON." *Combustion and Flame* 162 (6): 2311-21. https://doi.org/10.1016/j.combustflame.2015.01.004.
- 84. Zhou, Jianxi, Mathieu Cordier, Christine Mounaïm-Rousselle, and Fabrice Foucher. 2011. "Experimental estimate of the laminar burning velocity of iso-octane in oxygen-enriched and CO2-diluted air." *Combustion and Flame* 158 (12): 2375-83. https://doi.org/10.1016/j.combustflame.2011.05.002.
- 85. Galmiche, Bénédicte, Fabien Halter, and Fabrice Foucher. 2012. "Effects of high pressure, high temperature and dilution on laminar burning velocities and Markstein lengths of iso-octane/air mixtures." *Combustion and Flame* 159 (11): 3286-99. https://doi.org/10.1016/j.combustflame.2012.06.008.
- 86. Hassan, Mohamed, Kendrick Aung, and Gerard Faeth. 1998. "Measured and predicted properties of laminar premixed methane/air flames at various pressures." *Combustion and Flame* 115 (4): 539-50. https://doi.org/10.1016/S0010-2180(98)00025-X.
- 87. Rozenchan, Gilberto, Delin Zhu, Chung Law, and Stephen Tse. 2002. "Outward propagation, burning velocities, and chemical effects of methane flames up to 60 ATM." *Proceedings of the Combustion Institute* 29 (2): 1461-70. https://doi.org/10.1016/S1540-7489(02)80179-1.
- 88. Liao, Shiyong, Deming Jiang, Jian Gao, and Zuohua Huang. 2004. "Measurements of Markstein Numbers and Laminar Burning Velocities for Natural Gas—Air Mixtures." *Energy & Fuels* 18 (2): 316-26. https://doi.org/10.1021/ef034036z.
- 89. Halter, Fabien, Christian Chauveau, Nabiha Djebaïli-Chaumeix, and Iskender Gökalp. 2005. "Characterization of the effects of pressure and hydrogen concentration on laminar burning velocities of methane—hydrogen—air mixtures." *Proceedings of the Combustion Institute* 30 (1): 201-8. https://doi.org/10.1016/j.proci.2004.08.195.

- 90. Tahtouh, Toni, Fabien Halter, and Christine Mounaïm-Rousselle. 2009. "Measurement of laminar burning speeds and Markstein lengths using a novel methodology." *Combustion and Flame* 156 (9): 1735-43. https://doi.org/10.1016/j.combustflame.2009.03.013.
- 91. Hu, Erjiang, Zuohua Huang, Jiajia He, Chun Jin, and Jianjun Zheng. 2009. "Experimental and numerical study on laminar burning characteristics of premixed methane—hydrogen—air flames." *International Journal of Hydrogen Energy* 34 (11): 4876-88. https://doi.org/10.1016/j.ijhydene.2009.03.058.
- 92. Lowry, William, Jaap de Vries, Michael Krejci, Eric Petersen, Zeynep Serinyel, Wayne Metcalfe, Henry Curran, and Gilles Bourque. 2011. "Laminar Flame Speed Measurements and Modeling of Pure Alkanes and Alkane Blends at Elevated Pressures." *Journal of Engineering for Gas Turbines and Power* 133 (9): 091501. https://doi.org/10.1115/1.4002809.
- 93. Duva, Berk Can, Lauren Elizabeth Chance, and Elisa Toulson. 2020. "Experimental and Numerical Investigation of the CO2 Dilution Effect on Laminar Burning Velocities and Burned Gas Markstein Lengths of High/Low RON Gasolines and Isooctane Flames at Elevated Temperatures." *Energy & Fuels* 34 (1): 996-1004. https://doi.org/10.1021/acs.energyfuels.9b03854.
- 94. Duva, Berk Can, Lauren Elizabeth Chance, and Elisa Toulson. 2020. "Dilution effect of different combustion residuals on laminar burning velocities and burned gas Markstein lengths of premixed methane/air mixtures at elevated temperature." *Fuel* 267: 117153. https://doi.org/10.1016/j.fuel.2020.117153.
- 95. Duva, Berk Can, Yen-Cheng Wang, Lauren Chance, and Elisa Toulson. 2020. "The Effect of Exhaust Gas Recirculation (EGR) on Fundamental Characteristics of Premixed Methane/Air Flames." *SAE International* 2020-01-0339. https://doi.org/10.4271/2020-01-0339.
- 96. Duva, Berk Can, Yen-Cheng Wang, Lauren Elizabeth Chance, and Elisa Toulson. 2021. "Laminar Flame Characteristics of Sequential Two-Stage Combustion of Premixed Methane/Air Flames." *Journal of Engineering for Gas Turbines and Power* 143 (6): 061029. https://doi.org/10.1115/1.4048450.
- 97. Duva, Berk Can, Lauren Elizabeth Chance, and Elisa Toulson. 2021. "The critical lower radius limit approach for laminar flame speed measurement from spherically expanding stretched flames." *Experimental Thermal and Fluid Science* 121: 110284. https://doi.org/10.1016/j.expthermflusci.2020.110284.
- 98. Balusamy, Saravanan, Armelle Cessou, and Bertrand Lecordier. 2011. "Direct measurement of local instantaneous laminar burning velocity by a new PIV algorithm." *Experiments in Fluids* 50 (4): 1109-21. https://doi.org/10.1007/s00348-010-1027-5.
- 99. Varea, Emilien, Vincent Modica, Alexis Vandel, and Bruno Renou. 2012. "Measurement of laminar burning velocity and Markstein length relative to fresh gases using a new postprocessing procedure: Application to laminar spherical flames for methane, ethanol and

- isooctane/air mixtures." *Combustion and Flame* 159 (2): 577-90. https://doi.org/10.1016/j.combustflame.2011.09.002.
- 100. Faghih, Mahdi, and Zheng Chen. 2016. "The constant-volume propagating spherical flame method for laminar flame speed measurement." *Science Bulletin* 61 (16): 1296-310. https://doi.org/10.1007/s11434-016-1143-6.
- 101. Marshall, Stephen. 2010. "Measuring Laminar Burning Velocities." Doctoral dissertation, Oxford University. https://ora.ox.ac.uk/objects/uuid:81ea0ed8-3abd-4192-86ef-67bd5581c325
- 102. Moghaddas, Ali, Casey Bennett, Emad Rokni, and Hameed Metghalchi. 2014. "Laminar burning speeds and flame structures of mixtures of difluoromethane (HFC-32) and 1,1-difluoroethane (HFC-152a) with air at elevated temperatures and pressures." *HVAC&R Research* 20 (1): 42-50. https://doi.org/10.1080/10789669.2013.822252.
- 103. Almansour, Bader, Luke Thompson, Joseph Lopez, Ghazal Barari, and Subith Vasu. 2015. "Laser Ignition and Flame Speed Measurements in Oxy-Methane Mixtures Diluted With CO2." *Journal of Energy Resources Technology* 138 (3): 032201. https://doi.org/10.1115/1.4031967.
- 104. Takizawa, Kenji, Akifumi Takahashi, Kazuaki Tokuhashi, Shigeo Kondo, and Akira Sekiya. 2005. "Burning velocity measurement of fluorinated compounds by the spherical-vessel method." *Combustion and Flame* 141 (3): 298-307. https://doi.org/10.1016/j.combustflame.2005.01.009.
- 105. Moghaddas, Ali, Kian Eisazadeh-Far, and Hameed Metghalchi. 2012. "Laminar burning speed measurement of premixed n-decane/air mixtures using spherically expanding flames at high temperatures and pressures." *Combustion and Flame* 159 (4): 1437-43. https://doi.org/10.1016/j.combustflame.2011.12.005.
- 106. Rokni, Emad, Ali Moghaddas, Omid Askari, and Hameed Metghalchi. 2015. "Measurement of Laminar Burning Speeds and Investigation of Flame Stability of Acetylene (C2H2)/Air Mixtures." *Journal of Energy Resources Technology* 137 (1): 012204. https://doi.org/10.1115/1.4028363.
- 107. Chen, Zheng, Michael Burke, and Yiguang Ju. 2009. "Effects of compression and stretch on the determination of laminar flame speeds using propagating spherical flames." *Combustion Theory and Modelling* 13 (2): 343-64. https://doi.org/10.1080/13647830802632192.
- 108. Xiouris, Christodoulos, Tailai Ye, Jagannath Jayachandran, and Fokion Egolfopoulos. 2016. "Laminar flame speeds under engine-relevant conditions: Uncertainty quantification and minimization in spherically expanding flame experiments." *Combustion and Flame* 163: 270-83. https://doi.org/10.1016/j.combustflame.2015.10.003.
- 109. O'Donovan, K. H., and Costa Rallis. 1959. "A modified analysis for the determination of the burning velocity of a gas mixture in a spherical constant volume combustion vessel." *Combustion and Flame* 3: 201-14. https://doi.org/10.1016/0010-2180(59)90022-7.

- 110. Hill, Philip, and J. Hung. 1988. "Laminar Burning Velocities of Stoichiometric Mixtures of Methane with Propane and Ethane Additives." *Combustion Science and Technology* 60 (1-3): 7-30. https://doi.org/10.1080/00102208808923973.
- 111. Lewis, Bernard, and Guenther von Elbe. 1961. *Combustion, Flames and Explosions of Gases*. New York: Academic Press.
- 112. Metghalchi, Mohamad, and James Keck. 1980. "Laminar burning velocity of propane-air mixtures at high temperature and pressure." *Combustion and Flame* 38: 143-54. https://doi.org/10.1016/0010-2180(80)90046-2.
- 113. Saeed, Khizer, and Richard Stone. 2004. "Measurements of the laminar burning velocity for mixtures of methanol and air from a constant-volume vessel using a multizone model." *Combustion and Flame* 139 (1): 152-66. https://doi.org/10.1016/j.combustflame.2004.08.008.
- 114. Yates, Andy, Victor Burger, and Carl Viljoen. 2012. "A Method for Determining the Laminar Flame Speed of Jet Fuels Using Combustion Bomb Pressure." *Proceedings of the ASME Turbo Expo 2012: Turbine Technical Conference and Exposition, June 11-15, 2012.* Copenhagen, Denmark. https://doi.org/10.1115/GT2012-68117.
- 115. Bradley, Derek, and Alan Mitcheson. 1976. "Mathematical solutions for explosions in spherical vessels." *Combustion and Flame* 26: 201-17. https://doi.org/10.1016/0010-2180(76)90072-9.
- 116. Kuznetsov, Mike, Sven Kobelt, Joachim Grune, and Thomas Jordan. 2012. "Flammability limits and laminar flame speed of hydrogen—air mixtures at sub-atmospheric pressures." *International Journal of Hydrogen Energy* 37 (22): 17580-8. https://doi.org/10.1016/j.ijhydene.2012.05.049.
- 117. Luijten, Carlo, Erik Doosje, and Philip de Goey. 2009. "Accurate analytical models for fractional pressure rise in constant volume combustion." *International Journal of Thermal Sciences* 48 (6): 1213-22. https://doi.org/10.1016/j.ijthermalsci.2008.12.020.
- 118. Lewis, Bernard, and Guenther von Elbe. 1934. "Determination of the Speed of Flames and the Temperature Distribution in a Spherical Bomb from Time-Pressure Explosion Records." *The Journal of Chemical Physics* 2 (5): 283-90. https://doi.org/10.1063/1.1749464.
- 119. Oancea, Dumitru, Domnina Razus, and Niculae Ionescu. 2016. "Burning velocity determination by spherical bomb technique. I. A new model for burnt mass fraction." *Revue Roumaine de Chimie* 39: 1187-96.
- 120. Rallis, Costa, and G. E. B. Tremeer. 1963. "Equations for the determination of burning velocity in a spherical constant volume vessel." *Combustion and Flame* 7: 51-61. https://doi.org/10.1016/0010-2180(63)90155-X.
- 121. Nagy, John, John Conn, and Harry Verakis. 1969. *Explosion development in a spherical vessel*. Washington: Department of the Interior, Bureau of Mines.

- 122. Omari, Ahmad, and Leonid Tartakovsky. 2016. "Measurement of the laminar burning velocityusing the confined and unconfined spherical flame methods A comparative analysis." *Combustion and Flame* 168: 127-37. https://doi.org/10.1016/j.combustflame.2016.03.012.
- 123. Kim, Hwan Ho, Sang Hee Won, Jeffrey Santner, Zheng Chen, and Yiguang Ju. 2013. "Measurements of the critical initiation radius and unsteady propagation of n-decane/air premixed flames." *Proceedings of the Combustion Institute* 34 (1): 929-36. https://doi.org/10.1016/j.proci.2012.07.035.
- 124. Chen, Zheng. 2015. "On the accuracy of laminar flame speeds measured from outwardly propagating spherical flames: Methane/air at normal temperature and pressure." *Combustion and Flame* 162 (6): 2442-53. https://doi.org/10.1016/j.combustflame.2015.02.012.
- 125. Jayachandran, Jagannath, Runhua Zhao, and Fokion Egolfopoulos. 2014. "Determination of laminar flame speeds using stagnation and spherically expanding flames: Molecular transport and radiation effects." *Combustion and Flame* 161 (9): 2305-16. https://doi.org/10.1016/j.combustflame.2014.03.009.
- 126. Ronney, Paul, and Harold Wachman. 1985. "Effect of gravity on laminar premixed gas combustion I: Flammability limits and burning velocities." *Combustion and Flame* 62 (2): 107-19. https://doi.org/10.1016/0010-2180(85)90139-7.
- 127. Chen, Zheng. 2010. "Effects of radiation and compression on propagating spherical flames of methane/air mixtures near the lean flammability limit." *Combustion and Flame* 157 (12): 2267-76. https://doi.org/10.1016/j.combustflame.2010.07.010.
- 128. Santner, Jeffrey, Francis M. Haas, Yiguang Ju, and Frederick Dryer. 2014. "Uncertainties in interpretation of high pressure spherical flame propagation rates due to thermal radiation." *Combustion and Flame* 161 (1): 147-53. https://doi.org/10.1016/j.combustflame.2013.08.008.
- 129. Yu, Hao, Wang Han, Jeffrey Santner, Xiaolong Gou, Chae Hoon Sohn, Yiguang Ju, and Zheng Chen. 2014. "Radiation-induced uncertainty in laminar flame speed measured from propagating spherical flames." *Combustion and Flame* 161 (11): 2815-24. https://doi.org/10.1016/j.combustflame.2014.05.012.
- 130. Bonhomme, Adrien, Laurent Selle, and Thierry Poinsot. 2013. "Curvature and confinement effects for flame speed measurements in laminar spherical and cylindrical flames." *Combustion and Flame* 160 (7): 1208-14. https://doi.org/10.1016/j.combustflame.2013.02.003.
- 131. Burke, Michael, Zheng Chen, Yiguang Ju, and Frederick Dryer. 2009. "Effect of cylindrical confinement on the determination of laminar flame speeds using outwardly propagating flames." *Combustion and Flame* 156 (4): 771-9. https://doi.org/10.1016/j.combustflame.2009.01.013.

- 132. Balusamy, Saravanan, Armelle Cessou, and Bertrand Lecordier. 2009. "Measurement of laminar burning velocity—A new PIV approach." *Proceedings of the 4th European Combustion Meeting, April 14-17, 2009.* Vienna, Austria.
- 133. Alexandre Lefebvre, Hakim Larabi, Vincent Moureau, Ghislain Lartigue, Vincent Modica, Emilien Varea, and Bruno Renou. 2016. "Determination of the consumption speed from spherically expanding flame: a new experimental methodology." Paper presented at 18th International Symposium on the Application of Laser and Imaging Techniques to Fluid Mechanics, July 4-7, 2016. Lisbon, Portugal.
- 134. Varea, Emilien, Vincent Modica, Bruno Renou, and Abdelkrim Boukhalfa. 2013. "Pressure effects on laminar burning velocities and Markstein lengths for Isooctane–Ethanol–Air mixtures." *Proceedings of the Combustion Institute* 34 (1): 735-44. https://doi.org/10.1016/j.proci.2012.06.072.
- 135. Varea, Emilien, Joachim Beeckmann, Heinz Pitsch, Zheng Chen, and Bruno Renou. 2015. "Determination of burning velocities from spherically expanding H2/air flames." *Proceedings of the Combustion Institute* 35 (1): 711-9. https://doi.org/10.1016/j.proci.2014.05.137.
- 136. Andrews, Gordon, and Derek Bradley. 1972. "The burning velocity of methane-air mixtures." *Combustion and Flame* 19 (2): 275-88. https://doi.org/10.1016/S0010-2180(72)80218-9.
- 137. Wang, Shuang-Feng, Hai Zhang, Jozef Jarosinski, Andrzej Gorczakowski, and Jerzy Podfilipski. 2010. "Laminar burning velocities and Markstein lengths of premixed methane/air flames near the lean flammability limit in microgravity." *Combustion and Flame* 157 (4): 667-75. https://doi.org/10.1016/j.combustflame.2010.01.006.
- 138. Bradley, Derek, Ralph Hicks, Malcolm Lawes, Christopher Sheppard, and Robert Woolley. 1998. "The Measurement of Laminar Burning Velocities and Markstein Numbers for Isooctane—Air and Iso-octane—n-Heptane—Air Mixtures at Elevated Temperatures and Pressures in an Explosion Bomb." *Combustion and Flame* 115 (1): 126-44. https://doi.org/10.1016/S0010-2180(97)00349-0.
- 139. Gu, Xiaolei, Qianqian Li, Zuohua Huang, and Ni Zhang. 2011. "Measurement of laminar flame speeds and flame stability analysis of tert-butanol—air mixtures at elevated pressures." *Energy Conversion and Management* 52 (10): 3137-46. https://doi.org/10.1016/j.enconman.2011.05.002.
- 140. Kelley, Andrew, and Chung Law. 2009. "Nonlinear effects in the extraction of laminar flame speeds from expanding spherical flames." *Combustion and Flame* 156 (9): 1844-51. https://doi.org/10.1016/j.combustflame.2009.04.004.
- 141. Lamoureux, Nathalie, Nabiha Djebaili-Chaumeix, and Claude Etienne Paillard. 2003. "Laminar flame velocity determination for H2-air-He-CO2 mixtures using the spherical bomb method." *Experimental Thermal and Fluid Science* 27 (4): 385-93. https://doi.org/10.1016/S0894-1777(02)00243-1.

- 142. Jomaas, Grunde, Chung Law, and John Bechtold. 2007. "On transition to cellularity in expanding spherical flames." *Journal of Fluid Mechanics* 583: 1-26. https://doi.org/10.1017/S0022112007005885.
- 143. Lapalme, Denis, Romain Lemaire, and Patrice Seers. 2017. "Assessment of the method for calculating the Lewis number of H2/CO/CH4 mixtures and comparison with experimental results." *International Journal of Hydrogen Energy* 42 (12): 8314-28. https://doi.org/10.1016/j.ijhydene.2017.01.099.
- 144. Law, Chung, and Chihjen Sung. 2000. "Structure, aerodynamics, and geometry of premixed flamelets." *Progress in Energy and Combustion Science* 26 (4): 459-505. https://doi.org/10.1016/S0360-1285(00)00018-6.
- 145. Sun, C. J., Chihjen Sung, Longting He, and Chung Law. 1999. "Dynamics of weakly stretched flames: quantitative description and extraction of global flame parameters." *Combustion and Flame* 118 (1): 108-28. https://doi.org/10.1016/S0010-2180(98)00137-0.
- 146. Burke, Michael, Xiao Qin, Yiguang Ju, and Frederick Dryer. 2007. "Measurements of Hydrogen Syngas Flame Speeds at Elevated Pressures." Paper presented at *the 5th U.S. National Combustion Meeting, March 25-28, 2007.* San Diego, US.
- 147. Bechtold, John, and Moshe Matalon. 2001. "The dependence of the Markstein length on stoichiometry." *Combustion and Flame* 127 (1): 1906-13. https://doi.org/10.1016/S0010-2180(01)00297-8.
- 148. Chen, Zheng. 2011. "On the extraction of laminar flame speed and Markstein length from outwardly propagating spherical flames." *Combustion and Flame* 158 (2): 291-300. https://doi.org/10.1016/j.combustflame.2010.09.001.
- 149. Matalon, Moshe, and Bernard Matkowsky. 2006. "Flames as gasdynamic discontinuities." *Journal of Fluid Mechanics* 124: 239-59. https://doi.org/10.1017/S0022112082002481.
- 150. Gu, Xiaolei, Zuohua Huang, Si Wu, and Qianqian Li. 2010. "Laminar burning velocities and flame instabilities of butanol isomers—air mixtures." *Combustion and Flame* 157 (12): 2318-25. https://doi.org/10.1016/j.combustflame.2010.07.003.
- 151. Kwon, Sejin, Likeng Tseng, and Gerard Faeth. 1992. "Laminar burning velocities and transition to unstable flames in H2/O2/N2 and C3H8/O2/N2 mixtures." *Combustion and Flame* 90 (3): 230-46. https://doi.org/10.1016/0010-2180(92)90085-4.
- 152. Tian, Guohong, Ritchie Daniel, Haiying Li, Hongming Xu, Shijing Shuai, and Paul Richards. 2010. "Laminar Burning Velocities of 2,5-Dimethylfuran Compared with Ethanol and Gasoline." *Energy & Fuels* 24 (7): 3898-905. https://doi.org/10.1021/ef100452c.
- 153. Gomez Casanova, Carlos, Edwin Othen, John Sorensen, David Levin, and Madjid Birouk. 2016. "Measurement of Laminar Flame Speed and Flammability Limits of a Biodiesel Surrogate." *Energy & Fuels* 30 (10): 8737-45. https://doi.org/10.1021/acs.energyfuels.6b01513.

- 154. De, Anupam, David Ting, and David Checkel. 2006. "The Effects of Temperature and Pressure on Stretched, Freely Propagating, Premixed, Laminar Methane-Air Flame." *SAE International* 2006-01-0494. https://doi.org/10.4271/2006-01-0494.
- 155. Markstein, George. 1964. "Chapter D Experimental Studies of Flame-Front Instability." In *AGARDograph* 75: 75-105. Elsevier.
- 156. Clavin, Paul. 1985. "Dynamic behavior of premixed flame fronts in laminar and turbulent flows." *Progress in Energy and Combustion Science* 11 (1): 1-59. https://doi.org/10.1016/0360-1285(85)90012-7.
- 157. Bradley, Derek, and C. M. Harper. 1994. "The development of instabilities in laminar explosion flames." *Combustion and Flame* 99 (3): 562-72. https://doi.org/10.1016/0010-2180(94)90049-3.
- 158. Peters, Norbert. 2000. *Turbulent Combustion*. Cambridge: Cambridge University Press. https://doi.org/10.1017/CBO9780511612701.
- 159. Kelley, Andrew, John Bechtold, and Chung Law. 2011. "Premixed flame propagation in a confining vessel with weak pressure rise." *Journal of Fluid Mechanics* 691: 26-51. https://doi.org/10.1017/jfm.2011.439.
- 160. Wu, Fujia, Wenkai Liang, Zheng Chen, Yiguang Ju, and Chung Law. 2015. "Uncertainty in stretch extrapolation of laminar flame speed from expanding spherical flames." *Proceedings of the Combustion Institute* 35 (1): 663-70. https://doi.org/10.1016/j.proci.2014.05.065.
- 161. Courty, Léo, Khaled Chetehouna, Zheng Chen, Fabien Halter, Christine Mounaïm-Rousselle, and Jean-Pierre Garo. 2014. "Determination of Laminar Burning Speeds and Markstein Lengths of p-Cymene/Air Mixtures Using Three Models." *Combustion Science and Technology* 186 (4-5): 490-503. https://doi.org/10.1080/00102202.2014.883224.
- 162. Ronney, Paul, and Gregory Sivashinsky. 1989. "A Theoretical Study of Propagation and Extinction of Nonsteady Spherical Flame Fronts." *SIAM Journal on Applied Mathematics* 49 (4): 1029-46. https://doi.org/10.1137/0149062.
- 163. Bouvet, Nicolas, Christian Chauveau, Iskender Gökalp, and Fabien Halter. 2011. "Experimental studies of the fundamental flame speeds of syngas (H2/CO)/air mixtures." *Proceedings of the Combustion Institute* 33 (1): 913-20. https://doi.org/10.1016/j.proci.2010.05.088.
- 164. Askari, Mohammad Hossein, and Mehdi Ashjaee. 2017. "Experimental Measurement of Laminar Burning Velocity and Flammability Limits of Landfill Gas at Atmospheric and Elevated Pressures." *Energy & Fuels* 31 (3): 3196-205. https://doi.org/10.1021/acs.energyfuels.6b02941.
- 165. Halter, Fabien, Toni Tahtouh, and Christine Mounaïm-Rousselle. 2010. "Nonlinear effects of stretch on the flame front propagation." *Combustion and Flame* 157 (10): 1825-32. https://doi.org/10.1016/j.combustflame.2010.05.013.

- 166. Singh, Deepti, Takayuki Nishiie, and Li Qiao. 2011. "Experimental and Kinetic Modeling Study of the Combustion of n-Decane, Jet-A, and S-8 in Laminar Premixed Flames." *Combustion Science and Technology* 183 (10): 1002-26. https://doi.org/10.1080/00102202.2011.575420.
- 167. Chen, Zheng, Michael Burke, and Yiguang Ju. 2009. "Effects of Lewis number and ignition energy on the determination of laminar flame speed using propagating spherical flames." *Proceedings of the Combustion Institute* 32 (1): 1253-60. https://doi.org/10.1016/j.proci.2008.05.060.
- 168. Markstein, George. 1951. "Experimental and Theoretical Studies of Flame-Front Stability." *Journal of the Aeronautical Sciences* 18 (3): 199-209. https://doi.org/10.2514/8.1900.
- 169. Tse, Stephen, Delin Zhu, and Chung Law. 2000. "Morphology and burning rates of expanding spherical flames in H2/O2/inert mixtures up to 60 atmospheres." *Proceedings of the Combustion Institute* 28 (2): 1793-1800. https://doi.org/10.1016/S0082-0784(00)80581-0.
- 170. Matalon, Moshe, and John Bechtold. 1987. "Spherically Expanding Flames." *Proceedings of the 1987 ASME-JSME Thermal Engineering Joint Conference, March 22-27, 1987*. Honolulu, Hawaii.
- 171. Krejci, Michael, Olivier Mathieu, Andrew Vissotski, Sankaranarayanan Ravi, Travis Sikes, Eric Petersen, Alan Kérmonès, Wayne Metcalfe, and Henry Curran. 2013. "Laminar Flame Speed and Ignition Delay Time Data for the Kinetic Modeling of Hydrogen and Syngas Fuel Blends." *Journal of Engineering for Gas Turbines and Power* 135 (2): 021503. https://doi.org/10.1115/1.4007737.
- 172. Wang, Yang Lee, Adam Holley, Chungsheng Ji, Fokion Egolfopoulos, Theodore Tsotsis, and Henry Curran. 2009. "Propagation and extinction of premixed dimethyl-ether/air flames." *Proceedings of the Combustion Institute* 32 (1): 1035-42. https://doi.org/10.1016/j.proci.2008.06.054.
- 173. Ji, Chunsheng, Enoch Dames, Yang Wang, Hai Wang, and Fokion Egolfopoulos. 2010. "Propagation and extinction of premixed C5–C12 n-alkane flames." *Combustion and Flame* 157 (2): 277-87. https://doi.org/10.1016/j.combustflame.2009.06.011.
- 174. Veloo, Peter, Yang Wang, Fokion Egolfopoulos, and Charles Westbrook. 2010. "A comparative experimental and computational study of methanol, ethanol, and n-butanol flames." *Combustion and Flame* 157 (10): 1989-2004. https://doi.org/10.1016/j.combustflame.2010.04.001.
- 175. Jayachandran, Jagannath, Alexandre Lefebvre, Runhua Zhao, Fabien Halter, Emilien Varea, Bruno Renou, and Fokion Egolfopoulos. 2015. "A study of propagation of spherically expanding and counterflow laminar flames using direct measurements and numerical simulations." *Proceedings of the Combustion Institute* 35 (1): 695-702. https://doi.org/10.1016/j.proci.2014.05.031.

- 176. Gong, Xue, Jialong Huo, Zhuyin Ren, and Chung K. Law. 2019. "Extrapolation and DNS-mapping in determining laminar flame speeds of syngas/air mixtures." *Combustion and Flame* 200: 365-73. https://doi.org/10.1016/j.combustflame.2018.11.033.
- 177. Kelley, Andrew, Andrew Smallbone, Delin Zhu, and Chung Law. 2011. "Laminar flame speeds of C5 to C8n-alkanes at elevated pressures: Experimental determination, fuel similarity, and stretch sensitivity." *Proceedings of the Combustion Institute* 33 (1): 963-70. https://doi.org/10.1016/j.proci.2010.06.074.
- 178. Matalon, Moshe. 2009. "Flame dynamics." *Proceedings of the Combustion Institute* 32 (1): 57-82. https://doi.org/10.1016/j.proci.2008.08.002.
- 179. Huo, Jialong, Abhishek Saha, Tao Shu, Zhuyin Ren, and Chung Law. 2019. "Globally Oscillating Propagation of Cellular Expanding Flames in Constant Pressure." Paper presented at *the 11th U.S. National Combustion Meeting, March 24-27, 2019.* Pasadena, US.
- 180. Yang, Sheng, Abhishek Saha, Fujia Wu, and Chung Law. 2016. "Morphology and self-acceleration of expanding laminar flames with flame-front cellular instabilities." *Combustion and Flame* 171: 112-8. https://doi.org/10.1016/j.combustflame.2016.05.017.
- 181. Matalon, Moshe. 2018. "The Darrieus–Landau instability of premixed flames." *Fluid Dynamics Research* 50 (5): 051412. https://doi.org/10.1088/1873-7005/aab510.
- 182. Law, Chung, Grunde Jomaas, and John Bechtold. 2005. "Cellular instabilities of expanding hydrogen/propane spherical flames at elevated pressures: theory and experiment." *Proceedings of the Combustion Institute* 30 (1): 159-67. https://doi.org/10.1016/j.proci.2004.08.266.
- 183. Manton, John, Guenther von Elbe, and Bernard Lewis. 1952. "Nonisotropic Propagation of Combustion Waves in Explosive Gas Mixtures and the Development of Cellular Flames." *The Journal of Chemical Physics* 20 (1): 153-7. https://doi.org/10.1063/1.1700159.
- 184. Kochar, Yash, Jerry Seitzman, Timothy Lieuwen, Wayne Metcalfe, Sine´ad Burke, Henry Curran, Michael Krejci, William Lowry, Eric Petersen, and Gilles Bourque. 2011. "Laminar Flame Speed Measurements and Modeling of Alkane Blends at Elevated Pressures With Various Diluents." *Proceedings of the ASME Turbo Expo 2011: Turbine Technical Conference and Exposition, June 6-10, 2011.* Vancouver, Canada. https://doi.org/10.1115/GT2011-45122.
- 185. ASME International. 2015. ASME Boiler and Pressure Vessel Code. New York: ASME.
- 186. Shigley, Joseph, Charles Mischke, and Richard Budynas. 2003. *Mechanical Engineering Design*. New York: McGraw-Hill Press.
- 187. Portland Bolt. n.d. "Bolt Torque Chart." Accessed November 11, 2017. https://www.portlandbolt.com/technical/bolt-torque-chart/.

- 188. Crystran. n.d. "The Design of Pressure Windows." Accessed November 11, 2017. https://www.crystran.co.uk/documents.
- 189. G. Finkenbeiner Inc. n.d. "The Fusion of Art and Science." Accessed November 11, 2017. http://www.finkenbeiner.com/PRESSURE.htm.
- 190. Technical Glass Products. n.d. "Pressure Calculations and Formulas." Accessed November 11, 2017. http://www.technicalglass.com/pressure_calculations.html.
- 191. H. Baumbach & Co. Ltd. n.d. "Properties of Fused Quartz." Accessed November 11, 2017. http://www.h-baumbach.co.uk/Quartzproperties.htm.
- 192. Tse, Stephen, Delin Zhu, and Chung Law. 2004. "Optically accessible high-pressure combustion apparatus." *Review of Scientific Instruments* 75 (1): 233-9. https://doi.org/10.1063/1.1634358.
- 193. Watlow Ez-Zone PM. n.d. "User's Guide: Integrated Controller Models." 198-221.
- 194. Omega. n.d. "Wire Color Codes and Limits of Error." Accessed November 11, 2017. https://www.omega.com/techref/colorcodes.html.
- 195. ASTM International. 2009. E681-09 Standard Test Method for Concentration Limits of Flammability of Chemicals (Vapors and Gases). West Conshohocken: ASTM.
- 196. Ngo, My. 2009. "Determination of the Minimum Ignition Energy of Premixed Propane/Air." Master of Science thesis, University of Bergen. https://hdl.handle.net/1956/3423.
- 197. Babrauskas, Vytenis. 2003. *Ignition Handbook: Principles and Applications to Fire Safety Engineering, Fire Investigation, Risk Management and Forensic Science*. Bethesda: Fire Science.
- 198. Eckhoff, Rolf, My Ngo, and Werner Olsen. 2009. "On the minimum ignition energy (MIE) for propane/air." *Journal of Hazardous Materials* 175 (1-3): 293-7. https://doi.org/10.1016/j.jhazmat.2009.09.162.
- 199. Ko, Yongseo, Richard Anderson, and Vedat Arpaci. 1991. "Spark ignition of propane-air mixtures near the minimum ignition energy: Part I. An experimental study." *Combustion and Flame* 83 (1): 75-87. https://doi.org/10.1016/0010-2180(91)90204-O.
- 200. Ferguson, Colin, and James Keck. 1977. "On laminar flame quenching and its application to spark ignition engines." *Combustion and Flame* 28: 197-205. https://doi.org/10.1016/0010-2180(77)90025-6.
- 201. Friedman, Raymond, and W. C. Johnston. 1952. "Pressure Dependence of Quenching Distance of Normal Heptane, Iso-Octane, Benzene, and Ethyl Ether Flames." *The Journal of Chemical Physics* 20 (5): 919-20. https://doi.org/10.1063/1.1700600.

- 202. Harris, Margaret, Joseph Grumer, Guenther von Elbe, and Bernard Lewis. 1948. "Burning velocities, quenching, and stability data on nonturbulent flames of methane and propane with oxygen and nitrogen: Application of theory of ignition, quenching, and stabilization flames of propane and air." *Symposium on Combustion and Flame, and Explosion Phenomena* 3 (1): 80-9. https://doi.org/10.1016/S1062-2896(49)80010-9.
- 203. Harvard University. 2008. "The Physics of the Automotive Ignition System." Lecture, Harvard Instructional Physics Labs, Cambridge, MA. https://sites.fas.harvard.edu/~scphys/courses/E1b/E1b_3b.pdf.
- 204. Cui, Gan, Zili Li, Chao Yang, Zhen Zhou, and Jianle Li. 2016. "Experimental Study of Minimum Ignition Energy of Methane—Air Mixtures at Low Temperatures and Elevated Pressures." *Energy & Fuels* 30 (8): 6738-44. https://doi.org/10.1021/acs.energyfuels.6b00366.
- 205. Settles, Gary. 2001. Schlieren and Shadowgraph Techniques: Visualizing Phenomena in Transparent Media. 165-261. Berlin: Springer.
- 206. Dereniak, Eustace, and Teresa Dereniak. 2008. *Geometrical and Trigonometric Optics*. Cambridge: Cambridge University Press.
- 207. Wright, Frederic Eugene. 1911. "Spherical Aberrations." In *The Methods of Petrographic-microscopic Research: Their Relative Accuracy and Range of Application*, 204. Washington: Carnegie Institution of Washington.
- 208. Edmund Optics. n.d. "Comparison of Optical Aberrations." Accessed November 11, 2017. https://www.edmundoptics.com/resources/application-notes/optics/comparison-of-optical-aberrations/.
- 209. Edmund Optics. "Aspherized Achromatic Lenses." Accessed November 11, 2017. https://www.edmundoptics.com/resources/application-notes/optics/aspherized-achromatic-lenses/.
- 210. Krejci, Michael. 2012. "Development of a New Flame Speed Vessel to Measure the Effect of Steam Dilution on Laminar Flame Speeds of Syngas Fuel Blends at Elevated Pressures and Temperatures." Master of Science thesis, Texas A&M University. https://hdl.handle.net/1969.1/ETD-TAMU-2012-05-10978.
- 211. Toepler, August. 1867. "Optischen Studien nach der Methode der Schlierenbeobachtung." *Poggendorfs Annalen der Physik und Chemie* 131: 33-55. https://doi.org/10.1002/andp.18672070503.
- 212. Photron. n.d. "FASTCAM SAE5." Accessed November 11, 2017. https://photron.com/fastcam-sa-5/.
- 213. Gonzalez, Rafael, and Richard Woods. 2018. Digital Image Processing. Pearson.

- 214. Taylor, Stephen. 2008. "Radius detection of a spherical flame observed with Schlieren photography." EPSRC summer placement report, University of Oxford.
- 215. Kee, Robert, Joseph Grcar, Mitchell Smooke, James Miller, and Ellen Meeks. 1985. *PREMIX: a fortran program for modeling steady laminar one-dimensional premixed flames*. Livermore: Sandia National Laboratories.
- 216. Karpov, Vladimir, Andrei Lipatnikov, and Piotr Wolanski. 1997. "Finding the markstein number using the measurements of expanding spherical laminar flames." *Combustion and Flame* 109 (3): 436-48. https://doi.org/10.1016/S0010-2180(96)00166-6.
- 217. Li, Xiaotian, Erjiang Hu, Xin Meng, Cheng Peng, Xin Lu, and Zuohua Huang. 2017. "Effect of Lewis Number on Nonlinear Extrapolation Methods from Expanding Spherical Flames." *Combustion Science and Technology* 189 (9): 1510-26. https://doi.org/10.1080/00102202.2017.1305369.
- 218. Cai, Xiao, Jinhua Wang, Haoran Zhao, Yongliang Xie, and Zuohua Huang. 2018. "Effects of Initiation Radius Selection and Lewis Number on Extraction of Laminar Burning Velocities from Spherically Expanding Flames." *Combustion Science and Technology* 190 (2): 286-311. https://doi.org/10.1080/00102202.2017.1389912.
- 219. Lipatnikov, Andrei, Shenqyang Shy, and Wun-yi Li. 2015. "Experimental assessment of various methods of determination of laminar flame speed in experiments with expanding spherical flames with positive Markstein lengths." *Combustion and Flame* 162 (7): 2840-54. https://doi.org/10.1016/j.combustflame.2015.04.003.
- 220. Huo, Jialong, Sheng Yang, Zhuyin Ren, Delin Zhu, and Chung Law. 2018. "Uncertainty reduction in laminar flame speed extrapolation for expanding spherical flames." *Combustion and Flame* 189: 155-62. https://doi.org/10.1016/j.combustflame.2017.10.032.
- 221. Beeckmann, Joachim, Raik Hesse, J. Schaback, Heinz Pitsch, Emilien Varea, and Nabiha Chaumeix. 2019. "Flame propagation speed and Markstein length of spherically expanding flames: Assessment of extrapolation and measurement techniques." *Proceedings of the Combustion Institute* 37 (2): 1521-8. https://doi.org/10.1016/j.proci.2018.08.047.
- 222. ANSYS. 2016. Ansys Chemkin-Pro 17.2. San Diego: ANSYS Reaction Design.
- 223. Smith, Gregory, David Golden, Michael Frenklach, Nigel Moriarty, Boris Eiteneer, Mikhail Goldenberg, Thomas Bowman, Ronald Hanson, Soonho Song, William Gardiner, Vitali Lissianski, and Zhiwei Qin. n.d. "GRI-Mech 3.0." Accessed November 11, 2017. http://combustion.berkeley.edu/gri-mech/version30/text30.html#whatisnew.
- 224. Wang, Hai, Xiaoqing You, Ameya Joshi, Scott Davis, Alexander Laskin, Fokion Egolfopoulos, and Chung Law. 2007. "USC Mech Version II. High-Temperature Combustion Reaction Model of H2/CO/C1-C4 Compounds." Accessed November 11, 2017. http://ignis.usc.edu/USC_Mech_II.htm.

- 225. University of California at San Diego. n.d. "Chemical-Kinetic Mechanisms for Combustion Applications." Accessed November 11, 2017. http://web.eng.ucsd.edu/mae/groups/combustion/mechanism.html.
- 226. Yang, Xueliang, Xiaobo Shen, Jeffery Santer, Hao Zhao, and Yiguang Ju. 2017. "Princeton HP-Mech." Accessed June 13, 2017. http://engine.princeton.edu/mechanism/HP-Mech.html.
- 227. Burke, Ultan, Kieran Somers, Peter O'Toole, Chis Zinner, Nicolas Marquet, Gilles Bourque, Eric Petersen, Wayne Metcalfe, Zeynep Serinyel, and Henry Curran. 2015. "An ignition delay and kinetic modeling study of methane, dimethyl ether, and their mixtures at high pressures."

 Combustion and Flame 162 (2): 315-30.
 https://doi.org/10.1016/j.combustflame.2014.08.014.
- 228. Metcalfe, Wayne, Sinéad Burke, Syed Ahmed, and Henry Curran. 2013. "A Hierarchical and Comparative Kinetic Modeling Study of C1 C2 Hydrocarbon and Oxygenated Fuels." *International Journal of Chemical Kinetics* 45 (10): 638-75. https://doi.org/10.1002/kin.20802.
- 229. Vagelopoulos, Christine, Fokion Egolfopoulos, and Chung Law. 1994. "Further considerations on the determination of laminar flame speeds with the counterflow twin-flame technique." *Symposium (International) on Combustion* 25 (1): 1341-7. https://doi.org/10.1016/S0082-0784(06)80776-9.
- 230. Vagelopoulos, Christine, and Fokion Egolfopoulos. 1998. "Direct experimental determination of laminar flame speeds." *Symposium (International) on Combustion* 27 (1): 513-9. https://doi.org/10.1016/S0082-0784(98)80441-4.
- 231. Egolfopoulos, Fokion, Peck Cho, and Chung Law. 1989. "Laminar flame speeds of methaneair mixtures under reduced and elevated pressures." *Combustion and Flame* 76 (3): 375-91. https://doi.org/10.1016/0010-2180(89)90119-3.
- 232. Akram, Mohammad, and Sudarshan Kumar. 2012. "Measurement of Laminar Burning Velocity of Liquified Petrolium Gas Air Mixtures at Elevated Temperatures." *Energy & Fuels* 26 (6): 3267-74. https://doi.org/10.1021/ef300101n.
- 233. Park, Okjoo, Peter Veloo, David Sheen, Yujie Tao, Fokion Egolfopoulos, and Hai Wang. 2016. "Chemical kinetic model uncertainty minimization through laminar flame speed measurements." *Combustion and Flame* 172: 136-52. https://doi.org/10.1016/j.combustflame.2016.07.004.
- 234. Ren, Fei, Huaqiang Chu, Longkai Xiang, Weiwei Han, and Mingyan Gu. 2019. "Effect of hydrogen addition on the laminar premixed combustion characteristics the main components of natural gas." *Journal of the Energy Institute* 92 (4): 1178-90. https://doi.org/10.1016/j.joei.2018.05.011.
- 235. Santner, Jeffrey, Frederick Dryer, and Yiguang Ju. 2013. "The effects of water dilution on hydrogen, syngas, and ethylene flames at elevated pressure." *Proceedings of the Combustion Institute* 34 (1): 719-26. https://doi.org/10.1016/j.proci.2012.06.065.

- 236. Kéromnès, Alan, Wayne Metcalfe, Karl Heufer, Nicola Donohoe, Apurba Das, Chih-Jen Sung, Jürgen Herzler, Clemens Naumann, Peter Griebel, Olivier Mathieu, Michael Krejci, Eric Petersen, William Pitz, and Henry Curran. 2013. "An experimental and detailed chemical kinetic modeling study of hydrogen and syngas mixture oxidation at elevated pressures." *Combustion and Flame* 160 (6): 995-1011. https://doi.org/10.1016/j.combustflame.2013.01.001.
- 237. Burke, Sinéad, Wayne Metcalfe, Olivier Herbinet, Frédérique Battin-Leclerc, Francis Haas, Jeffrey Santner, Frederick Dryer, and Henry Curran. 2014. "An experimental and modeling study of propene oxidation. Part 1: Speciation measurements in jet-stirred and flow reactors."

 Combustion and Flame 161 (11): 2765-84.
 https://doi.org/10.1016/j.combustflame.2014.05.010.
- 238. National University of Ireland. 2013. "AramcoMech 1.3 Supplementary Material." Accessed January 29, 2020. http://www.nuigalway.ie/media/researchcentres/combustionchemistrycentre/files/mechanis mdownloads/supp_mat_v9.pdf.
- 239. Chaos, Marcos, Andrei Kazakov, Zhenwei Zhao, and Frederick Dryer. 2007. "A high-temperature chemical kinetic model for primary reference fuels." *International Journal of Chemical Kinetics* 39 (7): 399-414. https://doi.org/10.1002/kin.20253.
- 240. Jerzembeck, Sven, Norbert Peters, Perrine Pepiot-Desjardins, and Heinz Pitsch. 2009. "Laminar burning velocities at high pressure for primary reference fuels and gasoline: Experimental and numerical investigation." *Combustion and Flame* 156 (2): 292-301. https://doi.org/10.1016/j.combustflame.2008.11.009.
- 241. Li, Juan, Zhenwei Zhao, Andrei Kazakov, and Frederick Dryer. 2004. "An updated comprehensive kinetic model of hydrogen combustion." *International Journal of Chemical Kinetics* 36 (10): 566-75. https://doi.org/10.1002/kin.20026.
- 242. Zhao, Zhenwei, Juan Li, Andrei Kazakov, Frederick Dryer, and Stephen Zeppieri. 2004. "Burning Velocities and a High-Temperature Skeletal Kinetic Model for n-Decane." *Combustion Science and Technology* 177 (1): 89-106. https://doi.org/10.1080/00102200590883769.
- 243. Curran, Henry, Paolo Gaffuri, William Pitz, and Charles Westbrook. 2002. "A comprehensive modeling study of iso-octane oxidation." *Combustion and Flame* 129 (3): 253-80. https://doi.org/10.1016/S0010-2180(01)00373-X.
- 244. Mehl, Marco, William Pitz, Magnus Sjöberg, and John Dec. 2009. "Detailed Kinetic Modeling of Low-Temperature Heat Release for PRF Fuels in an HCCI Engine." *SAE International* 2009-01-1806. https://doi.org/10.4271/2009-01-1806.
- 245. Mehl, Marco, Henry Curran, William Pitz, and Charles Westbrook. 2009. "Chemical kinetic modeling of component mixtures relevant to gasoline." *Proceedings of the 4th European Combustion Meeting, April 14-17, 2009.* Vienna, Austria.

- 246. Konnov, Alexander. 2008. "Remaining uncertainties in the kinetic mechanism of hydrogen combustion." *Combustion and Flame* 152 (4): 507-28. https://doi.org/10.1016/j.combustflame.2007.10.024.
- 247. Ó Conaire, Marcus, Henry Curran, John Simmie, William Pitz, and Charles Westbrook. 2004. "A comprehensive modeling study of hydrogen oxidation." *International Journal of Chemical Kinetics* 36 (11): 603-22. https://doi.org/10.1002/kin.20036.
- 248. Mueller, Mark, T. J. Kim, Richard Yetter, and Frederick Dryer. 1999. "Flow reactor studies and kinetic modeling of the H2/O2 reaction." *International Journal of Chemical Kinetics* 31 (2): 113-25. https://doi.org/10.1002/(SICI)1097-4601(1999)31:2<113::AID-KIN5>3.0.CO;2-0.
- 249. Konnov, Alexander. 2004. "Refinement of the kinetic mechanism of hydrogen combustion." *Khimicheskaya Fizika* 23 (8): 5-18.
- 250. Baulch, Donald, Tom Bowman, Carlos Cobos, Richard Anthony Cox, Thomas Just, Alistair Kerr, Michael Pilling, D. Stocker, Juergen Troe, Wing Tsang, Raymond Walker, and Juergen Warnatz. 2005. "Evaluated Kinetic Data for Combustion Modeling: Supplement II." *Journal of Physical and Chemical Reference Data* 34 (3): 757-1397. https://doi.org/10.1063/1.1748524.
- 251. Atkinson, Richard, Donald Baulch, Richard Anthony Cox, John Crowley, Robert Hampson, Rebeka Hynes, Michael Jenkin, Michel Rossi, and Juergen Troe. 2004. "Evaluated kinetic and photochemical data for atmospheric chemistry: Volume I gas phase reactions of Ox, HOx, NOx and SOx species." *Atmospheric Chemistry and Physics* 4 (6): 1461-738. https://doi.org/10.5194/acp-4-1461-2004.
- 252. Qin, Zhiwei, Vitali Lissianski, Huixing Yang, William Gardiner, Scott Davis, and Hai Wang. 2000. "Combustion chemistry of propane: A case study of detailed reaction mechanism optimization." *Proceedings of the Combustion Institute* 28 (2): 1663-9. https://doi.org/10.1016/S0082-0784(00)80565-2.
- 253. Davis, Scott, Ameya Joshi, Hai Wang, and Fokion Egolfopoulos. 2005. "An optimized kinetic model of H2/CO combustion." *Proceedings of the Combustion Institute* 30 (1): 1283-92. https://doi.org/10.1016/j.proci.2004.08.252.
- 254. Wang, Hai, Alexander Laskin, Zoran Djurisic, Chung Law, Scott Davis, and Delin Zhu. 1999. "A comprehensive mechanism of C2Hx and C3Hx fuel combustion." Paper presented at *the 1999 Fall Technical Meeting of the Eastern States Section of the Combustion Institute, October 13-15, 1999.* Raleigh, US.
- 255. Davis, Scott, Chung Law, and Hai Wang. 1999. "Propene pyrolysis and oxidation kinetics in a flow reactor and laminar flames." *Combustion and Flame* 119 (4): 375-99. https://doi.org/10.1016/S0010-2180(99)00070-X.
- 256. Laskin, Alexander, Hai Wang, and Chung Law. 2000. "Detailed kinetic modeling of 1,3-butadiene oxidation at high temperatures." *International Journal of Chemical Kinetics* 32

- (10): 589-614. https://doi.org/10.1002/1097-4601(2000)32:10<589::AID-KIN2>3.0.CO;2-U.
- 257. Bramlette, Richard, and Christopher Depcik. 2020. "Review of propane-air chemical kinetic mechanisms for a unique jet propulsion application." *Journal of the Energy Institute* 93 (3): 857-77. https://doi.org/10.1016/j.joei.2019.07.010.
- 258. Davis, Scott, Chung Law, and Hai Wang. 1998. "An experimental and kinetic modeling study of propyne oxidation." *Symposium (International) on Combustion* 27 (1): 305-12. https://doi.org/10.1016/S0082-0784(98)80417-7.
- 259. Davis, Scott, Chung Law, and Hai Wang. 1999. "Propyne Pyrolysis in a Flow Reactor: An Experimental, RRKM, and Detailed Kinetic Modeling Study." *The Journal of Physical Chemistry A* 103 (30): 5889-99. https://doi.org/10.1021/jp982762a.
- 260. Akram, Mohammad, Ratna Kishore, and Sudarshan Kumar. 2012. "Laminar Burning Velocity of Propane/CO2/N2–Air Mixtures at Elevated Temperatures." *Energy & Fuels* 26 (9): 5509-18. https://doi.org/10.1021/ef301000k.
- 261. Moffat, Robert. 1988. "Describing the uncertainties in experimental results." *Experimental Thermal and Fluid Science* 1 (1): 3-17. https://doi.org/10.1016/0894-1777(88)90043-X.
- 262. Grubbs, Frank. 1969. "Procedures for Detecting Outlying Observations in Samples." *Technometrics* 11 (1): 1-21. https://doi.org/10.1080/00401706.1969.10490657.
- 263. Stefansky, Wilhelmine. 1972. "Rejecting Outliers in Factorial Designs." *Technometrics* 14 (2): 469-79. https://doi.org/10.1080/00401706.1972.10488930.
- 264. Dong, Chen, Qulan Zhou, Xiaoguang Zhang, Qinxin Zhao, Tongmo Xu, and Shi'en Hui. 2010. "Experimental study on the laminar flame speed of hydrogen/natural gas/air mixtures." *Frontiers of Chemical Engineering in China* 4 (4): 417-22. https://doi.org/10.1007/s11705-010-0515-8.
- 265. Pareja, Jhon, Hugo Burbano, and Yasuhiro Ogami. 2010. "Measurements of the laminar burning velocity of hydrogen—air premixed flames." *International Journal of Hydrogen Energy* 35 (4): 1812-8. https://doi.org/10.1016/j.ijhydene.2009.12.031.
- 266. Zhao, Zhenwei, Andrei Kazakov, Juan Li, and Frederick Dryer. 2004. "The Initial Temperature and N_2 Dilution Effect on the Laminar Flame Speed of Propane/Air." *Combustion Science and Technology* 176 (10): 1705-23. https://doi.org/10.1080/00102200490487553.
- 267. Dirrenberger, Patricia, Hervé Le Gall, Roda Bounaceur, Olivier Herbinet, Pierre-Alexandre Glaude, Alexander Konnov, and Frédérique Battin-Leclerc. 2011. "Measurements of Laminar Flame Velocity for Components of Natural Gas." *Energy & Fuels* 25 (9): 3875-84. https://doi.org/10.1021/ef200707h.

- 268. Miao, Jing, Chunwah Leung, Zuohua Huang, Chun Shun Cheung, Huibin Yu, and Yongliang Xie. 2014. "Laminar burning velocities, Markstein lengths, and flame thickness of liquefied petroleum gas with hydrogen enrichment." *International Journal of Hydrogen Energy* 39 (24): 13020-30. https://doi.org/10.1016/j.ijhydene.2014.06.087.
- 269. Endouard, Charles, Fabien Halter, Christian Chauveau, and Fabrice Foucher. 2016. "Effects of CO2, H2O, and Exhaust Gas Recirculation Dilution on Laminar Burning Velocities and Markstein Lengths of Iso-Octane/Air Mixtures." *Combustion Science and Technology* 188 (4-5): 516-28. https://doi.org/10.1080/00102202.2016.1138792.
- 270. Hu, Erjiang, Jinfeng Ku, Geyuan Yin, Chanchan Li, Xin Lu, and Zuohua Huang. 2018. "Laminar Flame Characteristics and Kinetic Modeling Study of Ethyl Tertiary Butyl Ether Compared with Methyl Tertiary Butyl Ether, Ethanol, iso-Octane, and Gasoline." *Energy & Fuels* 32 (3): 3935-49. https://doi.org/10.1021/acs.energyfuels.7b03636.
- 271. Cracknell, Roger, Arjun Prakash, and Robert Head. 2012. "Influence of Laminar Burning Velocity on Performance of Gasoline Engines." *SAE International* 2012-01-1742. https://doi.org/10.4271/2012-01-1742.
- 272. Huang, Yimin, Chihjen Sung, and James Eng. 2004. "Laminar flame speeds of primary reference fuels and reformer gas mixtures." *Combustion and Flame* 139 (3): 239-51. https://doi.org/10.1016/j.combustflame.2004.08.011.
- 273. Kumar, Kamal, Joshua Freeh, Chihjen Sung, and Yimin Huang. 2007. "Laminar Flame Speeds of Preheated iso-Octane/O2/N2 and n-Heptane/O2/N2 Mixtures." *Journal of Propulsion and Power* 23 (2): 428-36. https://doi.org/10.2514/1.24391.
- 274. van Lipzig, J. P. J., Elna Nilsson, Philip de Goey, and Alexander Konnov. 2011. "Laminar burning velocities of n-heptane, iso-octane, ethanol and their binary and tertiary mixtures." *Fuel* 90 (8): 2773-81. https://doi.org/10.1016/j.fuel.2011.04.029.
- 275. Sileghem, Louis, Vladimir Alekseev, Jeroen Vancoillie, Kevin Van Geem, Elna Nilsson, Sebastian Verhelst, and Alexander Konnov. 2013. "Laminar burning velocity of gasoline and the gasoline surrogate components iso-octane, n-heptane and toluene." *Fuel* 112: 355-65. https://doi.org/10.1016/j.fuel.2013.05.049.
- 276. Dirrenberger, Patricia, Pierre-Alexandre Glaude, Roda Bounaceur, Herve Le Gall, Antonio Pires da Cruz, Alexander Konnov, and Frederique Battin-Leclerc. 2014. "Laminar burning velocity of gasolines with addition of ethanol." *Fuel* 115: 162-9. https://doi.org/10.1016/j.fuel.2013.07.015.
- 277. Stanglmaier, Rudolf, Charles Roberts, Darius Mehta, Christopher Chadwell, Corwin Snyder, Matthew Watkins, and Noyes Avery. 2003. "Measurement of Laminar Burning Velocity of Multi-Component Fuel Blends for Use in High-Performance SI Engines." *SAE International* 2003-01-3185. https://doi.org/10.4271/2003-01-3185.

- 278. Zhao, Zhenwei, Jordan Conley, Andrei Kazakov, and Frederick Dryer. 2003. "Burning Velocities of Real Gasoline Fuel at 353 K and 500 K." *SAE International* 2003-01-3265. https://doi.org/10.4271/2003-01-3265.
- 279. Jerzembeck, Sven, Abhinav Sharma, and Norbert Peters. 2008. "Laminar Burning Velocities of Nitrogen Diluted Standard Gasoline-Air Mixture." *SAE International* 2008-01-1075. https://doi.org/10.4271/2008-01-1075.
- 280. Bhattacharya, Atmadeep, Deb Kumar Banerjee, Dmitrii Mamaikin, Amitava Datta, and Michael Wensing. 2015. "Effects of Exhaust Gas Dilution on the Laminar Burning Velocity of Real-World Gasoline Fuel Flame in Air." *Energy & Fuels* 29 (10): 6768-79. https://doi.org/10.1021/acs.energyfuels.5b01299.
- 281. Galmiche, Benedicte, Fabien Halter, Fabrice Foucher, and Philippe Dagaut. 2011. "Effects of Dilution on Laminar Burning Velocity of Premixed Methane/Air Flames." *Energy & Fuels* 25 (3): 948-54. https://doi.org/10.1021/ef101482d.
- 282. Zahedi, Peyman, and Kianoosh Yousefi. 2014. "Effects of pressure and carbon dioxide, hydrogen and nitrogen concentration on laminar burning velocities and NO formation of methane-air mixtures." *Journal of Mechanical Science and Technology* 28 (1): 377-86. https://doi.org/10.1007/s12206-013-0970-5.
- 283. Mendieta, Miguel, Dario Alviso, and Rogério Gonçalves dos Santos. 2016. "Numerical study of laminar premixed methane/air flames with carbon dioxide dilution." Paper presented at *16th Brazilian Congress of Thermal Sciences and Engineering, November 7-10, 2016.* Vitoria, Brazil.
- 284. Chan, Yii Leng, Ming Zhu, Zhezi Zhang, Peng Liu, and Dong Zhang. 2015. "The Effect of CO2 Dilution on the Laminar Burning Velocity of Premixed Methane/Air Flames." *Energy Procedia* 75: 3048-53. https://doi.org/10.1016/j.egypro.2015.07.621.
- 285. Qiao, Li, Yanan Gan, Takayuki Nishiie, Werner Dahm, and Elaine Oran. 2010. "Extinction of premixed methane/air flames in microgravity by diluents: Effects of radiation and Lewis number." *Combustion and Flame* 157 (8): 1446-55. https://doi.org/10.1016/j.combustflame.2010.04.004.
- 286. Khan, Abdul Rahman, S. Anbusaravanan, Lokesh Kalathi, Ratnakishore Velamati, and Chockalingam Prathap. 2017. "Investigation of dilution effect with N2/CO2 on laminar burning velocity of premixed methane/oxygen mixtures using freely expanding spherical flames." *Fuel* 196: 225-32. https://doi.org/10.1016/j.fuel.2017.01.086.
- 287. Van Maaren, A., D. S. Thung, and Philip De Goey. 1994. "Measurement of Flame Temperature and Adiabatic Burning Velocity of Methane/Air Mixtures." *Combustion Science and Technology* 96 (4-6): 327-44. https://doi.org/10.1080/00102209408935360.
- 288. Aung, Kendrick, Likeng Tseng, Mostafa Ismail, and Gerard Faeth. 1995. "Response to comment by S.C. Taylor and D.B. Smith on "laminar burning velocities and Markstein

- numbers of hydrocarbon/air flames"." *Combustion and Flame* 102 (4): 526-30. https://doi.org/10.1016/0010-2180(95)00035-5.
- 289. Chen, Zheng, Xiao Qin, Yiguang Ju, Zhenwei Zhao, Marcos Chaos, and Frederick Dryer. 2007. "High temperature ignition and combustion enhancement by dimethyl ether addition to methane—air mixtures." *Proceedings of the Combustion Institute* 31 (1): 1215-22. https://doi.org/10.1016/j.proci.2006.07.177.
- 290. Varea, Emilien. 2013. "Experimental analysis of laminar spherically expanding flames." Doctoral dissertation, INSA de Rouen. https://tel.archives-ouvertes.fr/tel-00800616/file/TheseEmilien.pdf.
- 291. Mazas, Antoine, Benoit Fiorina, Deanna Lacoste, and Thierry Schuller. 2011. "Effects of water vapor addition on the laminar burning velocity of oxygen-enriched methane flames." *Combustion and Flame* 158 (12): 2428-40. https://doi.org/10.1016/j.combustflame.2011.05.014.
- 292. Hu, Erjiang, Xue Jiang, Zuohua Huang, and Norimasa Iida. 2012. "Numerical Study on the Effects of Diluents on the Laminar Burning Velocity of Methane–Air Mixtures." *Energy & Fuels* 26 (7): 4242-52. https://doi.org/10.1021/ef300535s.
- 293. Han, Panfeng, David Checkel, Brian Fleck, and Natalie Nowicki. 2007. "Burning velocity of methane/diluent mixture with reformer gas addition." *Fuel* 86 (4): 585-96. https://doi.org/10.1016/j.fuel.2006.08.011.
- 294. Gülder, Ömer. 1984. "Correlations of Laminar Combustion Data for Alternative S.I. Engine Fuels." *SAE International* 841000. https://doi.org/10.4271/841000.
- 295. Moccia, Vincenzo, and Jacopo D'Alessio. 2013. "Burning Behaviour of High-Pressure CH4-H2-Air Mixtures." *Energies* 6 (1): 97-116. https://doi.org/10.3390/en6010097.
- 296. Hinton, Nathan, Richard Stone, and Roger Cracknell. 2018. "Laminar burning velocity measurements in constant volume vessels Reconciliation of flame front imaging and pressure rise methods." *Fuel* 211: 446-57. https://doi.org/10.1016/j.fuel.2017.09.031.
- 297. Amirante, Riccardo, Elia Distaso, Paolo Tamburrano, and Rolf Reitz. 2017. "Laminar flame speed correlations for methane, ethane, propane and their mixtures, and natural gas and gasoline for spark-ignition engine simulations." *International Journal of Engine Research* 18 (9): 951-70. https://doi.org/10.1177/1468087417720018.
- 298. Glassman, Irvin, Richard Yetter, and Nick Glumac. 2015. "Chapter 4 Flame phenomena in premixed combustible gases." In *Combustion*, 147-254. Boston: Academic Press.
- 299. Zeldovich, Yakov Borisovich, and David Frank-Kamenetsky. 1938. "Theory of the thermal flame propagation." *Zhurnal Fizicheskoi Khimii* 12: 100-5.
- 300. Lewis, Bernard, and Guenther von Elbe. 1934. "On the Theory of Flame Propagation." *The Journal of Chemical Physics* 2 (8): 537-46. https://doi.org/10.1063/1.1749523.

- 301. Lasdon, Leon, Allan Waren, Anil Kumar Jain, and M. Ratner. 1978. "Design and Testing of a Generalized Reduced Gradient Code for Nonlinear Programming." *ACM Transactions on Mathematical Software* 4 (1): 34-50. https://doi.org/10.1145/355769.355773.
- 302. Veynante, Denis, and Luc Vervisch. 2002. "Turbulent combustion modeling." *Progress in Energy and Combustion Science* 28 (3): 193-266. https://doi.org/10.1016/S0360-1285(01)00017-X.
- 303. Spaenaur. 2018. "Tension Loads / Tightening Torques." Accessed June 13, 2018. https://spaenaur.com/wp-content/uploads/2018/05/Tensioning-Loads-and-Tightening-Torques-Chart-and-Guide-R7.pdf.